Net Responses in Nonlinear Dynamical Systems

By

SEYYED MOHAMMAD HOSSEIN HASHEMI AMREI

DISSERTATION

Submitted in partial satisfaction of the requirements for the degree of

DOCTOR OF PHILOSOPHY

in

CHEMICAL ENGINEERING

in the

OFFICE OF GRADUATE STUDIES

of the

UNIVERSITY OF CALIFORNIA

DAVIS

Approved:

Gregory H. Miller, Chair

William D. Ristenpart

Ronald J. Phillips

Committee in Charge

2021

Abstract

This dissertation focuses on nonlinear dynamical systems with net responses. In particular, we discover a steady field induced within liquids by a sinusoidal potential, referred to as Asymmetric Rectified Electric Field (AREF). AREF helps explain several long-standing discrepancies regarding the behavior of particles and electrically induced fluid flows in response to oscillatory potentials, broadly impacts the interpretation of the experiments, and offers new avenues for research in electrokinetics.[1–5] Additionally, we demonstrate that non-antiperiodic, zero-time-average, excitation of a spatially symmetric system can yield net responses. We consider an object atop a flat surface that undergoes a dual-mode horizontal vibration. Our calculations, and subsequent experimental observations, show that the object experiences a net drift if the applied frequencies are the ratio of odd and even numbers (e.g., 1 Hz and 2 Hz). As a corollary, our theory suggests that swapping the powered (non-antiperiodic potential) and the grounded parallel electrodes of an electrochemical cell alters the system behavior, a prediction verified by our experimental observations on the AREF-induced electrophoresis.[6,7]

Publication List

[1] **S. M. H. Hashemi Amrei**, Scott C. Bukosky, Sean P. Rader, William D. Ristenpart, Gregory H. Miller. Oscillating electric fields in liquids create a long-range steady field. ***Physical Review Letters*** 121, 185504 (**2018**) *https://doi.org/10.1103/PhysRevLett.121.185504*.

[2] (*Co-first authors*) Scott C. Bukosky, **S. M. H. Hashemi Amrei**, Sean P. Rader, Jeronimo Mora, Gregory H. Miller, William D. Ristenpart. Extreme levitation of colloidal particles in response to oscillatory electric fields. ***Langmuir*** 35, 6971–6980 (**2019**) *https://doi.org/10.1021/acs.langmuir.9b00313*.

[3] **S. M. H. Hashemi Amrei**, Gregory H. Miller, William D. Ristenpart. Asymmetric rectified electric fields between parallel electrodes: numerical and scaling analyses. ***Physical Review E*** 99, 062603 (**2019**) *https://doi.org/10.1103/PhysRevE.99.062603*.

[4] (*Editors' Suggestion*) **S. M. H. Hashemi Amrei**, Gregory H. Miller, William D. Ristenpart. Asymmetric rectified electric fields generate flows that can dominate induced-charge electrokinetics. ***Physical Review Fluids*** 5, 013702 (**2020**) *https://doi.org/10.1103/PhysRevFluids.5.013702*.

[5] **S. M. H. Hashemi Amrei**, Gregory H. Miller, Kyle J. M. Bishop, William D. Ristenpart. A perturbation solution to the full Poisson–Nernst–Planck equations yields an asymmetric rectified electric field. ***Soft Matter*** 16, 7052–7062 (**2020**) *https://doi.org/10.1039/D0SM00417K*.

[6] **S. M. H. Hashemi Amrei**, Mehrdad Tahernia, T. C. Hui, William D. Ristenpart, Gregory H. Miller. Non-antiperiodic force excitations in isotropic media yield net motion of macroscopic objects. ***In Preparation***.

[7] **S. M. H. Hashemi Amrei**, T. C. Hui, Mehrdad Tahernia, William D. Ristenpart, Gregory H. Miller. Multimodal asymmetric rectified electric fields and long-range symmetry breaking in electric field orientation. ***In Preparation***.

Acknowledgements

I would like to thank the large group of people who have helped me on my way here at UC Davis. First, I would like to express my sincere gratitude to my advisors, *Professor Gregory H. Miller* and *Professor William D. Ristenpart*, for their exemplary academic guidance and mentorship throughout my PhD.

I would like to extend my gratitude to our collaborator *Prof. Kyle J. M. Bishop* at the Columbia University. Also, I like to thank the National Science Foundation (Grant No. DMS-1664679), and the corresponding Principal Investigators, *Prof. Robert D. Guy*, *Prof. Gregory H. Miller*, and *Prof. Becca Thomases*, for the partial financial support of my research.

Many thanks to my colleagues *Scott C. Bukosky* and *Timothy C. Hui* for the significant contributions to my research. Their experimental studies on the asymmetric rectified electric field helped verified my theory. I am also very thankful to *Bakytzhan Kallemov*, who kindly assisted me with the code development in Chombo. Furthermore, I would like to thank my brilliant friend, *Mehrdad Tahernia*, for the stimulating discussions on theory, and also, designing and performing experiments on the ratchet dynamics.

I am very thankful to all of *my teachers*, for their kindness, patience, and invaluable contributions. Special thanks to my family and friends for their love and support throughout my education and research journey.

Finally, and above all, I would like to thank my sweet wife and best friend, *Sima*, for her love, support, and encouragement.

This thesis is dedicated to Sima, the joy of my life.

Contents

Abstract ii

Publication List iii

Acknowledgements iv

1 Introduction & Outline 1
- 1.1 ASYMMETRIC RECTIFIED ELECTRIC FIELD . . . 1
- 1.2 RATCHET DYNAMICS . . . 2

2 Oscillating Electric Fields in Liquids Create a Long-Range Steady Field 4
- 2.1 INTRODUCTION . . . 5
- 2.2 TOY MODEL . . . 5
- 2.3 ELECTROKINETIC MODEL . . . 7
- 2.4 RESULTS, DISCUSSION, AND IMPLICATIONS . . . 7

3 Asymmetric Rectified Electric Fields between Parallel Electrodes: Numerical and Scaling Analyses 13
- 3.1 INTRODUCTION . . . 14
- 3.2 THEORY AND NUMERICAL METHODS . . . 16
  - 3.2.1 Standard electrokinetic model . . . 16
  - 3.2.2 Dimensionless form . . . 18
  - 3.2.3 Numerical solution . . . 21
- 3.3 NUMERICAL RESULTS . . . 22
  - 3.3.1 Representative field and charge distributions . . . 22
  - 3.3.2 Effect of applied potential (Φ_0) . . . 24
  - 3.3.3 Effect of diffusive length scale ($\mathcal{L}_D$) . . . 25
  - 3.3.4 Effect of ionic mobility mismatch (δ) . . . 27
  - 3.3.5 Effect of dimensionless Debye parameter (κH) . . . 28
  - 3.3.6 Effect of ionic valences ($z_\pm$) . . . 30
- 3.4 SCALING EXPRESSIONS . . . 31
  - 3.4.1 AREF length scale and structure . . . 31

3.4.2 AREF magnitude scaling . . . 34
3.5 CONCLUSIONS . . . 36

4 Asymmetric Rectified Electric Fields Generate Flows that Can Dominate Induced-Charge Electrokinetics 38
4.1 INTRODUCTION . . . 39
4.2 GENERALIZED ICEK FOR ARBITRARY ELECTRIC FIELD . . . 40
4.3 SOLUTION TO THE ELECTROKINETIC MODEL . . . 42
4.3.1 Linear solution . . . 44
4.3.2 Nonlinear solution . . . 44
4.4 ICEK FLOW WITH AREF . . . 46
4.5 CONCLUSIONS . . . 51

5 A Perturbation Solution to the Full Poisson–Nernst–Planck Equations Yields an Asymmetric Rectified Electric Field 53
5.1 INTRODUCTION . . . 54
5.2 THEORY . . . 56
5.2.1 Poisson–Nernst–Planck equations . . . 56
5.2.2 Dimensionless form . . . 57
5.3 APPROXIMATE SOLUTION . . . 59
5.3.1 Perturbation expansion in Φ_0 . . . 59
5.4 RESULTS AND DISCUSSION . . . 64
5.4.1 First-order solution . . . 64
5.4.2 Second-order solution . . . 66
5.5 CONCLUSIONS . . . 71

6 Non-Antiperiodic Force Excitations in Isotropic Media Yield Net Motion of Macroscopic Objects 72
6.1 SOLID-SOLID FRICTION . . . 73
6.2 ELECTROKINETICS . . . 76
6.3 OTHER EXAMPLES . . . 77
6.4 METHODS . . . 78

7 Multimodal Asymmetric Rectified Electric Fields and Long-Range Symmetry Breaking in Electric Field Orientation 80
7.1 INTRODUCTION . . . 81
7.2 ELECTROKINETIC MODEL . . . 81
7.3 RESULTS, DISCUSSION, AND IMPLICATIONS . . . 82

8 Concluding Remarks and Future Work **88**
8.1 MAIN FINDINGS . . . 88
8.2 FUTURE WORK SUGGESTIONS . . . 88
8.2.1 Numerical & perturbation solutions to the 2-D PNP equations . . . 88
8.2.2 Fast electrophoretic translation of charged colloids via AREF . . . 89
8.2.3 Physics behind the non-antiperiodic excitations & implications . . . 89

Appendices **90**

A Miscellaneous Supplemental Material **90**
A.1 TWO-ION MODEL . . . 90
A.2 NUMERICAL SOLUTION . . . 91
A.2.1 Governing equations . . . 91
A.2.2 Discretization . . . 92
A.2.3 Operator splitting . . . 93
A.2.4 Harmonic solution . . . 94
A.2.5 Validation . . . 95
A.2.6 FFT analysis . . . 96
A.2.7 Behavior of AREF near the electrode . . . 98
A.3 AREF-INDUCED FORCES . . . 98
A.4 STREAMLINES . . . 99
A.4.1 AREF-induced electroosmosis in bispherical coordinates . . . 100
A.5 SUPPLEMENTAL RESULTS . . . 103
A.6 PARTICLE HEIGHT BIFURCATION . . . 106
A.6.1 Hypothesis . . . 106
A.6.2 Materials and methods . . . 106

B Generalized ICEK **108**
B.1 VELOCITY PROFILES & STREAMLINES . . . 108
B.2 GENERALIZED INDUCED DIPOLE STRENGTH . . . 110

C Perturbation Solution **112**
C.1 FIRST-ORDER SOLUTION ($\gamma = 0$, $\beta^2\Omega^2 = \frac{1}{4}$) . . . 112
C.2 NUMERICAL SOLUTION TO Equation 5.49 . . . 113
C.3 PYTHON SOLVER OF Equation 5.49 . . . 114

D Two-Mode Potentials & Symmetry Arguments **121**
D.1 PERTURBATION SOLUTION (TWO-MODE) . . . 121
D.1.1 Second-order perturbation solution (single-mode) . . . 121
D.1.2 Second-order perturbation solution (two-mode) . . . 123
D.2 ANTIPERIODIC & NON-ANTIPERIODIC TWO-MODE POTENTIALS . . . 126

Bibliography **128**

Chapter 1

Introduction & Outline

1.1 ASYMMETRIC RECTIFIED ELECTRIC FIELD

Many systems of practical and scientific importance involve application of an oscillatory electric potential to a liquid, including electrohydrodynamic (EHD) manipulation of colloids and bioparticles,[8–14] induced-charge electrokinetics (ICEK),[15–19] and ac electroosmosis (ACEO),[20–23] to name a few. In continuum theory, analysis of such systems is based on the Poisson–Nernst–Planck (PNP) equations, also referred to as the standard electrokinetic model.[24] The Poisson equation relates the free charge density to the Laplacian of the electric potential via Gauss's law, and the transport of dissolved ions is governed by the electromigrative and diffusive fluxes. The PNP equations are nonlinear, extremely stiff, and coupled, and are characterized with an immense disparity of time and length scales for practical electrokinetic systems. As a result, researchers have often resorted to simplifying assumptions that significantly reduce the problem, but rarely pertains to actual systems.[25–31] The frequently invoked assumptions include the low applied potentials (less than the thermal potential), which allows linearization of the problem and various first-order perturbation solutions, and/or ions of equal mobilities. In practice, however, electrokinetic systems operate at $\sim$ 100 thermal potentials, and most ion pairs have a considerable mobility mismatch (e.g., hydroxide ion is four times faster than the sodium ion). More importantly, the reduced models fail to even *qualitatively* predict the experimental observations in a variety of electrokinetic systems. Despite a tremendous body of experimental and theoretical studies, the underlying reasons of the discrepancies remained obscure.[32,33]

The qualitative discrepancies between the experiments and theory (e.g., the direction of induced flows) indicate that there might be an unknown phenomenon contributing to the problem. Additionally, the discrepancies tend to intensify with the potential amplitude (increased nonlinearity), and also in liquids with a significant ionic mobility mismatch. Perhaps, an accurate solution to the PNP equations, with no simplifying assumptions, could potentially resolve the discrepancies. The first, and major, portion of this dissertation revolves around this problem. We considered the simplest possible configuration of a liquid confined between two parallel, planar, blocking electrodes that are powered by a sinusoidal electric potential. We, for the first time, numerically solved the

corresponding full nonlinear PNP equations, using operator splitting and mesh refinement. Our results indicate that the induced electric field within the liquid is multimodal and spatially nonuniform, with a zero-frequency component (a nonzero-time-average), given that the dissolved ions have an ionic mobility mismatch. In other words, we discover that a perfectly sinusoidal electric potential induces a steady field within the liquid.

The heretofore unsuspected nonuniform steady field, which we refer to as **Asymmetric Rectified Electric Field (AREF)**, helps explain several long-standing discrepancies in electrokinetics. Namely, AREF provides qualitative explanations for the electrolyte and frequency dependence of the aggregation/separation of charged colloids near electrodes, fluid flow reversals in ac electroosmosis pumps, and levitation of charged colloids against gravity. Note that AREF is necessarily a nonlinear effect and a direct result of the ionic mobility mismatch. Consequently, the prior reduced problems were oblivious to its existence.

The discovery of the AREF and its broad implications are provided in Chapter 2 and Appendix A. Chapter 3 focuses on a detailed parametric study and scaling analysis of the AREF between parallel electrodes. In Chapter 4 and Appendix B, we demonstrate how AREF-induced electroosmotic flows dominate the classical ICEK flows around charged objects, offering a qualitative explanation for the observed fluid flow reversals in ICEK, and more complicated systems such as ACEO pumps. In Chapter 5 and Appendix C, we develop a second-order perturbation solution to the PNP equations that predicts the existence of AREF and further corroborates our numerical results.

1.2 RATCHET DYNAMICS

The second part of the dissertation focuses on ratchet dynamics, with an important corollary implication to the AREF. The idea goes back to the classical Feynman–Smoluchowski ratchet and its modern implementations; periodic excitation of a system with a broken spatial-symmetry (a biased system) yields a net solution, despite the absence of any net driving force (zero-time-average excitation, e.g., a sinusoidal wave). We show that application of a multimodal excitation, with a certain broken time-symmetry, to an unbiased (spatially symmetrical) nonlinear system yields a ratchet as well.

In particular, we consider an object atop a flat surface that undergoes a two-mode (frequencies f and αf) lateral vibration. Intuitively, the object is expected to either stick to, or slip on, the surface and move in a periodic fashion, but remain stationary on average. We demonstrate, theoretically and experimentally, that this intuition is true only if the excitation is antiperiodic, i.e., second half-period of the excitation is the negative of its first half. For a two-mode excitation, antiperiodicity requires α (i.e., ratio of the two modes) to be in the form {odd integer}/{odd integer} (e.g., $1, 3, 5/3, \dots$). Counterintuitively, the object starts moving to left or right otherwise (e.g., $\alpha = 2, 4, 3/2, \dots$), resembling a ratchet. A very intriguing implication of our theory is in electrokinetics, where it suggests that swapping the powered and the grounded parallel electrodes of

an electrochemical cell alters the system behavior. More importantly, our experimental observations on the AREF-induced electrophoresis of charged colloids under oscillatory potentials corroborate this finding.

In Chapter 6, we introduce the existence of ratchets in a variety of unbiased nonlinear systems, including problems involving solid-solid friction, non-Newtonian fluids, nonlinear drags, and nonlinear springs. Lastly we report the surprising implication of our theory in electrokinetics: the induced AREF by non-antiperiodic potentials is dissymmetric in space, indicating that the system behavior is sensitive to which electrode is powered and which is grounded. Chapter 7 and D elaborate on the latter, and provide new evidence using perturbation solutions and symmetry arguments.

Finally, in Chapter 8 we summarize the main findings, and conclude with a brief discussion on the potential avenues for future work in further understanding the AREF and the ratchet dynamics, and their significant implications.

Chapter 2

Oscillating Electric Fields in Liquids Create a Long-Range Steady Field

Overview*

We demonstrate that application of an oscillatory electric field to a liquid yields a long-range steady field, provided the ions present have unequal mobilities. The main physics are illustrated by a two-ion harmonic oscillator, yielding an asymmetric rectified field whose time average scales as the square of the applied field strength. Computations of the fully nonlinear electrokinetic model corroborate the two-ion model and further demonstrate that steady fields extend over large distances between two electrodes. Experimental measurements of the levitation height of micron-scale colloids versus applied frequency accord with the numerical predictions. The heretofore unsuspected existence of a long-range steady field helps explain several longstanding questions regarding the behavior of particles and electrically-induced fluid flows in response to oscillatory potentials.

*This chapter was previously published by Hashemi Amrei et al. and is reproduced here with minor modifications. See: **S. M. H. Hashemi Amrei**, S. C. Bukosky, S. P. Rader, W. D. Ristenpart, and G. H. Miller, *Oscillating electric fields in liquids create a long-range steady field*, Phys. Rev. Lett. 121 (2018) 185504.[1]

2.1 INTRODUCTION

Many systems of practical and scientific importance involve application of an oscillatory electric potential to a liquid, including dielectric and impedance spectroscopy,[25,34,35] cyclic voltammetry,[36,37] electro-acoustics,[38,39] dielectrophoresis,[40,41] induced charge electrokinetics,[18,19,32,33] and electrohydrodynamic manipulation of colloids.[8,9,42,10,12] In contrast to perfect dielectrics, the presence of mobile ions in the liquid phase complicates interpretation of the electric field. The "standard electrokinetic model" is a continuum level model widely used to predict the behavior of charged ions in solution.[43,26] It couples Gauss's law for the electric potential with the Nernst–Planck conservation equations for each ionic species, yielding a system of nonlinear coupled differential equations. For most systems of interest, the model is characterized by extremely sharp gradients in the non-electroneutral ionic charge layer near any solid/liquid interfaces.[24] Accordingly, most theoretical and numerical analyses of the standard electrokinetic model have focused on asymptotic solutions in the limit of small applied potentials,[25–28] which for sinusoidal applied potentials invariably yield a sinusoidal electric field inside the liquid, albeit with phase lag and amplitude that depend on the system properties. Importantly, these linearized asymptotic solutions differ qualitatively from recent numerical computations of the fully nonlinear electrokinetic model by Olesen et al., who found that the electric field assumes a much more complicated shape at sufficiently high applied oscillatory potentials.[29] This finding, which was further corroborated analytically by Stout and Khair[30] and Schnitzer and Yariv,[31] is significant because analyses of the behavior of individual colloids or other objects in liquids typically begin with the assumption that the electric field is perfectly sinusoidal, and it is unclear what the influence of a non-sinusoidal field will be. Further complicating matters, the prior nonlinear analyses[29–31] restricted attention to situations where the ionic mobilities of the positive and negative ions were equal, which simplifies the analysis but rarely pertains to actual liquids.

2.2 TOY MODEL

To consider the effect of non-equal ionic mobilities, we first introduce a two-ion model that illustrates how an ionic mobility mismatch can yield a steady field nearby (Fig. 2.1). Consider two isolated ions, one positive and one negative with charge numbers q_+ and q_-, respectively, each oscillating in response to a 1-dimensional far-field sinusoidal electric field of magnitude $E_0 \cos(\omega t)$. The ions are treated as non-interacting points (consistent with the continuum approximation) but with mobilities that differ based on their drag coefficients in liquid with viscosity μ. Neglecting inertia and balancing the drag force with the electrostatic driving force yields

$$6\pi\mu a_i \frac{dz_i}{dt} - q_i e E_0 \cos(\omega t) = 0, \tag{2.1}$$

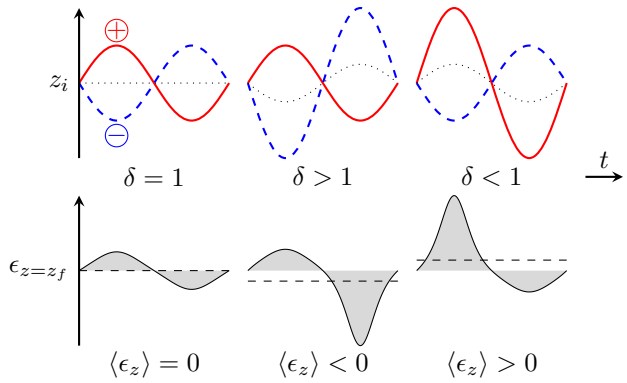

Figure 2.1: Two-ion harmonic oscillator model. (Top) Harmonic trajectories of two ions moving in response to a far-field sinusoidal electric field, for different ionic mobility ratios. (Bottom) Corresponding perturbation to the electric field evaluated at $z = z_f$.

where z_i denotes the instantaneous location of ion i with size a_i. Solving for the position yields

$$z_i = \frac{q_i e E_0}{\omega(6\pi\mu a_i)} \sin(\omega t). \tag{2.2}$$

The obtained harmonic oscillators of the ions $z_i(t)$ are shown schematically in Fig. 2.1 for different conditions, where $\delta = a_+/a_-$ is taken as a measure for the ionic mobility mismatch. For $\delta = 1$, ions oscillate with the same amplitude and the center of charge remains stationary. However, when $\delta \neq 1$, the fast moving ion exhibits a higher amplitude compared to the slow moving one, causing the center of charge itself to oscillate.

We now ask what happens at a point $z = z_f$ far from the ions due to their harmonic oscillation. Expansion of Coulomb's law in a Taylor series for $z_i/z_f \to 0$, followed by substitution of the harmonic solutions from Eq. 2.2 and rearrangement, yields the perturbed electric field

$$\epsilon(z_f, t) = \frac{\alpha}{z_f^2}[2\hat{E}(1+\delta)\sin(\omega t) + 3\hat{E}^2(1-\delta^2)\sin^2(\omega t) + 4\hat{E}^3(1+\delta^3)\sin^3(\omega t) + \dots], \tag{2.3}$$

where $\hat{E} = eE_0/(6\pi\mu a_+ \omega z_f)$ and $\alpha = e/(4\pi\varepsilon_\infty\varepsilon_0)$. (See Sec. A.1 for detail.) The observed electric field versus time is thus multimodal with frequency peaks at odd integer multiples of the imposed frequency for ions with $\delta = 1$, but with frequency peaks at both odd and even integer multiples of the imposed frequency for $\delta \neq 1$. This mobility dependence has an important consequence for the time average of the perturbation field near the oscillating ions. Integrating Eq. 2.3 yields the time average, to leading order,

$$\langle \epsilon(z_f) \rangle = \frac{\omega}{2\pi} \int_0^{2\pi/\omega} \epsilon(z_f, t) dt = \frac{3\alpha\hat{E}^2(1-\delta^2)}{2z_f^2}. \tag{2.4}$$

Provided $\delta \neq 1$, there is a non-zero time-average electric field due to the uneven oscillation of the ions. This phenomenon, which we denote as an "asymmetric rectified electric field" (AREF),

is depicted graphically along the bottom of Fig. 2.1. The perturbation to the net electric field at a location z_f is dominated by the faster moving ion, since it will be in closer proximity than the slower moving ion. This imbalance yields a net electric field that to leading order scales as the square of the applied field strength.

2.3 ELECTROKINETIC MODEL

The preceding toy model is suggestive, but it omits ion-ion interactions and the influence of thermal energy (i.e., diffusive motion). To capture these effects, one must invoke the standard electrokinetic model. For simplicity, here we focus on the 1-dimensional electric field between parallel electrodes separated by a distance H. The liquid contains two ionic species, each with concentration n_i and diffusivity $D_i = k_B T/(6\pi\mu a_i)$, which defines the ionic mobility mismatch $\delta = D_-/D_+$. The standard electrokinetic model couples Gauss's law,

$$\varepsilon_\infty \varepsilon_0 \frac{\partial^2 \phi}{\partial z^2} = -\sum_{i=1}^{2} e q_i n_i, \tag{2.5}$$

with Nernst–Planck continuity equations for each ionic species,

$$\frac{\partial n_i}{\partial t} = D_i \frac{\partial^2 n_i}{\partial z^2} + e q_i \frac{D_i}{k_B T} \frac{\partial}{\partial z}\left(n_i \frac{\partial \phi}{\partial z}\right). \tag{2.6}$$

The first and second terms on the right-hand side of Eq. 2.6 describe the ion diffusive motion and the electromigration in response to the local electric field, respectively. To complete the problem statement, we impose an oscillatory electric potential of amplitude ϕ_0 and frequency $f = \omega/(2\pi)$ on the lower electrode at $z = 0$, while keeping the upper electrode grounded. We further impose no flux of ions through each electrode, i.e., the electrodes are "blocking" and do not permit any electrochemical reactions. This assumption might not pertain for sufficiently large applied potentials; here we focus on the limiting case of negligible electrochemistry.

We emphasize that Eq. 2.5 and Eq. 2.6 are the classical starting point for analysis of the electrical behavior of fluids with ionic charge. In contrast to prior work, however, here we make no assumptions about the magnitude of the applied sinusoidal potential, nor about the values of the ionic mobilities. The system of equations was solved via finite difference methods with mesh refinement to capture the extremely thin Debye layers ($\sim$ 10 nm) near the boundaries (See Sec. A.2 for details.).

2.4 RESULTS, DISCUSSION, AND IMPLICATIONS

Examining first the case of equal ionic mobilities ($\delta = 1$), the electric field varies sinusoidally versus time for sufficiently low applied potentials (black curve, Fig. 2.2(a) ($\phi_0 e/(k_B T) = 1$)), with magnitude and phase lag as predicted by the linearized analytical solution (Fig. A.2). As the voltage

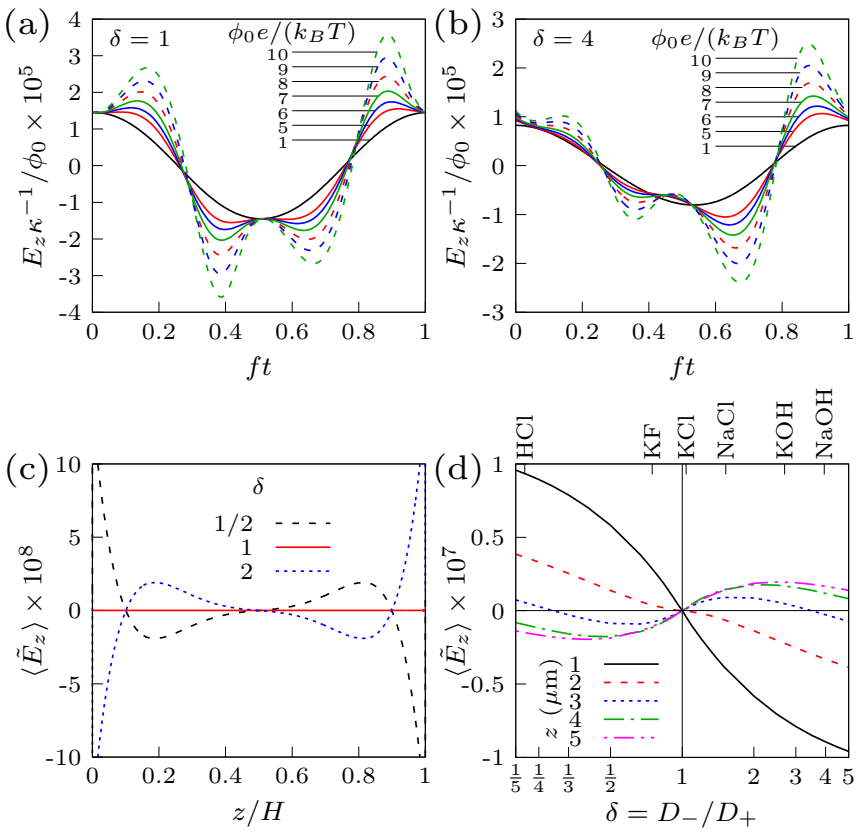

Figure 2.2: Effects of applied voltage and ionic mobility mismatch on the electric field between parallel electrodes. (a, b) Harmonic solutions of the normalized electric field $E_z\kappa^{-1}/\phi_0$ at $z = 1$ μm ($z/H = 0.04$) for different applied voltages: (a) $\delta = 1$, (b) $\delta = 4$. (c) Dimensionless time average electric field $\tilde{E}_z = E_z e\kappa^{-1}/(k_B T)$ versus z for different δ values. (d) Dimensionless time average electric field versus δ value at different locations. Parameters: $\phi_0 = 5k_B T/e$ (c, d), $f = 50$ Hz, $H = 25$ μm, $\min[D_+, D_-] = 1 \times 10^{-9}$ m^2/s, $c_\infty = 1$ mM.

increases, the contributions of the nonlinear terms yield increasingly large multi-modal peaks, a behavior that linearized models fail to predict. Qualitatively similar multi-modal peaks were found previously,[29–31] but here our numerics show that the multimodal peaks occur precisely at odd integer multiples of the imposed frequency, consistent with the two-ion model (cf. Eq. 2.3 and Fig. A.3). Note that the observed left-right asymmetry of the harmonic solution is a direct result of this multi-modal behavior. In the case of non-equal mobilities (Fig. 2.2(b)), for sufficiently low applied potential, the electric field is again a simple sinusoid versus time, and multi-modal peaks grow in magnitude as the applied potential increases. Unlike the case of equal mobilities, however, for $\delta = 4$ the shape of the electric field versus time is substantially shifted, with multi-modal peaks occurring at both odd and even integer multiples of the imposed frequency.

Numerical integration of the electric field to obtain the time-average (cf. Eq. 2.4) confirms that AREFs occur over large length scales across the entire domain (Fig. 2.2(c)). For $\delta = 1$, the time average is identically zero everywhere (solid red curve, Fig. 2.2(c)). In contrast, for $\delta = 2$ (dotted blue line, Fig. 2.2(c)), the time average electric field steeply rises from negative values near $z/H = 0$,

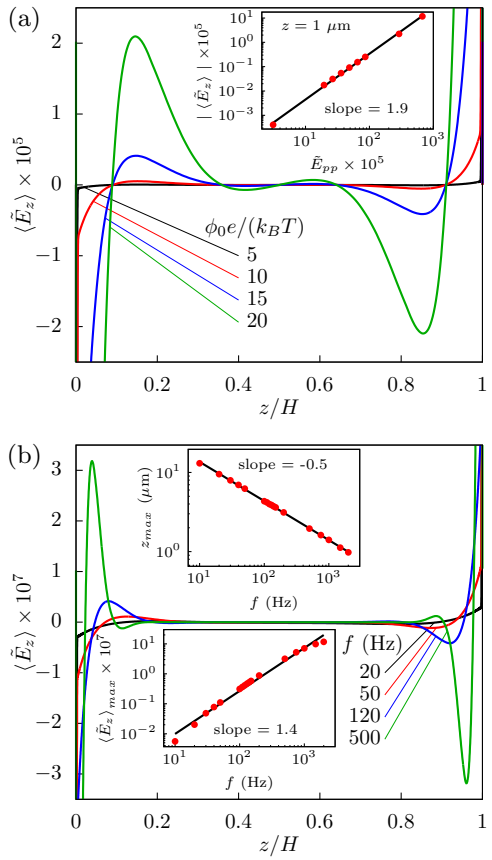

Figure 2.3: Effects of voltage and frequency on the AREF. Distribution of the dimensionless time average electric field for different voltages (a) and frequencies (b). Parameters: $\phi_0 = 5k_BT/e$ (b), $f = 100$ Hz (a), $H = 25$ μm (a) and 50 μm (b), $\delta = 4$, $D_+ = 1 \times 10^{-9}$ m^2/s (a) and 1.3×10^{-9} m^2/s (b), $c_\infty = 1$ mM.

passes through zero and reaches a maximum near $z/H = 0.2$, before decaying to identically zero at $z/H = 0.5$. The negative mirror image of this functionality occurs for $z/H > 0.5$, i.e., the AREF is antisymmetric with respect to position around $z/H = 0.5$. For the case of $\delta = 1/2$ (dashed black line, Fig. 2.2(c)), the AREF has the same magnitude but opposite sign everywhere as for the case of $\delta = 2$. The long-range steady field results from the uneven oscillation of the cations and anions, resulting in an augmentation or depletion of charge across the domain, provided $\delta \neq 1$ (Fig. A.7 and Fig. A.8). Numerical calculations over a wide range of values of δ confirm that the antisymmetric shape of the AREF is robust, and further demonstrate that the magnitude of the AREF increases with the difference between δ and unity (Fig. 2.2(d)). We emphasize that the symmetry in the system is broken by the ionic mobility mismatch, not the relative orientation of the electrodes; the magnitude and sign of the AREF are independent of which electrode is powered or grounded. In other words, near each electrode the AREF is directed toward the electrode for $\delta > 1$, but away from the electrode for $\delta < 1$.

A perhaps surprising aspect of the results shown in Fig. 2.2(c) and (d) is that the AREF occurs over such long length scales, well outside of the Debye layers (located here approximately at $z/H < 0.0004$ and $z/H > 0.9996$ for Debye length of 10 nm). Systematic calculations of the

AREF over a range of applied field strengths and frequencies confirm that this long-range behavior occurs over a wide range of parameter space (Fig. 2.3). As the applied sinusoidal potential increases (Fig. 2.3(a)), the shape of the AREF versus position is conserved (i.e., the curves collapse), but its magnitude increases as the 1.9 power of the local peak-to-peak electric field, defined here as $E_{pp}(z) = \max(E_z(z,t)) - \min(E_z(z,t))$. This behavior is consistent with the quadratic dependence predicted by the two-ion model (cf. Eq. 2.4); the slight discrepancy is presumably due to the more complicated shape of the actual local electric field (cf. Fig. 2.2(b)) compared to the simple sinusoid considered in the two-ion model. In contrast, the effect of frequency is more complicated (Fig. 2.3(b)). At very low imposed frequencies, the AREF is small in magnitude but peaks at locations relatively far from the electrodes. As the frequency increases, the peak magnitude increases sharply, scaling as $\omega^{1.4}$, while the peak location shifts closer to the electrode, scaling as $\omega^{-0.5}$. Similarly, Fig. A.6(a) shows that the position of the peak AREF outside the Debye layer scales as the square root of the diffusivity. Taken together, these observations indicate that the characteristic length for AREFs outside the Debye layer scales as $L/H \sim \sqrt{D/(\omega H^2)}$. As the frequency increases, and this characteristic length scale decreases, there are an increasing number of positions where the AREF reverses direction. At low frequencies, the AREF only changes direction once before the midplane (cf. Fig. 2.2(c)), but at higher frequencies it changes direction multiple times (cf. green curve in Fig. 2.3(b) ($f = 500$ Hz)).

The existence of a long-range steady field has significant implications for the behavior of colloids and electrically-driven flows at the microscale. Even for a relatively small applied potential of 0.5 V, applied at 100 Hz in water with $\delta = 4$, the AREF-induced electrophoretic force on a 1–μm particle at $z = 1$ μm is a factor of 10^3 to 10^5 larger than the Brownian, gravitational, and dielectrophoretic forces acting on it (Table A.1). A key experimental prediction, then, is that a particle placed between parallel electrodes will levitate upward against gravity provided the ions present have a sufficiently large ionic mobility mismatch.

Indeed, recent work[44,45] has established that oscillatory fields do cause micron scale colloids in millimolar NaOH ($\delta = 3.96$) to levitate many particle heights upward against gravity, while the same particles in millimolar KCl ($\delta = 1.04$) do not. The mechanism for this levitation has been obscure, with the exact frequency and voltage dependence unclear. The behavior is consistent with our AREF hypothesis: the long range steady field causes the particles to move upward until the AREF magnitude diminishes sufficiently for the electrophoretic force to balance with gravity. The complicated spatial dependence of the AREF also explains why some particles were observed to move upward against gravity, while others moved downward.[44,45] Note in Fig. 2.3(a) that the AREF is negative for $z/H < 0.1$, but positive for $0.1 < z/H < 0.35$; the direction of motion depends on the initial particle position (Fig. A.9). Our additional experiments reveal that the observed levitation height scales with frequency precisely as $h \propto \omega^{-0.5}$ (Fig. 2.4(b)), in accord with the frequency dependence predicted numerically (cf. top inset of Fig. 2.3(b)). Simultaneously, the magnitude of the applied voltage had little impact on the levitation height (Fig. 2.4(c)), again in accord with the numerical predictions (cf. Fig. 2.3(a)). These observations provide strong experimental evidence

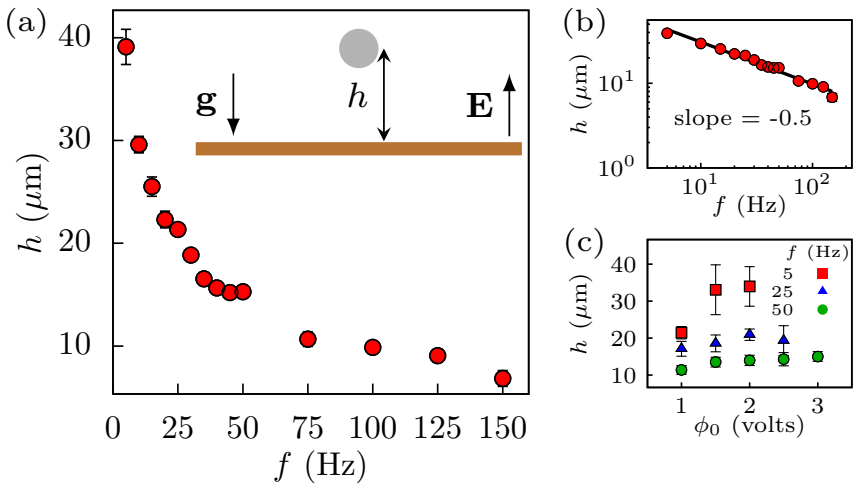

Figure 2.4: Experimental evidence for AREF: colloids levitating against gravity in response to an oscillatory field. (a, b) Stable levitation height of 2–μm diameter polystyrene particles in 1 mM NaOH solution subject to a 4 V applied potential (peak-to-peak) versus frequency. (c) Stable levitation height versus magnitude of the applied potential, using the same system as in (a, b).

for the existence of AREFs in response to oscillatory potentials. (See Sec. A.6 and Bukosky et al.[3] for details of the particle height bifurcation analysis and experiments.)

A previously unrecognized driving force of this magnitude will necessitate reconsideration of prior experimental studies involving oscillatory fields; here we note two other systems of interest where AREFs help resolve outstanding questions. First, there has been long-standing controversy regarding the aggregation of micron-scale particles near electrodes in response to oscillatory fields. Early workers[8,9,42] established that colloids aggregated laterally near the electrode, in the direction perpendicular to the applied field, and attributed the aggregation due to electrohydrodynamic (EHD) flows generated on the electrode surface near each particle (Fig. 2.5(a)); nearby particles were mutually entrained in the flows, resulting in aggregation. Other workers noted, however, that the particle behavior depended sensitively on the type of electrolyte in the liquid.[46–50] Despite a great deal of experimental and theoretical investigation, there is still no consensus as to the mechanism underlying the electrolyte type dependence.[50] The existence of AREFs provides a new explanation: the flow field around each particle will be the superposition of the EHD flow generated on the electrode,[51] and an electroosmotic flow due to the steady AREF field generated on the particle surface. If the ionic mobility mismatch is sufficiently large, then the AREF-induced electroosmotic flow dominates and the resulting flow pattern will favor separation of nearby particles (Fig. 2.5(b), and Table A.1).

Second, there are several unresolved aspects of "induced charge electrokinetics" (ICEK), a type of electrically-driven fluid flow first elucidated in 2004 by Bazant and Squires[18,19] that triggered much research aimed at using applied electric fields to manipulate flow and objects in lab-on-a-chip devices.[32,33] The archetypal example of ICEK is the quadrupolar flow induced around a metallic cylinder in response to the applied field (Fig. 2.5(c)). Scaling up this phenomenon for use as electrokinetic pumps in microfluidic devices, however, revealed experimental observations that

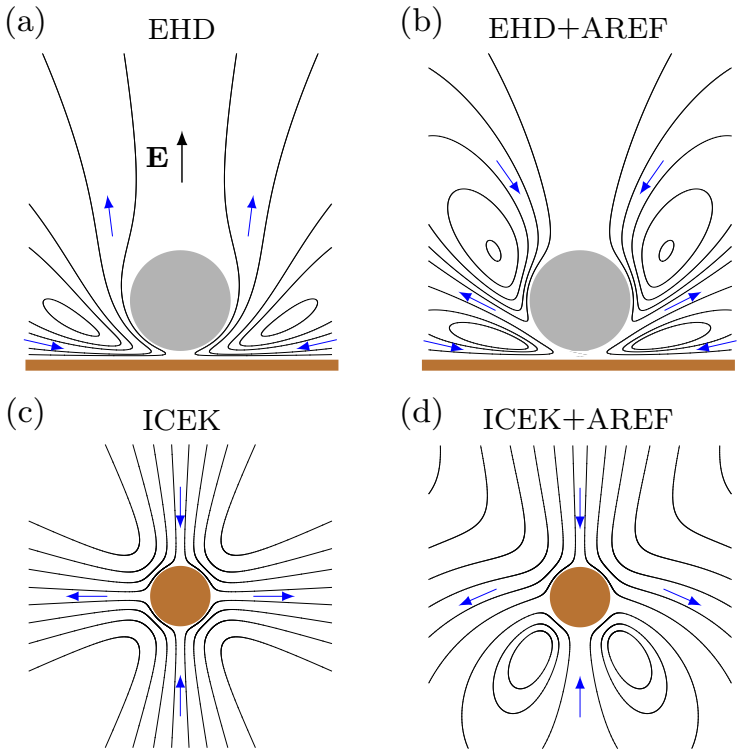

Figure 2.5: Impact of AREFs on electrically-induced fluid flows around (a, b) a charged non-conducting sphere near an electrode and (c, d) around an isolated metallic cylinder. (See Sec. A.4 for streamline calculations.)

ICEK theory fails to address.[23,32,33] Specifically, a reversal in fluid flow direction occurs at high frequencies; the standard ICEK theory predicts no such frequency effect. Similarly, the effect of ionic strength is unclear: fluid flows effectively cease at ionic strengths above 10 millimolar, again at odds with the theory. The existence of AREFs provides potential insight for both dilemmas. Taking the archetypal case of fluid flow around a conducting cylinder, the actual flow field will be the superposition of the ICEK flow and electroosmotic slip along the cylinder surface due to the AREF (Fig. 2.5(d)). Depending on the frequency and position of the cylinder, the AREF electroosmotic velocity can dominate the flow pattern. Moreover, the AREF-induced slip velocity scales as c_∞^{-1} (cf. Fig. A.6(b)). Therefore, any experiments aimed at elucidating the ionic strength dependence of ICEK would need to take into account the confounding effect of AREF-induced flows.

More research is needed; the analysis presented here should serve as a starting point for consideration of the influence of AREFs in these and more complicated systems.

Chapter 3

Asymmetric Rectified Electric Fields between Parallel Electrodes: Numerical and Scaling Analyses

Overview*

Recent computational and experimental work has established the existence of Asymmetric Rectified Electric Fields (AREFs), a type of steady electric field that occurs in liquids in response to an applied oscillatory potential, provided the ions present have different mobilities [Hashemi Amrei *et al.*, Phys. Rev. Lett. **121**, 185504, 2018]. Here we use scaling analyses and numerical calculations to elaborate the nature of one-dimensional AREFs between parallel electrodes. The AREF magnitude is shown to increase quadratically with applied potential at low potentials, increase nonlinearly at intermediate potentials, then increase with a constant rate slower than quadratically at sufficiently high potentials, with no impact at any potential on the spatial structure of the AREF. In contrast, the AREF peak location increases linearly with a frequency-dependent diffusive length scale for all conditions tested, with corresponding decreases in both the magnitude and number of sign changes in the directionality of AREF. Furthermore, both the magnitude and spatial structure of the AREF depend sensitively on the ionic mobilities, valencies, and concentrations, with a potential-dependent peak AREF magnitude occurring at an ionic mobility ratio of $D_-/D_+ \lessapprox 5$. The results are summarized with approximate scaling expressions that will facilitate interpretation of the steady component for oscillatory fields in liquid systems.

*This chapter was previously published by Hashemi Amrei et al. and is reproduced here with minor modifications. See: **S. M. H. Hashemi Amrei**, G. H. Miller, and W. D. Ristenpart *Asymmetric rectified electric fields between parallel electrodes: numerical and scaling analyses*, Phys. Rev. E 99 (2019) 062603.[2]

3.1 INTRODUCTION

The application of an oscillatory electric potential to a liquid is an integral aspect of a wide range of phenomena, including AC electroosmosis (ACEO) pumps,[20–23] induced charge electrokinetics (ICEK),[15,52,53,18,19,54,32,33,55] electrohydrodynamic (EHD) manipulation of colloids[8–12,56] and bioparticles,[57,13,14,58] dielectric and impedance spectroscopy,[25,35,34,59] cyclic voltammetry,[36,37,60] electro-acoustics,[38,61,39] dielectrophoresis,[62,40,41,63,64] and electroosmotic electrolyte transport through charged nanopores/nanotubes.[65,66] In all of these systems, interpretation of the experimental observations depends on information regarding the dynamic response of the liquid to the applied potential. In particular, a key question is the nature inside the liquid of the electric field itself, which is not directly measurable and thus must be calculated theoretically. Traditionally, the "standard electrokinetic model," which couples the Poisson equation with Nernst–Planck ion transport equations, has served as the starting point for analysis of liquids with dissociated ions.[24] Because the governing equations are coupled and highly nonlinear, and because under typical conditions large disparities in length and time scales render the equations extremely stiff, most analyses of the electric field have focused on asymptotically small applied potentials[26–28,25,67] or on higher applied potentials but for ions with equal mobilities.[29,31,30]

Despite being widely used, however, these linearized and equal-mobility models have yielded predictions at odds with experimental observations in a variety of systems. For example, researchers investigating ACEO pumps have long been stymied by the observed reversal of fluid flow direction upon varying the applied frequency.[23,32,33] Likewise, in work examining the EHD aggregation of colloids near electrodes, the effect of electrolyte type on the aggregation behavior has remained mysterious despite numerous theoretical and experimental studies.[46–50] Recent experimental studies revealed that colloidal particles can levitate several particle diameters upward against gravity in response to an oscillatory field, provided they were suspended in certain electrolytes (e.g., NaOH and KOH),[44,45] a result also inexplicable in terms of the traditional solutions to the standard electrokinetic model.

Recent work by Hashemi Amrei et al.[1] generated a new possible explanation for the above unresolved questions. Specifically, they showed that application of a perfectly sinusoidal potential to a liquid counterintuitively yields a long-range steady electric field. This steady field results from the asymmetry in motion of the positive and negative ions as they move back and forth in the oscillatory field, a phenomenon explicable even in the limit of just two isolated ions (Fig. 3.1). Denoted as an Asymmetric Rectified Electric Field (AREF), the magnitude of the steady field depends on the ratio $\delta = D_-/D_+$ of the relative diffusivities of the ions. We emphasize that AREF is necessarily a *nonlinear* effect; any sort of linearization results in a zero time average solution. Numerical solutions to the full nonlinear electrokinetic model further corroborated the existence of AREF.[1] The numerical results show that AREFs persist over large length scales between parallel electrodes, with a characteristic diffusive length scale given by $\ell_D \sim \sqrt{D/f}$, where D is a characteristic diffusivity and f is the applied frequency (Fig. 3.2). These predictions were shown to be consistent with the levitation behavior of colloids to extreme distances away from the electrode; the long

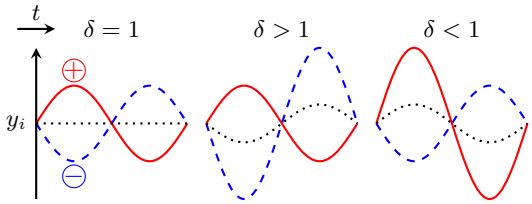

Figure 3.1: Illustration of two-ion model: harmonic oscillations ($y_i(t)$) of two oppositely charged isolated ions in response to a sinusoidal electric field for different $\delta = D_-/D_+$ values. The generated electric field at an arbitrary location $y = y_f$ due to these harmonic oscillations is asymmetrical and has a nonzero time average for $\delta \neq 1$. The dotted black curves denote the oscillations of the center of charge.

range steady field lifts particles electrophoretically upward until the AREF diminishes sufficiently to balance gravity.[1,3] As discussed by Hashemi Amrei et al., the existence of AREFs also potentially explains the unresolved frequency and electrolyte dependencies observed in ACEO pumps and EHD aggregation of particles near electrodes.[1]

Several fundamental questions about AREFs, however, to date remain unanswered. Notably, the scaling of the AREF with the magnitude of the applied potential was only elucidated for small potentials, and it is unclear how AREFs scale with larger applied potentials. It is also unclear how the spatial structure of the AREF varies with frequency (and the corresponding diffusive length scale ℓ_D), an important question since the earlier results indicated that even the sign of the AREF (i.e., the direction of the steady field) changes repeatedly as a function of frequency. Likewise, although a non-unity diffusivity ratio ($\delta \neq 1$) is clearly necessary for an AREF to occur, it is unclear how the magnitude and the spatial structure (shape) of the AREF scale with δ or with the valencies of the ions themselves.

In this work, we address the above questions by elaborating the nature of one-dimensional AREFs between parallel electrodes. We perform a systematic dimensional analysis and extensive numerical calculations over a large parameter space, focusing on the limit of negligible electrochemical and thermal effects. The analysis yields several key results:

Potential The AREF magnitude increases quadratically with applied potential at low potentials, increases nonlinearly at intermediate potentials, and increases slower than quadratically at sufficiently high potentials. The applied potential does not affect the AREF shape.

Frequency The AREF peak location far from the electrode is linearly proportional to $\ell_D = \sqrt{D/f}$ for all conditions tested, but the magnitude decreases with a power-law exponent ranging between ℓ_D^{-1} and ℓ_D^{-3} depending on the applied potential. As ℓ_D decreases (f increases), a series of pitchfork bifurcations occur for the number of zeros in the AREF (i.e., the number of sign changes increases.)

Ionic strength The AREF magnitude peaks at ion concentrations (c_∞) similar to those of deionized water, varying as c_∞^{-1} and $c_\infty^{-1/4}$ at low and high applied voltages, respectively.

Ionic mobilities The AREF magnitude increases with δ to a peak value near $\delta \lessapprox 5$, then decays

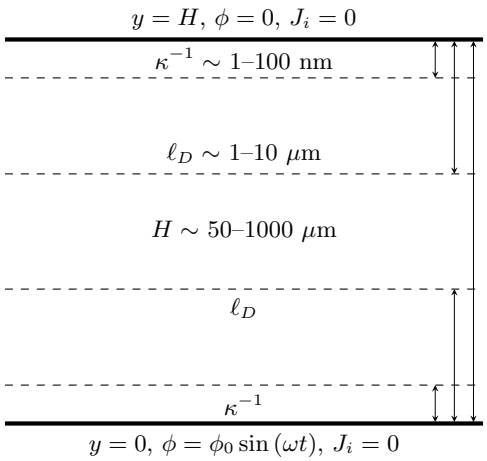

Figure 3.2: Schematic diagram of two parallel electrodes and not to scale comparison of different length scales. AREF varies over a diffusive length scale of $\ell_D = \sqrt{D/f}$ which is several order of magnitudes higher than the characteristic length scale of the Debye layer (κ^{-1}).

asymptotically back toward zero. The ion valencies dramatically alter the magnitude and sign of the AREF.

Each of the above points is elucidated in detail below. We begin with a formal dimensional analysis, and we demonstrate that under typical circumstances the system behavior is governed by four key dimensionless groups. We then present systematic numerical calculations versus those four parameters to corroborate the above list of key results. Because the numerical calculations are non-trivial, we finish by summarizing the results in terms of approximate scaling expressions that should assist researchers in interpretation of AREF effects in oscillatory fields.

3.2 THEORY AND NUMERICAL METHODS

3.2.1 Standard electrokinetic model

Our starting point is the standard electrokinetic model,[43,26,1] which is a continuum-level model that couples the electric field to the flux of dissociated ions. We restrict attention to fully dissociated binary electrolytes between parallel electrodes located at $y = 0$ and $y = H$ (cf. Fig. 3.2). The electric potential is governed by the Poisson equation

$$-\varepsilon \frac{\partial^2 \phi}{\partial y^2} = \rho = e(z_+ n_+ + z_- n_-), \tag{3.1}$$

relating the free charge density to the gradient of the electric field. The transport of ions in space is governed by the Nernst–Planck equations for each ion,

$$\frac{\partial n_i}{\partial t} = D_i \frac{\partial^2 n_i}{\partial y^2} + e z_i \frac{D_i}{k_B T} \frac{\partial}{\partial y}\left(n_i \frac{\partial \phi}{\partial y}\right). \tag{3.2}$$

Here the symbols stand for applied potential, ϕ_0; free charge density, ρ; elementary charge, e; charge number, z_i; permittivity, ε; electric potential, ϕ; number concentration of ion, n_i; diffusivity, D_i; Boltzmann constant, k_B; and absolute temperature, T.

The first and second terms on the right hand side of the Nernst–Planck equation (Eq. 3.2) are the diffusive and electromigrative contributions of the ion transport, respectively. It is the electromigration term that accounts for the transport of ions in direct response to the electric field and is responsible for the nonlinearity of the governing equations. We assume that the liquid is quiescent with no convection due to instabilities or flows generated around suspended objects.

To close the problem, we first subject the potential distribution to the following initial and boundary conditions:

$$\phi(0, y) = 0, \tag{3.3}$$

$$\phi(t, 0) = \phi_0 \sin(\omega t), \quad \phi(t, H) = 0. \tag{3.4}$$

At time equal to zero ($t = 0$) a sinusoidal electric potential of amplitude ϕ_0 and angular frequency $\omega = 2\pi f$ is applied on the lower electrode at $y = 0$, while the upper electrode at $y = H$ is kept grounded (Fig. 3.2).

The ions are initially evenly distributed between the two electrodes with number concentrations of n_i^∞,

$$n_i(0, y) = n_i^\infty. \tag{3.5}$$

The initial ion concentrations are related to the bulk concentration of the electrolyte (n^∞) through their respective charge numbers:

$$n_+^\infty = -z_- n^\infty, \quad n_-^\infty = z_+ n^\infty, \tag{3.6}$$

which satisfy the electroneutrality condition, $z_+ n_+^\infty + z_- n_-^\infty = 0$.

Finally, we assume that the electrodes are fully 'blocking,' such that the flux J_i of both ions through the electrodes is zero,

$$J_i = -D_i \Big(\frac{\partial n_i}{\partial y} + \frac{e z_i n_i}{k_B T} \frac{\partial \phi}{\partial y} \Big)_{y=0,H} = 0. \tag{3.7}$$

This assumption might not be justified at high applied voltages and sufficiently low frequencies. Similarly, we neglect any complications due to the formation of a compact Stern layer at the electrodes. This is while some results indicate that a significant potential drop might occur across the Stern layer.[29,68] We focus here on the limiting case of negligible Stern layer effects and negligible electrochemistry to provide a reference point for future work examining those more complicated physics.

Table 3.1: Quantities and dimensions in MLTQ system. M: mass, L: length, T: time, Q: charge. Notation $\doteq$ indicates dimensional equality.

quantity	**definition**	**dimension**
z_+	charge number of + ion	dimensionless
z_-	charge number of − ion	dimensionless
ε	permittivity	$\mathrm{F/m} \doteq \mathrm{M^{-1}L^{-3}T^2Q^2}$
k_BT	thermal energy	$\mathrm{N.m} \doteq \mathrm{ML^2T^{-2}}$
e	elementary charge	$\mathrm{C} \doteq \mathrm{Q}$
H	electrode spacing	$\mathrm{m} \doteq \mathrm{L}$
f	applied frequency	$\mathrm{1/s} \doteq \mathrm{T^{-1}}$
D_+	diffusivity of + ion	$\mathrm{m^2/s} \doteq \mathrm{L^2T^{-1}}$
D_-	diffusivity of − ion	$\mathrm{m^2/s} \doteq \mathrm{L^2T^{-1}}$
ϕ_0	applied electric potential	$\mathrm{V} \doteq \mathrm{ML^2T^{-2}Q^{-1}}$
n^∞	bulk concentration of electrolyte	$\mathrm{1/m^3} \doteq \mathrm{L^{-3}}$
ϕ	electric potential	$\mathrm{V} \doteq \mathrm{ML^2T^{-2}Q^{-1}}$
n_+	concentration of + ion	$\mathrm{1/m^3} \doteq \mathrm{L^{-3}}$
n_-	concentration of − ion	$\mathrm{1/m^3} \doteq \mathrm{L^{-3}}$
y	location	$\mathrm{m} \doteq \mathrm{L}$
t	time	$\mathrm{s} \doteq \mathrm{T}$

3.2.2 Dimensionless form

The important parameters and variables in our model and their corresponding dimensions are listed in Table 3.1. There are a total of $r = 16$ quantities and $k = 4$ independent dimensions, so by Buckingham's pi theorem there are $r - k = 12$ dimensionless groups. We choose H, f, k_BT, and e as the repeating quantities to define the dimensionless groups.

We use the gap size H and the inverse frequency $1/f$ to scale the independent spatial and temporal variables respectively as

$$\tilde{y} = y/H, \quad \tilde{t} = ft = \omega t/(2\pi). \tag{3.8}$$

The thermal potential $\phi_T = k_B T/e$ is used to nondimensionalize the applied potential ϕ_0,

$$\Phi_0 = \frac{\phi_0 e}{k_B T}, \tag{3.9}$$

while the applied potential scales the dependent potential $\phi(t, y)$ as

$$\tilde{\phi} = \phi/\phi_0. \tag{3.10}$$

Note that unlike the traditional linearized case for which ϕ_T is an appropriate characteristic potential, for this nonlinear problem ϕ can be as high as $\sim 100\phi_T$. Hence, the applied potential ϕ_0 offers a better normalization of the potential distribution. In addition, the ion concentrations are scaled as

$$\tilde{n}_+ = n_+/n_0, \quad \tilde{n}_- = n_-/n_0, \tag{3.11}$$

where n_0 is given by

$$n_0 = z_+^2 n_+^\infty + z_-^2 n_-^\infty. \tag{3.12}$$

Our numerical results (cf. subsection 3.3.3) suggest the characteristic diffusivity of the problem to be

$$\hat{D} = \sqrt{D_+ D_-}, \tag{3.13}$$

which is used to define the dimensionless diffusive length scale

$$\mathcal{L}_D = \ell_D/H = \frac{\sqrt{\hat{D}/f}}{H}. \tag{3.14}$$

The ionic mobility mismatch is denoted by the dimensionless parameter

$$\delta = D_-/D_+. \tag{3.15}$$

Table 3.2: Dimensionless groups (parameters (Π_1–Π_7) plus dependent and independent variables (Π_8–Π_{12})). $n_0 = z_+^2 n_+^\infty + z_-^2 n_-^\infty = n^\infty(z_-^2 z_+ - z_+^2 z_-)$, $\kappa^{-1} = \sqrt{\varepsilon k_B T/(n_0 e^2)}$, $\hat{D} = \sqrt{D_+ D_-}$.

Π_1	$\Phi_0 = \phi_0 e/(k_B T)$	Π_2	$\mathcal{L}_D = \ell_D/H = \sqrt{\hat{D}/f}/H$
Π_3	$\delta = D_-/D_+$	Π_4	κH
Π_5	z_+	Π_6	z_-
Π_7	$N^\infty = n_0 H^3$	Π_8	$\tilde{\phi} = \phi/\phi_0$
Π_9	$\tilde{n}_+ = n_+/n_0$	Π_{10}	$\tilde{n}_- = n_-/n_0$
Π_{11}	$\tilde{t} = ft$	Π_{12}	$\tilde{y} = y/H$

Finally, the ionic strength appears in two dimensionless groups, a dimensionless Debye length scale,

$$\kappa H = \sqrt{\frac{n_0 e^2}{\varepsilon k_B T}} H, \tag{3.16}$$

and an overall dimensionless number concentration,

$$N_\infty = n_0 H^3. \tag{3.17}$$

The dimensionless groups and variables are summarized in Table 3.2. If we narrow our focus to cases of aqueous electrolytes at ambient temperature (i.e., if we omit situations where thermal effects are important), then the dimensionless groups κH and $n_0 H^3$ become dependent since the only varying quantities in both groups are n_0 and H. Therefore, only one of them (κH) is taken here as a controlling dimensionless group. In other words, the six dimensionless parameters Φ_0, $\mathcal{L}_D$, δ, κH, and charge numbers z_+ and z_- completely govern the system behavior.

Using the above definitions, the dimensionless governing equations are written as

$$-\frac{\Phi_0}{(\kappa H)^2}\frac{\partial^2 \tilde{\phi}}{\partial \tilde{y}^2} = z_+ \tilde{n}_+ + z_- \tilde{n}_-, \tag{3.18}$$

$$\frac{\partial \tilde{n}_+}{\partial \tilde{t}} = \frac{\mathcal{L}_D^2}{\sqrt{\delta}}\Big[\frac{\partial^2 \tilde{n}_+}{\partial \tilde{y}^2} + z_+ \Phi_0 \frac{\partial}{\partial \tilde{y}}\Big(\tilde{n}_+ \frac{\partial \tilde{\phi}}{\partial \tilde{y}}\Big)\Big], \tag{3.19}$$

$$\frac{\partial \tilde{n}_-}{\partial \tilde{t}} = \sqrt{\delta}\mathcal{L}_D^2\Big[\frac{\partial^2 \tilde{n}_-}{\partial \tilde{y}^2} + z_- \Phi_0 \frac{\partial}{\partial \tilde{y}}\Big(\tilde{n}_- \frac{\partial \tilde{\phi}}{\partial \tilde{y}}\Big)\Big], \tag{3.20}$$

subject to the following dimensionless initial conditions,

$$\tilde{n}_i(0, \tilde{y}) = n_i^\infty / n_0, \tag{3.21a}$$

$$\tilde{\phi}(0, \tilde{y}) = 0, \tag{3.21b}$$

and dimensionless boundary conditions,

$$\Big(\frac{\partial \tilde{n}_i}{\partial \tilde{y}} + z_i \Phi_0 \tilde{n}_i \frac{\partial \tilde{\phi}}{\partial \tilde{y}}\Big)_{\tilde{y}=0,1} = 0, \tag{3.22a}$$

$$\tilde{\phi}(\tilde{t}, 0) = \sin(2\pi \tilde{t}), \quad \tilde{\phi}(\tilde{t}, 1) = 0. \tag{3.22b}$$

In Eq. 3.21a, the dimensionless initial ion concentrations can be written in terms of charge numbers (z_+ and z_-):

$$\frac{n_+^\infty}{n_0} = \frac{-z_-}{z_-^2 z_+ - z_+^2 z_-}, \quad \frac{n_-^\infty}{n_0} = \frac{z_+}{z_-^2 z_+ - z_+^2 z_-}. \tag{3.23}$$

Finally, using the above scalings, all forms of the electric field $E = -\partial\phi/\partial y$, including the

instantaneous and time average, become nondimensionalized by the nominal electric field ϕ_0/H,

$$\tilde{E} = EH/\phi_0. \tag{3.24}$$

The time average electric field is obtained by time integration over one AC cycle of the harmonic solution as

$$\langle \tilde{E} \rangle = \int_0^1 \tilde{E} d\tilde{t}. \tag{3.25}$$

Likewise, the dimensionless free charge density becomes

$$\tilde{\rho} = \rho/n_0 = (z_+ n_+ + z_- n_-)/n_0, \tag{3.26}$$

with its time average denoted by $\langle \tilde{\rho} \rangle$.

3.2.3 Numerical solution

Following the procedure outlined by Hashemi Amrei et al.,[1] the system of nonlinear partial differential equations (Eq. 3.18–Eq. 3.22) was numerically solved using multigrid finite difference methods[69,70] and mesh refinement.[71] Cell-centered finite difference methods were employed to discretize the governing equations and boundary conditions. A typical minimum cell size used for the simulations is of order $\kappa^{-1}/128$ which, for $\kappa^{-1} \approx 13$ nm, is equivalent to ≈ 0.1 nm. Such a small size step (compared to electrodes spacing which can be several hundred microns) restricts the time marching of the simulation. In the presence of convective terms (with a velocity of u), the Courant–Friedrichs–Lewy (CFL) number condition limits the maximum allowable time step of the numerical solution: $|u|\Delta t/h \leqslant 1$, with Δt and h as the temporal and spatial steps. In dimensional context, the electromigration term of the species continuity equation (Eq. 3.2) can be written as $\frac{\partial}{\partial y}(u n_i)$ with $u = \frac{e z_i D_i}{k_B T} \frac{\partial \phi}{\partial y}$ ($[u]$ = m/s), resembling a convective transport of ions. Therefore, we require

$$\left| \frac{e z_i D_i}{k_B T} \frac{\partial \phi}{\partial y} \right| \Delta t/h \leqslant 1. \tag{3.27}$$

It is not practical to cover the entire domain with a uniform cell size that is small enough to resolve the Debye layer (e.g., covering 100 μm with $h \approx 0.1$ nm requires 1 million cells). Therefore, we used mesh refinement near the electrode surfaces.[71]

Operator splitting is employed. For each time step, the Poisson equation (Eq. 3.18) is solved for Φ_0 (step i), which is subsequently used to find the ion concentrations from the Nernst-Plank equations (Eq. 3.19 and Eq. 3.20) (step ii). Our Poisson solver is based on the algorithm of Martin and Cartwright.[71] With some changes, a similar algorithm is devised to solve the species continuity equation. The main difference of the algorithm is the inclusion of the nonlinear electromigration term. To ensure solution stability, the CFL number is calculated prior to step ii. While the condition is not met, we set $\Delta t = \Delta t/2$ to find a $\Delta t = (\Delta t)_c$ that satisfies the condition. Then step ii breaks down into $\Delta t/(\Delta t)_c$ substeps.

Besides the above-mentioned challenges, achieving a harmonic solution by solving the dynamical equations is computationally intensive.[29] The simulation time t_f should be long enough for the ions to transfer back and forth between the electrodes in order to reach the harmonic solution. The ions transfer with diffusive and electromigrative mechanisms with corresponding time scales of $\tau_i^D = H^2/D_i$ and $\tau_i^e = \tau_i^D/(|z_i|\phi_0 e/(k_B T))$. Therefore, to ensure the harmonic conditions we require $t_f \gg \max[\tau_i^D, \tau_i^e]$. The time scale of the applied potential is also $\tau^{AC} = 1/f$ which is, for the range of parameters used in this study, far less than τ_i^D and τ_i^e. Therefore, the number of AC cycles should be $n_{AC} \gg \max[\tau_i^D, \tau_i^e]/\tau^{AC}$.

We performed several consistency checks. In this regard, an important issue to consider was the crowding effect.[72] The finite size of ions enforces a cutoff number concentration of $n_{\max} = 1/l^3$, where l is a characteristic length of the dissolved ions ($n_{\max} \approx 60$ M for $l = 0.3$ nm). We never observed concentrations higher than the maximum packing value. As another consistency check, the instantaneous electric field at the electrode surface was compared to the typical Debye layer field strength κH. Similarly, the maximum instantaneous induced zeta potential ζ on the electrode surface was of the same order of magnitude as the applied potential (i.e., $\zeta \sim \phi_0$). In other words, all of the potentials, field strengths, and ion concentrations are physical. Please see the supplemental material in Hashemi Amrei et al.[1] for further details.

3.3 NUMERICAL RESULTS

In this section, we systematically investigate the effect of the different system properties on the AREF. The results are provided at ambient temperature for 1-1 aqueous electrolytes, unless otherwise stated (cf. subsection 3.3.6). We first analyze univalent electrolytes ($z_+ = |z_-| = 1$), so that the contributing dimensionless parameters are Φ_0 (dimensionless applied potential), $\mathcal{L}_D$ (dimensionless diffusive length scale), δ (ionic mobility mismatch), and κH (dimensionless Debye parameter). Then we discuss the complications that charge numbers (z_+, z_-) and their potential asymmetry bear to the analysis.

3.3.1 Representative field and charge distributions

Fig. 3.3 shows representative time variations of the instantaneous electric field $\tilde{E}$ and free charge density $\tilde{\rho}$ for two different values of $\mathcal{L}_D$ and different Φ_0 values. At low applied potentials, the system behaves linearly and a single-mode sinusoidal solution is obtained ($\Phi_0 = 1$, dotted red curves), consistent with linearized asymptotic analyses.[25,67] As the applied potential increases, the nonlinear contribution gradually dominates, yielding multimodal solutions. This behavior is in marked contrast to that of linearized solutions, where regardless of the applied potential the solution is invariably a sinusoid. A comparison between the cases of different $\mathcal{L}_D$ values reveals an increase in the amplitude of the harmonic solutions for smaller dimensionless diffusive length scales. For instance, increasing the applied frequency, which results in lower values of $\mathcal{L}_D$, increases the AREF amplitude. The shape of the harmonics is also affected by $\mathcal{L}_D$, i.e., the curves for different

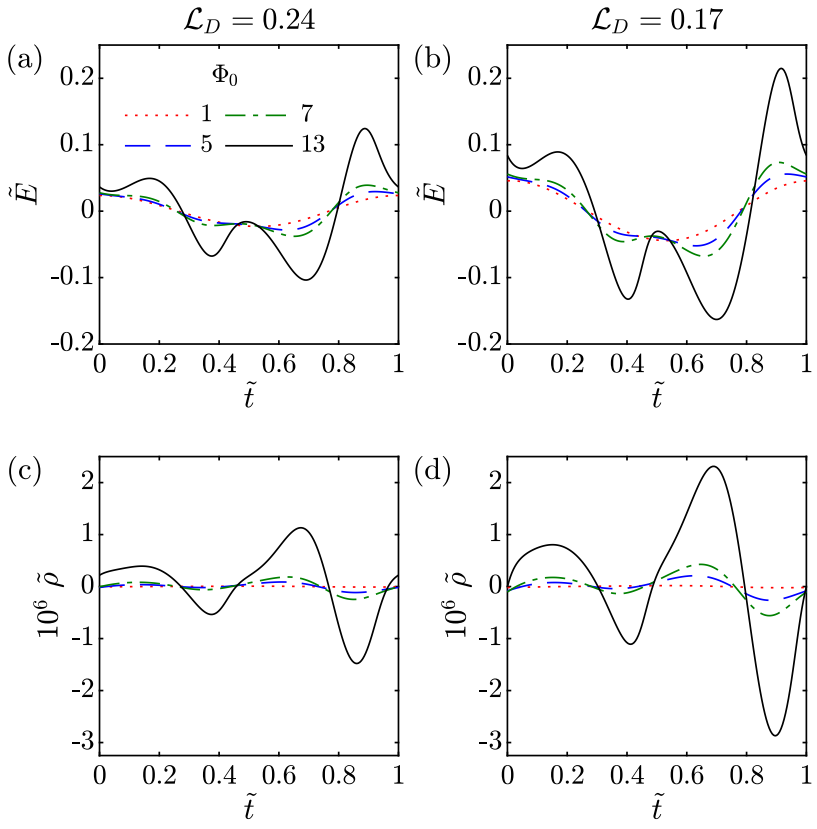

Figure 3.3: Representative time variations of the electric field ($\tilde{E}$) (a, b) and free charge density ($\tilde{\rho}$) (c, d) at $\tilde{y} = 0.04$ for different values of Φ_0 and $\mathcal{L}_D$. For all plots, $\delta = 3$, $\kappa H = 2600$.

$\mathcal{L}_D$ values do not collapse.

In this example the ionic mobility mismatch is held constant at $\delta = 3$; hence the time averages are nonzero and a net steady field ($\langle\tilde{E}\rangle$, AREF hereafter) exists within the liquid,[1] as shown in Fig. 3.4(a). The corresponding time average of the free charge density ($\langle\tilde{\rho}\rangle$) is provided in Fig. 3.4(b). Interestingly, the spatial distributions of AREF and $\langle\tilde{\rho}\rangle$ are, respectively, antisymmetrical and symmetrical with respect to the midplane as a consequence of the mathematical structure of the governing equations. We emphasize that swapping the grounded and powered electrodes does not change the sign or magnitude of $\langle\tilde{E}\rangle$ or $\langle\tilde{\rho}\rangle$; the symmetry of the system is broken by the ionic mobility mismatch, not the relative orientation of the electrodes. The magnitudes of both the time averages of electric field and free charge density increase with the applied potential. Note that wherever the gradient of AREF is zero, there is likewise a zero time average free charge density, consistent with Gauss's law (Eq. 3.1). In addition, the general shape of the AREF distribution is the same for different applied voltages. In other words, the curves for different Φ_0 values in Fig. 3.4(a) collapse under appropriate scaling, although as discussed below, the appropriate scaling is non-obvious.

Magnification of the AREF and $\langle\tilde{\rho}\rangle$ distributions near the electrode, on the Debye length scale, are shown in Fig. 3.4(c) and (d), respectively. The electric field starts from a nonzero value

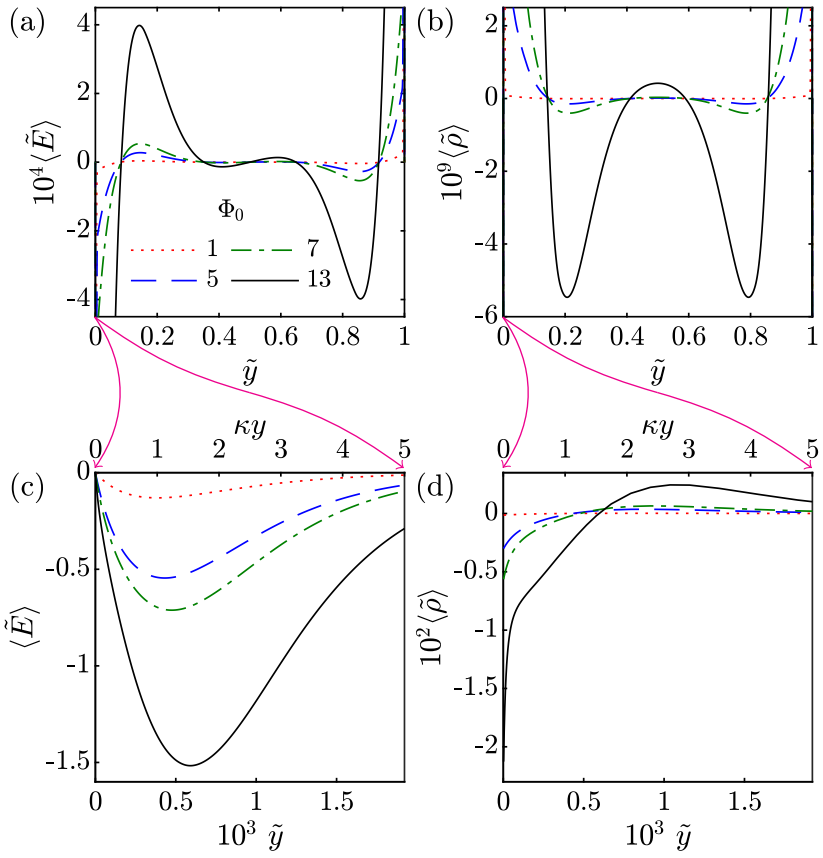

Figure 3.4: Representative spatial distribution of AREF ($\langle\tilde{E}\rangle$) and time average free charge density ($\langle\tilde{\rho}\rangle$) at micron scale (a, b) and close to the electrode surface (c, d) for different values of Φ_0. For all plots, $\mathcal{L}_D = 0.17$, $\delta = 3$, $\kappa H = 2600$.

(indiscernible at this scale) at the electrode ($\tilde{y} = 0$), then rises to an absolute maximum before decaying to the solution at the micron scale shown in Fig. 3.4(a). The free charge density has an absolute nonzero value near the electrode (negative in this representative example), consistent with the nonzero gradient of the AREF at $\tilde{y} = 0$ based on Gauss's law. The mismatch in ionic mobilities yields a net accumulation of ions near the electrodes which subsequently results in AREF.

We focus throughout this section on the AREF behavior at the micron scale, far outside of the Debye layer immediately next to the electrode, since it is in this regime where a steady field will most readily induce experimentally observable behavior with micron scale or larger objects.

3.3.2 Effect of applied potential (Φ_0)

To further analyze the effect of applied potential, consider an illustrative example of an AREF distribution depicted in Fig. 3.5(a). We denote the first peak of AREF outside the Debye layer as $\langle\tilde{E}\rangle_{\text{peak}}$, and $\tilde{y}_{\text{peak}}$ is the corresponding dimensionless location of the peak. As discussed in Fig. 3.4(a), the general shape of the AREF distribution is insensitive to the applied voltage; as a result, the peak location of AREF remains the same at different Φ_0 values. The peak magnitude

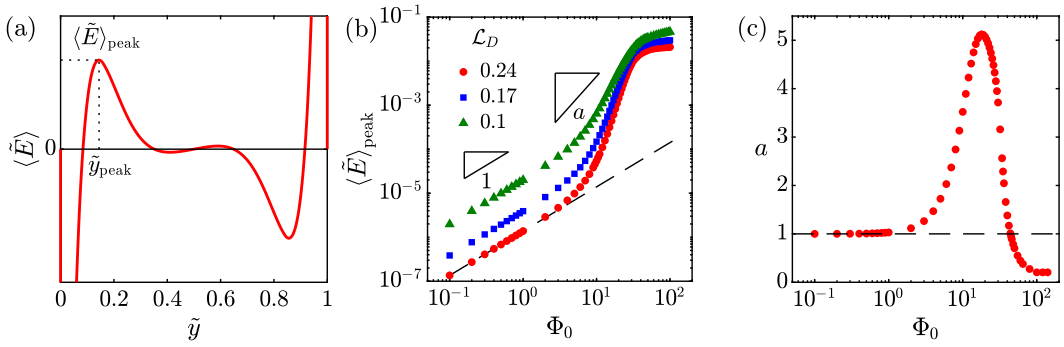

Figure 3.5: (a) Illustrative example of AREF distribution with its peak magnitude ($\langle\tilde{E}\rangle_{\text{peak}}$) and the corresponding peak location ($\tilde{y}_{\text{peak}}$) for $\delta > 1$. (b) AREF peak magnitude versus Φ_0 for different values of $\mathcal{L}_D$. (c) Effect of Φ_0 on the power-law exponent a ($\mathcal{L}_D = 0.24$) . For all plots, $\delta = 3$, $\kappa H = 2600$.

however is significantly affected by Φ_0. Fig. 3.5(b) shows $\langle\tilde{E}\rangle_{\text{peak}}$ versus Φ_0 for different values of $\mathcal{L}_D$. Regardless of $\mathcal{L}_D$, at low voltages ($\Phi_0 < 1$), $\langle\tilde{E}\rangle_{\text{peak}}$ increases as the first power of Φ_0. Recall that the electric field is scaled by ϕ_0/H; hence, the dimensional AREF accordingly varies as ϕ_0^2. At higher Φ_0 values, the behavior becomes more intricate. The power-law exponent a (local slope of the curves) initially increases due to the contribution of nonlinear terms. However, upon further increasing Φ_0, a starts dropping to reach a final constant, the value of which depends on the other dimensionless parameters. A representative example of this behavior is demonstrated in Fig. 3.5(c) for $\mathcal{L}_D = 0.24$. By increasing Φ_0, the power-law exponent a dramatically ascends from 1 and then drops to a constant value below 1. Qualitatively similar results were obtained for different δ and κH values, but the exact dependence of the power a on the applied voltage and other controlling parameters is unclear. Overall, we could not find a universal scaling argument at intermediate/high applied voltages (cf. Sec. 3.4).

Although the exact mathematical scaling is complicated, the overall physical picture is clear: higher applied oscillatory potentials invariably yield a higher steady field in the bulk. Any physical phenomena directly proportional to the magnitude of the AREF, such as instantaneous electrophoretic velocities, will likewise increase with the applied potential, following dependencies similar to those plotted in Fig. 3.5(b). Importantly, however, increases in the applied potential have no effect on the spatial structure of the steady AREF. This aspect has a key physical implication: any experimental observables that depend on the zeros in the AREF, such as the equilibrium heights of particles moving electrophoretically in response to the AREF, will be independent of the applied potential. Indeed, such behavior is observed experimentally with colloids balancing between gravity and electrophoresis.[3]

3.3.3 Effect of diffusive length scale ($\mathcal{L}_D$)

The second key dimensionless parameter is $\mathcal{L}_D$, the frequency-dependent diffusive length scale. Fig. 3.6(a) shows the effect of the dimensionless diffusive length scale $\mathcal{L}_D$ on the spatial distribution of AREF. In contrast to Φ_0, which had no impact on the spatial structure of the AREF, $\mathcal{L}_D$ has a

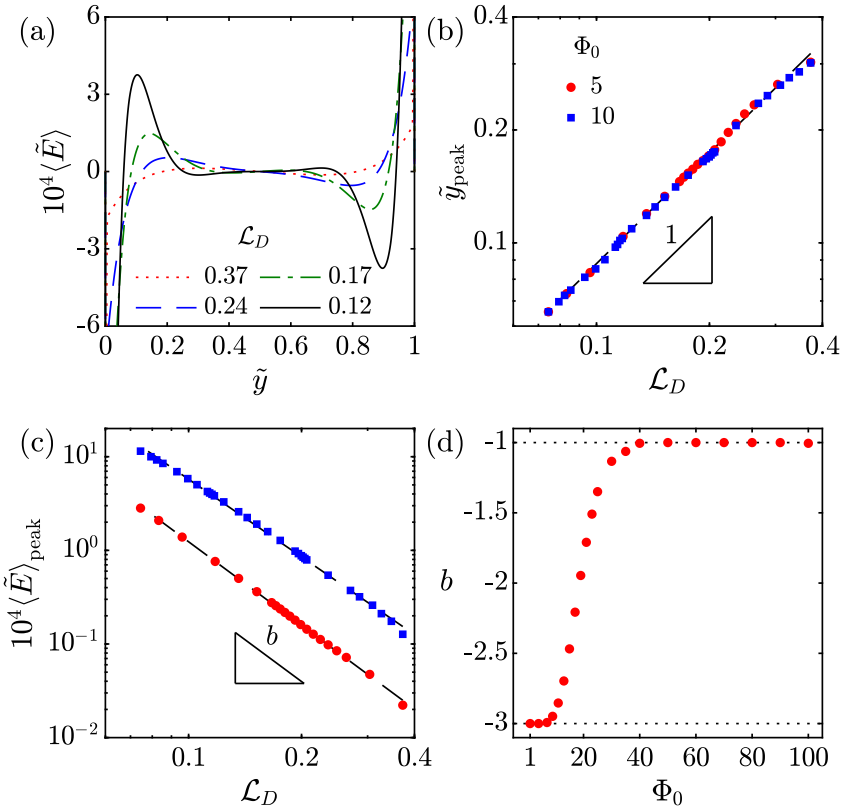

Figure 3.6: Effect of $\mathcal{L}_D$ on AREF behavior. (a) Spatial distribution of AREF for different $\mathcal{L}_D$ values ($\Phi_0 = 10$). (b) Peak location of AREF ($\tilde{y}_{\text{peak}}$) versus $\mathcal{L}_D$. (c) Peak magnitude of AREF ($\langle\tilde{E}\rangle_{\text{peak}}$) versus $\mathcal{L}_D$. (d) Effect of Φ_0 on the power-law exponent b. For all plots, $\delta = 3$, $\kappa H = 2600$.

tremendous impact on the shape of the AREF. By increasing the $\mathcal{L}_D$ value, the AREF shifts away from the electrode surface and its peak value decreases (Fig. 3.6(a)). At higher $\mathcal{L}_D$ values the ions move longer distances during each AC cycle; therefore, the nonlinear effects extend farther away from the electrode surface, with the AREF peak location shifting toward the midplane. Quantitative analysis of the peak location $\tilde{y}_{\text{peak}}$ reveals that it is linearly proportional to $\mathcal{L}_D$ (Fig. 3.6(b)). The AREF peaks at the same location for different voltages, consistent with the results presented in Fig. 3.4(a), where the general shape of AREF is conserved regardless of the applied potential. Further increasing the dimensionless diffusive length scale beyond the case of $\mathcal{L}_D = 0.37$ (Fig. 3.6(a), dotted red curve) eventually results in a curve with no peak outside the Debye layer. To be more precise, for a peak to exist, we require $\mathcal{L}_D < 1/2 \rightarrow \ell_D < H/2$, i.e., the diffusive length scale should not be larger than half of the domain size. Otherwise, the antisymmetric nature of AREF rules out the existence of a peak.

The peak magnitude of AREF is also plotted versus $\mathcal{L}_D$ in Fig. 3.6(c). The general trend is descending. This observation can be understood considering a case where the ions move much faster than the AC time scale (i.e., $\mathcal{L}_D \gg 1$). Under such conditions, on changing the applied potential with the time scale $1/f$, ions have enough time to spatially transfer and screen out any changes

in the potential distribution. It is feasible to argue that for AREF to occur, the ions should only partially screen the applied potential. In other words, the ions should fall behind the AC potential in oscillation. Therefore at very high $\mathcal{L}_D$ values AREF is expected to eventually descend to zero. The power-law exponent b of this descending trend, however, is a function of the applied voltage (Fig. 3.6(d)). The power-law exponent of the AREF magnitude on $\mathcal{L}_D$ is -3 in the linear regime of low applied voltages and approaches to -1 at high voltages. Qualitatively similar results are obtained for different δ and κH values. Despite the uncertainty in underlying impact of the applied voltage, asymptotic scaling arguments are straightforward:

$$\langle \tilde{E} \rangle_{\text{peak}} \propto \mathcal{L}_D^b, \tag{3.28}$$

where $b = -3$ and -1 for $\Phi_0 \sim 1$ and $\Phi_0 \gg 1$, respectively. It appears that by increasing the applied voltage, AREF becomes less sensitive to $\mathcal{L}_D$ value, or in dimensional context, to the applied frequency and ion diffusivities. The underlying reasons for the precise scaling exponents, however, remain obscure.

3.3.4 Effect of ionic mobility mismatch (δ)

The ionic mobility mismatch ($\delta = D_-/D_+$) is perhaps the most intriguing parameter of the AREF effect. The AREF is plotted versus position for different δ values in Fig. 3.7(a). The effect of δ is non-monotonic: by increasing the ionic mobility mismatch from $\delta = 1$, the peak magnitude of AREF increases initially and then starts decaying. Hashemi Amrei et al.[1] showed that for $\delta < 1$, the AREF distribution would be the exact mirror of the displayed curves with respect to the zero line, i.e., it is antisymmetric. While δ has a considerable impact on the oscillatory behavior of AREF and its shape, it does not alter the peak location. A quantitative analysis of the peak magnitude for different conditions in which we change the $\mathcal{L}_D$ and κH values reveals that the non-monotonic trend is robust (Fig. 3.7(b)).

The observed decay of the peak value can be explained via an asymptotic analysis of the problem. In the limit of $\delta \to \infty$ or $\delta \to 0$, one of the ions is extremely fast compared to the other nearly unmoving one. Under such conditions, the two-ion model (Fig. 3.1) predicts a zero time average electric field. In other words, the harmonic oscillations of the two ions are prerequisites of AREF effect: a single oscillating ion would not induce AREF as the time average of its sinusoidal oscillation is invariably zero.

The exact δ value at which $\langle \tilde{E} \rangle_{\text{peak}}$ reaches its maximum (δ_{max}) is however less straightforward. Based on the results shown in Fig. 3.7(b), δ_{max} is unresponsive to $\mathcal{L}_D$ and κH values; the curves collapse under normalization. However, δ_{max} significantly depends on the applied potential. As depicted in Fig. 3.7(c), by increasing the applied potential, the summit of the curve shifts toward $\delta = 1$. This shift is quantitatively demonstrated in Fig. 3.7(d) for a range of $\Phi_0 = 0.1$ to $\Phi_0 = 100$. As shown in this figure, δ_{max} indefinitely decays from ≈ 5.25 toward $\delta = 1$ by increasing the applied voltage.

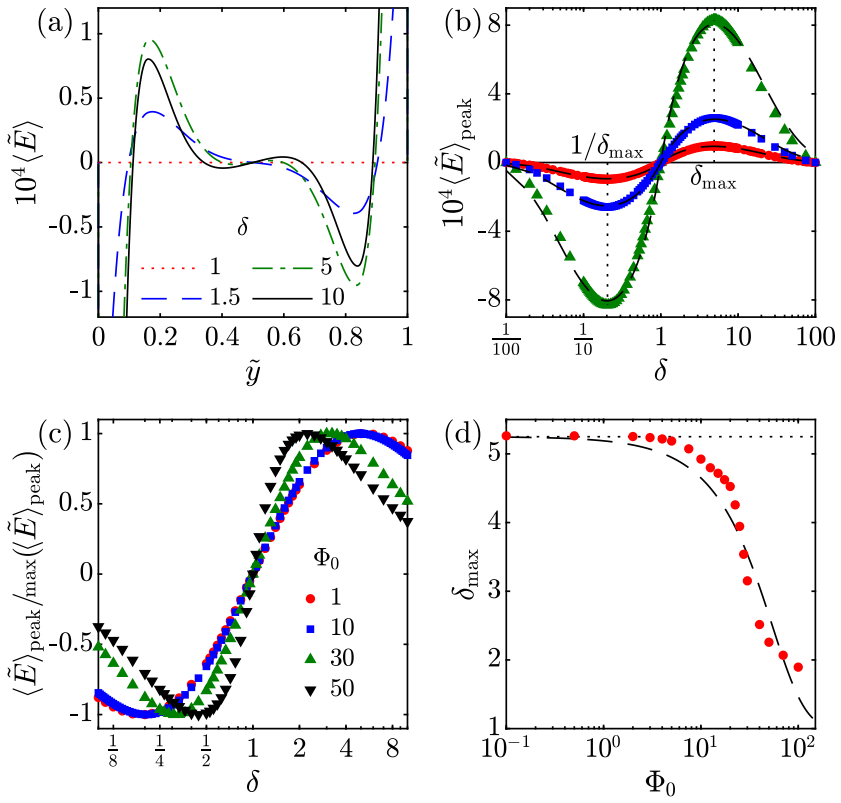

Figure 3.7: Effect of δ on AREF behavior. (a) Spatial distribution of AREF for different δ values ($\Phi_0 = 10$, $\mathcal{L}_D = 0.2$, $\kappa H = 2600$). (b) Peak magnitude of AREF ($\langle\tilde{E}\rangle_{\text{peak}}$) versus δ for different conditions; markers: red circles, $\Phi_0 = 10$, $\mathcal{L}_D = 0.2$, $\kappa H = 2600$; blue squares, $\Phi_0 = 10$, $\mathcal{L}_D = 0.14$, $\kappa H = 2600$; green triangles, $\Phi_0 = 10$, $\mathcal{L}_D = 0.2$, $\kappa H = 822$; dashed black curves are empirical fits; cf. Sec. 3.4. (c) Normalized peak magnitude of AREF ($\langle\tilde{E}\rangle_{\text{peak}}/\max(\langle\tilde{E}\rangle_{\text{peak}})$) versus δ for different Φ_0 values ($\mathcal{L}_D = 0.2$, $\kappa H = 2600$). (d) $\delta_{\max}$ versus Φ_0 ($\mathcal{L}_D = 0.2$, $\kappa H = 2600$); dashed black curve is an empirical fit; cf. Sec. 3.4.

Physically, one way to understand this impact of the applied potential on the peak ionic mobility mismatch is as a measure of how far the ions displace during each cycle. At higher applied potentials, the ions are able to move further away from each other, and accordingly a higher fraction of the faster moving ions are able to 'escape' from the bulk into the double layers adjacent to each electrode. Since the existence of AREF depends on the mismatch between the two species of ions, the decrease in concentration of the speedier ions correspondingly decreases the magnitude of the AREF. At higher applied potentials, only smaller values of delta allow for the two ionic species to coexist at comparably high concentrations without one species escaping from the bulk, and $\delta_{\max}$ decreases accordingly.

3.3.5 Effect of dimensionless Debye parameter (κH)

The dimensionless Debye parameter, which can be thought of as a measure of the ionic strength, also strongly affects the AREF behavior. As demonstrated in Fig. 3.8(a), upon changing the κH value, the general shape and peak location of the AREF distribution is conserved (similar to the effect of

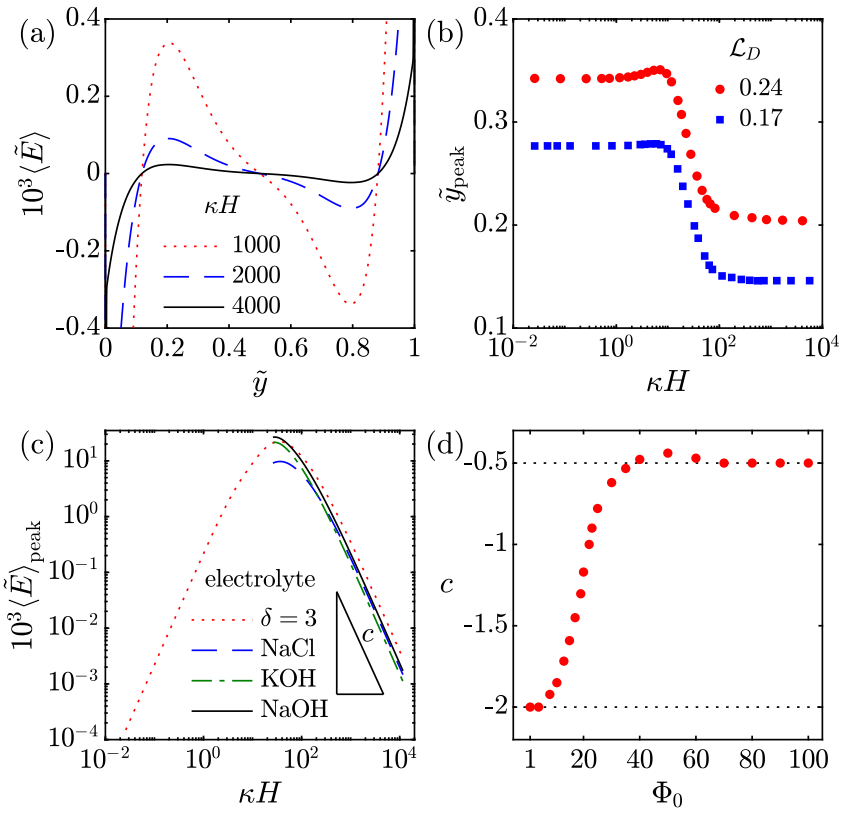

Figure 3.8: Effect of κH on AREF behavior. (a) Spatial distribution of AREF for different κH values ($\Phi_0 = 10$, $\mathcal{L}_D = 0.24$, $\delta = 3$). (b) Peak location of AREF ($\tilde{y}_{\text{peak}}$) versus κH for two different values of $\mathcal{L}_D$ ($\Phi_0 = 10$, $\delta = 3$). (c) Peak magnitude of AREF ($\langle\tilde{E}\rangle_{\text{peak}}$) versus κH for four different electrolytes of $\delta = 3$ ($\mathcal{L}_D = 0.24$), NaCl ($\delta = 1.52$, $\mathcal{L}_D = 0.23$), KOH ($\delta = 2.7$, $\mathcal{L}_D = 0.32$), and NaOH ($\delta = 3.95$, $\mathcal{L}_D = 0.29$) ($\Phi_0 = 10$). (d) Effect of Φ_0 on the power-law exponent c ($\mathcal{L}_D = 0.24$, $\delta = 3$).

Φ_0). Recall that our focus is on the micron scale behavior of AREF; changing the κH value can alter the shape of AREF near the electrodes and within the Debye layer (not shown here). A more accurate analysis of the peak location however shows that the peak location depends only weakly on κH (Fig. 3.8(b)). A transition in the AREF behavior occurs at $10 \lesssim \kappa H \lesssim 100$ that abruptly changes the peak location. As an illustrative example, consider the case of $\mathcal{L}_D = 0.24$ in Fig. 3.8(b). For $\kappa H \gtrsim 100$, AREF peaks at $\tilde{y}_{\text{peak}} \approx 0.2$ (compare to curves in Fig. 3.8(a)). By decreasing the κH value, the peak location experiences a significant jump to ≈ 0.34 for $\kappa H \lesssim 10$. Still, for practical conditions of electrokinetic systems where $H \sim 100$ μm and $c_\infty > 10^{-5}$ M, $\kappa H \gg 100$ for aqueous electrolytes and the peak location remains unresponsive to changes in κH. So, in experiments such as particle height bifurcation,[44,45,3] where the location of the peak is far more important than its magnitude (as long as it is large enough to result in electrophoretic levitation of colloidal particles), the results are not affected by κH.

Note that the transition in $\tilde{y}_{\text{peak}}$ occurs near $\kappa H = 1$ to 10, i.e., in a range where the Debye layer is comparable in size to the electrodes spacing itself. Physically this suggests that the AREF spatial structure has two regimes: one in which the diffusive length scale interacts with the nature

Debye length scale, and one in which they act more independently. Since $\kappa H \gg 1$ for many aqueous systems, it is the latter regime that is more relevant experimentally.

Fig. 3.8(a) shows that how lower values of κH result in higher AREF magnitudes. This behavior is demonstratd in Fig. 3.8(c) for a wide range of κH values and four different electrolytes of $\delta = 3$ ($D_+ = 1 \times 10^{-9}$ m^2/s), NaCl, KOH, and NaOH. The results for all four electrolytes show that for practical electrolyte concentrations and electrode spacings, the AREF magnitude is inversely proportional to κH. The power-law exponent c however is a function of applied voltage (Fig. 3.8(c)). At low Φ_0 values, $c = -2$ and approaches to -0.5 at higher applied voltages, which translates to c_∞^{-1} and $c_\infty^{-1/4}$ dependencies of the peak AREF magnitude on the electrolyte concentration, respectively. By decreasing κH to values where the Debye length is comparable to electrodes spacing, the peak magnitude starts dropping. This drop can be explained through the ionic strength; low κH can be a result of low electrolyte concentration and in asymptotically diluted solutions, the system is depleted of dissolved ions which drive the AREF effect.

3.3.6 Effect of ionic valences ($z_\pm$)

The preceding sections focused on 1-1 electrolytes where $z_+ = |z_-| = 1$. We can introduce more asymmetry to the system by considering nonidentical valences (charge numbers) for the ions. Similar to the definition of $\delta = D_-/D_+$, we define $Z = \mid z_-/z_+ \mid$ as the valence mismatch of the ions. Fig. 3.9(a) and (b) present the AREF distribution for different combinations of z_+ and z_- values and two different δ values. For $\delta = 3$ (Fig. 3.9(a)), decreasing the Z value from 2 to 1/3 (dotted red curve to solid black curve) the peak magnitude of AREF decreases. This descending impact of the Z value on the AREF peak magnitude is more significant when δ is smaller (Fig. 3.9(b)), where changing the Z can even change the AREF direction. The results shown in Fig. 3.9(a) and (b) suggest that δ and Z affect AREF in the same qualitative way. In both cases of $\delta = 3$ and $\delta = 1.5$, decreasing the Z appears to reduce the impact of ionic mobility mismatch. However, if Z is small enough compared to $1/\delta$ (equivalently, if Z is large enough compared to $1/\delta$ when $\delta < 1$), it can even qualitatively deform the AREF distribution (Fig. 3.9(b)). This behavior is analyzed more systematically in Fig. 3.9(c), which demonstrates the normalized magnitude and sign of the AREF peak for various combinations of z_+, z_- and a constant ionic mobility mismatch of $\delta = 1.5$. Note how changing the Z from 2 ($z_+, z_- = 1, -2$) to 1/2 ($z_+, z_- = 2, -1$) changes the AREF direction. Also note that for the case of $z_+, z_- = 3, -2$ which yields $\delta Z = 1$, the AREF peak magnitude is very close to zero. Another interesting observation is that increasing the valences at a constant Z (possible only for z-z electrolytes, assuming a maximum valence number of 3), appears to significantly increase the AREF peak magnitude (e.g., compare the cases of $z_+, z_- = 1, -1$ and $z_+, z_- = 3, -3$.).

A rough approximation is that the product δZ determines the AREF direction. In the two ion model (Fig. 3.1), this idea can be incorporated easily by redefining the ionic mobility mismatch as $\delta = \mid D_- z_-/(D_+ z_+) \mid$. With the standard electrokinetic model however, the problem is more delicate. Although the electromigration term of the Nernst–Planck equation includes the product

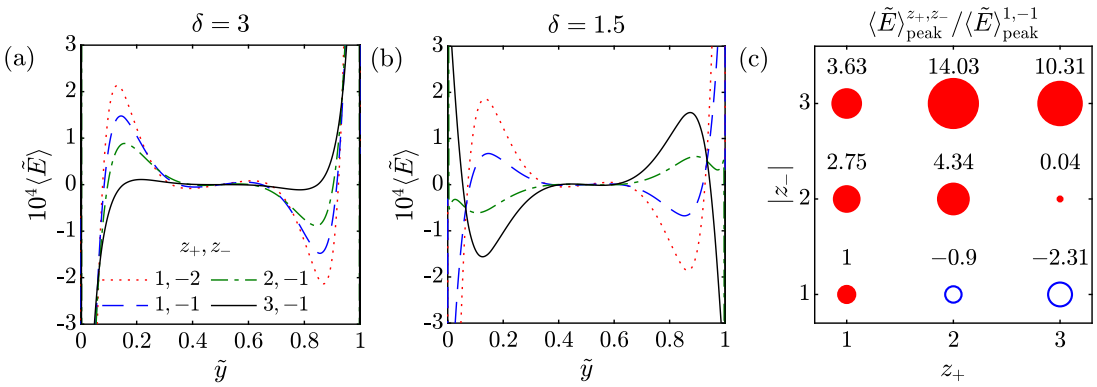

Figure 3.9: Effect of the ion valences (z_+ and z_-) on the AREF behavior. (a, b) Spatial distribution of AREF for different z_+, z_- combinations and two values of δ. (c) Normalized peak magnitude of AREF ($\langle\tilde{E}\rangle^{z_+,z_-}_{\text{peak}}/\langle\tilde{E}\rangle^{1,-1}_{\text{peak}}$) for different z_+, z_- combinations and $\delta = 1.5$. Parameters: $\Phi_0 = 10$, $\mathcal{L}_D = 0.17$, $\kappa H = 2600$ for $z_+ = |z_-| = 1$ ($H = 25$ μm, 1 mM electrolyte).

$D_i z_i$, the diffusivity and charge number appear separately in the diffusive contribution of the Nernst–Planck equation and free charge density term of the Poisson equation, respectively. In other words, the problem cannot be formulated by δZ as the sole term responsible for asymmetry.

3.4 SCALING EXPRESSIONS

The preceding numerical results indicate that both the spatial structure and the magnitude of AREFs depend in a complicated fashion on the system parameters. In this section, we further elaborate the spatial structure, with an emphasis on identifying scaling expressions for where the AREF peaks in magnitude and how often it changes direction with respect to position. Furthermore, we present scaling expressions for the magnitude of the AREF in various asymptotic limits. For simplicity, the analyses are performed for 1-1 electrolytes.

3.4.1 AREF length scale and structure

The dimensionless analysis indicates that $\mathcal{L}_D$ is the only dimensionless parameter that affects the first peak location of AREF. This result is corroborated by a comparison of the numerically observed peak locations of AREF, $\tilde{y}_{\text{peak}}$ plotted simply against the dimensionless diffusive length scale (Fig. 3.10). As shown in this figure, the diffusive length scale nicely predicts the peak location of AREF over a wide parameter space (more than 5000 numerical results). In other words, the peak location scales as

$$\tilde{y}_{\text{peak}} = K\mathcal{L}_D, \tag{3.29}$$

where the fitting prefactor $K \approx 0.83$ is obtained by linear regression. This result is significant since it provides an accurate and straightforward prediction for the AREF peak location for any condition (at least, over the wide range of values tested here). This finding also justifies $\hat{D} = \sqrt{D_+ D_-}$ as the correct characteristic diffusivity governing the AREF behavior.

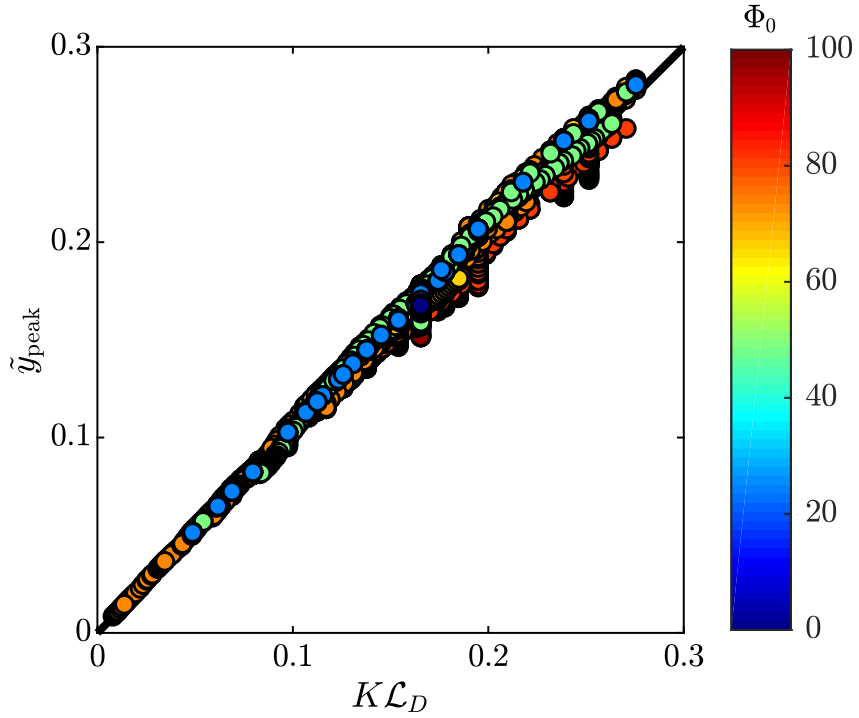

Figure 3.10: Numerically observed peak location of AREF ($\tilde{y}_{\text{peak}}$) versus the predictions of the empirical formula $K\mathcal{L}_D = K\sqrt{\bar{D}/f}/H$ for conditions that $\mathcal{L}_D < 1/3$. The correction coefficient is $K \approx 0.83$. Range of dimensional parameters (≈ 5000 data points): $0.1 \leqslant \phi_0 \leqslant 100$ k_BT/e, $1 \leqslant f \leqslant 30000$ Hz, $2 \leqslant H \leqslant 100$ μm, $0.01 \leqslant \delta \leqslant 100$, $5 \times 10^{-10} \leqslant D_+ \leqslant 5 \times 10^{-9}$ m^2/s, $10^{-5} \leqslant c_\infty \leqslant 2 \times 10^{-2}$ M.

Another important point to consider is the spatially oscillatory behavior of AREF (Fig. 3.11), which is controlled by the dimensionless parameters $\mathcal{L}_D$ and δ; as demonstrated in subsection 3.3.2 and subsection 3.3.5, Φ_0 and κH do not affect the spatial structure of the AREF. For large values of $\mathcal{L}_D$, AREF passes zero only once with no peak outside the Debye layer (Fig. 3.11(a), $\mathcal{L}_D = 0.74$). Upon decreasing $\mathcal{L}_D$ (or equivalently, increasing the frequency), first a peak appears with AREF passing zero three times (Fig. 3.11(b), $\mathcal{L}_D = 0.24$). Further decreasing the $\mathcal{L}_D$ value results in 5 and then 7 zeros (Fig. 3.11(c) and (d)). In other words, when $\mathcal{L}_D$ decreases, there is more space for AREF to oscillate and change sign. Note that AREF is always zero at the midplane. The oscillatory behavior of the AREF can be further analyzed by the bifurcation diagram demonstrated in Fig. 3.12(a). Consistent with the results provided in Fig. 3.11, at high $\mathcal{L}_D$ values, there is only one zero which occurs at the midplane. As $\mathcal{L}_D$ decreases, pitchfork bifurcations[73] occur at the midplane. After each bifurcation, two more zeros are added to the system while the slope of the AREF at the midplane switches.

Despite the fact that $\mathcal{L}_D$ determines the peak location of AREF, it is not the only dimensionless parameter controlling the number of zeros. Fig. 3.7(a) shows that, for constant $\mathcal{L}_D$, the first AREF peak is independent of the precise δ value. However, the δ value can shift and deform the smaller peaks of the distribution and consequently the overall number of zeros (cf. the cases of $\delta = 1.5$ and

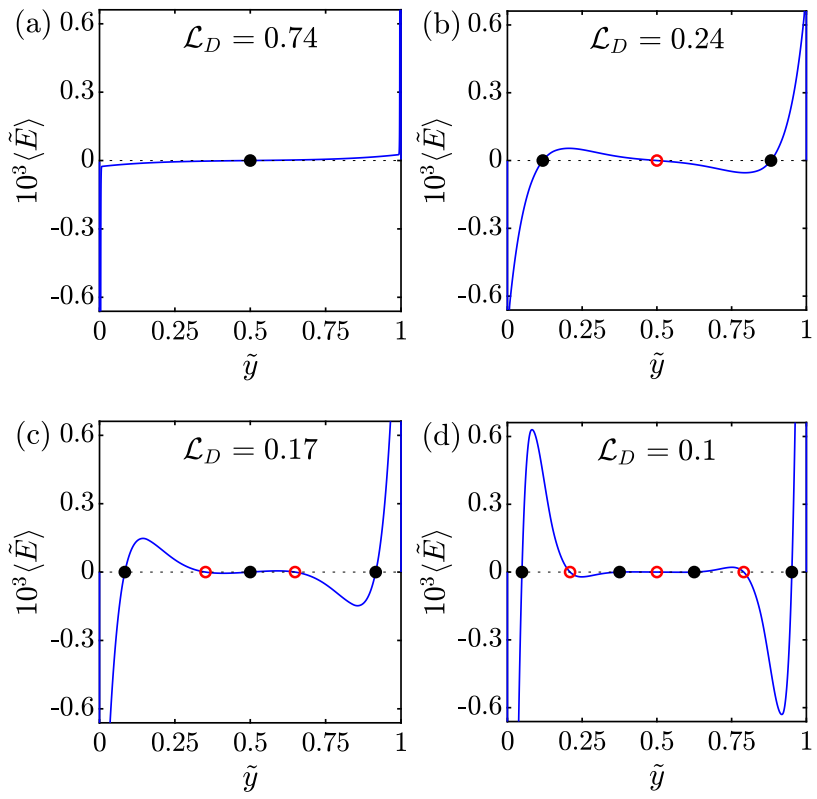

Figure 3.11: Oscillatory behavior of AREF for different values of $\mathcal{L}_D$. Filled black and empty red circles are the points that AREF passes zero with positive and negative slopes, respectively. Parameters: $\Phi_0 = 10$, $\delta = 3$, $\kappa H = 2600$.

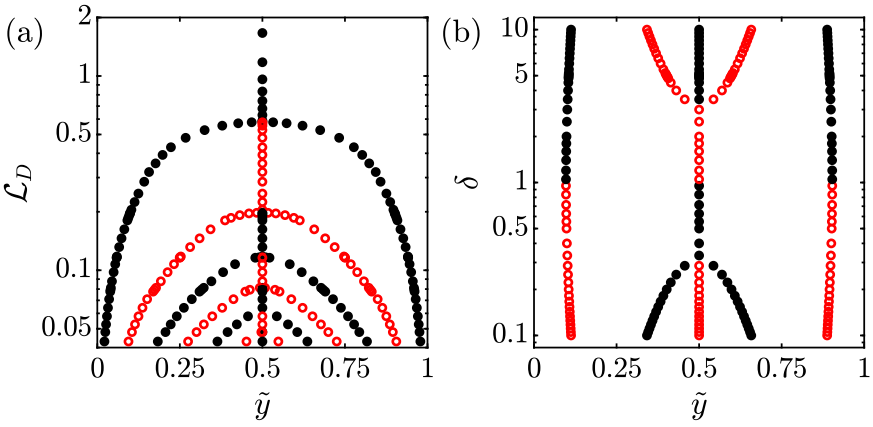

Figure 3.12: Bifurcation diagrams of AREF for $\mathcal{L}_D$ (a) and δ (b) as varying parameters. Filled black and empty red circles are the points that AREF passes zero with positive and negative slopes, respectively. Parameters: $\Phi_0 = 10$, $\mathcal{L}_D = 0.2$ (b), $\delta = 3$ (a), $\kappa H = 2600$.

10 in Fig. 3.7(a)). This behavior is plotted quantitatively in the bifurcation diagram in Fig. 3.12(b), showing the number of zeros for different δ values. For δ values close to 1, the AREF passes zero three times; by increasing/decreasing the δ value from 1 pitchfork bifurcations happen at the

midplane.

3.4.2 AREF magnitude scaling

Based on the results presented in Sec. 3.3, $\langle\tilde{E}\rangle_{\text{peak}} \propto \Phi_0^a$, $\langle\tilde{E}\rangle_{\text{peak}} \propto \mathcal{L}_D^b$, and $\langle\tilde{E}\rangle_{\text{peak}} \propto (\kappa H)^c$. Here the power a increases non-monotonically from 1 in the linear regime ($\Phi_0 \sim 1$) to a maximum in the nonlinear regime, before decaying to a small constant value at very high applied voltages (cf. Fig. 3.5(c)). The powers b and c are -3 and -2 for $\Phi_0 \sim 1$ and approach to -1 and -0.5 for $\Phi_0 \gg 1$, respectively.

The effect of δ is more complicated. The non-monotonic behavior demonstrated in Fig. 3.7(b) may be approximated by the empirical fits

$$\langle\tilde{E}\rangle_{\text{peak}} = c_1 \alpha \exp\left(-c_2|\alpha|\right), \tag{3.30}$$

where

$$\alpha = \sqrt{\delta} - 1/\sqrt{\delta} = (D_- - D_+)/\hat{D}. \tag{3.31}$$

Knowing $\delta_{\max}$, one can easily find the coefficient c_2 by differentiation of the fitting curve formula as $c_2 = 1/\alpha_{\max}$, where

$$\alpha_{\max} = \sqrt{\delta_{\max}} - 1/\sqrt{\delta_{\max}}. \tag{3.32}$$

Finally we get

$$\langle\tilde{E}\rangle_{\text{peak}} \propto \alpha \exp\left(-|\alpha|/\alpha_{\max}\right), \tag{3.33}$$

where $\alpha_{\max}$ is a function of the applied voltage (Fig. 3.7(d)). Unlike b and c, $\delta_{\max}$ does not appear to approach a certain value at high voltages. Hence, to provide scaling expressions at high voltages, we use an empirical formula to fit the $\delta_{\max}$ vs Φ_0 data. The fitting curve in Fig. 3.7(d) is a sigmoid function

$$\delta_{\max} = k_1 - k_2 \frac{e^{k_3 \Phi_0}}{1 + e^{k_3 \Phi_0}}. \tag{3.34}$$

We can find the coefficients k_1 and k_2 enforcing the conditions $\delta_{\max} \to 5.25$ as $\Phi_0 \to 0$ and $\delta_{\max} \to \delta_\infty$ as $\Phi_0 \to \infty$. The final value of $\delta_{\max} = \delta_\infty$ is unclear, due to the lack of numerical results at extremely high voltages. However, we can make a reasonable assumption: note that $\delta_{\max}$ indefinitely gets closer to 1 by increasing the Φ_0; considering this descending trend, along with the fact that it is already below 2 for $\Phi_0 = 100$, we hypothesize that $\delta_{\max}$ eventually approaches 1. Using these conditions, we find the coefficients $k_1 = 9.5$ and $k_2 = 8.5$. The last coefficient k_3 is found by fitting as $k_3 \approx 0.03$. Of course a better fitting formula could be employed but at the expense of simplicity.

A possible scaling of the AREF peak magnitude can then be obtained by multiplication of all scaling arguments as

$$\langle\tilde{E}\rangle_{\text{peak}} \propto \Phi_0^a \mathcal{L}_D^b (\kappa H)^c \gamma, \tag{3.35}$$

where $\gamma = \alpha \exp\left(-|\alpha|/\alpha_{\max}\right)$ with $\alpha_{\max} = \sqrt{\delta_{\max}} - 1/\sqrt{\delta_{\max}}$ and $\delta_{\max}$ given by the empirical

formula in Eq. 3.34.

Although the complicated impact of Φ_0 obscures any generalized scaling analysis, asymptotic expressions can be obtained. We consider two different regimes of applied voltages as low-intermediate ($0 < \Phi_0 \leqslant 20$) and intermediate-high ($20 \leqslant \Phi_0 \leqslant 100$). The underlying reason of this division is the variations of b, c, and $\delta_{\max}$ with Φ_0. The applied voltage of $\Phi_0 = 20$ is approximately at the middle of transition from low to high applied voltages regimes (cf. Fig. 3.6(d), Fig. 3.7(d), and Fig. 3.8(d)). Besides, the summit of power a in Fig. 3.5(c), occurs around $\Phi_0 \approx 20$, regardless of the system properties.

Substituting $a = 1, b = -3, c = -2$ gives the simplified scaling argument at low-intermediate

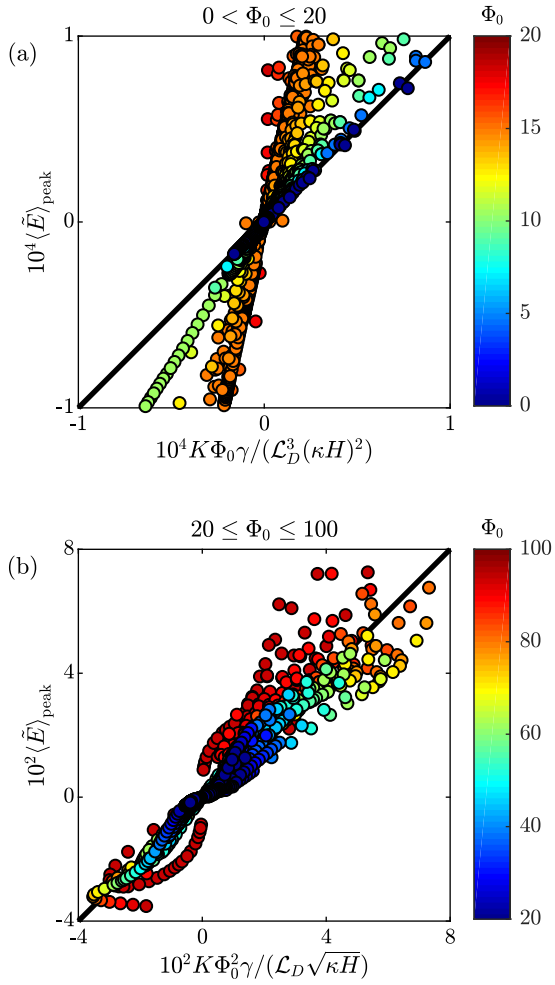

Figure 3.13: Numerically observed peak magnitude of AREF ($\langle\tilde{E}\rangle_{\text{peak}}$) versus the predictions of the empirical formula $\langle\tilde{E}\rangle_{\text{peak}} \approx \Phi_0^a \mathcal{L}_D^b \gamma(\kappa H)^c$ for conditions that $\mathcal{L}_D < 1/3$. (a) Low to moderate voltages ($0 < \Phi_0 \leqslant 20$): fitting is performed using low voltage data ($\Phi_0 < 5$, $K \approx 0.19$). (b) Moderate to high voltages ($20 \leqslant \Phi_0 \leqslant 100$): fitting is performed using all data points ($K \approx 2 \times 10^{-4}$). Range of dimensional parameters ($\approx$ 5000 data points): $0.1 \leqslant \phi_0 \leqslant 100$ $k_B T/e$, $1 \leqslant f \leqslant 30000$ Hz, $2 \leqslant H \leqslant 100$ μm, $0.01 \leqslant \delta \leqslant 100$, $5 \times 10^{-10} \leqslant D_+ \leqslant 5 \times 10^{-9}$ m^2/s, $10^{-5} \leqslant c_\infty \leqslant 2 \times 10^{-2}$ M.

applied voltages:

$$\Phi_0 \leqslant 20: \quad \langle \tilde{E} \rangle_{\text{peak}} \approx K \frac{\Phi_0 \gamma}{\mathcal{L}_D^3 (\kappa H)^2}, \tag{3.36}$$

where the coefficient K is obtained by fitting as $K \approx 0.19$. Fig. 3.13(a) shows a comparison between the numerically observed peak magnitude of AREF and predictions of Eq. 3.36. Note that Eq. 3.36 captures the AREF peak magnitude extremely well for $\Phi_0 < 5$ (blue points in Fig. 3.13(a)). For intermediate voltages, it is only the power a that is increasing from 1, while the data points are still nicely linear. Recall that the power a increases monotonically from 1 at low-intermediate values of Φ_0 (cf. Fig. 3.5(c)).

Similarly, we can insert $b = -1, c = -0.5$ to find the scaling expression at intermediate-high applied voltages. Since this range of applied voltage ($0.5 \leqslant \phi_0 \leqslant 2.5$ volts, or peak-to-peak applied voltages of 1–5 volts) is frequently used in electrokinetic experiments we prefer to fit the data using all results. So instead of substituting an a value below 1 (cf. Fig. 3.5(c) at very high Φ_0 values), we heuristically find a value that collapse all data points. Our analysis shows that an average of summit and final a values ($a \approx 2$) is a good choice. Hence, the scaling expression at intermediate-high applied voltages can be written as

$$\Phi_0 \geqslant 20: \quad \langle \tilde{E} \rangle_{\text{peak}} \approx K \frac{\Phi_0^2 \gamma}{\mathcal{L}_D \sqrt{\kappa H}}, \tag{3.37}$$

with $K \approx 2.1 \times 10^{-4}$ obtained from linear regression. The corresponding comparison provided in Fig. 3.13(b) shows that the prediction of Eq. 3.37 is in the right neighborhood, (R-square ≈ 0.9), differing by at most a factor of 2 over the entire range of parameters tested. This scaling estimate should help in interpretation of experimental results involving AREFs.

3.5 CONCLUSIONS

In summary, we have comprehensively investigated the AREF phenomenon reported recently by Hashemi Amrei et al.[1] The effects of various parameters including the applied voltage and frequency, ionic mobility mismatch, mobilities of the dissolved ions, ionic strength, electrodes spacing, and valences of the ions on the spatial structure and magnitude of the AREF were analyzed in detail.

Dimensionless analysis of the problem shows that the diffusive length scale ℓ_D, with $\sqrt{D_+ D_-}$ as the characteristic diffusivity, can accurately predict the peak location of the AREF in a wide spectrum of system properties. The AREF magnitude, in contrast, is found to be more complicated, mainly due to the confounding nonlinear impacts of the applied voltage. Regardless of the system properties, at low applied voltages ($\Phi_0 \sim 1$), the peak magnitude of AREF varies as Φ_0. No universal correlation is found for $\Phi_0 > 1$, except that the power-law exponent a ($\langle \tilde{E} \rangle_{\text{peak}} \propto \Phi_0^a$) increases nonlinearly from 1 by increasing the applied voltage and then drops to a small constant value at sufficiently high applied voltages ($\Phi_0 \gg 1$). This peculiar influence of Φ_0 complicates the analyses of the other dimensionless parameters. Our observations indicate that the AREF

peak magnitude decreases by increasing the $\mathcal{L}_D$, with a rate that depends on the applied voltage. The power-law exponent b ($\langle\tilde{E}\rangle_{\text{peak}} \propto \Phi_0^a$) is -3 at low applied voltages and approaches to -1 as Φ_0 increases. In other words, the AREF magnitude becomes less sensitive to the $\mathcal{L}_D$ at higher voltages. The ionic mobility mismatch has a non-monotonic impact on the AREF magnitude. By increasing the deviation form $\delta = 1$, $\langle\tilde{E}\rangle_{\text{peak}}$ ascends to a maximum at $\delta_{\max}$ and then starts dropping. Here, $\delta_{\max}$ depends on Φ_0: $\delta_{\max} \approx 5.25$ at low Φ_0 values and gets indefinitely closer to 1 by increasing the applied voltage. Finally, we find that for most electrokinetic systems $\langle\tilde{E}\rangle_{\text{peak}} \propto (\kappa H)^c$, where $c = -2$ and -0.5 at low and high applied voltages, respectively. Therefore the AREF is less sensitive to κH at higher Φ_0 values. Using the obtained results from the dimensionless analysis, we provide simplified scaling arguments that can be use of researchers in interpretation and control of experiments.

While the above-mentioned results were obtained for univalent electrolytes, we also demonstrated that introducing asymmetry through nonidentical ion valences is as important as the ionic mobility mismatch. Furthermore, the results presented here are limited to situations where electrochemical and convective contributions to the flux are negligible, and there is no formation of Stern layers at the electrodes. These more complicated effects are deferred to future studies.

Chapter 4

Asymmetric Rectified Electric Fields Generate Flows that Can Dominate Induced-Charge Electrokinetics

Overview*

We derive a generalized induced-charge electrokinetic (ICEK) velocity around a conducting object placed in an arbitrary multimodal electric field. The generalized model allows consideration of asymmetric rectified electric fields (AREFs), which have recently been established to occur in liquids where the ions present have unequal mobilities. Including the AREF yields fluid velocities in which both the direction and the magnitude depend sensitively on the applied potential, frequency, ionic type and strength, and even the exact placement of the object between parallel electrodes. The results provide a new explanation for the long-standing question of flow reversals observed in ICEK systems.

*This chapter was previously published by Hashemi Amrei et al. and is reproduced here with minor modifications. See: **S. M. H. Hashemi Amrei**, G. H. Miller, and W. D. Ristenpart *Asymmetric rectified electric fields generate flows that can dominate induced-charge electrokinetics*, Phys. Rev. Fluids 5 (2020) 013702.[4]

4.1 INTRODUCTION

Nonlinear electroosmotic flows around colloidal particles, also known as electrokinetic phenomena of the 2nd kind, were first formulated theoretically by Dukhin and co-workers in the 1980s.[15–17] They demonstrated that application of an external electric field induces a charge cloud near the surface of a polarizable object; the field then creates a body force on the charge cloud, creating an electroosmotic fluid flow. In contrast to standard electroosmosis, the fluid velocity scales as the square of the electric field, so that flow results from both steady and oscillatory applied fields. One early application of nonlinear electroosmotic flows was liquid pumping via asymmetric electrodes subject to AC electric potentials, also known as AC electroosmosis (ACEO).[20–23] More recently, Bazant and Squires[18,19] unified nonlinear electrokinetic phenomena around polarizable objects (particles, electrodes, etc.) under the name induced-charge electrokinetics (ICEK).[32,33,74,75] The general theoretical approach has been to solve either the Laplace equation or the standard electrokinetic model (Poisson–Nernst–Planck) to predict the electric field distribution and polarization of the charge layer around the objects, and then determine the induced flow. The archetypal example of ICEK theory is the quadrupolar fluid flow around a conducting sphere or cylinder in response to steady or time varying electric fields,[18,19] a system which has been experimentally observed in a number of studies using metallic spheres[76,77] and wires.[78–80]

Despite extensive research, however, there are several unresolved discrepancies between theoretical predictions and experimental observations.[32,33] In particular, extant theories fail to predict the observed reversal in the direction of fluid flow in ACEO pumps at sufficiently high frequencies.[23,81–84] Similarly, experimental work revealed that the flow direction in ACEO pumps also depends on the identity of the electrolyte present; for example, at particular voltages and frequencies, simply swapping KCl with KOH caused the flow to reverse direction. Because neither the frequency nor electrolyte dependence are explicable in terms of the standard ICEK theory, much work focused on whether the continuum approximation incorrectly neglected ion-ion interactions and steric effects, thus yielding unrealistically high ion concentrations near the electrodes.[85,86,83,72,29] By introducing the effective ion size as a fitting parameter, Bazant and co-workers qualitatively predicted a fluid flow reversal in AC electroosmosis pumps upon changing the applied frequency. However, an unrealistically large ion size (several nanometers) was found to be necessary, casting doubt on this approach.

Notably, all theoretical studies on ICEK to date have assumed that the dissolved ions have equal mobilities, an assumption that considerably simplifies the modeling but rarely pertains to real electrolytes. Recent work by Hashemi Amrei et al.[1,2] has demonstrated that application of a perfectly sinusoidal oscillating potential generates a highly multimodal, long-range electric field between parallel electrodes. Furthermore, if the ions present have unequal mobilities, the multimodal field has a non-zero time average, i.e., the sinusoidal applied potential generates a steady field component. This phenomenon, referred to as Asymmetric Rectified Electric Field (AREF), acts like a DC field and induces electrophoretic motion consistent with experimental observations of particle levitation against gravity.[3] These findings suggest that AREFs will also

generate a net fluid flow around a charged object placed in the field via electroosmosis, and thus affect ICEK flows. It remains unclear, however, under what conditions AREFs play a significant role in ICEK flows, and whether they are associated with the flow reversals observed experimentally.

In this work, we analyze theoretically the impact of AREFs on ICEK flows. Because extant theories only consider unimodal electric fields, we begin by deriving a generalized ICEK model valid for arbitrary, multi-modal electric fields. We then insert numerical solutions to the fully nonlinear standard electrokinetic model to assess the impact of AREFs on the ICEK flow. Focusing on the flow around a conductive cylinder, we demonstrate that under many conditions the higher order modes and the zeroth mode (the AREF) dominate the overall flow velocity around the cylinder. In particular, the calculations predict significant flow reversals with respect to frequency, electrolyte type, and even the exact placement of the cylinder between conducting electrodes. Our results point toward a resolution of the long-standing discrepancies between ICEK theory and experiments.

4.2 GENERALIZED ICEK FOR ARBITRARY ELECTRIC FIELD

The central idea of ICEK is that the electric field induces a charge cloud (or an equivalent zeta potential) immediately adjacent to a conductive surface. The tangential component of the same electric field then acts on the induced charge cloud, creating an electroosmotic fluid flow with a slip velocity given by Smoluchowski's formula. Bazant and Squires[18,19] showed that for a steady electric field of magnitude E, i.e., $E(t) = E$, the angular slip velocity around a conductive cylinder of radius a is

$$u_\theta^s = 2\frac{\varepsilon a E^2}{\mu}\sin(2\theta) + 2\frac{\varepsilon \zeta_0 E}{\mu}\sin(\theta) \tag{4.1}$$

where θ is the polar angle (cf. Fig. 1), ε and μ are the permittivity and viscosity of the electrolyte, respectively, and ζ_0 is the intrinsic zeta potential of the cylinder surface. The first term on the right hand side is the quadrupolar flow due to the action of the tangential component of the electric field on the surface of the cylinder ($E_\theta|_{r=a}$) on the induced zeta potential, while the second term is the dipolar flow due to the same field acting on the intrinsic zeta potential. Depending on the relative strength of these two terms, various net flows of different shapes that are more or less quadrupolar occur for a steady applied electric field.

In contrast, for a sinusoidal electric field of amplitude E and angular frequency ω_0, i.e., $E(t) = E\cos(\omega_0 t)$, the time average of the slip velocity is[18,19]

$$\langle u_\theta^s \rangle = \frac{\varepsilon a E^2}{\mu}\frac{\sin(2\theta)}{\omega_0^2\tau_c^2 + 1}. \tag{4.2}$$

Here $\tau_c = \kappa^{-1}a/\hat{D}$ is the charging time scale of the ionic cloud around the cylinder, where κ^{-1} is the Debye length scale and $\hat{D}$ is a characteristic diffusivity of the dissolved ions. Importantly, the electroosmotic flow due to the action of the sinusoidally varying electric field on the constant

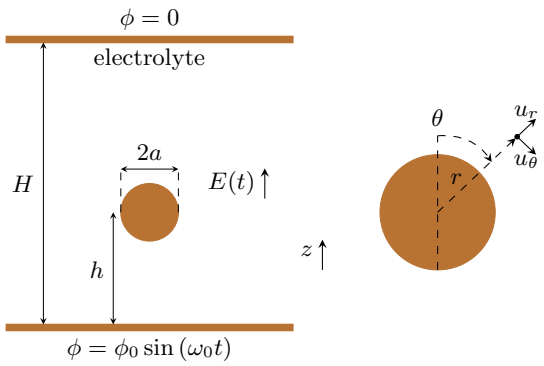

Figure 4.1: Schematic diagram of the problem. Left: a conducting cylinder of radius a is immersed in an electrolyte between two parallel electrodes at height h. An oscillatory electric potential is applied on one electrode while the other is grounded. Right: problem in cylindrical coordinates with scalar velocity components in r and θ directions.

intrinsic zeta potential has zero time average, and hence the dipolar component is identically zero for a unimodal applied field. Note also that the velocity is expected to decay monotonically as frequency increases or the electrolyte diffusivity decreases, i.e., no reversals in the flow direction are predicted to occur as frequency changes or for different electrolytes.

We now ask, what happens if the applied field is multimodal? We follow the same basic framework proposed by Bazant and Squires,[18,19] but we generalize it to find the slip velocity when $E(t)$ is an arbitrary function of time. Assuming a thin double layer limit ($\kappa a \gg 1$), the solution to the Laplace equation for the electric potential around the cylinder is

$$\psi = -E(t) r \cos(\theta) \left(1 + g \frac{a^2}{r^2}\right), \tag{4.3}$$

where g is the induced dipole strength, and (r, θ) are the cylindrical coordinates (cf. Fig. 4.1). The induced surface charge on the cylinder, q, obeys charge conservation such that conduction of ions from the bulk in the radial direction are balanced by charge accumulation, such that

$$\frac{\partial q}{\partial t} = \sigma E_r|_{r=a} = \sigma E(t) \cos(\theta)(1 - g). \tag{4.4}$$

Here σ is the effective electrolyte conductivity and $E_r = -\frac{\partial \psi}{\partial r}$ is the radial component of the electric field. Simultaneously, the induced zeta potential is

$$\zeta = -\psi|_{r=a} = E(t) a \cos(\theta)(1 + g), \tag{4.5}$$

where we assumed that electric potential of the perfectly conducting cylinder remains zero at all times. The induced zeta potential is then related to the surface charge with $q = \varepsilon \kappa \zeta$. Note that this equality is justified only at low voltages and is used for simplicity; use of more sophisticated models is straightforward but complicates interpretation. Substituting this equality into Eq. 4.5

and differentiation with respect to time yields

$$\frac{\partial q}{\partial t} = \varepsilon\kappa a \cos(\theta)\left[\frac{dE(t)}{dt}(1+g) + E(t)\frac{dg}{dt}\right]. \tag{4.6}$$

Combining Eq. 4.4 and Eq. 4.6 yields an ordinary differential equation for g that can be solved for an arbitrary electric field $E(t)$ (See Sec. B.2 for details),

$$g = 2\frac{\int e^{\hat{t}}E(\hat{t})d\hat{t}}{e^{\hat{t}}E(\hat{t})} - 1, \tag{4.7}$$

where $\hat{t} = t/\tau_c$ is a dimensionless time, normalized on the charging time scale $\tau_c = \kappa^{-1}a/\hat{D} = \varepsilon\kappa a/\sigma$,[67,24] and the term $\int e^{\hat{t}}E(\hat{t})d\hat{t}$ is an indefinite integral. Substituting the obtained induced dipole g into Eq. 4.3 yields the potential distribution, which is subsequently used to find the induced zeta potential and tangential component of the electric field ($E_\theta = -\frac{1}{r}\frac{\partial\psi}{\partial\theta}$) on the cylinder surface. Finally, Smoluchowski's formula for electroosmosis gives the induced slip velocity for an arbitrary field,

$$u_\theta^s = -\frac{\varepsilon(\zeta+\zeta_0)E_\theta|_{r=a}}{\mu} = \frac{2\varepsilon a}{\mu}\left[\frac{\int e^{\hat{t}}E(\hat{t})d\hat{t}}{e^{\hat{t}}}\right]^2\sin(2\theta) + \frac{2\varepsilon\zeta_0}{\mu}\left[\frac{\int e^{\hat{t}}E(\hat{t})d\hat{t}}{e^{\hat{t}}}\right]\sin(\theta). \tag{4.8}$$

If the product $e^{\hat{t}}E(\hat{t})$ is simply integrable, then analytical simplifications are straightforward. For a steady (time invariant) applied field, Eq. 4.1 is immediately recovered. Likewise, for a unimodal oscillating field $E(t) = E\cos(\omega_0 t)$, the instantaneous slip velocity is

$$u_\theta^s = \frac{2\varepsilon a E^2}{\mu}\left[\frac{\omega_0\tau_c\sin(\omega_0 t) + \cos\omega_0 t}{1+\omega_0^2\tau_c^2}\right]^2\sin(2\theta) + \frac{2\varepsilon\zeta_0 E}{\mu}\left[\frac{\omega_0\tau_c\sin(\omega_0 t) + \cos\omega_0 t}{1+\omega_0^2\tau_c^2}\right]\sin(\theta), \tag{4.9}$$

which upon time averaging reduces to the classic ICEK flow velocity for oscillatory fields (cf. Eq. 4.2),

$$\langle u_\theta^s\rangle = \frac{\omega_0}{2\pi}\int_0^{\frac{2\pi}{\omega_0}} u_\theta^s dt = \frac{\varepsilon a E^2}{\mu}\frac{\sin(2\theta)}{\omega_0^2\tau_c^2+1}. \tag{4.10}$$

4.3 SOLUTION TO THE ELECTROKINETIC MODEL

With a generalized ICEK model for arbitrary electric fields in hand, we now ask what happens for the multimodal fields that occur in electrolytes at sufficiently high applied voltages. The details of these fields have been elaborated elsewhere;[1,2] here we provide a brief summary. We focus on 1-1 binary electrolytes between parallel electrodes separated by a distance H (cf. Fig. 4.1), and we assume that the presence of the cylinder and any resulting flows do not appreciably alter the electric field between parallel electrodes. In other words, we assume that both $a/H \ll 1$ and $a/h \ll 1$ so that we can use the electric field solution $E(t,z)$ in the absence of the cylinder, and we then take $E(t,h)$ (the electric field at the cylinder height, $z = h$) as the field to implement the generalized ICEK velocity. We emphasize that this approach is approximate since it neglects the impact of the

cylinder itself on the applied electric field, but our goal is to examine the limiting case of 'small' cylinders to shed light on the influence of AREFs on the ICEK flow and to serve as a limiting case for more detailed future calculations.

To obtain the multimodal electric field (in the absence of the cylinder), the Poisson equation relates the free charge density to the electric field gradient,

$$-\varepsilon\frac{\partial^2\phi}{\partial z^2} = e(n_+ - n_-), \tag{4.11}$$

while the transport of ions is governed by Nernst–Planck equations,

$$\frac{\partial n_\pm}{\partial t} = D_\pm\frac{\partial^2 n_\pm}{\partial z^2} \pm e\frac{D_\pm}{k_BT}\frac{\partial}{\partial z}\Big(n_\pm\frac{\partial\phi}{\partial z}\Big). \tag{4.12}$$

Here the symbols stand for permittivity of the electrolyte, ε; electric potential, ϕ; elementary charge, e; number concentration of ion, $n_\pm$; diffusivity, $D_\pm$; Boltzmann constant, k_B; absolute temperature, T; location with respect to the lower electrode, z; and time, t. The terms on the right-hand-side of the Nernst–Planck equation represent diffusive (thermal) motion and electromigration of the ions; the nonlinearity of the problem stems from the latter term. To close the problem we apply the initial conditions

$$n_\pm(0,z) = n_\pm^\infty, \tag{4.13a}$$

$$\phi(0,z) = 0, \tag{4.13b}$$

and specified potential and no-flux boundary conditions,

$$-D_\pm\Big(\frac{\partial n_\pm}{\partial z} \pm \frac{en_\pm}{k_BT}\frac{\partial\phi}{\partial z}\Big)_{z=0,H} = 0, \tag{4.14a}$$

$$\phi(t,0) = \phi_0\sin(\omega_0 t), \quad \phi(t,H) = 0. \tag{4.14b}$$

Note that we assume blocking electrodes where no electrochemistry occurs, such that the flux of ions through the electrodes is identically zero (Eq. 4.14a). In addition, we neglect the formation of a compact Stern layer at the electrodes. A sinusoidal electric potential of amplitude ϕ_0 and angular frequency $\omega_0 = 2\pi f_0$ is applied on the lower electrode at $z = 0$ while the upper electrode at $z = H$ is kept grounded (Eq. 4.14b and Fig. 4.1). Here we use the approach outlined by Hashemi Amrei et al.[2] to non-dimensionlize the system of equations. The electrode spacing H and inverse frequency $1/f_0$ are taken as the characteristic length and time scales, while ϕ_0/H is used to normalize the electric field:

$$\tilde{z} = \frac{z}{H}, \quad \tilde{t} = f_0 t, \quad \tilde{E} = \frac{EH}{\phi_0}. \tag{4.15}$$

Moreover, for binary 1-1 electrolytes, there are four dimensionless parameters that uniquely describe

the system:

$$\Phi_0 = \frac{\phi_0 e}{k_B T}, \quad \delta = \frac{D_-}{D_+}, \quad \kappa H = \sqrt{\frac{n_0 e^2}{\varepsilon k_B T}} H, \quad \mathcal{L}_D = \frac{\sqrt{\hat{D}/f_0}}{H}. \tag{4.16}$$

Here $n_0 = 2n_\infty$, where n_∞ is the bulk electrolyte concentration, and we have defined $\hat{D} = \sqrt{D_+ D_-}$ as the characteristic diffusivity.[2] Alternatively, we could use the ambipolar diffusivity;[87] however, Hashemi Amrei et al.[2] showed that choosing $\hat{D} = \sqrt{D_+ D_-}$ yields accurate predictions of the AREF length scale and its spatial structure, which are key elements of the present study (cf. subsection 4.3.2).

4.3.1 Linear solution

A linearized approximate solution to the problem was derived by Hollingsworth and Saville for low applied voltages and equal ionic mobilities (i.e., $\Phi_0 \ll 1$ and $\delta = 1$).[25] The linearized solution is necessarily unimodal, albeit with phase lag and amplitude that depend on the system properties and location:

$$\tilde{E} = \mathrm{Im}\left[\frac{\alpha \cosh(\alpha\tilde{y}) \operatorname{csch}(\alpha) + i\alpha\nu^2 \coth(\alpha)}{1 + i\alpha\nu^2 \coth(\alpha)} e^{i2\pi\tilde{t}}\right], \tag{4.17}$$

where $\tilde{y} \equiv 2\tilde{z} - 1$ and the coefficients are

$$\alpha^2 \equiv \frac{1}{4}\left[(\kappa H)^2 + i\frac{2\pi}{\mathcal{L}_D^2}\right], \qquad \nu^2 \equiv \frac{2\pi}{(\kappa H)^2 \mathcal{L}_D^2}. \tag{4.18}$$

Note that only two dimensionless groups, κH and $\mathcal{L}_D$, contribute to the approximate linear electric field solution because low applied potential and equal mobilities are assumed. In these limits, then, Eq. 4.17 can be written in the form

$$\tilde{E}(\tilde{t}) = \tilde{E}_1 \cos(2\pi\tilde{t} + \gamma_1), \tag{4.19}$$

where the amplitude $\tilde{E}_1$ and phase lag γ_1 are functions of both position and the system properties (i.e., κH and $\mathcal{L}_D$). The subscript 1 denotes the frequency mode of the solution; for this unimodal field, there is only one mode corresponding to the applied frequency f_0.

4.3.2 Nonlinear solution

As reported by Hashemi Amrei et al.,[1,2] numerical calculations show that the full nonlinear electrokinetic model yields an electric field with much more complicated spatial and temporal structures than the linearized result. See Hashemi Amrei et al.[1,2] for details on the numerical methodology and solutions; here we focus on the results and how they pertain to ICEK. Fig. 4.2(a) shows representative examples of the numerically calculated instantaneous electric field versus time at $\tilde{z} = 0.04$ for low and high dimensionless applied voltages and for electrolytes of equal and non-equal ionic mobilities. At the low voltage $\Phi_0 = 1$ and for $\delta = 1$ (Fig. 4.2(a), dotted red curve, $\Phi_0 = 1$), the electric field solution is a simple unimodal sinusoid consistent with the linearized prediction; indeed,

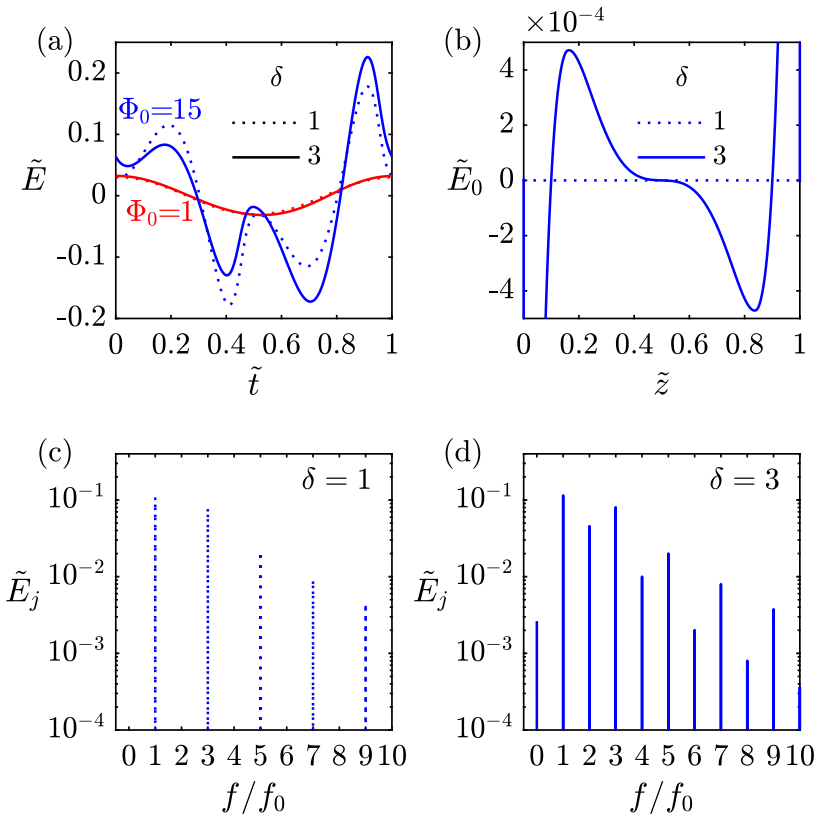

Figure 4.2: Representative examples of the one-dimensional AREF. (a) Effect of the applied voltage on time variations of the harmonic electric field ($\tilde{E}$) at $\tilde{z} = 0.04$ for $\delta = 1$ (dashed) and $\delta = 3$ (solid), at applied potentials of $\Phi_0 = 1$ (red) and $\Phi_0 = 15$ (blue). (b) Spatial distribution of the time average electric field ($\tilde{E}_0 = \langle \tilde{E} \rangle$, AREF) for $\delta = 1$ (dashed) and $\delta = 3$ (solid). Note that for $\delta \neq 1$, at locations very close to the electrodes ($\tilde{z} \to 0$ or 1), the AREF reaches a maximum magnitude before sharply decaying toward zero (not discernible here; cf. Hashemi Amrei et al.[1,2]). (c) & (d) FFT analysis of the harmonic electric field for $\delta = 1$ (c) and $\delta = 3$ (d). Parameters: $\Phi_0 = 15$ (b, c, d), $\mathcal{L}_D = 0.2$, $\kappa H = 2600$.

the linearized result in Eq. 4.17 is not distinguishable from the nonlinear result at this scale. At a higher applied voltages, the contribution from the nonlinear electromigrative terms yield multi-modal peaks (Fig. 4.2(a), dotted blue curve, $\Phi_0 = 15$). Qualitatively similar results are obtained for $\delta \neq 1$; the electric field is close to a sinusoid at low voltages and develops nonlinear behavior upon increasing voltage (Fig. 4.2(a), solid red ($\Phi_0 = 1$) and blue ($\Phi_0 = 15$) curves, respectively).

The time average of the electric field ($E_0 = \langle E \rangle$), however, shows a significant difference between the cases of $\delta = 1$ and $\delta = 3$ (Fig. 4.2(b)). For $\delta = 1$ the electric field time average is identically zero everywhere. In contrast, there is a significant nonzero time average electric field (i.e., a DC field) generated for $\delta \neq 1$. The first peak location of this AREF outside the Debye layer closely follows a diffusive length scale, $\tilde{z}_{\text{peak}} \approx 0.83\mathcal{L}_D$ (cf. Fig. 10 of Hashemi Amrei et al.[2]). Also note that the peak occurs far away from the electrode (≈ 5 μm in Fig. 4.2(b)); this behavior, along with the spatially non-uniform AREF, stem from a non-zero time average free charge density far outside the Debye layer. While the magnitude of AREF appears small when compared to the magnitude of the

harmonic electric field, the AREF-induced electrophoretic force was shown to be several order of magnitudes larger than gravitational and colloidal forces.[1] Although indiscernible from Fig. 4.2(b), as $z \to 0$ or 1, within a few Debye lengths from the electrodes, AREF reaches to a peak and then drops toward zero (cf. Hashemi Amrei et al.[1,2]).

An FFT analysis of the electric field modes shows that for $\delta = 1$ (Fig. 4.2(c)) the field has frequency components at odd integer multiples of the applied frequency. In other words, the multimodal electric field can be modeled by a sum of sinusoids with frequencies of $f_0, 3f_0, 5f_0, \ldots$ and amplitudes that depend on system properties and location. For $\delta \neq 1$ (Fig. 4.2(d)), in contrast, the electric field has frequency components at all integer multiples of the applied frequency, including zero (i.e., a steady field). In this case the electric field includes a sum of sinusoids with frequencies of $f_0, 2f_0, 3f_0, \ldots$ plus a steady contribution. Note that the effect of δ on these frequency modes is consistent with a simpler toy model of just two ionic oscillators.[1].

Based on these numerical results, the instantaneous nonlinear electric field at any location can be expressed as

$$\tilde{E}(\tilde{t}) = \tilde{E}_0 + \sum_{j=1}^{\infty} \tilde{E}_j \cos\left(2\pi j\tilde{t} + \gamma_j\right), \tag{4.20}$$

where $\tilde{E}_j$ and γ_j are the z-dependent amplitude and phase lag of the frequency component jf_0, respectively. Note that there are two key differences compared to the linearized result (Eq. 4.19). First, the full nonlinear expression has a steady component, $\tilde{E}_0$, whereas the linearized solution does not. Second, the nonlinear expression has an infinite series of all the multiple modes of the imposed frequency, whereas the linear solution is unimodal. In the limit where $\delta \to 1$, the steady component $\tilde{E}_0$ and the even modes $\tilde{E}_{2j} = 0$ for any integer j all vanish. The higher order odd modes, however, are retained even when $\delta \to 1$.

4.4 ICEK FLOW WITH AREF

The sinusoidal nature of the linearized solution (Eq. 4.19) indicates that the induced fluid flow pattern is quadrupolar and symmetrical. Substitution of Eq. 4.19 into Eq. 4.8 and subsequent time averaging gives the linear ICEK slip velocity as

$$\langle \tilde{u}_\theta^s \rangle = \frac{\langle u_\theta \rangle}{\varepsilon a \phi_0^2/(\mu H^2)} = \tilde{E}_1^2 \frac{\sin(2\theta)}{\omega_0^2 \tau_c^2 + 1}. \tag{4.21}$$

Inserting the nonlinear electric field solution from Eq. 4.20 into Eq. 4.8 and time averaging gives the nonlinear ICEK slip velocity:

$$\langle \tilde{u}_\theta^s \rangle = \sum_{j=1}^{\infty} \left[\tilde{E}_j^2 \frac{\sin(2\theta)}{j^2 \omega_0^2 \tau_c^2 + 1} \right] + 2\tilde{E}_0^2 \sin(2\theta) + 2\tilde{\zeta}_0 \tilde{E}_0 \sin(\theta), \tag{4.22}$$

where $\tilde{\zeta}_0 = \frac{\zeta_0 H}{a\phi_0}$. Note that Eq. 4.22 has three contributions: (i) an ICEK quadrupolar flow due to the first and all higher order modes of the nonlinear field, (ii) an ICEK quadrupolar flow due to

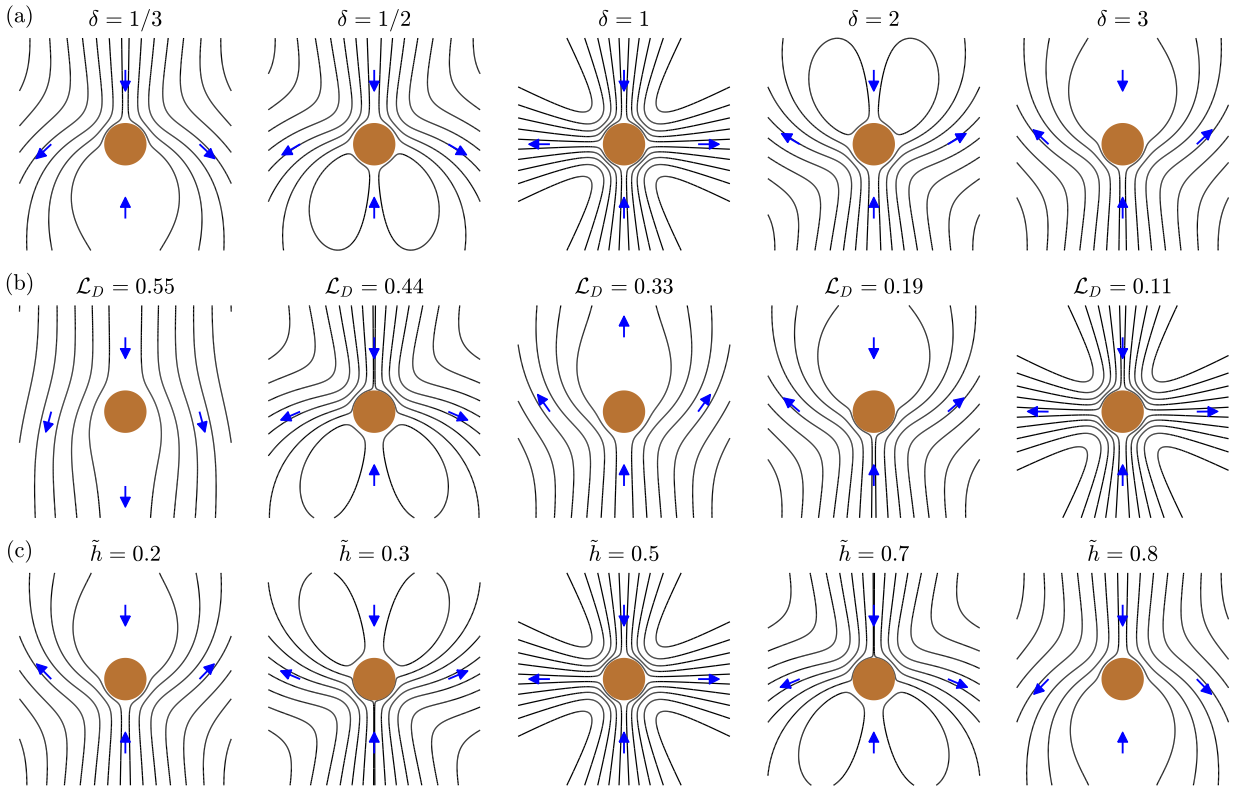

Figure 4.3: Effects of (a) mobility mismatch, (b) frequency-dependent diffusive length scale, and (c) cylinder position on the induced fluid flow pattern around the cylinder, as calculated using Eq. (21) and the nonlinear solution to the standard electrokinetic model [cf. Eq (19)]. Parameters: $\Phi_0 = 10$, $\delta = 3$ (b, c), $\mathcal{L}_D = 0.2$ (a, c), $\kappa H = 2600$, $\tilde{\zeta}_0 = -10$, $\tilde{h} = 0.22$ (a, b).

the steady AREF, and (iii) an electroosmotic dipolar flow due to the action of the steady AREF on the intrinsic charge on the cylinder. For $\delta = 1$ ($\tilde{E}_0 = 0$), as voltage goes to zero $\tilde{E}_{j\neq 1} \to 0$, and the nonlinear and linear slip velocities asymptotically converge. Unlike the linear slip velocity which predicts an invariably quadrupolar and symmetrical fluid flow, the nonlinear one is in general asymmetrical due to the dipolar electroosmotic term stemming from the steady field component. In other words, any mismatch in the mobilities of the dissolved ions breaks the symmetry and induces net fluid flow around a charged cylinder under AC polarization.

As discussed in detail by Hashemi Amrei et al.[2], $\tilde{E}_0$ and $\tilde{E}_j$ are complicated functions of the four dimensionless parameters Φ_0, $\mathcal{L}_D$, δ, and κH. Eq. 4.22 introduces two more dimensionless groups, $\tilde{\zeta}_0$ and $\omega_0 \tau_c$, that also affect the flow behavior. Under typical experimental conditions, however, $\omega_0 \tau_c \ll 1$ and its impact is negligible; we do not consider it further here. A parameter that is important, however, is the location of the cylinder between the two electrodes (i.e., h), which is included in the dimensionless group $\tilde{h} = h/H$. In other words, the flow structure and magnitude is governed by the six dimensionless parameters Φ_0, $\mathcal{L}_D$, δ, κH, $\tilde{\zeta}_0$, and $\tilde{h}$.

Using the slip velocity given by Eq. 4.22 for nonlinear ICEK, the radial velocity, angular velocity,

and corresponding stream function around the charged cylinder are, respectively

$$\tilde{u}_r = \left(\frac{1}{\tilde{r}^2} - 1\right)\tilde{\zeta}_0\tilde{E}_0\cos(\theta) + 2\left(\frac{1-\tilde{r}^2}{\tilde{r}^3}\right)\tilde{E}_0^2\cos(2\theta) + \sum_{j=1}^{\infty}\left(\frac{1-\tilde{r}^2}{\tilde{r}^3}\right)\frac{\tilde{E}_j^2}{(\omega_0^2\tau_c^2+1)}\cos(2\theta), \tag{4.23a}$$

$$\tilde{u}_\theta = \left(\frac{1}{\tilde{r}^2} + 1\right)\tilde{\zeta}_0\tilde{E}_0\sin(\theta) + \frac{2}{\tilde{r}^3}\tilde{E}_0^2\sin(2\theta) + \sum_{j=1}^{\infty}\frac{1}{\tilde{r}^3}\frac{\tilde{E}_j^2}{(\omega_0^2\tau_c^2+1)}\sin(2\theta), \tag{4.23b}$$

$$\tilde{\Psi} = \left(\frac{1}{\tilde{r}} - \tilde{r}\right)\tilde{\zeta}_0\tilde{E}_0\sin(\theta) + \left(\frac{1}{\tilde{r}^2} - 1\right)\tilde{E}_0^2\sin(2\theta) + \sum_{j=1}^{\infty}\left(\frac{1}{\tilde{r}^2} - 1\right)\frac{\tilde{E}_j^2}{2(\omega_0^2\tau_c^2+1)}\sin(2\theta). \tag{4.23c}$$

Here $\tilde{\Psi} = \Psi\mu H^2/(\varepsilon a^2\phi_0^2)$ is the dimensionless stream function and $\tilde{r} = r/a$. (Please refer to Sec. B.1 for details.) For linear ICEK, note that the velocity and stream function are simply expressed by the first series terms on the right hand side of Eq. 4.23 (i.e., $\tilde{E}_j = 0$ for $j \neq 1$).

The streamlines for the linearized solution are invariably quadrupolar, i.e., the shape of the flow never changes in the linearized field limit (although the flow velocity varies). In contrast, the flow structure for the full nonlinear solution is highly sensitive to the system parameters. Representative streamlines for the induced fluid flows from the nonlinear solution are provided in Fig. 4.3. Focusing first on the mobility mismatch (Fig. 4.3(a)), the fluid flow pattern for an electrolyte with $\delta = 1$ is perfectly quadrupolar. In contrast, electrolytes with an ionic mobility mismatch ($\delta \neq 1$) generate a net fluid flow as a result of the dipolar contribution of the slip velocity (i.e., standard electroosmosis due to the AREF). Note that the direction of the fluid flow depends sensitively on the magnitude of δ; in other words, swapping out an electrolyte with $\delta < 1$ (e.g., HCl) with an electrolyte that has $\delta > 1$ (e.g., NaOH) and holding all other parameters constant will result in a reversal in the direction of flow.

A similar flow reversal also occurs for different magnitudes of the frequency-dependent diffusive length scale, $\mathcal{L}_D$ (Fig. 4.3(b)). For sufficiently large values of $\mathcal{L}_D$, i.e., sufficiently low frequencies, the fluid flow is dominated by the dipolar steady AREF-driven electroosmosis. For $\mathcal{L}_D = 0.55$ and $\tilde{h} = 0.2$ the flow is directed downward (in the negative z-direction). This particular directionality stems from the direction of the steady field component at this specific frequency and location. As discussed by Hashemi Amrei et al.,[2] the direction of the steady field at a given location depends sensitively on the applied frequency; note in Fig. 4.2(b) that the direction of the field is negative for $0 < \tilde{z} < 0.1$, positive for $0.1 < \tilde{z} < 0.5$, and antisymmetric for $\tilde{z} > 0.5$. The precise positions where the field direction changes depend on frequency, with more zeros in the field strength (i.e., reversals in the field direction) as frequency increases ($\mathcal{L}_D$ decreases). The corresponding flow thus changes dramatically, with the direction of the steady dipolar flow switching as $\mathcal{L}_D$ decreases to 0.33 (Fig. 4.3(b)). Further decreases in $\mathcal{L}_D$ (increases in frequency) further diminish the dipolar contribution, and the fluid flow pattern becomes increasingly quadrupolar because $\tilde{E}_0$ at this particular location tends to decrease as $\mathcal{L}_D$ decreases. The effect of cylinder location, with all other parameters fixed, is shown in Fig. 4.3(c). At the midplane (i.e., $\tilde{h} = 0.5$) where AREF necessarily

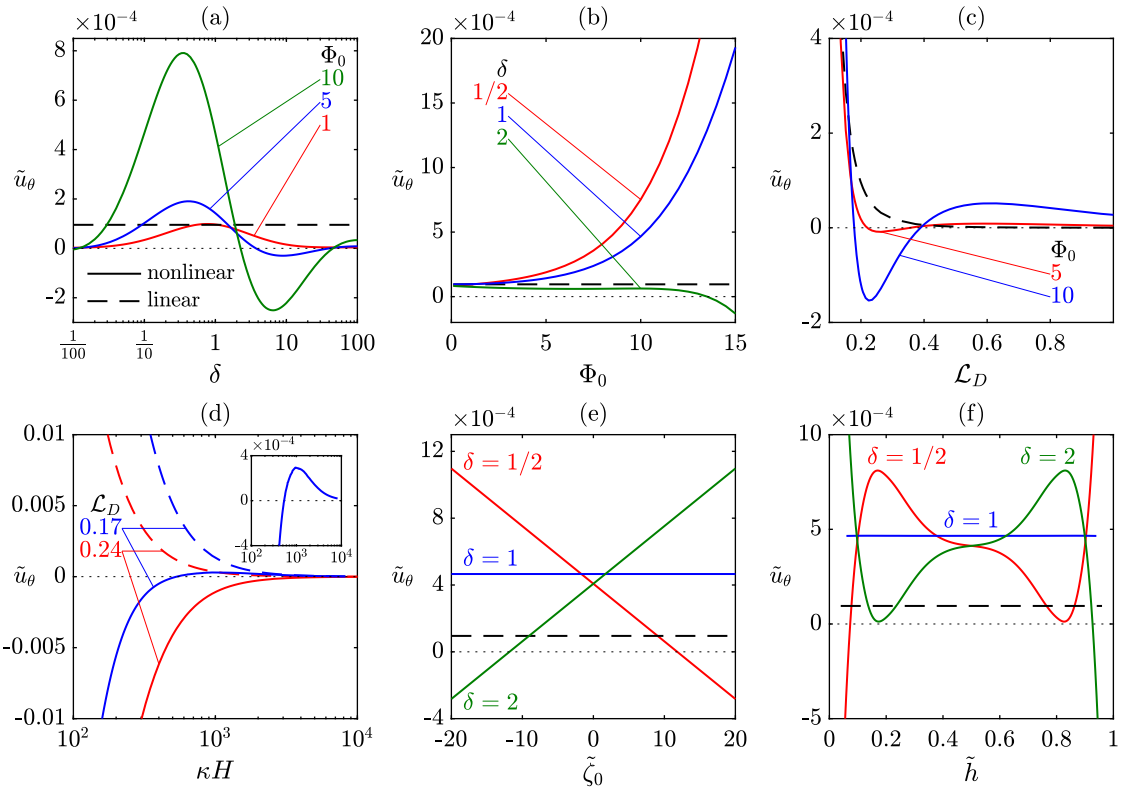

Figure 4.4: Influence of the six dimensionless parameters that govern $\tilde{u}_\theta^s$, evaluated at $r = 2a$ and $\theta = \pi/6$. In all figures, dashed black lines represent the velocity calculated using the linearized electric field, while solid colored lines represent the velocity calculated using the full nonlinear solution for various parametric values. Parameters: $\Phi_0 = 10$ (d, e, f), $\delta = 3$ (c, d), $\mathcal{L}_D = 0.2$ (a, b, e, f), $\kappa H = 2600$ (a, b, c, e, f), $\tilde{\zeta}_0 = -10$ (a, b, c, d, f), $\tilde{h} = 0.22$ (a, b, c, d, e). The inset of (d) shows a magnification of the nonlinear solution for $\mathcal{L}_D = 0.17$.

vanishes due to symmetry, the fluid flow is entirely quadrupolar. Away from the midplane (any location $\tilde{h} \neq 0.5$), there can be a net dipolar flow induced with direction dependent on the sign of AREF.

We emphasize that the exact conditions upon which the flow reversal occurs is a sensitive function of all six dimensionless parameters governing the system behavior and the location of the cylinder, due to the complicated spatial structure of AREF.[2] Linearized theories with slip velocity given by Eq. 4.21 will not capture these flow reversals, which are a direct result of ionic mobility mismatch and the consquent AREF. In other words, solutions to the full nonlinear problem with $\delta \neq 1$ will yield flow reversals, whereas more sophisticated solutions to the electrokinetic model at high voltages,[29,31,30] but with the assumption of equal ionic mobilities, will not.

To further quantify the induced flow behavior, the effects of the dimensionless parameters on the scalar component of the fluid velocity in θ direction ($\tilde{u}_\theta$) at a fixed location of $r = 2a$ and $\theta = \pi/6$ are shown in Fig. 4.4. We stress that these results are not general; the curves and critical values of flow reversal are crucially dependent on the system properties and complicated spatial structure of the AREF. Fig. 4.4(a) shows the effect of mobility mismatch (δ) on $\tilde{u}_\theta$ at three

different applied potentials. Changes in δ have no impact on the linear solution, but δ dramatically affects the predictions of the nonlinear solution. As expected, at a low voltage of $\Phi_0 = 1$, the linear and nonlinear solutions converge at $\delta = 1$. At higher voltages however, even when the steady AREF component is zero for $\delta = 1$, there is a considerable difference between the linear and nonlinear predicted velocities, stemming from the contribution of the higher order frequency modes. Furthermore, changing the mobility mismatch alters the fluid flow both qualitatively and quantitatively. For instance, at $\Phi_0 = 10$, the fluid velocity varies from $\tilde{u}_\theta \approx 4.5 \times 10^{-4}$ at $\delta = 1.04$ (e.g., KCl) to $\approx -2 \times 10^{-4}$ at $\delta = 3.95$ (e.g., NaOH).

An important point to consider is that the effect of δ is non-monotonic.[2] The AREF is always identically zero at $\delta = 1$, and vanishes as $\delta \to \infty$. Where the peak AREF magnitude occurs as a function of δ, however, depends on the applied voltage. At low voltages, the peak occurs near $\delta \approx 5$ (or $\delta \approx 1/5$). Thus in the representative examples shown in Fig. 4.4(a), the absolute magnitude of the velocity tends to peak near $\delta \approx 5$ and $\delta \approx 1/5$; for the range of Φ_0 shown here, these are the specific values of δ where the field strength is greatest. As the applied voltage increases, however, the AREF peaks in magnitude at values of δ closer to 1. In other words, at higher voltages, AREF in electrolytes with δ close to 1 (e.g., KCl with $\delta \approx 1.04$) might be stronger than that in electrolytes with a significant ionic mobility mismatch (e.g., NaOH with $\delta \approx 3.95$). Indeed, many of the peculiar experimental observations such as fluid flow reversal upon changing the frequency and voltage were reported for KCl electrolyte at relatively large voltages.[23,88,82,32]

The effect of the applied potential Φ_0 is shown in Fig. 4.4(b) for different values of δ. Again, the linearized dimensionless solution is insensitive to changes in Φ_0; dimensionally, the flow is predicted to increase as ϕ_0^2 (cf. Eq. 4.21). At low applied voltages and regardless of δ, the nonlinear solution approaches the linear solution (dashed black curve). As Φ_0 increases, however, the velocity increases rapidly, i.e., the velocity increases faster than quadratically. For $\delta = 1/2$, the increase is even steeper. Interestingly, for $\delta = 2$, increasing the applied voltage sufficiently will alter the fluid flow direction. In contrast, for cases of $\delta = 1$ and $\delta = 1/2$ it is only the magnitude of $\tilde{u}_\theta$ that is affected by Φ_0 and no change in direction is observed.

Fig. 4.4(c) illustrates the effect of $\mathcal{L}_D$ on the fluid velocity. The linear solution predicts an exponential decay in $\tilde{u}_\theta$ with no direction change. In contrast, the nonlinear solution predicts multiple direction changes upon varying $\mathcal{L}_D$. Recalling that the dimensionless parameter $\mathcal{L}_D$ has an inverse frequency dependence (Eq. 4.16), increasing $\mathcal{L}_D$ can be seen as deceasing the applied frequency f_0. Therefore, the results indicate how solutions to the full nonlinear electrokinetic model are capable of capturing the fluid flow reversal by changing the applied frequency.

The effect of κH on the induced fluid velocity is depicted in Fig. 4.4(d) for two different values of $\mathcal{L}_D$. The results are presented only for high κH values, where the assumption of $\omega_0 \tau_c \ll 1$ holds. Note that for the most part the linear and nonlinear solutions predict the fluid flow in opposite directions, which is a consequence of $\delta \neq 1$ (cf. Fig. 4.4(a)). The magnitudes of both the linear and nonlinear solutions drop by increasing κH, which corresponds to increasing the ionic concentration. At higher concentrations, the Debye layer shrinks and it becomes less effective

in micron scale electrokinetic phenomena. Likewise, some experimental studies have reported a strong concentration dependence of the fluid velocity magnitude in ACEO micropumps that tends to strongly suppress the flows.[23,82] Hence, any future interpretation of the concentration effect in ACEO pumps and similar systems should take into account the potentially confounding impact of AREFs. Also, a peculiar direction change in the nonlinear solution happens for the case of $\mathcal{L}_D = 0.17$ at $\kappa H \approx 500$. This result is qualitatively similar to a flow reversal with electrolyte concentration that was reported in a different geometry of ACEO experiments.[82]

Fig. 4.4(e), demonstrates the effect of dimensionless zeta potential $\tilde{\zeta}_0$ on the fluid velocity. The linear solution prediction has no electroosmotic contribution, making it insensitive to $\tilde{\zeta}_0$. Regarding the nonlinear solution, for $\delta = 1$, AREF is zero and again the cylinder charge has no impact on the fluid velocity. When $\delta \neq 1$ however, the fluid velocity linearly depends on the zeta potential, but with direction that depends on the sign of the AREF.

Finally, the location of the cylinder $\tilde{h}$ has a significant impact on the fluid velocity distribution. As shown in Fig. 4.4(f), the linear solution has no dependency on $\tilde{h}$, at least when, like in all practical examples, the cylinder is placed far outside the Debye layer ($\kappa H\tilde{h} \gg 1$ and $\kappa H(1-\tilde{h}) \gg 1$ for $\tilde{h} < 1/2$ and $\tilde{h} > 1/2$, respectively). For the nonlinear solution and for $\delta = 1$, again the cylinder location does not affect the model predictions. This location independence is due to the fact that AREF, which is responsible for the spatial non-uniformity of the electric field, is zero when $\delta = 1$. Therefore, we conclude that for electrolytes with $\delta = 1$, regardless of the cylinder location, the fluid flow pattern would be quadrupolar. When $\delta \neq 1$, interesting behavior is observed (Fig. 4.4(f), $\delta = 1/2$ and 2). Changing the location dramatically alters both the magnitude and direction of the fluid velocity. Moreover, the cases of $\delta = 1/2$ and 2 predict the same fluid velocity at the midplane. Knowing that AREF is always zero at the midplane, the fluid flow pattern would again be quadrupolar there, regardless of the precise value of δ.

4.5 CONCLUSIONS

A key implication of the results presented here is that they point toward a resolution of long-standing shortfalls of the ICEK theory, in particular the reversals in fluid flow direction upon changes in the applied frequency and electrolyte type in AC electroosmosis pumps. To our knowledge, the model presented here is the first to predict a flow reversal in an ICEK system that retains the continuum approximation, i.e., without invoking finite ion size or crowding effects. The model predicts that the flow structure will depend sensitively on several dimensionless parameters, including ionic mobility mismatch ($\delta = D_-/D_+$), diffusive length scale ($\mathcal{L}_D$, defined based on the applied frequency), and even the location of cylinder between the electrodes, all of which complicate experimental interpretation. To date, all reported experiments on ICEK around charged cylinders or spheres have placed the object exactly at the midplane between the two electrodes, or used an electrolyte solution with $\delta \approx 1$ (e.g., KCl). In both of these cases, the results provided here predict a quadrupolar fluid flow pattern, in qualitative agreement to the experiments. We are unaware of

published experimental results where the object is placed at a location other than the midplane in an electrolyte with $\delta \neq 1$.

A key limitation of our model is that it pertains only in the limits $a/h \ll 1$ and $a/H \ll 1$, so that the presence of the cylinder has negligible impact on the electric field distribution obtained from the one-dimensional solution. An improved model would take into account the effect of the cylinder presence on the electric field itself, and how that alters the consequent flow. Such a full two-dimensional numerical simulation for the electrokinetic equations will remove the necessity of the above assumptions and will provide a better understanding of the phenomena. Likewise, ACEO pumps intrinsically involve two-dimensional electrode arrays, so the influence of AREFs in these systems will also require more sophisticated numerical techniques. Furthermore, we focused here on the consequence of asymmetries in the ionic mobility and cylinder position, but the symmetry of the system can be broken in other ways, including in the shape and/or surface chemistry of the object or the applied electric field gradient, all of which have been shown to generate net fluid flows and electrophoretic motion of conducting particles.[18,89,54,90] Finally, we focused here on dilute solutions, but transport in more concentrated solutions will require consideration of Stefan–Maxwell coupled ionic fluxes.[87,91] The influence of AREFs on ICEK flows in two dimensional systems with these more complicated broken symmetries is deferred to future studies.

Chapter 5

A Perturbation Solution to the Full Poisson–Nernst–Planck Equations Yields an Asymmetric Rectified Electric Field

Overview*

We derive a perturbation solution to the one-dimensional Poisson–Nernst–Planck (PNP) equations between parallel electrodes under oscillatory polarization for arbitrary ionic mobilities and valences. Treating the applied potential as the perturbation parameter, we show that the second-order solution yields a nonzero time-average electric field at large distances from the electrodes, corroborating the recent discovery of Asymmetric Rectified Electric Fields (AREFs) via numerical solution to the full nonlinear PNP equations [Hashemi Amrei *et al. Phys. Rev. Lett.*, 2018, **121**, 185504]. Importantly, the first-order solution is analytic, while the second-order AREF is semi-analytic and obtained by numerically solving a single linear ordinary differential equation, obviating the need for full numerical solutions to the PNP equations. We demonstrate that at sufficiently high frequencies and electrode spacings the semi-analytical AREF accurately captures both the complicated shape and the magnitude of the AREF, even at large applied potentials.

*This chapter was previously published by Hashemi Amrei et al. and is reproduced here with minor modifications. See: **S. M. H. Hashemi Amrei**, G. H. Miller, Kyle J. M. Bishop, and W. D. Ristenpart *A perturbation solution to the full Poisson–Nernst–Planck equations yields an asymmetric rectified electric field*, Soft Matter 16 (2020) 7052–7062.[5]

5.1 INTRODUCTION

The dynamic response of a fluid to an applied oscillatory electric potential is of fundamental importance in many electrokinetic systems, including induced-charge electrokinetics (ICEK),[15–19] ac electroosmosis,[20–23] electrohydrodynamic manipulation of colloids,[8–12,56] electroconvection,[92] and ionic winds in atmospheric plasmas.[93,94] In continuum theory, analysis of such systems is based on the Poisson–Nernst–Planck (PNP) equations, also referred to as the standard electrokinetic model.[24] The Poisson equation relates the free charge density to the Laplacian of the electric potential via Gauss's law, and the transport of dissolved ions is governed by the electromigrative and diffusive fluxes.

The PNP equations are nonlinear and coupled; as a result, researchers have often invoked simplifying assumptions to solve them. The most common of these assumptions is that the applied potential (ϕ_0) is less than the thermal potential, i.e., $\phi_0 \ll k_B T/e$ where k_B, T, and e are the Boltzmann constant, absolute temperature, and elementary charge, respectively. This assumption allows linearization of the problem via a perturbation expansion, written in terms of $\Phi_0 = \phi_0 e/(k_B T) \ll 1$. In most cases, the solution is assumed to include an equilibrium contribution (unperturbed) plus a perturbation linear in the applied potential (i.e., first-order expansion, $O(\Phi_0)$). White and coworkers[26,95,28] and Hinch et al.[27] were among the first to follow this procedure in their analysis of dilute colloidal suspensions, obtaining information about the dipole coefficient and electrophoretic mobility of spherical colloids subject to an oscillating electric field.

Researchers have also focused on finding the dynamic response of quiescent electrolytes (no colloids) between parallel electrodes. Hollingsworth and Saville[25] used a first-order perturbation expansion to derive an analytical approximate solution to the electric potential. Note that for a sinusoidal applied potential, a first-order perturbation expansion invariably yields a single-mode sinusoidal solution, albeit with a phase lag and amplitude that depend on location and system properties. It was later shown, however, that the nonlinear terms in the PNP equations yield multimodal solutions for $\Phi_0 > 1$.[29,31,30] Olesen et al.[29] numerically solved the PNP equations to show the significance of nonlinear terms at high potentials. This multimodal behavior, which was later corroborated by analytical solutions at asymptotically high[31] and moderate potentials,[30] casts doubt on the common interpretation of electrokinetic systems based on linearized theories.

Even more counterintuitively, recent work has revealed that electrolytes with non-equal mobilities generate multimodal electric fields with a long-range, nonzero time-average.[1,2] In other words, an oscillatory electric potential can induce a steady electric field within the liquid. Referred to as an Asymmetric Rectified Electric Field (AREF), the steady field in essence results from the mismatch in the ionic mobilities; the uneven magnitudes of the oscillatory motion of the ions give rise to a net free charge density, in turn creating a steady field component. The spatial distribution and magnitude of the AREF depends sensitively on the applied frequency and magnitude of the ionic mobility mismatch. Notably, the induced AREF persists several microns away from the electrodes, with a characteristic diffusive length scale $\ell_D \sim$ 1–10 μm. This long-range behavior of AREF is at odds with the common assumption that most of the important electrokinetic phenomena are

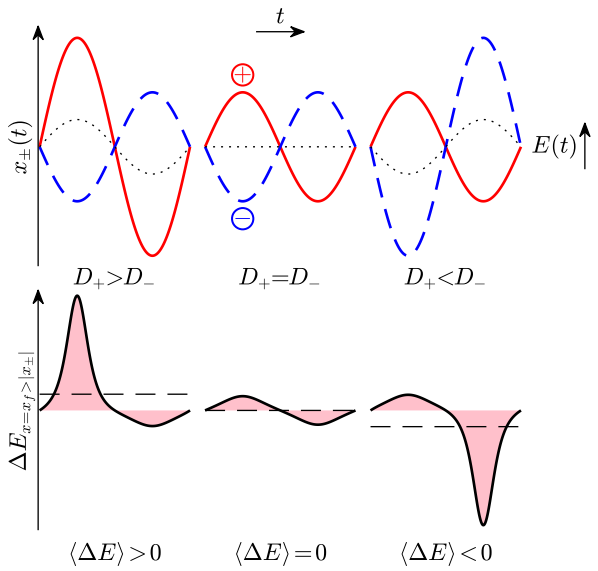

Figure 5.1: Two-ion model illustrating AREF. Top row: oscillation of a pair of ions ($x_\pm$ vs time) with diffusivities $D_\pm$ in response to an electric field $E(t) = E_0 \cos(\omega t)$ for $D_+ > D_-$, $D_+ = D_-$, and $D_+ < D_-$. The dotted curves show the oscillation of the center of charge. Bottom row: induced electric field (ΔE) at an arbitrary point $x_f > |\ x_\pm\ |$ due to the ion oscillations vs. time. The horizontal dashed lines show the time-average electric field $\langle \Delta E \rangle$.

governed solely by the Debye length scale ($\kappa^{-1} \sim$ 1–100 nm). Importantly, the calculated AREF is consistent with observations of colloidal levitation against gravity,[3] and is potentially responsible for the otherwise unexplained observations of flow reversal in ICEK systems.[4]

Hashemi Amrei et al. demonstrated that even a toy model of two ions undergoing asymmetric harmonic oscillation could yield an AREF.[1] Consider two ions, one positive and one negative, oscillating (as $x_\pm(t)$) in response to an external sinusoidal electric field as illustrated in Fig. 5.1. When the two ions have equal diffusivities ($D_+ = D_-$), they oscillate with the same amplitude in response to the external electric field. However, when there is a mismatch between the ion diffusivities, the fast moving ion undergoes an oscillation with a higher amplitude compared to the slow moving one. Then one can use Coulomb's law to evaluate an induced electric field (ΔE) due to the ion oscillations at an arbitrary point $x_f > |\ x_\pm\ |$. It turns out that when $D_+ = D_-$, the induced electric field is symmetrical in time with a zero time-average. However, for $D_+ \neq D_-$, a non-zero time-average electric field is induced. One can illustrate that this non-zero steady field component varies to leading order as the square of the applied field, i.e., $\Delta E \propto E_0^2$ (cf. Hashemi Amrei et al.[1]).

The two-ion model serves as a toy model only to provide some intuition about the importance of ionic mobility mismatch. As such, it lacks some fundamental aspects of an electrokinetic system such as the ion-ion interactions and the influence of thermal energy. To capture these effects, one must invoke the PNP equations. Consequently, all quantitative predictions to date have depended on complicated and time-consuming numerical solutions to the PNP equations. Progress assessing the impact of AREFs on other systems has been hindered by the lack of analytical insight. Note that

AREF is necessarily a nonlinear effect; therefore, first-order perturbation schemes cannot capture AREF, even when considering the asymmetry of electrolytes.[26,95,28,27] Additionally, Hashemi Amrei et al. demonstrated that AREF is identically zero for symmetric electrolytes;[1,2] as a result, prior studies considering the nonlinear effects at high potentials but neglecting the asymmetry of ions could not predict the AREFs either.[29,31,30] In short, only solutions to the full nonlinear PNP equations for asymmetric electrolytes predict AREF.

In this work, we provide a new, simpler, solution to the PNP equations for a 1-dimensional system with arbitrary ionic mobilities and valences. We use a perturbation approach for small applied oscillatory potentials to find an exact analytical solution accurate to first-order. The first-order solution provides insight on how mobility mismatches alter the charge and potential distributions versus time and position. Furthermore, we derive a governing ordinary differential equation (ODE) for the time-average second-order solution, i.e., the AREF. We demonstrate that in the limit of small applied potentials this analytical AREF asymptotically converges in both spatial dependence and magnitude to numerical solutions of the full PNP equations. This approach yields the first independent theoretical corroboration of the existence of AREFs, and furthermore provides researchers with a rapid means of calculating the AREF without requiring a numerical solution to the full PNP system of equations.

The paper is organized as follows. We start by reviewing the PNP equations in Sec. 5.2. A detailed derivation of the approximate perturbation solution is provided in Sec. 5.3. The results for the first and second order solutions are presented and discussed in Sec. 5.4. We finish with some concluding remarks on the key results and implications for the electrokinetics community in Sec. 5.5.

5.2 THEORY

5.2.1 Poisson–Nernst–Planck equations

We consider a binary electrolyte confined by two parallel electrodes separated by distance 2ℓ as depicted in Fig. 5.2. The Laplacian of the electric potential $\phi(x,t)$ is related to the free charge density $\rho(x,t)$ by the Poisson equation

$$-\varepsilon\frac{\partial^2\phi}{\partial x^2} = \rho = e(z_+n_+ + z_-n_-). \tag{5.1}$$

Here subscripts $\pm$ stand for positive and negative ions and the symbols denote liquid permittivity, ε; elementary charge, e; charge numbers, $z_\pm$; and ion concentrations, $n_\pm$. The transport of ions is governed by the Nernst–Planck equation

$$\frac{\partial n_\pm}{\partial t} + \frac{\partial j_\pm}{\partial x} = 0, \tag{5.2}$$

where the ion flux $j_\pm(x,t)$ accounts for transport due both to diffusion and electromigration in the electric field:

$$j_\pm(x,t) = -D_\pm \frac{\partial n_\pm}{\partial x} - \frac{z_\pm e D_\pm}{k_B T} n_\pm \frac{\partial \phi}{\partial x}, \tag{5.3}$$

where $D_\pm$ and $k_B T$ are the ion diffusivities and thermal energy, respectively.

Initially, no electric potential is applied and the electrolyte is spatially homogeneous,

$$n_\pm(x,0) = n_\pm^\infty = \mp z_\mp n^\infty, \tag{5.4}$$

where n_∞ is the bulk number concentration of the electrolyte. An oscillatory potential of amplitude ϕ_0 and angular frequency ω is applied across the electrodes such that

$$\phi(\pm\ell, t) = \mp\phi_0 \sin(\omega t). \tag{5.5}$$

Note that field-induced ion motion depends only on the potential gradient (not the potential itself). We can therefore measure the potential from any time-dependent reference we choose without altering the system dynamics. For example, we can add $\phi_0 \sin(\omega t)$ to the applied potential at $\pm\ell$ in Eq. 5.5 to describe the common experimental scenario of a grounded electrode at one boundary (namely, $x = \ell$). However, this antisymmetric boundary condition, along with placing the origin at the midplane and electrodes at $x = \pm\ell$ (cf. Fig. 5.2), significantly simplifies the analytical analysis.

To close the problem, we assume no ion flux at the electrodes (i.e., no electrochemistry),

$$j_\pm(\pm\ell, t) = 0. \tag{5.6}$$

We acknowledge the fact that the assumption of negligible electrochemistry is justified only at low applied potentials. Additionally, we neglect the possible creation of a compact Stern layer at the electrodes which is known to cause a considerable potential drop between the electrode and electrolyte.[29] Also note that we focus on dilute electrolytes where the system dynamics is governed solely by the transport of the dissolved ions. For concentrated solutions, Stefan-Maxwell equations are required to account for the transport of all components including the solvent.[91,87]

5.2.2 Dimensionless form

The diffusivities D_+ and D_- can be expressed by two parameters characterizing the diffusivity magnitude D and the diffusivity difference β as

$$D = \frac{2D_+D_-}{D_+ + D_-} \quad \text{and} \quad \beta = \frac{D_+ - D_-}{D_+ + D_-}, \tag{5.7}$$

where $-1 \leqslant \beta \leqslant 1$. Similarly, the charge numbers z_+ and z_- can be expressed by a magnitude parameter z and a difference parameter γ:

$$z = \tfrac{1}{2}(z_+ - z_-) \quad \text{and} \quad \gamma = \frac{z_+ + z_-}{z_+ - z_-}, \tag{5.8}$$

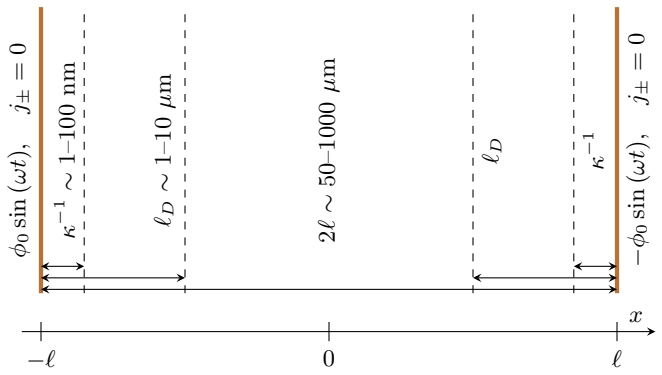

Figure 5.2: Schematic diagram of the problem and not-to-scale comparison of different characteristic length scales, i.e., Debye length (κ^{-1}), diffusive length scale (ℓ_D), and electrode spacing (ℓ). A single-mode oscillatory electric potential of $\mp\phi_0 \sin(\omega t)$ is applied on the parallel electrodes at $x = \pm\ell$.

where $-1 \leqslant \gamma \leqslant 1$. Note that the charge numbers $z_\pm$ are signed quantities and $\gamma = 0$ for equal-valence ($z_+ = -z_- = z$) electrolytes. The two difference parameters β and γ will play a central role in characterizing asymmetries in the binary electrolyte.

We nondimensionalize the governing equations using the following characteristic scales. Lengths are scaled by the Debye length

$$\kappa^{-1} = \sqrt{\frac{\varepsilon k_B T}{2e^2 z^2 n_0}}, \tag{5.9}$$

where the concentration n_0 is defined as

$$n_0 = \frac{1}{2z^2}(z_+^2 n_+^\infty + z_-^2 n_-^\infty) = \frac{1}{2z^2}(z_+ z_-^2 - z_+^2 z_-) n^\infty. \tag{5.10}$$

All concentrations are scaled by n_0. The electric potential is scaled by $k_B T/(ze)$, and time is scaled by $1/(\kappa^2 D)$. Using these scalings, the dimensionless variables are obtained as

$$\tilde{x} = \kappa x, \quad \tilde{t} = t\kappa^2 D, \quad \tilde{n}_\pm = \frac{n_\pm}{n_0}, \quad \tilde{\phi} = \frac{\phi z e}{k_B T}. \tag{5.11}$$

There are also five dimensionless parameters β, γ, $\kappa\ell$, $\Phi_0 = \phi_0 ze/(k_B T)$, and $\Omega = \omega/(\kappa^2 D)$ that uniquely describe the system.

Using the above dimensionless groups, the dimensionless governing equations become

$$\frac{\partial \tilde{n}_\pm}{\partial \tilde{t}} = \frac{1}{1 \mp \beta}\left[\frac{\partial^2 \tilde{n}_\pm}{\partial \tilde{x}^2} \pm (1 \pm \gamma)\frac{\partial}{\partial \tilde{x}}\left(\tilde{n}_\pm \frac{\partial \tilde{\phi}}{\partial \tilde{x}}\right)\right], \tag{5.12}$$

$$-\frac{\partial^2 \tilde{\phi}}{\partial \tilde{x}^2} = \tilde{\rho} = \tfrac{1}{2}(1+\gamma)\tilde{n}_+ - \tfrac{1}{2}(1-\gamma)\tilde{n}_- \,. \tag{5.13}$$

The dimensionless initial and boundary conditions are

$$\tilde{n}_\pm(\tilde{x}, 0) = \frac{1}{1 \pm \gamma}, \tag{5.14}$$

$$\tilde{\phi}(\pm\kappa\ell,\tilde{t}) = \mp\Phi_0 \sin(\Omega\tilde{t}), \tag{5.15}$$

$$\tilde{j}_{\pm}(\pm\kappa\ell,\tilde{t}) = 0. \tag{5.16}$$

Here the dimensionless ion flux is

$$\tilde{j}_{\pm} = \frac{j_{\pm}}{\kappa D n_0} = -\frac{1}{1\mp\beta}\left[\frac{\partial\tilde{n}_{\pm}}{\partial\tilde{x}} \pm (1\pm\gamma)\left(\tilde{n}_{\pm}\frac{\partial\tilde{\phi}}{\partial\tilde{x}}\right)\right]. \tag{5.17}$$

5.3 APPROXIMATE SOLUTION

As discussed before, the system of equations given by Eq. 5.12–Eq. 5.16 is coupled and nonlinear with significant disparity of length and time scales. In particular, accounting for ionic mobility and valence mismatches complicates the numerical solution to the problem.[1,2] Alternatively, using a perturbation expansion, we can derive an approximate analytical solution that captures the system behavior, especially for asymmetric cases (i.e., $\beta \neq 0$ and/or $\gamma \neq 0$).

5.3.1 Perturbation expansion in Φ_0

In the limit of small potentials ($\Phi_0 \ll 1$), the solution can be approximated by the power series

$$\tilde{n}_{\pm}(\tilde{x},\tilde{t}) = \tilde{n}_{\pm}^{(0)}(\tilde{x},\tilde{t}) + \Phi_0\tilde{n}_{\pm}^{(1)}(\tilde{x},\tilde{t}) + \Phi_0^2\tilde{n}_{\pm}^{(2)}(\tilde{x},\tilde{t}) + \ldots \tag{5.18}$$

$$\tilde{\phi}(\tilde{x},\tilde{t}) = \tilde{\phi}^{(0)}(\tilde{x},\tilde{t}) + \Phi_0\tilde{\phi}^{(1)}(\tilde{x},\tilde{t}) + \Phi_0^2\tilde{\phi}^{(2)}(\tilde{x},\tilde{t}) + \ldots \tag{5.19}$$

We substitute these expansions into the governing equations and initial/boundary conditions, and collect like powers of Φ_0. Below, we solve for the zeroth-order solution, the first-order solution, and the time-average second-order electric field.

Zeroth-order

One can show that the zeroth-order solution is simply

$$\tilde{n}_{\pm}^{(0)}(\tilde{x},\tilde{t}) = \frac{1}{1\pm\gamma}, \tag{5.20}$$

$$\tilde{\phi}^{(0)}(\tilde{x},\tilde{t}) = 0. \tag{5.21}$$

Here, we have neglected the intrinsic zeta potential of the electrodes for simplicity. Therefore, the zeroth-order solution is specified by the initial conditions of the problem. However, inclusion of a zeta potential is straightforward; the zeroth-order solution can be replaced by an analytical solution to the equilibrium problem with constant potential boundary condition. Nonetheless, we should emphasize that this assumption affects only the solution at the Debye scale (close to the electrodes), while we are particularly interested in the behavior of the system at the micron scale (several Debye lengths to microns away from the electrodes).

First-order

Using the zeroth-order solution, the first-order system of equations can be expressed as

$$\frac{\partial \tilde{n}_{\pm}^{(1)}}{\partial \tilde{t}} + \frac{\partial \tilde{j}_{\pm}^{(1)}}{\partial \tilde{x}} = 0, \tag{5.22}$$

$$-\frac{\partial^2 \tilde{\phi}^{(1)}}{\partial \tilde{x}^2} = \tfrac{1}{2}(1+\gamma)\tilde{n}_{+}^{(1)} - \tfrac{1}{2}(1-\gamma)\tilde{n}_{-}^{(1)}, \tag{5.23}$$

subject to the following boundary conditions:

$$\tilde{\phi}^{(1)}(\pm\kappa\ell, \tilde{t}) = \mp \sin(\Omega \tilde{t}), \tag{5.24a}$$

$$\tilde{j}_{\pm}^{(1)}(\pm\kappa\ell, \tilde{t}) = 0. \tag{5.24b}$$

Here, the first-order ion flux $\tilde{j}_{\pm}^{(1)}(\tilde{x}, \tilde{t})$ is

$$\tilde{j}_{\pm}^{(1)}(\tilde{x}, \tilde{t}) = -\frac{1}{1 \mp \beta}\left[\frac{\partial \tilde{n}_{\pm}^{(1)}}{\partial \tilde{x}} \pm \frac{\partial \tilde{\phi}^{(1)}}{\partial \tilde{x}}\right]. \tag{5.25}$$

We consider solutions of the form

$$\tilde{n}_{\pm}^{(1)}(\tilde{x}, \tilde{t}) = \mathrm{Im}\left[\hat{n}_{\pm}^{(1)}(\tilde{x}) e^{i\Omega \tilde{t}}\right], \quad \tilde{\phi}^{(1)}(\tilde{x}, \tilde{t}) = \mathrm{Im}\left[\hat{\phi}^{(1)}(\tilde{x}) e^{i\Omega \tilde{t}}\right]. \tag{5.26}$$

The complex amplitudes $\hat{n}_{\pm}^{(1)}(\tilde{x})$ and $\hat{\phi}^{(1)}(\tilde{x})$ are governed by

$$i\Omega \hat{n}_{\pm}^{(1)} = \frac{1}{1 \mp \beta}\left[\frac{\partial^2 \hat{n}_{\pm}^{(1)}}{\partial \tilde{x}^2} \pm \frac{\partial^2 \hat{\phi}^{(1)}}{\partial \tilde{x}^2}\right], \tag{5.27}$$

$$-\frac{\partial^2 \hat{\phi}^{(1)}}{\partial \tilde{x}^2} = \tfrac{1}{2}(1+\gamma)\hat{n}_{+}^{(1)} - \tfrac{1}{2}(1-\gamma)\hat{n}_{-}^{(1)}. \tag{5.28}$$

The corresponding boundary conditions are

$$\hat{\phi}^{(1)}(\pm\kappa\ell) = \mp 1, \tag{5.29a}$$

$$-\frac{1}{1 \mp \beta}\left[\frac{\partial \hat{n}_{\pm}^{(1)}}{\partial \tilde{x}} \pm \frac{\partial \hat{\phi}^{(1)}}{\partial \tilde{x}}\right]_{\pm\kappa\ell} = 0. \tag{5.29b}$$

Note that this problem has odd symmetry about $\tilde{x} = 0$ ($\hat{n}_{\pm}^{(1)}(0) = \hat{\phi}^{(1)}(0) = 0$). Substituting Eq. 5.28 for the potential into Eq. 5.27 for the ion concentrations, we obtain an eigenvalue problem from which one can derive the following solution for $\hat{n}_{\pm}^{(1)}(\tilde{x})$

$$\hat{n}_{+}^{(1)}(\tilde{x}) = A(-\gamma + s)\sinh(\lambda_{-}\tilde{x}) + B(1-\gamma)\sinh(\lambda_{+}\tilde{x}), \tag{5.30}$$

$$\hat{n}_{-}^{(1)}(\tilde{x}) = A(1+\gamma)\sinh(\lambda_{-}\tilde{x}) - B(-\gamma + s)\sinh(\lambda_{+}\tilde{x}), \tag{5.31}$$

with

$$s = 2i\beta\Omega + \sqrt{\Delta}, \tag{5.32a}$$

$$\Delta = 1 - 4\beta\Omega(i\gamma + \beta\Omega). \tag{5.32b}$$

The eigenvalues $\lambda_\pm$ are

$$\lambda_\pm = \frac{1}{\sqrt{2}}\left(1 + 2i\Omega \pm \sqrt{\Delta}\right)^{1/2}. \tag{5.33}$$

Substituting the solutions from Eq. 5.30 and Eq. 5.31 for the ion concentrations into Eq. 5.28 and subsequent integration yields

$$\hat{\phi}^{(1)}(\tilde{x}) = Cx - A(1+\gamma)\,(s-1)\,\frac{\sinh(\lambda_-\tilde{x})}{2\lambda_-^2} - B(1-\gamma)\,(s+1)\,\frac{\sinh(\lambda_+\tilde{x})}{2\lambda_+^2}. \tag{5.34}$$

The constants A, B, and C are determined by the boundary conditions at $\tilde{x} = \kappa\ell$:

$$A = \frac{s-1}{\lambda_-\kappa\ell\cosh(\lambda_-\kappa\ell)\Gamma}, \quad B = \frac{s+1}{\lambda_+\kappa\ell\cosh(\lambda_+\kappa\ell)\Gamma}, \tag{5.35}$$

$$C = \frac{1}{\kappa\ell}\left(-1 + A(1+\gamma)(s-1)\frac{\sinh(\lambda_-\kappa\ell)}{2\lambda_-^2} + B(1-\gamma)(s+1)\frac{\sinh(\lambda_+\kappa\ell)}{2\lambda_+^2}\right). \tag{5.36}$$

Here the parameter Γ is

$$\Gamma = s^2 - 2\gamma s + 1 - \frac{1}{2\kappa\ell}\left[\frac{(\gamma+1)(s-1)^2(\lambda_-\kappa\ell - \tanh(\lambda_-\kappa\ell))}{\lambda_-^3} - \frac{(\gamma-1)(s+1)^2(\lambda_+\kappa\ell - \tanh(\lambda_+\kappa\ell))}{\lambda_+^3}\right]. \tag{5.37}$$

Finally, having the zeroth and first order perturbation terms, the overall first-order solution (denoted by superscript [1]) becomes:

$$\tilde{n}_\pm^{[1]}(\tilde{x},\tilde{t}) = \tilde{n}_\pm^{(0)}(\tilde{x},\tilde{t}) + \Phi_0\tilde{n}_\pm^{(1)}(\tilde{x},\tilde{t}), \tag{5.38}$$

$$\tilde{\phi}^{[1]}(\tilde{x},\tilde{t}) = \tilde{\phi}^{(0)}(\tilde{x},\tilde{t}) + \Phi_0\tilde{\phi}^{(1)}(\tilde{x},\tilde{t}). \tag{5.39}$$

One can show that for the special case of symmetric electrolytes (i.e., $\beta = \gamma = 0$), this first-order solution becomes identical to the solution provided by Hollinsworth and Saville.[25]

Note that many electrolytes have $z_+ = |z_-|$ for which $\gamma = 0$ (e.g., NaCl, NaOH, KCl, KOH, etc.). For such electrolytes, $\Delta = 1 - 4\beta^2\Omega^2$ (cf. Eq. 5.32b). Then an interesting case occurs when $\beta^2\Omega^2 = \frac{1}{4}$, yielding $\Delta = 0$ and hence, $\lambda_+ = \lambda_-$. In this case a separate solution is necessary; please see Sec. C.1 for details. Our independent numerical calculations (not shown) and our separate analytical solution (Sec. C.1) indicate that the solution behavior does not qualitatively change when $\gamma = 0$ and $\beta^2\Omega^2 = \frac{1}{4}$, i.e., there is no special physical significance to this combination of parameter values.

Second-order

The second-order governing equations for $\tilde{n}_\pm^{(2)}$ and $\tilde{\phi}^{(2)}$ are

$$\frac{\partial \tilde{n}_\pm^{(2)}}{\partial \tilde{t}} + \frac{\partial \tilde{j}_\pm^{(2)}}{\partial \tilde{x}} = 0, \tag{5.40}$$

$$-\frac{\partial^2 \tilde{\phi}^{(2)}}{\partial \tilde{x}^2} = \tfrac{1}{2}(1+\gamma)\tilde{n}_+^{(2)} - \tfrac{1}{2}(1-\gamma)\tilde{n}_-^{(2)}, \tag{5.41}$$

where

$$\tilde{j}_\pm^{(2)}(\tilde{x},\tilde{t}) = -\frac{1}{1\mp\beta}\left[\frac{\partial \tilde{n}_\pm^{(2)}}{\partial \tilde{x}} \pm \frac{\partial \tilde{\phi}^{(2)}}{\partial \tilde{x}} \pm (1\pm\gamma)\tilde{n}_\pm^{(1)}\frac{\partial \tilde{\phi}^{(1)}}{\partial \tilde{x}}\right]. \tag{5.42}$$

The boundary conditions are

$$\tilde{\phi}^{(2)}(\pm\kappa\ell,\tilde{t}) = 0, \tag{5.43a}$$

$$\tilde{j}_\pm^{(2)}(\pm\kappa\ell,\tilde{t}) = 0. \tag{5.43b}$$

One can show that the time-average of Eq. 5.40 over a period of the applied potential (i.e., $\tilde{t} = 0$ to $2\pi/\Omega$) yields:

$$\frac{\partial \langle \tilde{j}_\pm^{(2)} \rangle}{\partial \tilde{x}} = 0, \rightarrow \langle \tilde{j}_\pm^{(2)} \rangle = \text{constant} \tag{5.44}$$

with

$$\langle \tilde{j}_\pm^{(2)} \rangle = -\frac{1}{1\mp\beta}\left[\frac{\partial \langle \tilde{n}_\pm^{(2)} \rangle}{\partial \tilde{x}} \pm \frac{\partial \langle \tilde{\phi}^{(2)} \rangle}{\partial \tilde{x}} \mp \tfrac{1}{4}(1\pm\gamma)\left(\hat{n}_\pm^{(1)}\bar{E}^{(1)} + \bar{n}_\pm^{(1)}\hat{E}^{(1)}\right)\right]. \tag{5.45}$$

Here $\langle X \rangle$ is the time-average of X, $\hat{E}^{(1)} = -\partial\hat{\phi}^{(1)}/\partial\tilde{x}$, and overbars denote complex conjugates, e.g., $\bar{E}^{(1)} = \text{conj}(\hat{E}^{(1)})$. All electric fields ($E = -\partial\phi/\partial x$) are scaled by $k_B T\kappa/(ze)$.

Note that Eq. 5.44 combined with the time-average of the ion flux boundary condition (i.e., $\langle \tilde{j}_\pm^{(2)} \rangle_{\pm\kappa\ell} = 0$) imply that $\langle \tilde{j}_\pm^{(2)} \rangle = 0$ everywhere. Therefore using Eq. 5.45 one can write

$$\frac{\partial \langle \tilde{n}_\pm^{(2)} \rangle}{\partial \tilde{x}} = \pm\langle \tilde{E}^{(2)} \rangle \pm \tfrac{1}{4}(1\pm\gamma)\left(\hat{n}_\pm^{(1)}\bar{E}^{(1)} + \bar{n}_\pm^{(1)}\hat{E}^{(1)}\right). \tag{5.46}$$

On the other hand, the time-average of Eq. 5.41 becomes

$$-\frac{\partial^2 \langle \tilde{\phi}^{(2)} \rangle}{\partial \tilde{x}^2} = \tfrac{1}{2}(1+\gamma)\langle \tilde{n}_+^{(2)} \rangle - \tfrac{1}{2}(1-\gamma)\langle \tilde{n}_-^{(2)} \rangle, \tag{5.47}$$

which can be differentiated with respect to $\tilde{x}$ as

$$\frac{\partial^2 \langle \tilde{E}^{(2)} \rangle}{\partial \tilde{x}^2} = \tfrac{1}{2}(1+\gamma)\frac{\partial \langle \tilde{n}_+^{(2)} \rangle}{\partial \tilde{x}} - \tfrac{1}{2}(1-\gamma)\frac{\partial \langle \tilde{n}_-^{(2)} \rangle}{\partial \tilde{x}}. \tag{5.48}$$

Then substituting $\partial\langle \tilde{n}_\pm^2 \rangle/\partial\tilde{x}$ from Eq. 5.46 yields the following ODE for the time-average electric

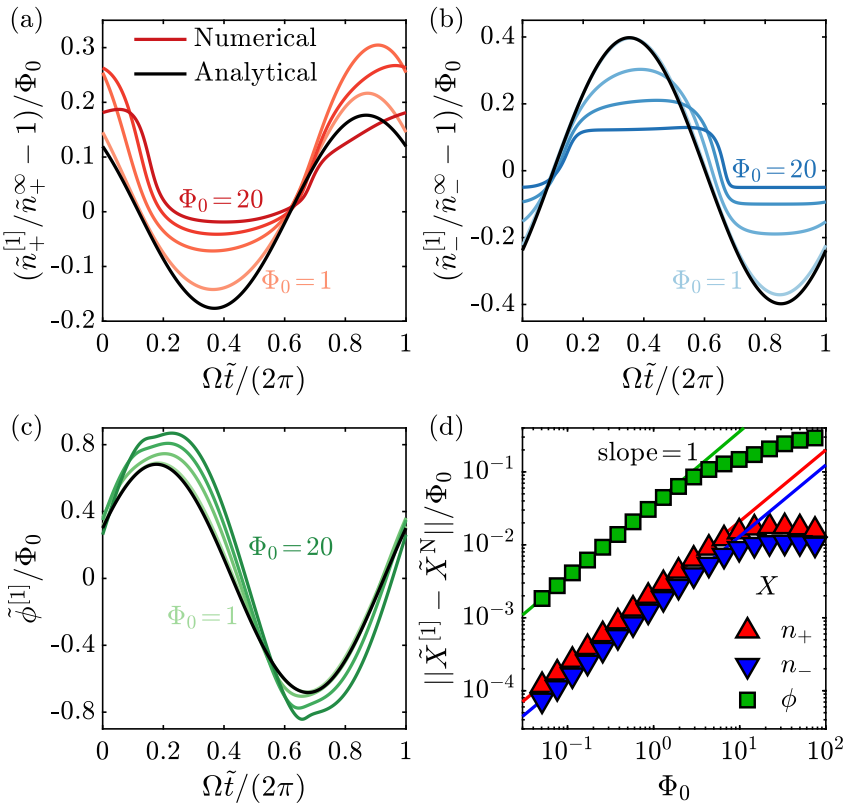

Figure 5.3: Comparison of the first-order approximate and full numerical solutions to the PNP equations. (a, b, c) Time variations of the normalized ion concentrations (a, b) and potential (c) for the approximate solution and numerical solution at different potentials ($\Phi_0 = 20, 10, 5, 1$), evaluated at a fixed location of $\kappa y = 1$ (i.e., one Debye layer away from the left electrode). (d) Normalized norm of the difference between approximate and numerical solutions vs potential. Parameters: $\beta = -1/3$, $\gamma = -1/3$, $\kappa\ell = 100$, $\Omega = 0.01$.

field:

$$\frac{\partial^2 \langle \tilde{E}^{(2)} \rangle}{\partial \tilde{x}^2} - \langle \tilde{E}^{(2)} \rangle = f, \tag{5.49}$$

where

$$f = \tfrac{1}{8}\left[\left((1+\gamma)^2 \hat{n}_+^{(1)} + (1-\gamma)^2 \hat{n}_-^{(1)} \right) \bar{E}^{(1)} + \left((1+\gamma)^2 \bar{n}_+^{(1)} + (1-\gamma)^2 \bar{n}_-^{(1)} \right) \hat{E}^{(1)} \right]. \tag{5.50}$$

At the boundaries $\tilde{x} = \pm\kappa\ell$, we assume $\langle \tilde{E}^{(2)} \rangle_{\pm\kappa\ell} = 0$ to close the problem. Note that this assumption is consistent with all of our numerical solutions for single-mode sinusoidal applied potentials.

The right hand side f in Eq. 5.49 is known from the first-order solution. However we could not find an explicit expression for this complicated function in terms of the dimensionless parameters and variables. Therefore, we numerically solve this ODE to find a semi-analytical approximation to AREF. (Please refer to Sec. C.2 and Sec. C.3 for details of the corresponding numerical solution.)

5.4 RESULTS AND DISCUSSION

In the following subsections, we present and discuss the results of first-order and second-order solutions, focusing mainly on the impacts of β and γ. We also compare these low-potential approximate solutions with the numerical solution to the full nonlinear PNP equations. For visual purposes, we change the origin of the spatial domain from midplane to the left electrode, i.e., $y = x + \ell$ with $y \in [0, 2\ell]$.

5.4.1 First-order solution

Fig. 5.3 compares the first-order (Eq. 5.38 and Eq. 5.39) and numerical solutions to the ion concentrations and electric potential at different voltages. (Detail of the numerical solution algorithm are provided elsewhere.[1]) The values are normalized by Φ_0 to render the analytical solution independent of the applied potential. Time variations of excess positive and negative ion concentrations and electric potential are depicted in Fig. 5.3(a)–(c) at a certain location of $\kappa y = 1$ (i.e., at the edge of the Debye layer). The highly multimodal numerical solutions approach the analytical solution by decreasing the applied potential to $\Phi_0 \sim 1$. As expected, the first-order analytical solution is sinusoidal, oscillating at the same frequency as the applied potential (i.e., Ω), with its amplitude and phase lag depending on location and other dimensionless groups. Fig. 5.3(d) quantitatively compares the numerical and analytical solutions in the time and space domains. The integral norm of the difference, defined as

$$\left\| \tilde{X}^{[1]} - \tilde{X}^{\mathrm{N}} \right\| = \frac{1}{(2\kappa\ell)(\frac{2\pi}{\Omega})} \int_0^{\frac{2\pi}{\Omega}} \int_0^{2\kappa\ell} \left| \tilde{X}^{[1]} - \tilde{X}^{\mathrm{N}} \right|_{\tilde{y},\tilde{t}} d\tilde{y} d\tilde{t}, \tag{5.51}$$

is plotted against Φ_0, where the superscripts [1] and N denote the first-order and numerical solutions, respectively, and $X = n_{\pm}, \phi$. Note that the observed convergence rate is $O(\Phi_0)$ as expected for this first-order approximation.

The effect of β on the first-order solution is demonstrated in Fig. 5.4 for $\gamma = 0$. The excess ion concentrations, free charge density, and electric potential are shown vs position at a certain time of $\Omega\tilde{t} = \pi/2$ (i.e., when the applied potential reaches to its peak magnitude). For symmetric electrolytes ($\beta = 0$, thick black curves) the ion concentrations reach to the bulk values after a few Debye layers. However, for $\beta \neq 0$, where there is a mismatch between the mobilities of ions, a non-monotonic behavior is observed. The ion concentrations oscillate spatially with an amplitude decaying to zero at the midplane (Fig. 5.4(a) and (b)). (Please see the supplementary animated movie for the time variations of the spatial distributions.[†]) Far away from the electrode (insets in Fig. 5.4(a) and (b)), the negative and positive ions appear to have the same distribution and dependency on the β value. But an analysis of the free charge density distribution ($\rho^{[1]}$) reveals a systematic difference (Fig. 5.4(c)). For a symmetric electrolyte the free charge density approaches to zero after a few Debye layers. For $\beta \neq 0$ however, $\rho^{[1]}$ spatially oscillates to become identically zero at the midplane. Note that the free charge density is three orders of magnitude smaller

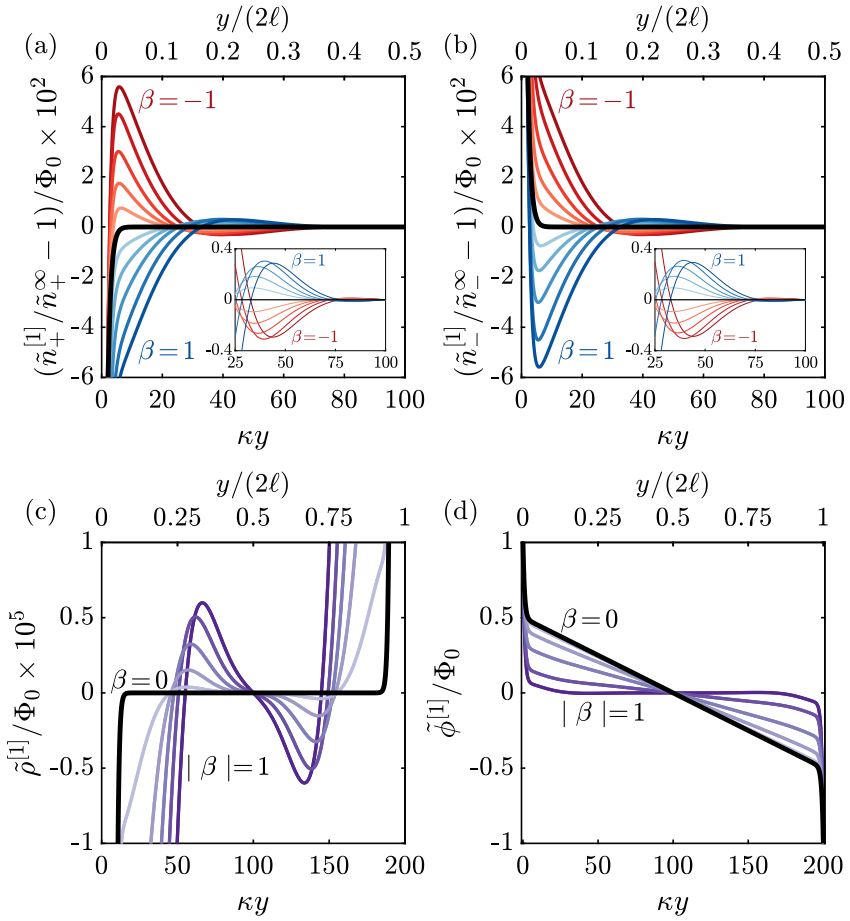

Figure 5.4: Effect of β on the first-order solution. Spatial variations of the normalized positive and negative ion concentrations (a, b), free charge density (c), and potential (d) for different β, evaluated at a fixed time of $\Omega\tilde{t}=\pi/2$. The black curves in all figures correspond to $\beta=0$. Note that the insets in (a) and (b) look very similar but are quantitatively distinct. Parameters: $\gamma=0$, $\kappa\ell=100$, $\Omega=0.01$.

than the nominal ion concentrations. However it was shown that, despite its small magnitude, it yields electrophoretic forces (AREF-induced) that are several orders of magnitude higher than gravitational and colloidal forces in electrokinetic systems.[1] Finally, Fig. 5.4(d) shows the impact of β on the electric potential distribution. Regardless of β, a considerable portion of the potential drop occurs within a few Debye layers from the electrodes. The screening strength of the Debye layer seems to increase for $\beta\neq 0$, further dropping the potential toward zero in the bulk.

Fig. 5.5(a) shows the impact of γ on the free charge density distribution for $\beta=0$ and $-1/2$. We consider the most common values of $\gamma=-1/3,0,1/3$ which correspond to 1–2, 1–1, and 2–1 electrolytes, respectively. Interestingly, when $\beta=0$, γ has no effect on the spatial distribution of free charge density. Similar to the results illustrated in Fig. 5.4(c), $\rho^{[1]}$ approaches to zero within a few Debye layers away from the electrodes. When $\beta\neq 0$, the valence mismatch becomes important. For this representative example shown in Fig. 5.5(a), γ can even qualitatively change the spatial oscillation of the distribution, e.g., dashed red curve ($\gamma=-1/3$) changes sign (charge reversal) near the midplane which does not happen for the other two γ cases. Note that depending on the applied

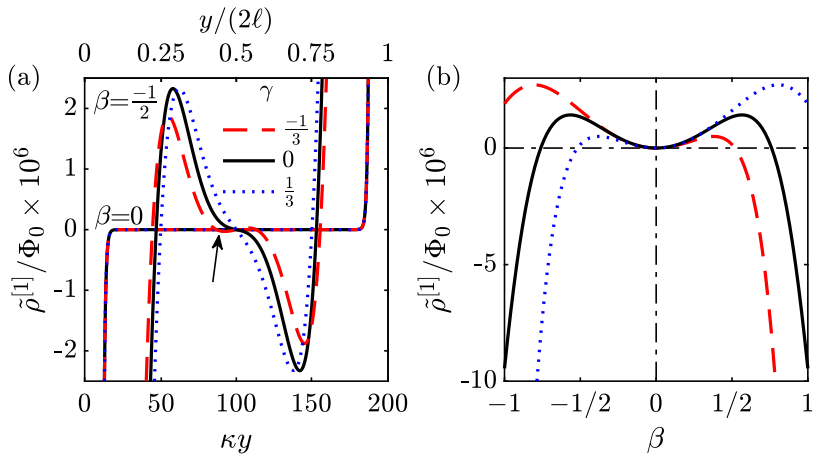

Figure 5.5: Effects of γ and β on the first-order solution. (a) Spatial variations of the normalized free charge density for different γ and two different β values of 0 and $-1/2$, evaluated at a fixed time of $\Omega\tilde{t} = \pi/2$. The arrow points to the tiny charge reversal that occurs for $\beta = -1/2, \gamma = -1/3$ near the midplane. (b) Normalized Free charge density vs β for different γ values, evaluated at fixed time and location of $\Omega\tilde{t} = \pi/2$ and $\kappa y = 50$. Parameters: $\kappa\ell = 100$, $\Omega = 0.01$.

frequency and the electrolyte type, multiple charge reversals can occur. The results presented here serve as a representative example. (Please see Hashemi Amrei et al.[2] for a detailed analysis of charge reversals.) Additionally, $\gamma = 0$ seems to provide the maximum nonzero free charge density in the bulk. A notable observation in Fig. 5.4(c) and (d) is that $\mid \beta \mid$ (not β) governs the system behavior. For example, cases of $\beta = -1/3$ ($D_- = 2D_+$) and $\beta = 1/3$ ($D_+ = 2D_-$) yield the same results. As shown in Fig. 5.5(b), this behavior breaks when $\gamma \neq 0$. At fixed location of $\kappa y = 50$ and time of $\Omega\tilde{t} = \pi/2$, the free charge density is plotted vs β for different γ values. We notice that for $\gamma = 0$, it is the absolute value of β that determines the system behavior, consistent with the results in Fig. 5.4(c). But when $\gamma \neq 0$, the corresponding curves of positive and negative γ are mirrored about $\beta = 0$, and the system is governed by the product $\beta\gamma$. Moreover, for $\beta = 0$, the free charge density at the micron scale is zero for all γ values, in accordance to the spatial distributions in Fig. 5.5(a).

5.4.2 Second-order solution

The semi-analytical AREF from Eq. 5.49 is compared to that obtained from numerical solution to the PNP equations in Fig. 5.6 at different applied potentials. Hereafter, we refer to these two AREFs as semi-analytical ($\langle\tilde{E}\rangle^{\mathrm{sA}}$) and numerical ($\langle\tilde{E}\rangle^{\mathrm{N}}$), respectively. The AREF is normalized by Φ_0^2 to make the semi-analytical AREF independent of the applied potential. (Note that $\langle\tilde{E}\rangle^{\mathrm{sA}} = \Phi_0^2\langle\tilde{E}^{(2)}\rangle$.) Fig. 5.6(a) shows the comparison for $\Omega = 0.001$. We realize that as Φ_0 gets smaller, the numerical AREF approaches to the semi-analytical one. More importantly at the micron scale, which is of interest to most researchers, the semi-analytical solution accurately captures the complicated spatial structure of AREF. As a matter of fact, the curves of different Φ_0 collapse under appropriate normalization. This behavior is robust, even at higher frequencies (Fig. 5.6(b))

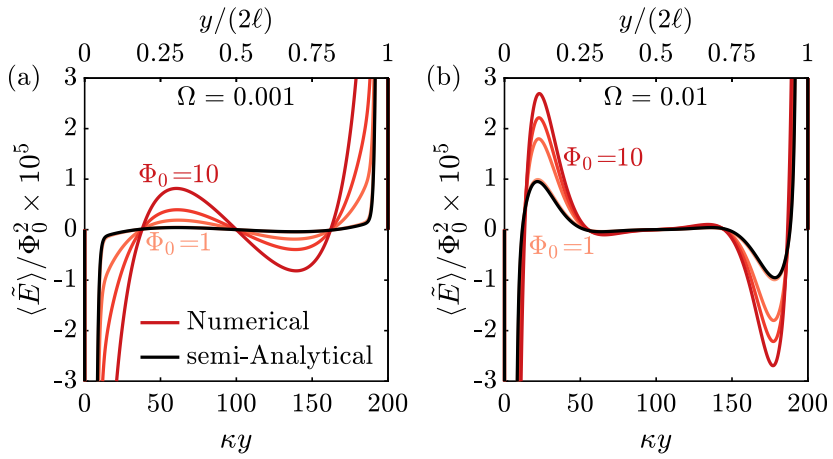

Figure 5.6: Comparison of the second-order approximate (semi-analytical) and numerically calculated AREF (i.e., time-average electric field, $\langle\tilde{E}\rangle$). Spatial variations of the normalized AREF for approximate solution and numerical solution at different potentials ($\Phi_0 = 10, 7, 5, 1$) and for $\Omega = 0.001$ (a) and $\Omega = 0.01$ (b). Parameters: $\beta = -1/3$, $\gamma = -1/3$, $\kappa\ell = 100$.

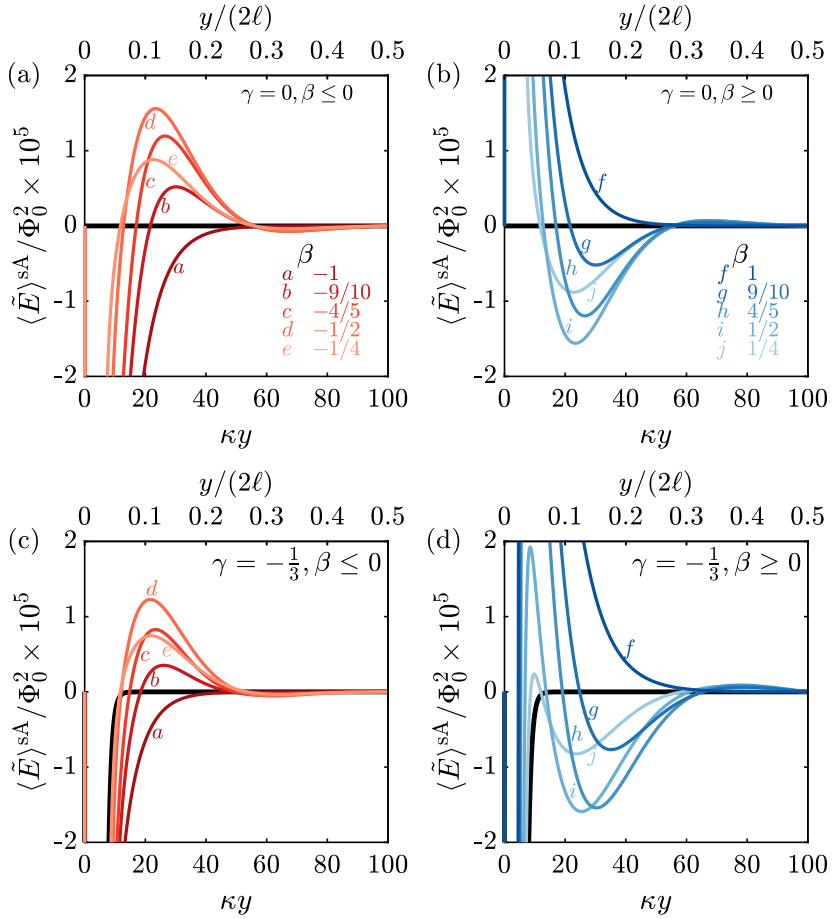

Figure 5.7: Effect of β on the second-order approximate (semi-analytical) AREF (i.e., time-average electric field, $\langle\tilde{E}\rangle$) for $\gamma = 0$ (a, b) and $\gamma = -1/3$ (c, d). The black curves in all figures correspond to $\beta = 0$. Parameters: $\kappa\ell = 100$, $\Omega = 0.01$.

where AREF has multiple sign changes. In other words, the semi-analytical solution correctly predicts the AREF sign and zeros. Therefore, instead of the complicated numerical solution to the PNP equations, researchers can safely use this approximation to find the direction of AREF-induced electrophoretic force. (We will discuss these issues in more detail; cf. Fig. 5.9 and the corresponding discussion.)

We have analyzed the impact of β on the semi-analytical AREF in Fig. 5.7 when $\gamma = 0$ and $-1/3$. For $\gamma = 0$, Fig. 5.7(a) and (b) show a non-monotonic β dependence of the AREF peak magnitude. By increasing the $\mid \beta \mid$ from 0 (identically zero AREF) to 1, AREF peak magnitude at the micron scale first ascends to a maximum and then drops. Notably, when $\mid \beta \mid \rightarrow 1$ the spatial structure is significantly affected and the peak disappears (curves a and f in Fig. 5.7(a) and (b), respectively). Similar observations were reported for the numerical AREF calculation.[2] The problem gets more intricate for a nonzero γ. A representative case of $\gamma = -1/3$ is depicted in Fig. 5.7(c) and (d). When $\beta < 0$, changing the γ from 0 to $-1/3$ slightly affects the AREF distribution, decreasing its magnitude (cf. curves in Fig. 5.7(a) and (c)). However, when $\beta > 0$, a qualitative difference is observed between cases of $\gamma = 0$ and $-1/3$ (e.g., compare j curves in Fig. 5.7(b) and (d)). As pointed out by Hashemi Amrei et al.,[2] when the faster ion has a smaller valence (and vice versa), there will be a competition between ionic mobility and valence mismatches to determine the sign of AREF. In the context of this study, the competition exists when $\beta\gamma < 0$. When $\beta\gamma > 0$, the both sources of asymmetry work in accord to determine the AREF sign. Another notable observation is that when $\beta = 0$, regardless of γ, AREF is identically zero at the micron scale.

It would be helpful to compare the AREF for actual electrolytes of different (β, γ) combinations (Fig. 5.8). The diffusivity of an ion can be expressed in terms of its drag coefficient (λ_i) as[26,27,25]

$$D_i = \frac{k_B T}{\lambda_i}, \quad \lambda_i = \frac{N_A e^2 \mid z_i \mid}{\Lambda_i^\infty}, \tag{5.52}$$

where Λ_i^∞ is the limiting conductance of the ion and N_A is the Avogadro's number. Limiting conductance data of different ions can be found in physical chemistry textbooks.[96] NaOH has the highest negative β value ($D_- > D_+$) among the selected electrolytes and provides the maximum positive peak. As β gets closer to zero, the AREF peaks at lower magnitudes; e.g., compare NaCl with $\beta = -0.21$ to NaOH with $\beta = -0.6$. As expected, electrolytes with positive β (HCl, $\beta = 0.64$) have negative peaks. An interesting case would be KCl with a nearly zero ionic mobility mismatch ($\beta = -0.02$) for which the AREF is nearly zero. However, recall that the β effect on AREF peak magnitude is non-monotonic (Fig. 5.7), a behavior that was explained at length by Hashemi Amrei et al.[2] Using a different set of dimensionless parameters (e.g., $\delta = D_-/D_+$ instead of β as a measure for ionic mobility mismatch), they showed that $\delta_{\max}$ for which AREF has its maximum peak depends on Φ_0. By increasing Φ_0, $\delta_{\max}$ gets indefinitely closer to 1 (equivalently, $\beta_{\max}$ gets closer to 0). Therefore, at high applied potentials, KCl may have a higher peak than NaOH. It is worth mentioning that for the dimensionless parameters used in the present study, the $\beta_{\max}$ is not

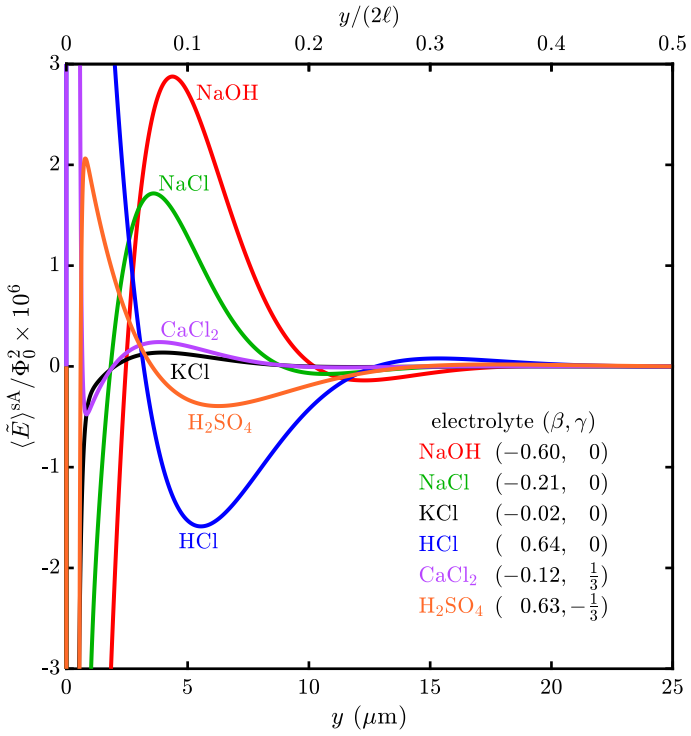

Figure 5.8: Spatial variations of the second-order approximate (semi-analytical) AREF (i.e., time-average electric field, $\langle\tilde{E}\rangle$) for different electrolytes. Dimensional parameters: $\ell = 25$ μm, $\varepsilon = 78$, $T = 298.15$ K, $n^\infty = 6.022 \times 10^{21}$ m^{-3} (10^{-5} M), $f = 100$ kHz.

governed solely by Φ_0. Finally, electrolytes with valence mismatch ($\gamma \neq 0$) show intriguing behavior ($CaCl_2$ and H_2SO_4). As discussed in discussion of Fig. 5.7, a balance between asymmetries due to β and γ determines the AREF distribution.

Finally, we comprehensively analyze the collapse of numerical AREF curves for different potentials in Fig. 5.9. Fig. 5.9(a) shows the numerical AREF distribution for different voltages normalized by their corresponding peak values (dashed curves of different color intensities), along with the semi-analytical AREF plotted as solid. Each color corresponds to a different dimensionless frequency (Ω). We notice that by increasing the Ω, a better collapse is obtained. Additionally, the ratio of numerical to semi-analytical AREF peak is plotted versus Φ_0 in Fig. 5.9(b) for different Ω. Interestingly, as Ω increases, the ratio decays to nearly 1, even at very high voltages. We perform a similar analysis by changing the $\kappa\ell$. We find that collapse of data improves by increasing the $\kappa\ell$ value (Fig. 5.9(c)). Moreover, semi-analytical solution appears to accurately predict the AREF peak magnitude at high $\kappa\ell$ (Fig. 5.9(d)). Therefore, we conclude that at high Ω and $\kappa\ell$ values, semi-analytical solution accurately captures 1) the spatial structure of AREF (better collapse), and 2) the AREF magnitude.

It appears that regardless of the system properties, there is a 'threshold' Φ_0 above which the numerical AREF curves do not collapse, and this threshold tends to increase with Ω or $\kappa\ell$. At low applied potentials and fixed other system properties, all AREF distributions collapse onto the semi-analytical solution; but as Φ_0 passes the threshold potential, the shape of AREF at the micron

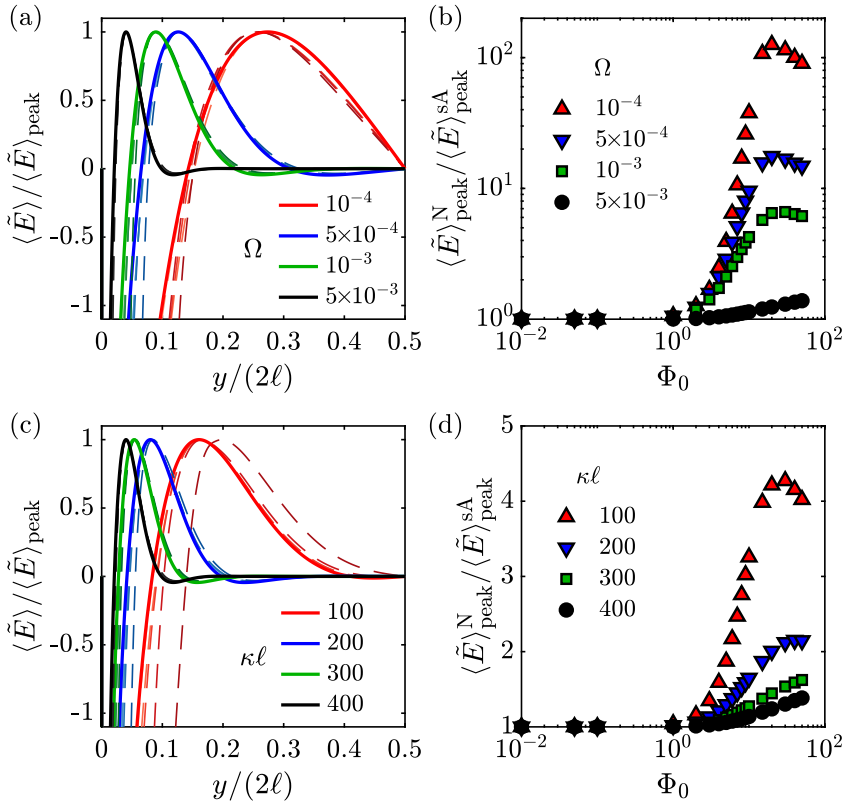

Figure 5.9: Collapse of AREF (i.e., time-average electric field, $\langle\tilde{E}\rangle$) spatial distribution at different voltages. Dashed (with different color intensities) and solid curves in (a, c) show the numerical AREF at different potentials and semi-analytical AREF, respectively. (a, b) Collapse of AREF curves for different Ω values and $\kappa\ell = 400$. (c, d) Collapse of AREF curves for different $\kappa\ell$ values and $\Omega = 5 \times 10^{-3}$. Parameters: $\beta = -1/3$, $\gamma = 0$.

scale starts deviating from the semi-analytical solution. For sufficiently large Ω or $\kappa\ell$ values, this threshold potential is simply beyond the considered Φ_0 range. However, the underlying physics behind the collapse of the AREF distributions and its sensitivity to Ω and $\kappa\ell$ remain unclear.

Parameters Ω and $\kappa\ell$ can be combined into one dimensionless parameter as

$$\mathcal{L}_D = \frac{\ell_D}{\ell} = \sqrt{\frac{1}{\Omega(\kappa\ell)^2}} = \frac{\sqrt{D/\omega}}{\ell}. \tag{5.53}$$

Hashemi Amrei et al.[2] showed that this dimensionless diffusive length scale governs the location of peak AREF for a wide range of parameter space. Note that small $\mathcal{L}_D$ corresponds to large Ω and $\kappa\ell$. Hence, the semi-analytical solution can be used to predict the both shape and magnitude of AREF when $\mathcal{L}_D \ll 1$. This is extremely important since for most practical cases in electrokinetics $\mathcal{L}_D$ is indeed very small.

5.5 CONCLUSIONS

Following the discovery of AREF by Hashemi Amrei et al.,[1] we have demonstrated by a new approach that a steady electric field may be induced by an applied oscillatory potential. We have developed an analytical approximate solution to the PNP equations at low applied potentials. Specifically, we focused on the impacts of ionic mobility and valence mismatches to find approximations to the one-dimensional AREF between parallel electrodes.[1] In this regard, we have shown that the second-order perturbation solution corroborates the existence of AREF. Interestingly, at sufficiently small $\mathcal{L}_D = \sqrt{D/\omega}/\ell$ (dimensionless diffusive length scale), this simple approximate solution accurately predicts both the complicated spatial structure and the magnitude of AREF, even at extremely high potentials. We emphasize that for most electrokinetic systems $\mathcal{L}_D \ll 1$. Hence, researchers can safely use this approximate solution to calculate AREF. It is significant, considering the extremely complicated alternative of finding AREF via numerical solution to the full nonlinear PNP equations.

Chapter 6

Non-Antiperiodic Force Excitations in Isotropic Media Yield Net Motion of Macroscopic Objects

Overview

It is well known that application of an oscillatory driving force to objects placed in an anisotropic medium gives rise to the so-called "ratchet" effect, where the spatial asymmetry in the resistance to motion yields net drift in one direction.[97] Less well known is that application of an oscillatory excitation with zero-time average but temporal asymmetry can also yield net drift, even in isotropic media.[98,99] To date, this type of 'externally induced' ratchet has been considered in the context of point particles,[99–101] as well as optical[102–105] and quantum[106,107] lattice systems. Here, we use both theory and experiment to extend the concept of externally induced ratchets to macroscopic objects. Two exemplary systems are considered: solid centimeter-scale objects placed on a uniform flat surface made to vibrate laterally, and charged colloidal particles in water placed between parallel electrodes with an applied oscillatory electric potential. In both cases, net motion is observed if the driving force has dual frequency modes that are the ratio of odd and even numbers (e.g., 3 Hz and 2 Hz). Furthermore, the direction of motion in each case is reversed by flipping the sign of the applied waveform, for example by swapping which electrode is powered and grounded. We provide generalized theoretical arguments indicating that non-antiperiodic force excitations will yield net motion in isotropic media, provided there is a non-linear component in the equation of motion, and we show how similar ratchet-like responses occur in other systems involving nonlinearities like non-Newtonian fluids and non-Hookean springs.

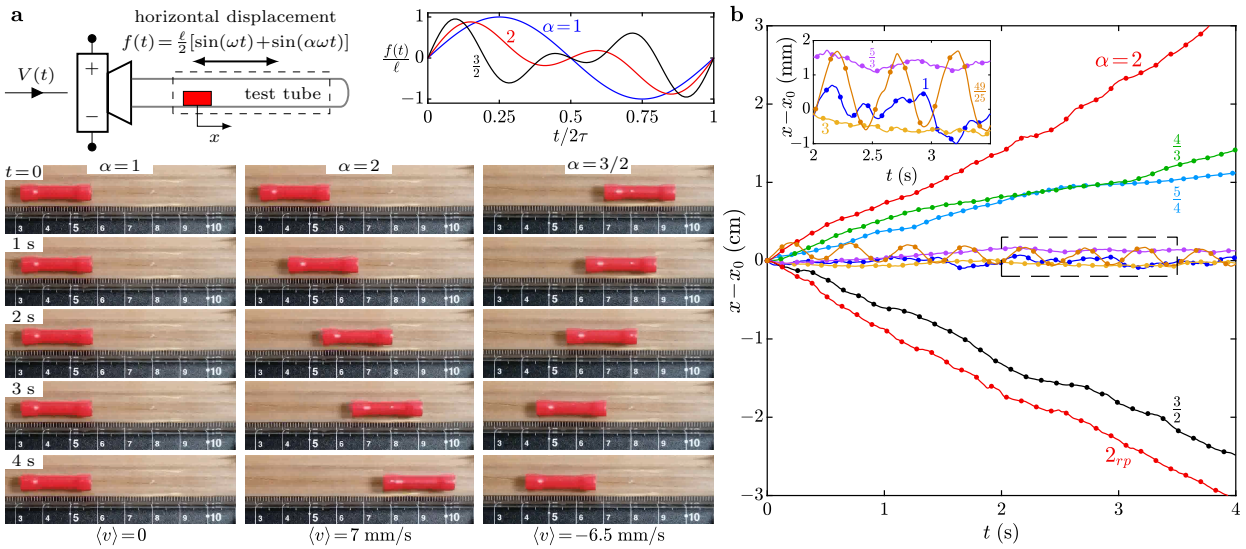

Figure 6.1: Experimental evidence for ratchets in the solid-solid friction problem. **a**, top: Schematic diagram of the system; an object is placed in a test tube that is glued to the diaphragm of a speaker. A dual-mode sound wave is fed to the speaker, which in turn excites the tube as $f(t) = \frac{\ell}{2}[\sin(\omega t) + \sin(\alpha\omega t)]$ ($\omega/2\pi = 50$ Hz for the present results). Please see Methods for details. **a**, bottom: Time lapses of the object dynamics for $\alpha = 1$, 2, and 3/2. **b**: Object location versus time for different α values. Typical uncertainty (standard deviation of at least three trial replicates) was ~ 1 mm.

6.1 SOLID-SOLID FRICTION

We designed a simple experiment to demonstrate the existence of a ratchet-like behavior in a solid-solid friction problem (Fig. 6.1a). An object is placed in a test tube attached perpendicularly to a TV speaker. A dual-mode digital sound wave is fed to the speaker, ensuing a periodic back and forth movement of the diaphragm, which, in turn, induces a dual-mode lateral vibration of the test tube, $f(t) = \frac{\ell}{2}[\sin(\omega t) + \sin(\alpha\omega t)]$ (with α as a rational number). Note that the tube remains stationary on average, i.e., the excitation f has a zero time-average, $\langle f\rangle = 0$. (Please see Methods for details.) Intuitively, the object is expected to either stick to, or slip on, the surface and move in a periodic fashion, but remain stationary on average. We demonstrate, however, that this intuition is not necessarily true. As shown in Fig. 6.1a (time lapses), for $\alpha = 1$, the object does not move on average, and $\langle v\rangle = 0$ (the object velocity), while it experiences a net drift for $\alpha = 2$ and $\frac{3}{2}$. We further monitored the object's behavior for several different α values (Fig. 6.1b). It appears that depending on α, the system may indeed act as a ratchet. Note that here, unlike the classical Feynman–Smoluchowski ratchet, the system domain has no asymmetry. Instead, the phenomenon stems from a certain time-symmetry break in the excitation. We provide an explanation for this observation.

The dimensionless equation of motion can be expressed as (cf. Fig. 6.2a)

$$\dot{v} = \begin{cases} \ddot{f} & \text{if} \quad v = \dot{f} \text{ and } |\ \ddot{f}\ | < \lambda_s, \\ -\lambda_k \mathrm{sgn}(v - \dot{f}) & \text{otherwise,} \end{cases} \tag{6.1}$$

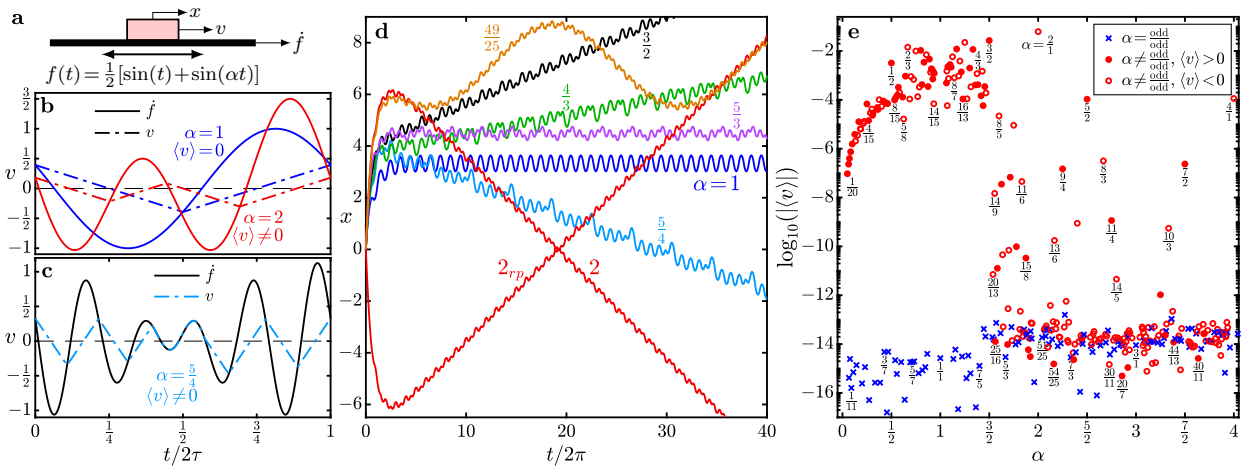

Figure 6.2: Dynamic response of an object placed atop a solid surface (solid-solid friction) to a dual-mode displacement excitation of the surface $f(t) = \frac{1}{2}[\sin(t) + \sin(\alpha t)]$ (dimensionless form). **a**: schematic diagram of the problem. **b, c**: representative solutions to the harmonic object and surface velocities (v and $\dot{f}$, respectively) versus time, for different α values. **d**: object location, x, versus time for different α values. The case α_{rp} denotes the response due to the reverse polarization excitation $f(t) = -\frac{1}{2}[\sin(t) + \sin(\alpha t)]$. **e**: absolute value of the harmonic time-average object velocity, $|\langle v \rangle|$, versus α. Here, time is scaled by the inverse angular frequency $1/\omega$, and the dimensionless period is $2\tau = 2\pi/\gcd(1, \alpha)$, where $\gcd(1, \alpha)$ denotes the greatest common divisor of 1 and α. The solution is considered 'harmonic' if it is invariant between different periodic intervals (i.e., we let $t \to \infty$). Dimensionless parameters: $\lambda_s = 0.5, \lambda_k = 0.25$.

Here, length and time dimensions are scaled by ℓ (vibration amplitude) and $1/\omega$ (inverse base angular frequency), $\lambda_s = \mu_s g/\ell\omega^2$ and $\lambda_k = \mu_k g/\ell\omega^2$ are the dimensionless static and kinetic friction coefficients, and $f(t) = \frac{1}{2}[\sin(t) + \sin(\alpha t)]$ is the dimensionless dual-mode vibration. Therefore, the system behavior is governed by three dimensionless parameters α, λ_s, and λ_k. We focus on α. Representative numerical solutions to the object velocity are depicted in Fig. 6.2b,c. For $\alpha = 1$ and 2, the object slips back and forth, and changes direction whenever $v = \dot{f}$ (Fig. 6.2b). However, Fig. 6.2c shows an example where a significant stick-slip transition occurs, which tremendously complicates the analysis. Nonetheless, these representative numerical results indicate the existence of ratchets (i.e., $\langle v \rangle \neq 0$) for specific α values (cf. $\alpha = 2$ and $\frac{5}{4}$ in Fig. 6.2b,c). Below, we use a symmetry argument to explicate the observed phenomenon.

The system is spatially symmetric, and if v is a unique solution to the problem, then $-v$ would be the unique solution to the problem with the reverse polarization excitation $-f$, i.e., $f \to -f \Rightarrow v \to -v$; that is, the functional $v(t) = \psi(f, t)$ is odd in f. Now consider antiperiodic excitations, for which $f(t + \tau) = -f(t)$; in other words, for a given periodic interval $t \in [0, 2\tau]$, f in the second half of the period ($t \in [\tau, 2\tau]$) is the negative of f in the first half ($t \in [0, \tau]$). We prove that for antiperiodic excitations, the time-average of the harmonic solution, $\langle v \rangle$, is zero: one can write

$$v(t + \tau) = \psi(f, t + \tau) = \psi(-f, t) = -v(t) \Rightarrow v(t + \tau) = -v(t). \tag{6.2}$$

Then, taking the time-average of the latter equality, and noting that a time lag should not alter

the time-average solution (i.e., $\langle v(t+\tau)\rangle = \langle v(t)\rangle$), we get: $\langle v(t)\rangle = -\langle v(t)\rangle \Rightarrow \langle v(t)\rangle = 0$. The counterintuitive observation is that if f is non-antiperiodic, $\langle v\rangle$ might be nonzero and the object drifts. As a matter of fact, the drift happens for most non-antiperiodic excitations. With the dual-mode excitation, f is antiperiodic if α, in its most simplified form, can be expressed as {odd integer}/{odd integer} (e.g., $\alpha = 1$, Fig. 6.2b). For antiperiodicity, we need $\sin(t+\tau) + \sin(\alpha(t+\tau)) = -[\sin(t) + \sin(\alpha t)]$, which implies that $\tau = (2j+1)\pi$ and $\alpha\tau = (2k+1)\pi$ (the phase lags must be odd multiples of π), and consequently, $\alpha = (2k+1)/(2j+1)$. For α ={even integer}/{odd integer} or {odd integer}/{even integer}, f is non-antiperiodic (e.g, $\alpha = 2, \frac{5}{4}$, Fig. 6.2b,c).

Let us now discuss the numerical results in more detail. Fig. 6.2d shows the time evolution of the object location, x, for different α values. When $\alpha = 1$ and $\frac{5}{3}$, the object's time-average location remains constant through time. Note that we are interested in the harmonic behavior, and hence, disregard the transient drift of the object in the first few cycles. With non-antiperiodic excitations, the object moves, on average, to the left and right for $\alpha = 2, \frac{5}{4}$ ($\langle v\rangle = d\langle x\rangle/dt < 0$) and $\frac{4}{3}, \frac{3}{2}$ ($\langle v\rangle > 0$), respectively. Furthermore, consistent with the odd property of the model problem, $\alpha = 2_{rp}$ yields an object velocity equal to that of $\alpha = 2$, but in the opposite direction (red curves in Fig. 6.2d). Here, α_{rp} denotes the reverse polarization excitation $f = -\frac{1}{2}[\sin(t) + \sin(\alpha t)]$ (i.e., with the negative sign).

For all the models considered here, $\alpha = 2$ provides the most significant ratchet effect (e.g., here, the drifting velocity is the highest for $\alpha = 2$). A natural question is that what happens if α is very close to 2, but it is in the form {odd integer}/{odd integer}, and so, is expected to provide a zero time-average? A representative result is provided in Fig. 6.2d for $\alpha = \frac{49}{25} \approx 2$. The object goes through a considerable oscillation but remains in the same location on average. Note that the period of the solution for $\alpha = \frac{49}{25}$ is 25 times longer than that for $\alpha = 2$. The object moves, for half of its period, as if $\alpha = 2$ (the descending region of the curve), and reverses direction for the rest of the period, and moves as if $\alpha = 2_{rp}$ (the ascending region). In other words, the descent and ascent of the $\alpha = 49/25$ curve resemble the cases of $\alpha = 2$ and 2_{rp}, respectively.

Fig. 6.2e shows the absolute time-average velocity of the object, $|\langle v\rangle|$, for about 400 different α values between 0 and 4. We notice that $|\langle v\rangle| = 0$ ($\sim$numerical noise) for all α ={odd integer}/{odd integer} (i.e., antiperiodic). However, when the excitation is non-antiperiodic (filled and empty circles in Fig. 6.2b), $|\langle v\rangle|$ can be either zero or nonzero. It appears that for antiperiodic excitations, the zero-frequency components of the solution cancel each other out, yielding an overall zero time-average. But, they do not necessarily cancel out when the excitation is non-antiperiodic. However, a seemingly simple question is left unanswered: what determines the direction of the movement, i.e., $\langle v\rangle > 0$ versus $\langle v\rangle < 0$? Our theory explains why the time-average solution is zero for antiperiodic excitations. But it does not provide sufficient insights on what governs the observed net movement for non-antiperiodic excitations. A proper answer would rely on an analytical analysis of the corresponding differential equations.

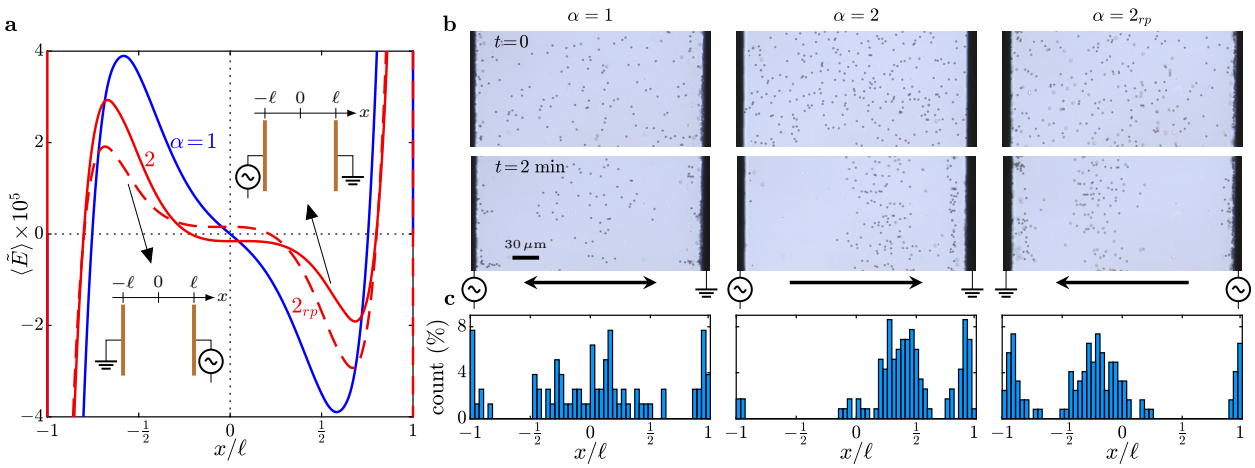

Figure 6.3: Ratchets in the induced steady electric field between two parallel electrodes, placed at $\pm\ell$, and under a dual-mode potential excitation $\phi(t) = \frac{1}{2}\phi_0(\sin(\omega t) + \sin(\alpha\omega t))$. a (Numerical solution): spatial distribution of the dimensionless time-average electric field, $\langle \tilde{E} \rangle = 2\ell\langle E \rangle/\phi_0$, at the micron scale, for $\alpha = 1$, 2, and 2_{rp}. The case α_{rp} denotes the response due to the reverse polarization excitation (the powered and grounded electrodes are swapped). Parameters: $\phi_0 = 10\phi_T$, $\omega/2\pi = 50$ Hz, $2\ell = 30$ μm, 1 mM NaOH solution. **b, c (Experimental evidence)**: electrophoresis of charged colloidal particles due to asymmetric rectified electric field (AREF). **b**: cluster of the colloids at $t = 0$ (no field) and $t = 2$ min (equilibrium conditions) for $\alpha = 1$, 2, and 2_{rp}. The black arrows show the drift direction of the colloids. **c**: the corresponding histograms of the percent particle count after $t = 2$ min. Parameters: $\phi_0 = 4$ V, $\omega/2\pi = 2$ Hz, $2\ell = 270$ μm, 0.01 mM NaOH solution, 2–μm sulfonated polystyrene particles.

6.2 ELECTROKINETICS

An interesting implication of our theory is in nonlinear electrokinetics. Recent numerical, theoretical, and experimental study established that a single-mode sinusoidal potential induces a nonzero time-average electric field within the liquid, referred to as asymmetric rectified electric field (AREF).[1,2,5] Now we ask what happens if we apply a dual-mode potential $\phi(t) = \frac{1}{2}\phi_0(\sin(\omega t) + \sin(\alpha\omega t))$ to the system?

Consider a 1-1 binary electrolyte confined between two planar, parallel, electrodes at $x = \pm\ell$. A dual-mode potential $\phi(t)$ (or $-\phi(t)$ for the reverse polarization) is applied on the electrode at $x = -\ell$, and the electrode at $x = \ell$ is grounded. Fig. 6.3a represents the numerically computed AREF, $\langle E \rangle$. The case of $\alpha = 1$ illustrates the standard AREF (i.e., single-mode potential), which is antisymmetric in space, and is identically zero at the midplane. Such a spatial structure indicates that swapping the powered and the grounded electrodes, which is equivalent to applying the reverse polarization potential $-\phi(t)$, does not alter the system behavior. In fact, the induced AREFs due to $\phi(t)$ and $-\phi(t)$ would be superimposed. When $\alpha = 2$, a dissymmetric AREF is induced. Here, swapping the powered and grounded electrodes *does* alter the system; notably, the direction of AREF at the midplane changes ($\alpha = 2$ and 2_{rp} in Fig. 6.3a). The existence of AREF ratchets is verified by our experimental observations. As demonstrated in Fig. 6.3b, when $\alpha = 2$, swapping the powered and grounded electrodes reverses the AREF-induced drift direction of the charged colloids. Please see Methods for details of the electrokinetic experiments.

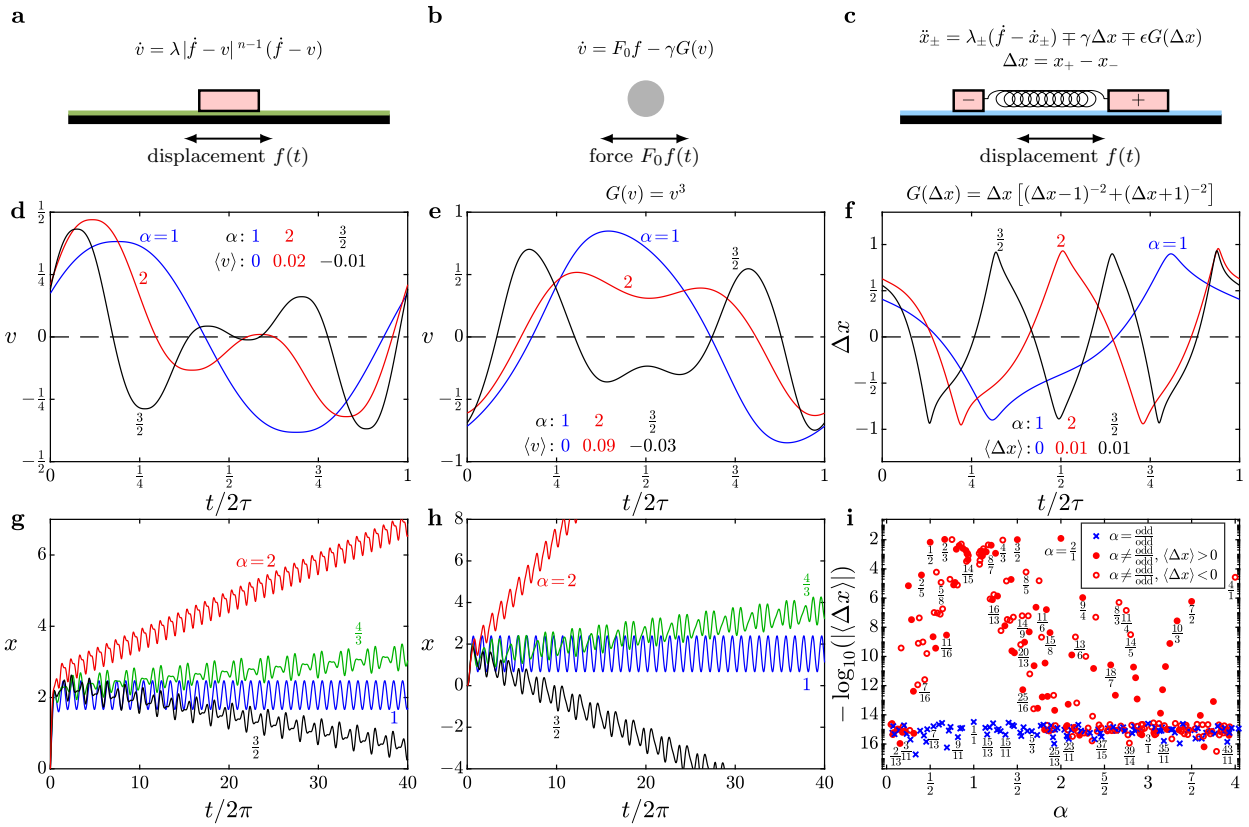

Figure 6.4: Existence of ratchet-like behavior in various nonlinear dynamical systems. Each triplet figure panel corresponds to one problem. **a, b, c**: schematic diagrams of various nonlinear dynamical systems under a dual-mode excitation $f(t) = \frac{1}{2}[\sin(t)+\sin(\alpha t)]$, with their dimensionless governing equations. **a**: an object subject to the drag of a non-Newtonian liquid film on an excited surface. **b**: an object subject to a force excitation and a nonlinear drag. **c**: a pair of asymmetric objects connected by a nonlinear spring, and subject to the drag of a Newtonian liquid film on an excited surface. **d, e, f**: numerically evaluated harmonic solutions (v versus t) of the corresponding systems for different α. **g, h**: time evolution of the object location (x versus t) for different α. **i**: time-average dimensionless distance between the two masses for different α. Dimensionless parameters: **a, d, g**: $\lambda = 0.5, n = 1.5$; **b, e, h**: $F_0 = 1, \gamma = 1$; **c, f, i**: $\lambda_+ = 10, \lambda_- = 0.1, \gamma = 0.1, \epsilon = 0.1$.

6.3 OTHER EXAMPLES

The described concept can be extended to a wide range of physical systems (Fig. 6.4). We could replace the solid-solid friction with the drag of a non-Newtonian fluid film (Fig. 6.4a). Another example would be an object subject to a dual-mode periodic force excitation and a nonlinear drag $G(v)$ (Fig. 6.4b). Note that we are interested in nonlinear drag terms that do not favor a direction over another; in other words, G is an odd function of v. We used a variety of odd nonlinear drags such as $G(v) = v^3, \mathrm{sgn}(v), |v|v, \sinh(v), \ldots$ and observed the same qualitative behavior. A slightly more complex system is demonstrated in Fig. 6.4c; a pair of asymmetric masses are connected by a nonlinear spring, and placed atop an excited surface wetted with a Newtonian fluid film (linear shear). Similar to the system in Fig. 6.4b, we could use various odd nonlinear spring forces. The considered spring force model imposes two 'solid walls' at $\Delta x = 1$ and $\Delta x = -1$. Physically, the

model ensures that the spring does not elongate to more than double of its resting value, and it does not compress to negative values. We note that when $\alpha = 1$, time-average of $\Delta x = x_+ - x_-$ is zero. This indicates that the average distance between the two masses remains equal to the resting value. However, $\langle \Delta x \rangle \neq 0$ for $\alpha = 2, \frac{3}{2}$; for the given example, the masses stay farther apart than their resting condition ($\langle \Delta x \rangle > 0$). Future works include an in-depth analysis of the aforementioned problems.

We emphasize that our theory is not limited to the dual-mode excitations. Any zero-time-average, non-antiperiodic, excitation (e.g., triangle waves, pulses, etc.) can induce a ratchet-like behavior in the systems analyzed here. Our study extends the current theory of ratchet dynamics to a variety of nonlinear problems, and offers a readily accessible method of investigating ratchets in macroscopic systems. Future work includes further elucidation of the underlying physics and its broad implications.

6.4 METHODS

Numerical solutions. The following loop solves the solid-solid friction problem (Fig. 6.2). Initially, the object is resting on the surface, i.e., $v = \dot{f}$. Then,

i) $v = \dot{f}$ as long as $|\ddot{f}| < \lambda_s$.

ii) Once $|\ddot{f}| > \lambda_s$, slipping starts: $\dot{v} = -\lambda_k \text{sgn}(v - \dot{f})$, until $v = \dot{f}$ again.

iii) Go to step ii.

The time t is updated in each step as well. Whenever t increases by 2τ is considered a cycle of the solution. We repeat the cycles until a harmonic solution is achieved. Let $v_k(t)$ with $t \in [2(k-1)\tau, 2k\tau]$ denote the solution in the k^{th} cycle. The solution is considered harmonic if $\|v_k - v_{k-1}\| < \epsilon$, where ϵ is a tolerance. We also check $|\langle v_k \rangle - \langle v_{k-1} \rangle| < \epsilon$.

The toy problems in Fig. 6.4 are solved by the Runge–Kutta 4^{th} order method. The same criteria is used for the harmonic solution check. Details of the numerical solution to the nonlinear electrokinetic problem (Fig. 6.3a), and the corresponding consistency checks are provided elsewhere.[1,2]

Solid-solid friction experiments. An object (a wire splice connector) is placed in a glass test tube of length 15 cm and outer diameter 18 mm (IWAKI TE-32 PYREX), that is glued to the diaphragm of a used television speaker ($R = 8\ \Omega$). A dual-mode sound wave, created by MATLAB, enters a generic class D amplifier. The amplified current is then fed to the speaker as an excitation. The sound actuator behaves linearly, i.e., its movement is linearly proportional to the passing current. Harmonic oscillations of the diaphragm translate to a one-dimensional displacement excitation of the tube. Note that the tube geometry restricts the object to move in one dimension. A digital camera is used to record the object dynamics at 60 frames per second. Note that the passing current, and consequently, the displacement amplitude, are kept sufficiently

low to ensure a linear behavior of the sound actuator. As a result, the movement of the tube itself is not easily discernible.

Electrokinetic experiments. The experimental setup consists of a microchannel constructed using two flat sheets of polydimethylsiloxane (PDMS), that were separated by two 16 μm thick 304 stainless steel plates spaced 270 μm apart. (In Fig. 6.3b, the electrodes (stainless steel plates) are 270 μm apart, the depth of the cell is 16 μm (through the page), and the point of view is through the PDMS sheet.) The channel had a total length of 15 mm. Two polyethylene tubes of 0.58 mm inner diameter were inserted into the top PDMS layer to introduce and remove the fluid. Copper tape was used to connect the stainless-steel sheets to the powered and grounded wires. The device was then sealed using epoxy around the edges and fixed in place over a glass substrate using clamps.

A 0.01 mM NaOH solution (conductivity, $\sigma = 2$ μS/cm) was prepared using DI water (18.2 MΩ.cm), and 2–μm diameter fluorescent sulfonated polystyrene particles were added at a volume fraction of 1×10^{-4} to the solution. The colloidal suspension was washed three times by centrifugation and resuspension, and then injected into the microchannel using a syringe pump (PHD 2000, Harvard apparatus). Once the flow inside the microchannel was stable and the particle density appeared uniform, a function generator (Agilent 33220A) was used to apply a sum modulated field of 4 V_{pp} (Volts peak-to-peak) at 2 Hz and 4 V_{pp} at 4 Hz. A digital camera mounted on an optical microscope (Leica DM2500 M) was used to record the particle behavior at 15 frames per second. After two minutes, the field was removed and the channel was then flushed for a minute. The powered electrode was changed by physically exchanging the wire leads on the device, upon which the same field was then applied. For the unimodal case ($\alpha = 1$), an 8 V_{pp} at 2 Hz field was applied using the same procedure. Furthermore, when $\alpha = 1$, swapping the powered and grounded electrodes had no significant impact on the system behavior.

Chapter 7

Multimodal Asymmetric Rectified Electric Fields and Long-Range Symmetry Breaking in Electric Field Orientation

Overview

We report the existence of a spatially dissymmetric steady field within liquids between parallel electrodes powered by two-mode oscillatory electric potentials (frequencies f and αf). Our results indicate that for specific values of α (i.e., ratio of the two frequencies), the induced steady field is dissymmetric, with a nonzero value at the midplane. An intriguing implication is then that swapping the powered and grounded electrodes alters the system behavior, an observation at odds with the classical understanding of the electrokinetics. We further generalize our theory by demonstrating that the dissymmetric field occurs for all classes of zero-time-average (no dc bias) periodic potentials (e.g., triangular and rectangular pulses). The discovery of such steady field can tremendously change the interpretation, design, and applications of the electrokinetic systems.

7.1 INTRODUCTION

Application of ac electric potentials to liquids is a ubiquitous element of electrokinetic systems, including induced-charge-electrokinetics (ICEK),[18,19] ac electroosmosis (ACEO),[20–23] and electrohydrodynamic (EHD) manipulation of colloids.[8,10–12] Over the last few decades, a great body of research has focused on evaluating the dynamic response of liquids to ac polarization, in order to find the induced electric field and ion concentrations within the liquid.[67,32,75] However ion-containing liquids respond to ac polarizations in intricate ways, especially when the dissolved ions have unequal mobilities. Recently, Hashemi Amrei et al. established the existence of an induced, long-range, steady field in liquids, referred to as asymmetric rectified electric field (AREF).[1,2,5] A perfectly sinusoidal potential induces an electric field with a nonzero time-average, a zero-frequency component, as a direct result of the nonlinear effects and ionic mobility mismatch. AREF was shown to provide qualitative explanations for several long-standing questions in electrokinetics and significantly change the interpretation of experimental observations.[1,3,4]

For a sinusoidal applied potential of amplitude ϕ_0 and angular frequency ω, the one-dimensional AREF between parallel electrodes is antisymmetric with respect to the midplane.[1] Depending on the applied frequency, electrolyte type, and electrode spacing, AREF may change sign several times within the liquid.[2] However, it remains identically zero at the midplane and at the electrodes. Note that the antisymmetric shape indicates that the AREF does not change upon swapping the powered and the grounded electrodes, or introducing any time/phase lag to the applied potential.

We demonstrate here that the aforementioned characteristics of AREF are not necessarily hold for other classes of zero-time-average (no dc bias) periodic potentials. Specifically we focus on two-mode potentials, and show that for certain conditions, the induced AREF is dissymmetric (as different from antisymmetric).

7.2 ELECTROKINETIC MODEL

Consider a dilute binary 1–1 electrolyte confined by two parallel, planar, electrodes spaced by a gap 2ℓ. The starting point in theory is the Poisson–Nernst–Planck (PNP) model. The Poisson equation relates the free charge density to the electric field gradient,

$$-\varepsilon\frac{\partial^2\phi}{\partial x^2}=\rho=e(n_+-n_-), \tag{7.1}$$

while the transport of ions is governed by the Nernst–Planck equations,

$$\frac{\partial n_\pm}{\partial t}=D_\pm\frac{\partial^2 n_\pm}{\partial x^2}\pm\frac{D_\pm}{\phi_T}\frac{\partial}{\partial x}\left(n_\pm\frac{\partial\phi}{\partial x}\right). \tag{7.2}$$

Here the symbols denote permittivity of the electrolyte, ε; electric potential, ϕ; free charge number density, ρ; charge of a proton, e; thermal potential, ϕ_T; ion number concentration, $n_\pm$; diffusivity, $D_\pm$; location with respect to the midplane, x; and time, t.

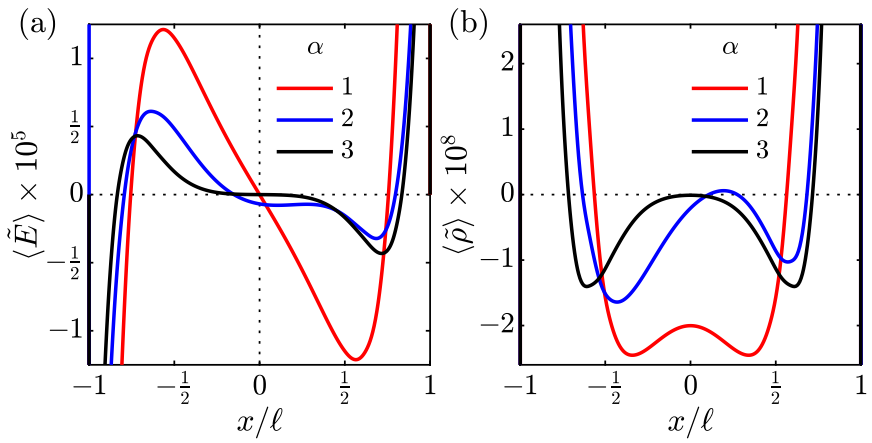

Figure 7.1: Representative numerical solutions to the AREF $\langle\tilde{E}\rangle = \langle E\rangle/(\kappa\phi_T)$ (a) and time-average free charge density $\langle\tilde{\rho}\rangle = \langle\rho\rangle/n^\infty$ (b) for two-mode applied potentials ($\phi(t,-\ell) = \phi_0\left[\sin(\omega t) + \sin(\alpha\omega t)\right]$, $\phi(\ell,t) = 0$) at the micron scale. Parameters: $\phi_0 = 10\phi_T$, $f = \omega/(2\pi) = 50$ Hz, $2\ell = 20$ μm, $D_+ = 10^{-9}$ m^2/s, $D_-/D_+ = 2$, $c^\infty = 1$ mM.

Initially, the ions are uniformly distributed $n_\pm(x,0) = n^\infty$ (the bulk electrolyte concentration), and the electric potential is zero everywhere $\phi(x,0) = 0$. Note that for simplicity, we neglect the intrinsic zeta potential of the electrodes. At $x = \pm\ell$ (i.e., the electrodes), we set the flux of ions equal to zero (i.e., no electrochemistry). And, a two-mode potential $\psi(t) = \phi_0\left[\sin(\omega t) + \sin(\alpha\omega t)\right]$ is applied on the electrodes as

$$\phi(-\ell,t) = \psi(t), \quad \phi(\ell,t) = 0. \tag{7.3}$$

7.3 RESULTS, DISCUSSION, AND IMPLICATIONS

The system of equations is solved numerically following the algorithm reported by Hashemi Amrei et al.[1] We focus primarily on the time-average of the harmonic solutions defined by

$$\langle\chi\rangle = \frac{1}{2\tau}\int_t^{t+2\tau}\chi dt, \quad 2\tau = \frac{2\pi}{\omega\,\gcd(1,\alpha)}, \tag{7.4}$$

where 2τ is the period of the applied potential/harmonic solution, and $\gcd(1,\alpha)$ is the greatest common divisor of 1 and α. Representative solutions to the AREF (time-average electric field) are provided in Fig. 7.1(a) at the micron scale (i.e., several microns away from the electrodes). The electric field is scaled by $\kappa\phi_T$. When $\alpha = 1$, the applied potential is a single-mode sinusoid which yields the antisymmetric AREF (Fig. 7.1(a), red curve). The case of $\alpha = 2$ reveals a surprising phenomena: the shape of the AREF becomes dissymmetric with a nonzero value even at the midplane (Fig. 7.1(a), blue curve). Further complicating matters, for $\alpha = 3$, the AREF is again perfectly antisymmetric (Fig. 7.1(a), black curve). Therefore, it appears that depending on α, the induced AREF can be either antisymmetric with a zero value at the midplane or dissymmetric.

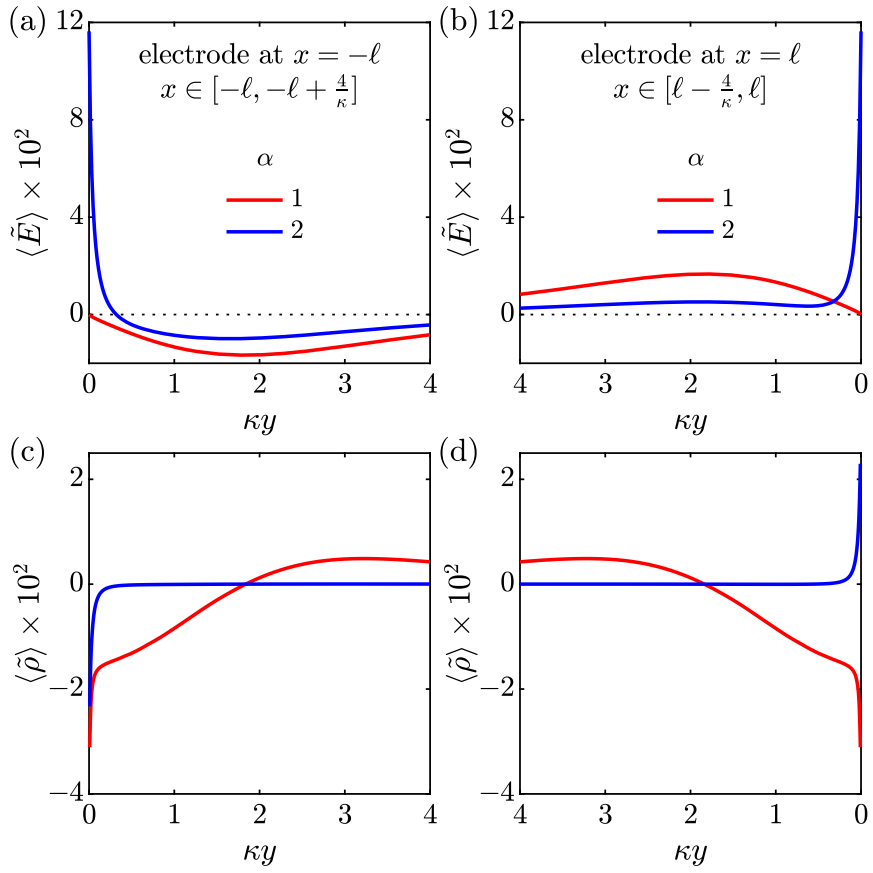

Figure 7.2: Representative numerical solutions to the AREF $\langle \tilde{E} \rangle = \langle E \rangle / (\kappa \phi_T)$ (a, b) and time-average free charge density $\langle \tilde{\rho} \rangle = \langle \rho \rangle / n^\infty$ (c, d) for two-mode applied potentials ($\phi(t, -\ell) = \phi_0 [\sin(\omega t) + \sin(\alpha \omega t)]$, $\phi(\ell, t) = 0$) at the Debye scale. For visualization purposes, the $\langle \tilde{\rho} \rangle$ data for $\alpha = 2$ in (c, d) are divided by 100. The spatial variable y denotes the distance from the corresponding electrode. Parameters: $\phi_0 = 10\phi_T$, $f = \omega/(2\pi) = 50$ Hz, $2\ell = 20$ μm, $D_+ = 10^{-9}$ m^2/s, $D_-/D_+ = 2$, $c^\infty = 1$ mM.

The corresponding spatial distributions of the time-average free charge density $\langle \rho \rangle$ are illustrated in Fig. 7.1(b) for different α values. Consistent with the AREF distributions in Fig. 7.1(a), the $\langle \rho \rangle$ is spatially even for $\alpha = 1$ and 3, but deviates and takes a dissymmetric shape for $\alpha = 2$.

The behavior becomes more complicated at the Debye scale (i.e., up to a few Debye lengths away from the electrodes). Fig. 7.2(a) and (b) show the AREF within 4 Debye lengths away from the electrodes for $\alpha = 1$ and 2. When $\alpha = 1$ (i.e., a single-mode sinusoidal potential), AREF is zero at the electrodes, which is a direct result of the antisymmetric shape of the AREF and the total charge neutrality. The former can be clarified by a parity analysis of the second-order perturbation solution to the problem (cf. Sec. D.1). The total charge neutrality on the other hand enforces the AREF at one electrode to be equal to that on the other electrode (i.e., $\langle E \rangle_{-\ell} = \langle E \rangle_\ell = K$). But, for AREF to be antisymmetric K has to be zero.

When $\alpha = 2$, an astonishingly large AREF is induced on the electrodes (≈ 4 orders of magnitude larger than the AREF at the micron scale). We note however that the total charge neutrality is still hold. The mere observation of a nonzero AREF at the electrodes for $\alpha = 2$ is consistent

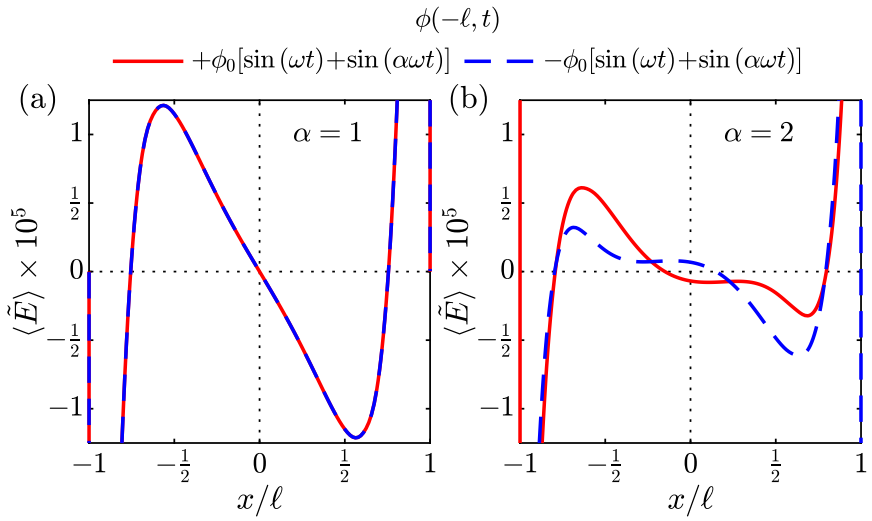

Figure 7.3: Flipping the sign of the applied potential at $x=-\ell$ for $\alpha=1$ (a) and 2 (b). Parameters: $\phi_0=10\phi_T$, $f=\omega/(2\pi)=50$ Hz, $2\ell=20$ μm, $D_+=10^{-9}$ m^2/s, $D_-/D_+=2$, $c^\infty=1$ mM.

with the dissymmetric shape of AREF at the micron scale: the integral of AREF over the entire domain has to be zero, i.e., $\int_{-\ell}^{\ell}\langle E\rangle dx=\langle\phi\rangle_{-\ell}-\langle\phi\rangle_{\ell}=0$. In other words, the nonzero AREF at the electrodes and the dissymmetric shape of the AREF at the micron scale are interrelated. A qualitatively consistent behavior is observed for the distribution of ρ (Fig. 7.2(c) and (d)). The induced $\langle\rho\rangle$ on the two electrodes are the same for $\alpha=1$. However, when $\alpha=2$, there is a sign flip in the time-average free charge densities induced at the two electrodes ($\langle\rho\rangle_{-\ell}=-\langle\rho\rangle_{\ell}$).

We now ask what happens if we flip the sign of the applied potential ($-\psi(t)$ instead of $\psi(t)$). For $\alpha=1$ (antisymmetric AREF), the curves of the induced AREF by $\psi(t)$ and $-\psi(t)$ potentials are superimposed (Fig. 7.3(a)). However, flipping the sign of the potential when $\alpha=2$ (dissymmetric AREF) yields a mirrored version of the AREF with respect to the midplane (Fig. 7.3(b)). It is worth mentioning that the sum of the solid red ($\psi(t)$) and dashed blue ($-\psi(t)$) curves in Fig. 7.3(b) is antisymmetric and zero at the midplane. In other words, the dissymmetric components of the AREFs due to $\psi(t)$ and $-\psi(t)$ potentials cancel each other.

We provide an explanation for this numerical observation using symmetry arguments. Note that the field-induced ion motion depends only on the potential gradient (not the potential itself). Therefore, one can show that flipping the sign of a periodic, time-varying, potential $\psi(t)$ at $x=-\ell$ is equivalent to swapping the powered and grounded electrodes (by adding the potential $\psi(t)$ to the both electrodes). In other words, $\{\phi(-\ell,t)=-\psi(t),\phi(\ell,t)=0\}\equiv\{\phi(-\ell,t)=0,\phi(\ell,t)=\psi(t)\}$. Now, a simple change of variable $x\to-x$ clarifies that if the potential $\psi(t)$ yields the electric field $E(x,t)$, the potential $-\psi(t)$ would yield the mirrored version, $-E(-x,t)$. Of course, the same statement stands for the time-average electric field, AREF (cf. Fig. 7.3).

Focusing on the midplane ($x=0$), one can write that the functional $E(0,t)=\epsilon(t)=f(\psi,t)$ is odd in ψ. In other words, if $\epsilon(t)$ is the induced electric field at the midplane due to the potential $\psi(t)$, $-\epsilon(t)$ would be that due to the potential $-\psi(t)$. Now consider antiperiodic potentials, i.e.,

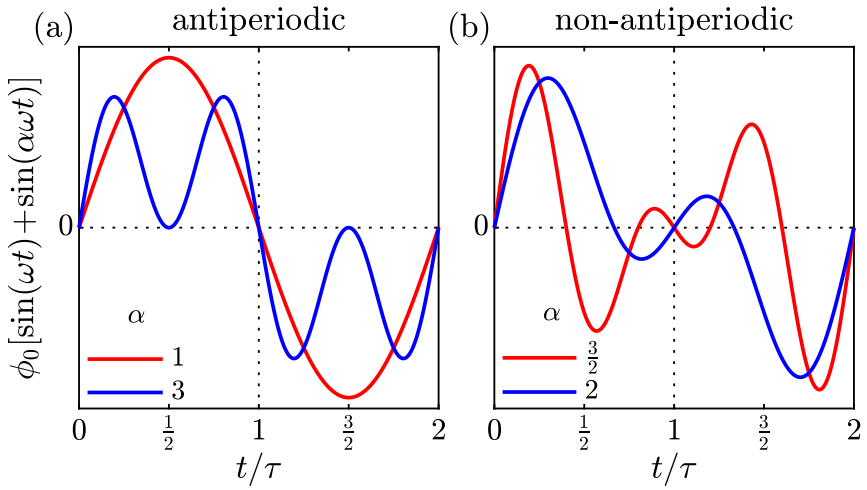

Figure 7.4: Examples of antiperiodic (a) and non-antiperiodic (b) two-mode applied potentials $\phi_0\,[\sin(\omega t)+\sin(\alpha\omega t)]$.

$\psi(t+\tau)=-\psi(t)$. We prove that $\langle\epsilon\rangle$ (i.e., AREF at the midplane) has to be zero for antiperiodic potentials:

$$\epsilon(t+\tau)=f(\psi,t+\tau)=f(-\psi,t)=-\epsilon(t)\Rightarrow\epsilon(t+\tau)=-\epsilon(t).$$

Then, taking the time-average of the latter equality yields $\langle\epsilon\rangle=-\langle\epsilon\rangle$, indicating $\langle\epsilon\rangle=0$. It is worth mentioning that the above argument is general and holds for any antiperiodic potential $\psi(t)$. It appears that for such potentials the zero-frequency components of the induced electric field cancel each other at the midplane, yielding an antisymmetric AREF. However, they do not necessarily cancel out when the excitation is non-antiperiodic. It is important to note that an antisymmetric AREF would be superimposed to its mirrored version (cf. Fig. 7.3(a)), and hence, is insensitive to swapping the powered and the grounded electrodes. But, if the induced AREF is dissymmetric, swapping the electrodes alters the system behavior; notably, it changes the AREF direction (cf. Fig. 7.3(b)).

Fig. 7.4 illustrates several examples of the antiperiodic and non-antiperiodic two-mode potentials. One can show that $\psi(t)$ is antiperiodic if α, in its simplified fractional form, can be expressed as {odd integer}/{odd integer} (e.g., $\alpha=1,\frac{5}{3},3,5,\dots$). Otherwise, the two-mode potential is non-antiperiodic (e.g., $\alpha=2,\frac{4}{3},\frac{3}{2},4,\dots$). (Please see Sec. D.2 for proof.) Our numerical results for a wide range of α values corroborate our theory. For all antiperiodic potentials tested, the AREF is zero at the midplane, and is antisymmetric in space (e.g., $\alpha=1$ and 3 in Fig. 7.1(a)). Furthermore, a dissymmetric AREF with a nonzero value at the midplane is induced for non-antiperiodic potentials (e.g., $\alpha=2$ in Fig. 7.1(a)). It should be noted though that the degree by which the AREF becomes dissymmetric is a complicated function of α. However, regardless of the system parameters, $\alpha=2$ appears to induce the most significant dissymmetric behavior.

A mathematical analysis of the high-order perturbation solutions to the PNP equations suggests that the dissymmetric AREF is a consequence of the odd-order $(3,5,\dots)$ contributions. Indeed, the second-order solution derived by Hashemi Amrei et al.[5] predicts that, regardless of α, the induced

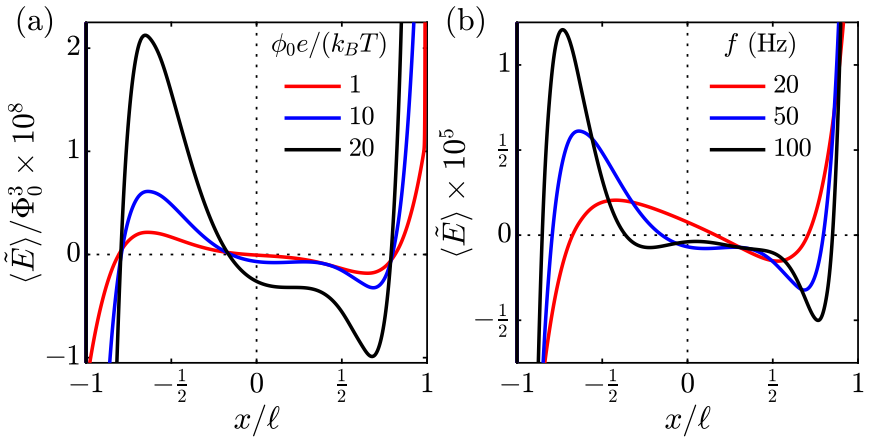

Figure 7.5: Effects of the two-mode potential amplitude (a) and frequency (b) on the dissymmetric AREF. For visualization purposes the data in (a) are scaled by Φ_0^3 with $\Phi_0 = \phi_0/\phi_T$. Parameters: $\phi_0 = 10\phi_T$ (b), $f = \omega/(2\pi) = 50$ Hz (a), $\alpha = 2$, $2\ell = 20$ μm, $D_+ = 10^{-9}$ m^2/s, $D_-/D_+ = 2$, $c^\infty = 1$ mM.

AREF under two-mode polarization is simply the superposition of the AREF due to each mode (ω and $\alpha\omega$) and is, therefore, antisymmetric. The third-order solution however, provides some insights, indicating a dissymmetric AREF for $\alpha = 2$. However, the third-order solution is zero for all other α values, including the ones for which we expect a dissymmetric behavior. We argue that the numerically obtained dissymmetric AREF for other α values is a contribution of yet higher odd-order solutions (e.g., $5, 7, \dots$). (Please see Sec. D.1 for details.)

The effect of the two-mode potential amplitude, ϕ_0, on the induced AREF is evaluated in Fig. 7.5(a) for $\alpha = 2$. As a high-order nonlinear phenomena, the dissymmetry rapidly grows with the amplitude. At sufficiently low amplitudes, the dissymmetry disappears and the AREF is almost antisymmetric (cf. Fig. 7.5(a), red curve). The effect of the applied frequency $f = \omega/(2\pi)$ is more complicated. Similar to the antisymmetric AREF, increasing the frequency amplifies the AREF peak magnitude at the micron scale and shifts the peak location toward the electrodes.[1,2] Furthermore, we note that the dissymmetry significantly intensifies with frequency. More importantly, the sign of AREF at the midplane is changed upon changing the frequency. It might be due to the established finding that the spatial oscillation of AREF (its shape) is very sensitive to frequency.[1,2]

Following Hashemi Amrei et al.,[1] we have performed several consistency checks on the numerical results, such as the feasibility of the calculated instantaneous ion concentrations, electric field, and induced zeta potential at the electrode surface. Furthermore, the numerical solution converges and the total mass is conserved. We have inspected the total charge neutrality by $\int_{-\ell}^{\ell} \partial^2\langle\phi\rangle/\partial x^2 dx = 0$ and, alternatively, by $\langle E\rangle_{-\ell} = \langle E\rangle_{\ell}$. The condition $\int_{-\ell}^{\ell}\langle E\rangle = 0$ is also checked to ensure that the numerical solution satisfies the boundary conditions. A concern in dynamic solution of the PNP equations under oscillatory polarization is that if the quasi-steady state conditions (harmonic solution) is achieved. We have accurately examined the present numerical results regarding the harmonic behavior.

We emphasize that our theory is not limited to any specific potential wave form. Any zero-time-

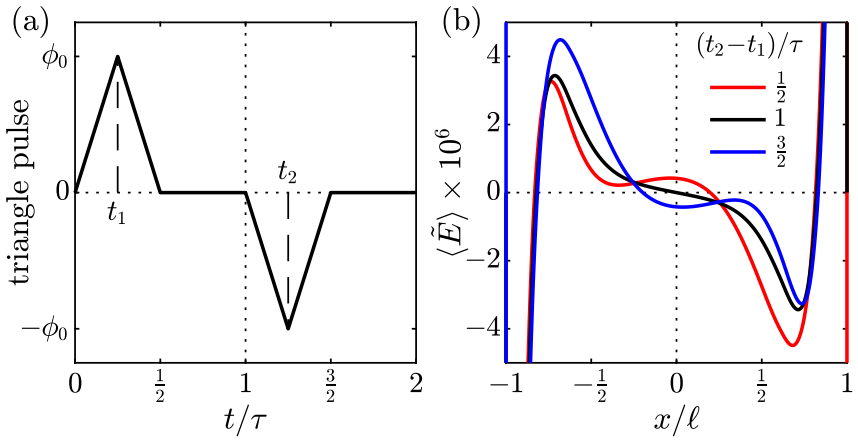

Figure 7.6: Dissymmetric AREF due to a zero-time-average triangular pulse potential applied at $x = -\ell$. (a) Positive (at $t = t_1$) and negative (at $t = t_2$) triangular pulses of width $\frac{1}{2}\tau$ and amplitude ϕ_0. (b) The corresponding induced AREF for different values of $(t_2 - t_1)/\tau$. Parameters: $\phi_0 = 20\phi_T$, $1/(2\tau) = 50$ Hz, $2\ell = 20$ μm, $D_+ = 10^{-9}$ m^2/s, $D_-/D_+ = 2$, $c^\infty = 1$ mM.

average (unbiased), antiperiodic, potential yields an antisymmetric AREF, while non-antiperiodic potentials can induce a dissymmetric AREF. An important implication is then that for a given applied potential $\psi(t)$ in the first half of the period $t \in [0, \tau]$, there is a unique antiperiodic potential that occurs by setting $\psi(t+\tau) = -\psi(t)$. But an infinite number of non-antiperiodic potentials can be constructed. We demonstrate this argument for a triangular pulse of period 2τ, illustrated in Fig. 7.6. Two pulses of amplitude ϕ_0 and width $\frac{1}{2}\tau$ are applied at $t_1 = \frac{1}{4}\tau$ and $\frac{3}{4}\tau \leqslant t_2 \leqslant \frac{7}{4}\tau$. We keep t_1 fixed and vary t_2 to cover all possible cases. The induced AREFs are shown in Fig. 7.6(b) for different $t_2 - t_1$ values. The AREF is antisymmetric only if $t_2 - t_1 = \tau$ for which the potential in the second half period becomes the negative of that in the first half (Fig. 7.6(b), black curve). All other constructions yield a dissymmetric AREF. It is interesting to note that the cases $t_2 - t_1 = \frac{1}{2}\tau$ (consecutive pulses in the first half) and $t_2 - t_1 = \frac{3}{2}\tau$ (maximally apart pulses) provide the maximum dissymmetry and are mirrored. A simple time shift $t \to \frac{3}{2}\tau$ shows that the condition of maximally apart pulses is actually the negative version of the back-to-back pulses, and therefore yields the mirrored version of the AREF (cf. Fig. 7.3(b)).

The dissymmetric AREF can tremendously change the design of electrokinetic systems and their applications. It was recently shown at length that the AREF-induced electrophoretic forces are several orders of magnitude larger that gravitational and colloidal forces.[1,3,4] Researchers can therefore use the dissymmetric AREF to design electrochemical cells that selectively (to some extent) separate charged colloidal particles or bioparticles near the powered or the grounded electrodes. Moreover, the sole physical implications of the dissymmetric AREF opens a new chapter for the researchers in the electrokinetic community. More research is needed; the present study should serve as a strong indication of the existence of the previously unknown dissymmetric AREF.

Chapter 8

Concluding Remarks and Future Work

8.1 MAIN FINDINGS

(i) *Asymmetric Rectified Electric Field (AREF)*

We discovered a previously unknown phenomena in nonlinear electrokinetics. A sinusoidal electric potential induces a steady field within liquids, which we refer to as asymmetric rectified electric field (AREF). The discovery of AREF broadly impacts the future of electrokinetics, and offers explanations for several unresolved mysteries regarding the behavior of charged objects and electrically-induced fluid flows in response to ac potentials.

(ii) *Ratchets in Unbiased Nonlinear Systems*

We demonstrated the existence of externally induced ratchets in a variety of spatially symmetric macroscopic systems. Our study generalizes the current understanding of the ratchets to different fields of physics, and provides a readily accessible approach of investigating the ratchet dynamics.

8.2 FUTURE WORK SUGGESTIONS

8.2.1 Numerical & perturbation solutions to the 2-D PNP equations

As mentioned, the 1-dimensional AREF provides qualitative explanations for several open questions in ACEO and EHD. A possible future project is to develop a 2-dimensional numerical solution to the PNP model, coupled with the momentum equations, to 'quantitatively' investigate these problems. The algorithm will be based on operator splitting, mesh refinement, and multigrid.[1] The main challenges are the computation time, contribution of the fluid flows, and the inevitable presence of irregular boundary conditions. The C++ Chombo parallel computing library (Software for Adaptive Solutions of Partial Differential Equations)[108,109] allows a relatively straightforward treatment

of the irregular boundary conditions. An alternative approach would be to use full approximation scheme to directly solve the nonlinear system of equations (instead of operator splitting and multigrid). If successful, it tremendously enhances the computation time. A quantitative comparison of the numerical results and the extensively available experimental data will be a significant contribution to the electrokinetics. Of particular importance is to examine if the obtained solutions accurately predict the effects of the applied frequency and the electrolyte type.

Another idea is to develop a second-order perturbation solution that reasonably approximates the 2-dimensional ACEO and EHD systems in some range of the parameter space. With ACEO, one can imagine a 2-dimensional system with regular boundary conditions, which should be solvable analytically via a perturbation expansion. To avoid the irregular boundaries in EHD, bispherical coordinates will be used.

8.2.2 Fast electrophoretic translation of charged colloids via AREF

Electrophoresis refers to the translation of charged particles in response to electric fields, with extensive applications in separation and analysis of macromolecules and colloids. Consider a randomly located cluster of charged colloids immersed in an electrolyte, and confined between parallel horizontal electrodes. Researchers often need to move the colloids to a certain location for further analysis, e.g., in EHD, the colloids should be placed near the lower electrode. Traditionally, researchers wait (∼hours) for the colloids to sediment by gravity. Another idea would be to use a dc field to electrophoretically move the colloids. But charged colloids tend to adhere to the oppositely charged electrode under dc polarization. AREF can be used instead. Unlike normal dc fields, AREF changes direction spatially, and either repels the charged colloids from the electrodes or traps them in a fixed point. (Fixed points are the stable heights, created by a balance between the AREF-induced electrophoretic and the gravitational forces.) For a given set of colloids in an electrolyte, the number of fixed points depends on the frequency of the applied potential. Therefore, one can conceive an approach of moving the fixed points up and and down in space by changing the frequency. Considering the available analytical approximation to the 1-dimensional AREF,[5] I believe that the idea is promising and worth pursuing. Once developed mathematically, the method can be tested by experimental collaborates.

8.2.3 Physics behind the non-antiperiodic excitations & implications

The discussion in Chapter 6 and Chapter 7 lefts a seemingly simple question unanswered: what determines the direction of the movement? Our theory explains why the time-average solution is zero for antiperiodic excitations. But it does not provide sufficient insights on what governs the observed net responses for the non-antiperiodic excitations. A proper answer would rely on an analytical analysis of the corresponding differential equations. Additionally, it would be interesting to further generalize this theory to other physical systems, and investigate the potentially valuable implications.

Appendix A

Miscellaneous Supplemental Material

This appendix serves as a supplemental material for Chapter 2.

A.1 TWO-ION MODEL

For a 1-1 electrolyte, the perturbation to the electric field at $z = z_f$ (restricting attention to positions such that $z_f > \mid z_i \mid$; $i = +/-$) is, by Coulomb's law,

$$\epsilon(z_f, t) = \frac{\alpha}{{z_f}^2}\left[\frac{1}{(1 - z_+/z_f)^2} - \frac{1}{(1 - z_-/z_f)^2}\right]. \tag{A.1}$$

One can then write the Taylor series expansion of $\epsilon(z_f, t)$, with $\ell_i \equiv z_i/z_f$, as

$$\epsilon(z_f, t) = \frac{\alpha}{{z_f}^2}\left[2\ell_+ + 3\ell_+^2 + \cdots - 2\ell_- - 3\ell_-^2 - \ldots\right]. \tag{A.2}$$

The far-field solution when $z_f \to \infty$ (i.e., $\ell_i \to 0$) is therefore

$$\epsilon(z_f, t) = \frac{2\alpha}{{z_f}^2}(\ell_+ - \ell_-). \tag{A.3}$$

For $\delta = 1$, where $\ell_+(t) = -\ell_-(t) = \ell/2$, this reduces to

$$\epsilon(z_f, t) = \frac{2\alpha\ell}{{z_f}^2}, \tag{A.4}$$

which is equivalent to the well-known electric field generated by a dipole. Regardless of the value of δ, note that the far-field solution has zero time average.

To highlight the effect of non-equal mobilities at intermediate distances, we rearrange Eq. A.2 to obtain

$$\epsilon(z_f, t) = \frac{\alpha}{{z_f}^2}\left[2(\ell_+ - \ell_-) + 3(\ell_+^2 - \ell_-^2) + 4(\ell_+^3 - \ell_-^3) + \ldots\right]. \tag{A.5}$$

Substituting the harmonic oscillators (Eq. 2.2) into Eq. A.5 yields

$$\epsilon(z_f,t)=\frac{\alpha}{{z_f}^2}\Big[2\big(\hat{\ell}_+-\hat{\ell}_-\big)\sin(\omega t)+3\big(\hat{\ell}_+^2-\hat{\ell}_-^2\big)\sin^2(\omega t)+4\big(\hat{\ell}_+^3-\hat{\ell}_-^3\big)\sin^3(\omega t)+\dots\Big], \tag{A.6}$$

where $\hat{\ell}_i=z_{i,max}/z_f$ and $z_{i,max}$ denotes the maximum amplitude of the harmonic oscillation. For equal mobilities (i.e., $\hat{\ell}_+=-\hat{\ell}_-=\hat{\ell}/2$) this simplifies to

$$\epsilon(z_f,t)=\frac{\alpha}{{z_f}^2}\Big[2\hat{\ell}\sin(\omega t)+\hat{\ell}^3\sin^3(\omega t)+\dots\Big], \tag{A.7}$$

which can be rewritten as

$$\epsilon(z_f,t)=\frac{\alpha}{{z_f}^2}\Big[2\hat{\ell}\sin(\omega t)+\frac{\hat{\ell}^3}{4}(3\sin(\omega t)-\sin(3\omega t))+\dots\Big]. \tag{A.8}$$

Therefore, for $\delta=1$, the solution has frequency components at odd multiples of the applied frequency. When $\delta\neq 1$ (i.e., $\hat{\ell}_+\neq-\hat{\ell}_-$), none of the terms cancel and both even and odd multiples of the frequency remain:

$$\begin{aligned}\epsilon(z_f,t)=\frac{\alpha}{{z_f}^2}\Big[&2\big(\hat{\ell}_+-\hat{\ell}_-\big)\sin(\omega t)+\frac{3}{2}\big(\hat{\ell}_+^2-\hat{\ell}_-^2\big)(1-\cos(2\omega t))\\&+\big(\hat{\ell}_+^3-\hat{\ell}_-^3\big)(3\sin(\omega t)-\sin(3\omega t))+\dots\Big].\end{aligned} \tag{A.9}$$

As it can be observed, Eq. A.9 includes frequency components of the form $k\omega$ for any nonnegative integer k. Moreover, the time average of Eq. A.9 is

$$\langle\epsilon(z_f,t)\rangle=\frac{3\alpha}{2{z_f}^2}\big(\hat{\ell}_+^2-\hat{\ell}_-^2\big)\propto E_0^2\big(\frac{1}{a_+^2}-\frac{1}{a_-^2}\big). \tag{A.10}$$

which is the leading term of the AREF (Eq. 2.4).

A.2 NUMERICAL SOLUTION

In this section, we first concisely describe the model and solution algorithm. Then, the solution is validated via comparison to an available approximate solution to the problem for low voltages and equal ionic mobilities.

A.2.1 Governing equations

The model includes Poisson and species continuity equations:

$$\rho^{(f)}=\sum_{i=1}eq_in_i=-\varepsilon_\infty\varepsilon_0\frac{\partial^2\phi}{\partial z^2}, \tag{A.11}$$

$$\frac{\partial n_i}{\partial t} = D_i \frac{\partial^2 n_i}{\partial z^2} + eq_i \frac{D_i}{k_B T} \frac{\partial}{\partial z}\Big(n_i \frac{\partial \phi}{\partial z}\Big), \tag{A.12}$$

subject to the following initial and boundary conditions:

$$n_i(0, z) = n_i^{\infty}, \tag{A.13a}$$

$$- D_i \Big(\frac{\partial n_i}{\partial z} + \frac{eq_i n_i}{k_B T} \frac{\partial \phi}{\partial z}\Big)_{z=0,H} = 0, \tag{A.13b}$$

$$\phi(0, z) = 0, \tag{A.13c}$$

$$\phi(t, 0) = \phi_0 \sin(\omega t), \quad \phi(t, H) = 0. \tag{A.13d}$$

The symbols stand for applied voltage, ϕ_0; applied angular velocity, ω; electrode spacing, H;free charge density, $\rho^{(f)}$; elementary charge, e; charge number, q_i; dielectric constant of the medium, ε_∞; permittivity of free space, ε_0; electric potential, ϕ; number concentration of ion, n_i; diffusivity, D_i; Boltzmann constant, k_B; absolute temperature, T; and bulk concentration of ion, n_i^{∞}.

One can rearrange Eq. A.12 as

$$\frac{\partial n_i}{\partial t} = -\frac{\partial}{\partial z}(J_D + J_e), \tag{A.14}$$

where J_D and J_e are the diffusive and electromigrative fluxes:

$$J_D = -D_i \frac{\partial n_i}{\partial z}, \tag{A.15a}$$

$$J_e = -D_i \frac{eq_i n_i}{k_B T} \frac{\partial \phi}{\partial z}. \tag{A.15b}$$

Note that the electromigrative flux is the source of nonlinearity in both the governing equations and boundary conditions.

A.2.2 Discretization

Cell-centered finite difference methods are employed to discretize the governing equations and boundary conditions. A typical minimum cell size used for the simulations is of order $\kappa^{-1}/128$ (with κ as the Debye parameter) which, for $\kappa^{-1} \approx 13$ nm, is equivalent to ≈ 0.1 nm (compared to electrode spacing which can be several hundred microns). Such a small size step restricts the time marching of the simulation. In the presence of convective terms (with a velocity of u), the Courant-Friedrichs-Lewy (CFL) number condition limits the maximum allowable time step of the numerical solution: $|u|\Delta t/h \leqslant 1$ with Δt and h as the temporal and spatial steps. The electromigration term of the species continuity equation can be written as $\frac{\partial}{\partial z}(un_i)$ with $u = \frac{eq_i D_i}{k_B T} \frac{\partial \phi}{\partial z}$ ($[u]$ = m/s), resembling a convective transport of ions. Therefore, we need to have

$$\Big|\frac{eq_i D_i}{k_B T} \frac{\partial \phi}{\partial z}\Big| \Delta t/h \leqslant 1. \tag{A.16}$$

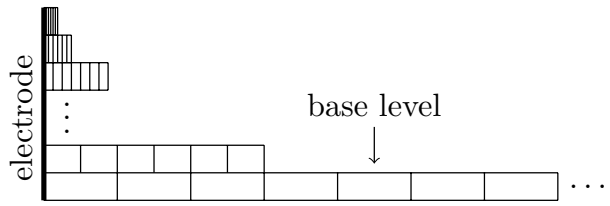

Figure A.1: Mesh refinement levels (computational levels) near an electrode surface: Base level covers the entire domain (not shown) while mesh refinement levels are added to resolve the Debye layer. Detailed explanation of the adaptive mesh refinement is provided by Martin and Cartwright.[71]

It is not practical to cover the entire domain with a uniform cell size that is small enough to resolve the Debye layer (e.g., covering 100 μm with $h \approx 0.1$ nm requires 1 million cells). To obviate the need of millions cells, we use mesh refinement near electrode surfaces. Consider a grid structure shown in Fig. A.1. There are K levels of resolution with $k = 1$ and $k = K$ denoting the finest and base levels, respectively. Hereafter, for any variable/parameter x, ${}^k x$ is the value of that variable/parameter on level k. The refinement ratio is 2, so that ${}^{k+1}h = 2 \times {}^k h$. The physical variables and source terms are defined only on cells that are not overlain by the upper finer levels.[71] To put it another way, on any level k the physical domain is specified by ${}^k\Omega - R({}^{k-1}\Omega)$ where R is the restriction operator. However, the corrections and residuals are defined on the entire of each level.[71,69,70] On each level, the spatial discretization is as follows:

$$ {}^k z_1 = {}^k h/2, \tag{A.17a} $$

$$ {}^k z_j = {}^k z_{j-1} + {}^k h. \tag{A.17b} $$

Similarly, the discretized time domain can be expressed as

$$ t^1 = 0, \tag{A.18a} $$

$$ t^p = t^{p-1} + \Delta t. \tag{A.18b} $$

In the above equations, j and p are the indices of the discretized spatial and temporal domains, respectively.

A.2.3 Operator splitting

We use operator splitting to solve the problem. For each time step, the procedure is:

(i) Solve for $[\phi]_j^p$ from Eq. A.11:

$$ -\varepsilon_\infty \varepsilon_0 \left[\frac{\partial^2 \phi}{\partial z^2}\right]_j^p = e\left[q_1 n_1 + q_2 n_2\right]_j^p, \tag{A.19a} $$

$$ [\phi]_j^1 = 0, \tag{A.19b} $$

$$ [\phi]_{z=0}^p = \phi_0 \sin(\omega t^p), \quad [\phi]_{z=H}^p = 0. \tag{A.19c} $$

(ii) Solve for $[n_i]_j^{p+1}$ from Eq. A.14:

$$\left[\frac{\partial n_i}{\partial t}\right]_j^{p+1} = \frac{\partial}{\partial z}\left[D_i\frac{\partial n_i}{\partial z} + un_i\right]_j^{p+1}, \tag{A.20a}$$

$$[n_i]_j^1 = n_i^\infty, \tag{A.20b}$$

$$\left[D_i\frac{\partial n_i}{\partial z} + un_i\right]_{z=0,H}^{p+1} = 0, \tag{A.20c}$$

where u is given from step (i).

Our Poisson solver is based on the algorithm of Martin and Cartwright.[71] With some changes, a similar algorithm is devised to solve the species continuity equation. The main difference of the algorithm is the inclusion of the nonlinear electromigration term. Neither stability nor the rate of convergence was improved by upwinding, so we use central differences. To ensure solution stability, the CFL number is calculated prior to step (ii). While the condition is not met, we set $\Delta t = \Delta t/2$ to find a $\Delta t = (\Delta t)_c$ that satisfies the condition. Then step (ii) breaks down into $\Delta t/(\Delta t)_c$ substeps to reach the time t^{p+1}.

A.2.4 Harmonic solution

Besides the above-mentioned challenges, achieving a harmonic solution by solving dynamical equations is recognized as a computational challenge.[29] The simulation time t_f should be long enough for the ions to transfer between the electrodes back and forth in order to reach equilibrium. The ions transfer with diffusive and electromigrative mechanisms with the corresponding time scales of $\tau_i^D = H^2/D_i$ and $\tau_i^e = \tau_i^D/(|q_i|\phi_0 e/(k_B T))$. Therefore, in order to ensure the equilibrium conditions we need to have $t_f \gg \max[\tau_i^D, \tau_i^e]$. The time scale of the applied potential is also $\tau^{AC} = 1/f$ which is, for the range of parameters used in this study, far less than τ_i^D and τ_i^e. Therefore, the number of AC cycles should be $n_{AC} \gg \max[\tau_i^D, \tau_i^e]/\tau^{AC}$. For example, consider a case of NaOH electrolyte with $D_+ = 1.3 \times 10^{-9}$ m^2/s and $D_- = 5.3 \times 10^{-9}$ m^2/s, electrode spacing of $H = 50$ μm, and applied potential of $\phi_0 = 5k_BT/e$ and $f = 100$ Hz, the times scales are $\tau_+^D = 1.87$ s, $\tau_-^D = 0.48$ s, $\tau_+^e = 0.37$ s, $\tau_-^e = 0.09$ s, and $\tau^{AC} = 0.01$ s. Here we need $\gg \max[\tau_i^D, \tau_i^e]/\tau^{AC} \approx 187$ AC cycles to achieve the harmonic solution. The relative difference between two consecutive cycles is:

$$\frac{\|\phi^c - \phi^{c-1}\|}{\|\phi^c\|}, \tag{A.21}$$

where superscript c denotes the cycle number and the norms are defined as

$$\|\phi^c\| = \frac{1}{H}\int_0^H |\langle\phi\rangle^c| \, dz, \tag{A.22a}$$

$$\|\phi^c - \phi^{c-1}\| = \frac{1}{H}\int_0^H |\langle\phi\rangle^c - \langle\phi\rangle^{c-1}| \, dz. \tag{A.22b}$$

We terminate the calculations when the relative difference drops below 10^{-6}. It is heuristically found that $n_{AC} \sim \max[\tau_i^D, \tau_i^e]/\tau^{AC}$ suffices to reach this tolerance and the equilibrium condition.

A.2.5 Validation

To validate the numerical solution let us consider an available analytical solution to the linearized problem for low voltages and equal mobilities derived by Hollingsworth and Saville.[25] For equal mobilities, the numerical solution is expected to converge to the analytical solution at low voltages. We define an integral norm as

$$\|\phi_N - \phi_A\| = \frac{1}{\tau H} \int_0^{\tau} \int_0^{H} |\phi_N(t,z) - \phi_A(t,z)| dz dt, \tag{A.23}$$

where the symbols stand for numerical solution, ϕ_N; analytical solution, ϕ_A; period of AC field, τ; and electrode spacing, H. Fig. A.2(a) shows the norm for different applied voltages. The numerical solution to the nonlinear problem approaches the approximate analytical solution in the asymptotic region of low voltages and equal mobilities.

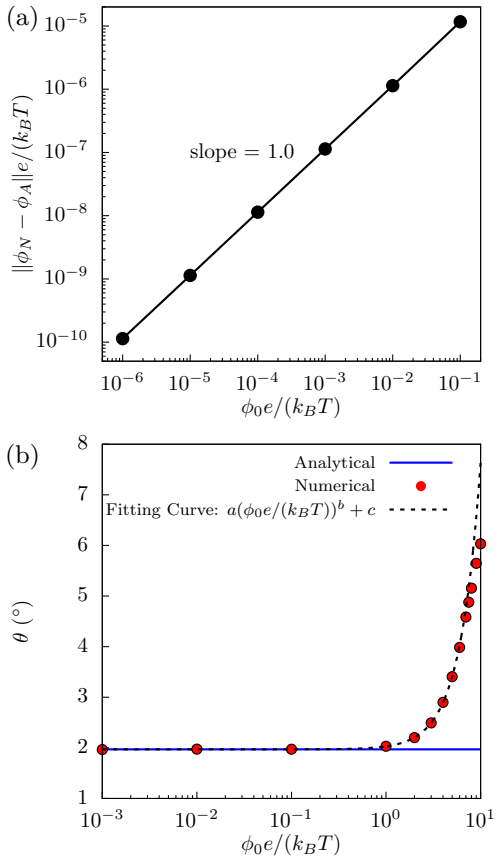

Figure A.2: Validation of the numerical solution: (a) $\|\phi_N - \phi_A\|$ versus the applied potential. (b) Calculated phase angles of the numerical and analytical solutions at $z = 1$ μm versus the applied potential. Parameters: $f = 5000$ Hz (a) and 50 Hz (b), $H = 14\kappa^{-1}$ (a) and 25 μm (b), $D_+ = D_- = 1.3 \times 10^{-9}$ m^2/s (a) and 1×10^{-9} m^2/s, $c_\infty = 1$ mM.

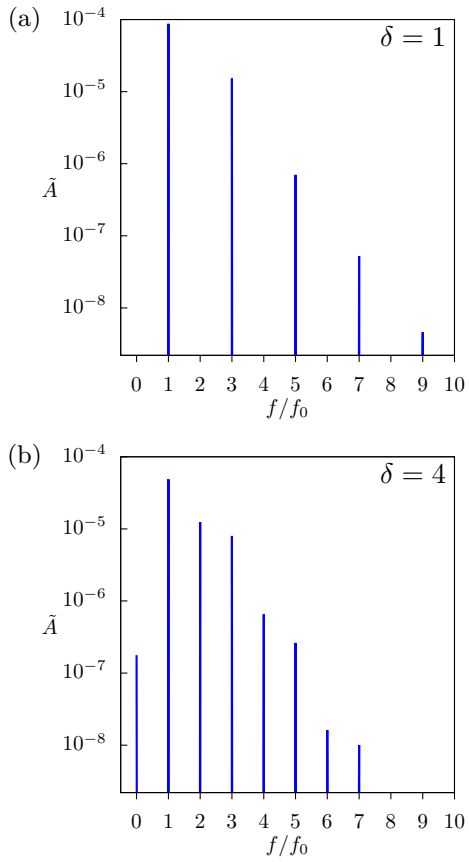

Figure A.3: FFT analysis of the harmonic electric field solutions for $\delta = 1$ (a) and $\delta = 4$ (b): numerical solution to the problem suggest the same frequency components as that of the two-ion model. Dimensionless amplitude of the frequency components ($\tilde{A} = Ae\kappa^{-1}/(k_BT)$) is sketched versus normalized frequency (f/f_0 with f_0 as the applied frequency). Parameters: $\phi_0 = 5k_BT/e$, $f = 50$ Hz, $H = 25$ μm, $D_+ = 1 \times 10^{-9}$ m^2/s, $c_\infty = 1$ mM.

The phase angle between the applied potential and responsive potential within the liquid is an important information obtainable from the both numerical and analytical solutions for $\delta = 1$.[47–49] Therefore, another validation of the numerical solution is performed by comparing of these calculations (Fig. A.2(b)). As it can be seen, the numerically predicted phase angle approaches that of the linearized model for low applied potentials. In those simulations presented here, the phase lag of the leading Fourier component is small ($\theta < 10^\circ$).

A.2.6 FFT analysis

Here, FFT analysis of the problem is provided in Fig. A.3. In agreement with the two-ion model, numerically obtained solutions to the full non-linear model indicate odd and integer multiples of the applied frequency for $\delta = 1$ and $\delta = 4$, respectively.

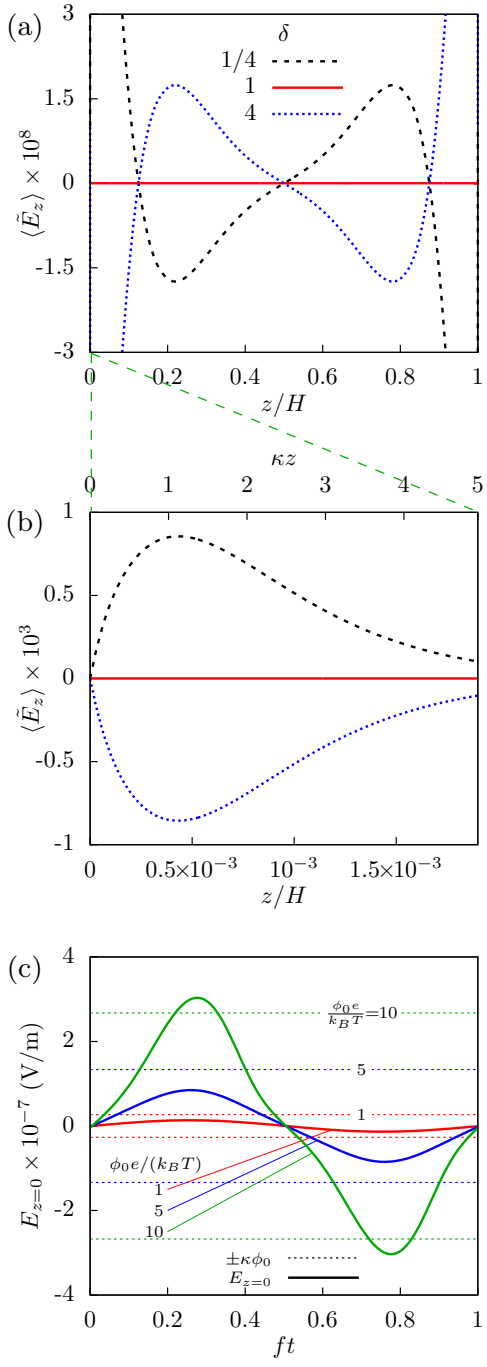

Figure A.4: Numerical results in micron (a) and Debye (b, c) scales. (a) Time average electric field in micron scale. (b) Time average electric field near the lower electrode in Debye scale. (c) Time variations of the electric field on the lower electrode surface. Parameters: $\phi_0 = 5k_BT/e$ (a, b), $f = 50$ Hz (a, b) and 100 Hz (c), $H = 25$ μm, $\delta = 4$ (c), $\min[D_+, D_-] = 1 \times 10^{-9}$ m^2/s, $c_\infty = 1$ mM.

A.2.7 Behavior of AREF near the electrode

Fig. A.4(a) shows the time average electric field for different δ values at the micron scale (similar to Fig. 2.2(c)). The magnification near the electrode, on the Debye length scale, is shown in Fig. A.4(b). The electric field $\langle \tilde{E}_z \rangle$ starts from a nonzero value (indiscernible at this scale) at the electrode ($z = 0$) for $\delta \neq 1$, then rises to an absolute maximum before decaying to the solution at the micron scale shown in Fig. A.4(a).

Fig. A.4(c) shows the instantaneous electric field a the electrode surface, $E_{z=0}$, for different applied potentials. As a consistency check, the electric field values are compared to the typical Debye layer field strength $\kappa\phi_0$. The numerically obtained electric field at all times is of the same order of magnitude as $\kappa\phi_0$. Similarly, the maximum instantaneous induced potential on the electrode surface is of the same order of magnitude as ϕ_0 ($\zeta = \sigma/(\kappa\varepsilon_\infty\varepsilon_0) = E_{z=0}/\kappa \sim \phi_0$). In other words, all of the potentials, field strengths, and ion concentrations are physical, at least over the parameter range investigated here.

Table A.1: AREF-induced electrophoresis, dielectrophoresis, and electroosmosis versus other forces for micron scale colloids and electrically-driven flows. Dimensionless ratios calculated using characteristic parametric values: particle radius $a = 0.5$ μm; zeta potential of particle $\zeta = 100$ mV; electrode spacing $H = 25$ μm; applied voltage $20k_BT/e$; applied frequency 100 Hz; $\delta = 4$; $D_+ = 1 \times 10^{-9}$ m^2/s; ionic strength $c_\infty = 1$ mM; $\kappa = 1.04 \times 10^8$ m^{-1}; dipole coefficient $C_0 = 0.1$; and density difference $\Delta\rho = 50$ kg/m^3. Calculations are done at $z = 1$ μm which gives $|\langle \tilde{E}_z \rangle| = 1.7 \times 10^{-4}$ (= 315 V/m) and $\tilde{E}_{pp} = 0.0095$ (= 1.8×10^4 V/m). (Please see the inset of Fig. 2.3(a).)

$\frac{\text{AREF electrophoresis}}{\text{gravitational}}$	$\frac{\varepsilon_\infty\varepsilon_0\kappa\zeta\langle E_z\rangle}{\Delta\rho g a}$	$\approx 10^5$
$\frac{\text{AREF electrophoresis}}{\text{Brownian}}$	$\frac{\varepsilon_\infty\varepsilon_0 a^3\kappa\zeta\langle E_z\rangle}{k_BT}$	$\approx 10^3$
$\frac{\text{AREF dielectrophoresis}}{\text{gravitational}}$	$\frac{\varepsilon_\infty\varepsilon_0 C_0\nabla(\langle E_z^2\rangle)}{\Delta\rho g}$	≈ 10
$\frac{\text{AREF dielectrophoresis}}{\text{Brownian}}$	$\frac{\varepsilon_\infty\varepsilon_0 C_0 a^4\nabla(\langle E_z^2\rangle)}{k_BT}$	$\approx 10^{-1}$
$\frac{\text{AREF electroosmosis}}{\text{EHD}}$	$\frac{\kappa\zeta\langle E_z\rangle}{C_0 E_{pp}^2}$	$\approx 10^3$
$\frac{\text{AREF electroosmosis}}{\text{ICEK}}$	$\frac{\zeta\langle E_z\rangle}{a E_{pp}^2}$	≈ 1

A.3 AREF-INDUCED FORCES

Table A.1 compares the scale of AREF-induced electrophoresis (F_{EP}) and dielectrophoresis (F_{DEP}) to typical forces in colloidal systems such as gravitational (F_G) and Brownian (F_B) forces given by

$$F_{EP} \sim \varepsilon_\infty\varepsilon_0\zeta\kappa\langle E_z\rangle a^2, \tag{A.24a}$$

$$F_{DEP} \sim \varepsilon_\infty\varepsilon_0 C_0 a^3\nabla(\langle E_z^2\rangle), \tag{A.24b}$$

$$F_G \sim \Delta\rho g a^3, \tag{A.24c}$$

$$F_B \sim k_B T/a. \tag{A.24d}$$

Moreover, an AREF-induced electroosmotic velocity (u_{AREF}) is compared to electrohydrodynamic (u_{EHD}) and induced charge electroosmosis (u_{ICEK}) velocity scales:

$$u_{AREF} \sim \varepsilon_\infty \varepsilon_0 \zeta \langle E_z \rangle / \mu, \tag{A.25a}$$

$$u_{EHD} \sim \varepsilon_\infty \varepsilon_0 C_0 E_{pp}^2 / (\mu\kappa), \tag{A.25b}$$

$$u_{ICEK} \sim \varepsilon_\infty \varepsilon_0 E_{pp}^2 a / \mu. \tag{A.25c}$$

The electrophoretic and dielectrophoretic forces depend on the location and these comparisons are specific to $z = 1$ μm. They can exponentially increase near the electrodes, making the force ratios much higher than reported in Table A.1.

A.4 STREAMLINES

The streamlines presented in Fig. 2.5 were obtained following the procedures presented by Ristenpart et al.,[51] Squires and Bazant,[19] and Solomentsev et al.[110] for EHD, ICEK, and AREF-induced electroosmotic flows respectively.

In this regard, EHD flow field was analytically solved in bispherical coordinates system. The parameters used in the calculations were as follows: applied field $E_{pp} = 2400$ V/m; frequency $f = 100$ Hz; Debye parameter $\kappa = 10^8$ 1/m; viscosity $\mu = 10^{-3}$ Pa $\cdot$ s; dielectric constant of the medium $\varepsilon_\infty = 78$; temperature $T = 298$ K; dipole coefficient $C_0 = 0.06$; electrode spacing $H = 250$ μm; particle radius $a = 0.5$ μm; zeta potential of the particle $\zeta = 50$ mV; and particle's height (distance between the electrode and particle surface) $h = 0.1a$. With the AREF-induced electroosmotic flow, a dimensionless time average electric field of $\langle \tilde{E}_z \rangle = 1.12 \times 10^{-5}$ was used to calculate the slip velocity on the particle surface via the Helmholtz-Smoluchowski equation (similar to Solomentsev et al.[110] where the applied DC field was responsible for the electroosmotic slip velocity). (Please see subsection A.4.1 for details.) Then linear superposition of the obtained EHD and AREF-induced electroosmotic flows resulted in the overall flow field provided in Fig. 2.5(b).

The flow field in Fig. 2.5(c) was calculated using the analytical solution to the standard problem of ICEK around a metal cylinder with a given quadrupolar slip velocity.[19] Likewise, an analytical solution was derived for the case of the AREF-induced electroosmotic flow around the cylinder. Again, summation of these two solutions yields the overall streamlines demonstrated in Fig. 2.5(d). (Please refer to Sec. B.1 for details.) The parameters were identical to those used in Fig. 2.5(a) and (b), except that applied field $E_{pp} = 5369$ V/m and cylinder radius $a = 0.5$ μm (yields $u_{AREF} = 0.1 u_{ICEK}$).

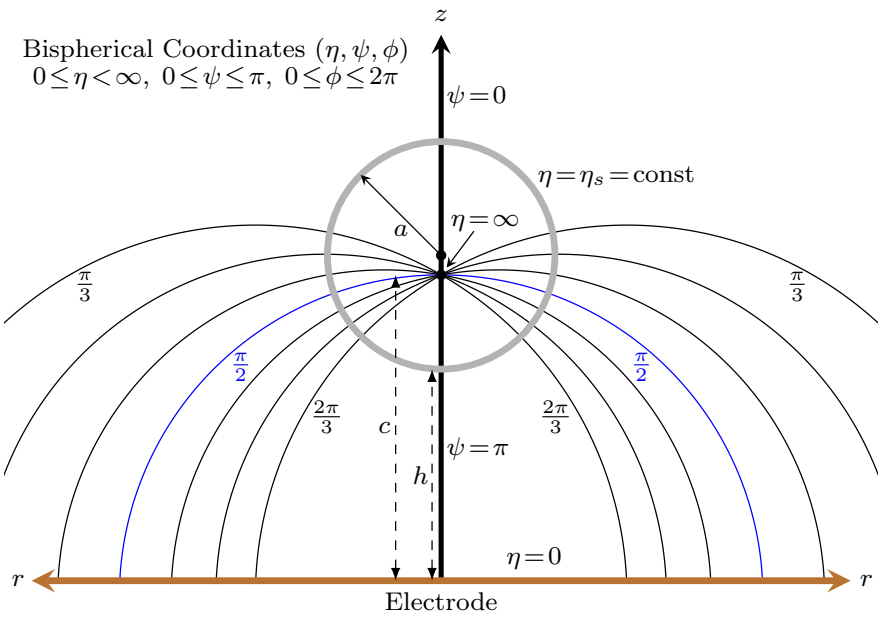

Figure A.5: Definition sketch for the bispherical coordinate system: a spherical colloid at height h above a planar electrode. Curves of constant ψ and η are governed by $r^2 + z^2 - 2cr\cot(\psi) = c^2$ and $r^2 + (z - c\coth(\eta))^2 = c^2/\sinh^2(\eta)$, respectively.

A.4.1 AREF-induced electroosmosis in bispherical coordinates

Fig. A.5 illustrates a colloid of radius a, resting at height h above a planar electrode in bispherical coordinates.[111] The problem is invariant in the ϕ direction (not shown in the schematic), and $r = \sqrt{x^2 + y^2}$ denote the redial distance from the sphere's center. Curves of constant ψ start from a focal point inside the sphere, at $z = c = \sqrt{h(h + 2a)}$, where $\eta = \infty$, and end on the electrode surface, at $r = c\sin(\psi)/(1 - \cos(\psi))$, where $\eta = 0$. Curves of constant η are circles, with $\eta = \eta_s = \sinh^{-1}(c/a)$ denoting the colloid's surface. The angle ψ direction is clockwise, with $\psi = 0$ and π referencing regions above and below the sphere, respectively. The bispherical coordinates can be expressed in terms of the Cartesian coordinates as

$$x = \frac{c\sin(\psi)\cos(\phi)}{\cosh(\eta) - \cos(\psi)}, \tag{A.26a}$$

$$y = \frac{c\sin(\psi)\sin(\phi)}{\cosh(\eta) - \cos(\psi)}, \tag{A.26b}$$

$$z = \frac{c\sinh(\eta)}{\cosh(\eta) - \cos(\psi)}. \tag{A.26c}$$

Using the expressions for x and y one can write:

$$r = \sqrt{x^2 + y^2} = \frac{c\sin(\psi)}{\cosh(\eta) - \cos(\psi)}. \tag{A.26d}$$

The general solution (in terms of the stream function $\Psi(\eta, \psi)$) to the Stokes' problem in bi-

spherical coordinates is[112]

$$\Psi = (\cosh(\eta) - \cos(\psi))^{-\frac{3}{2}} \sum_{n=1}^{\infty} W_n(\eta) G_{n+1}^{-\frac{1}{2}}(\cos(\psi)), \tag{A.27}$$

where

$$W_n(\eta) = a_n \cosh[(n-\tfrac{1}{2})\eta] + b_n \sinh[(n-\tfrac{1}{2})\eta] + c_n \cosh[(n+\tfrac{3}{2})\eta] + d_n \sinh[(n+\tfrac{3}{2})\eta], \tag{A.28}$$

and $G_{n+1}^{-\frac{1}{2}}(\cos(\psi))$ is the Gegenbauer polynomial of order $n+1$ and degree $-1/2$, given by

$$G_{n+1}^{-\frac{1}{2}}(\cos(\psi)) = \frac{P_{n-1}(\cos(\psi)) - P_{n+1}(\cos(\psi))}{2n+1}, \tag{A.29}$$

with $P_m(\cos(\psi))$ as the Legendre polynomial of order m, in terms of $\cos(\psi)$. The scalar velocity components are related to the stream function by

$$u_\eta = \frac{(\cosh(\eta) - \cos(\psi))^2}{c^2 \sin(\psi)} \frac{\partial \Psi}{\partial \psi}, \tag{A.30a}$$

$$u_\psi = -\frac{(\cosh(\eta) - \cos(\psi))^2}{c^2 \sin(\psi)} \frac{\partial \Psi}{\partial \eta}. \tag{A.30b}$$

We let $\Psi = 0$ at $\eta = 0$ (electrode surface) and $\eta = \eta_s$ (colloid surface) which yield

$$a_n = -c_n, \tag{A.31}$$

$$a_n \cosh[(n-\tfrac{1}{2})\eta_s] + b_n \sinh[(n-\tfrac{1}{2})\eta_s] + c_n \cosh[(n+\tfrac{3}{2})\eta_s] + d_n \sinh[(n+\tfrac{3}{2})\eta_s] = 0. \tag{A.32}$$

Using $u_\psi = 0 \rightarrow \partial\Psi/\partial\eta = 0$ at the electrode surface ($\eta = 0$), we find

$$d_n = -\frac{n-\frac{1}{2}}{n+\frac{3}{2}} b_n. \tag{A.33}$$

Additionally, inserting Eq. A.31 and Eq. A.33 into Eq. A.32 yields

$$b_n = \Gamma_n a_n, \tag{A.34}$$

where,

$$\Gamma_n = -\frac{\cosh[(n-\frac{1}{2})\eta_s] - \cosh[(n+\frac{3}{2})\eta_s]}{\sinh[(n-\frac{1}{2})\eta_s] - \frac{n-\frac{1}{2}}{n+\frac{3}{2}} \sinh[(n+\frac{3}{2})\eta_s]}. \tag{A.35}$$

Therefore, we have all of the coefficients in terms of a_n, i.e.,

$$b_n = \Gamma_n a_n, \quad c_n = -a_n, \quad d_n = -\frac{n-\frac{1}{2}}{n+\frac{3}{2}} \Gamma_n a_n. \tag{A.36}$$

At the colloid surface ($\eta = \eta_s$), the slip velocity is given by

$$u_t(\theta) = 2U \sin(\theta), \tag{A.37}$$

where, θ is the polar coordinate angle, and $\sin\theta = r(\eta_s, \psi)/a$. ($r(\eta_s, \psi)$ denotes the r on the colloid surface.) In terms of the bispherical coordinates, we can write

$$u_t(\psi) = 2U \frac{\frac{c}{a}\sin(\psi)}{\cosh(\eta_s) - \cos(\psi)} = 2U \frac{\sinh(\eta_s)\sin(\psi)}{\cosh(\eta_s) - \cos(\psi)}. \tag{A.38}$$

the magnitude of the slip velocity, U, is given by the Helmholtz-Smoluchowski formula:

$$U = \frac{\varepsilon_\infty \varepsilon_0 \zeta \langle E \rangle}{\mu}, \tag{A.39}$$

where $\langle E \rangle$ is evaluated at $z = h + a$ (height of the particle's center).

Using the stream function formulation, we have

$$u_t(\psi) = -\frac{(\cosh(\eta_s) - \cos(\psi))^2}{c^2 \sin(\psi)} \frac{\partial \Psi(\eta_s)}{\partial \eta} = 2U \frac{\sinh(\eta_s)\sin(\psi)}{\cosh(\eta_s) - \cos(\psi)}, \tag{A.40}$$

which leads to

$$\sum_{n=1}^{\infty} \frac{dW_n(\eta_s)}{d\eta} G_{n+1}^{-\frac{1}{2}}(\cos(\psi)) = -2c^2 U \frac{\sinh(\eta_s)\sin^2(\psi)}{(\cosh(\eta_s) - \cos(\psi))^{\frac{3}{2}}}, \tag{A.41}$$

with

$$\frac{dW_n(\eta_s)}{d\eta} = a_n \Omega_n, \tag{A.42}$$

$$\begin{aligned} \Omega_n =& (n - \tfrac{1}{2}) \sinh[(n - \tfrac{1}{2})\eta_s] + \Gamma_n (n - \tfrac{1}{2}) \cosh[(n - \tfrac{1}{2})\eta_s] \\ & -(n + \tfrac{3}{2}) \sinh[(n + \tfrac{3}{2})\eta_s] - \frac{n - \frac{1}{2}}{n + \frac{3}{2}} \Gamma_n (n + \tfrac{3}{2}) \cosh[(n + \tfrac{3}{2})\eta_s]. \end{aligned} \tag{A.43}$$

Letting $\zeta = \cos(\psi)$ and $\alpha = -2c^2 U \sinh(\eta_s)$, Eq. A.41 becomes

$$\sum_{n=1}^{\infty} a_n \Omega_n G_{n+1}^{-\frac{1}{2}}(\zeta) = \alpha \frac{1 - \zeta^2}{(\cosh(\eta_s) - \zeta)^{\frac{3}{2}}}. \tag{A.44}$$

Multiply both sides by $P_m(\zeta)$ and integrate from -1 to 1. On the left hand side, we use the orthogonality properties of the Legendre polynomials, i.e.,

$$\int_{-1}^{1} P_m(\zeta) P_n(\zeta) d\zeta = \frac{2}{2n + 1} \delta_{mn}, \tag{A.45}$$

which yields

$$\int_{-1}^{1}\sum_{n=1}^{\infty}a_n\Omega_n G_{n+1}^{-\frac{1}{2}}(\zeta)P_m(\zeta)d\zeta=\begin{cases}\frac{2a_{m+1}\Omega_{m+1}}{(2m+1)(2m+3)}-\frac{2a_{m-1}\Omega_{m-1}}{(2m-1)(2m+1)} & \text{if } m\geqslant 1;\\ \frac{2a_{m+1}\Omega_{m+1}}{(2m+1)(2m+3)} & \text{if } m=0,1.\end{cases} \tag{A.46}$$

The right hand side of Eq. A.44 multiplied by $P_m(\zeta)$ yields

$$\frac{\alpha(1-\zeta^2)P_m(\zeta)}{(\cosh(\eta_s)-\zeta)^{\frac{3}{2}}}=\frac{\alpha}{(\cosh(\eta_s)-\zeta)^{\frac{3}{2}}}\Bigg[-\frac{m(m-1)}{(2m+1)(2m-1)}P_{m-2}(\zeta)$$
$$\left(1-\frac{(m+1)^2}{(2m+1)(2m+3)}-\frac{m^2}{(2m+1)(2m-1)}\right)P_m(\zeta)-\frac{(m+1)(m+2)}{(2m+1)(2m+3)}P_{m+2}(\zeta)\Bigg] \tag{A.47}$$

where we used the Bonnet's recursion formula

$$\zeta P_m(\zeta)=\frac{(m+1)P_{m+1}(\zeta)+mP_{m-1}(\zeta)}{2m+1}. \tag{A.48}$$

Integrating Eq. A.47 from $\zeta=-1$ to 1 gives

$$\int_{-1}^{1}\frac{\alpha(1-\zeta^2)P_m(\zeta)}{(\cosh(\eta_s)-\zeta)^{\frac{3}{2}}}d\zeta=\frac{2\sqrt{2}\alpha}{\sinh(\eta_s)}\times$$
$$\Bigg[\left(1-\frac{(m+1)^2}{(2m+1)(2m+3)}-\frac{m^2}{(2m-1)(2m+1)}\right)\exp(-(m+\tfrac{1}{2})\eta_s)$$
$$-\frac{m(m-1)}{(2m-1)(2m+1)}\exp(-(m-\tfrac{3}{2})\eta_s)-\frac{(m+1)(m+2)}{(2m+1)(2m+3)}\exp(-(m+\tfrac{5}{2})\eta_s)\Bigg]. \tag{A.49}$$

Finally, equating Eq. A.46 and Eq. A.49, we find a_m, and subsequently, b_m, c_m, and d_m using Eq. A.36.

A.5 SUPPLEMENTAL RESULTS

Effects of c_∞ and D on the AREF are provided in Fig. A.6. Fig. A.6(a) demonstrates the effect of diffusivity on the results. Keeping $\delta=2$, diffusivities of the cation and anion are changed simultaneously. Our calculations show that the peak position (i.e., z_{max}) outside the Debye layer increases as the square root of the diffusivity. The bulk ionic concentration strongly affects the magnitude of dimensionless AREF field (Fig. A.6(b)), decreasing as $c_\infty^{-1.5}$, presumably because increased ionic concentrations help "screen" the electric field. Recall that $\tilde{E}=Ee\kappa^{-1}/(k_BT)$ with $\kappa^{-1}=\sqrt{\varepsilon_\infty\varepsilon_0k_BT/(e^2n_\infty)}$; this means that the dimensional AREF field is actually decreasing as c_∞^{-1}. The shape of the AREF versus position, however, is conserved across the range of concentrations tested here.

Time variations of the cation and anion concentrations are demonstrated in Fig. A.7. In the

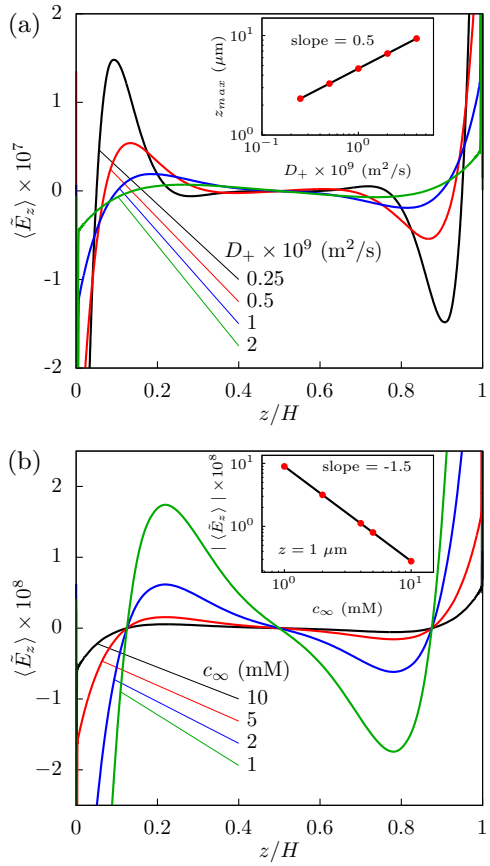

Figure A.6: Effects of diffusivity and ionic strength on the AREF. Distribution of the dimensionless time average electric field for different diffusivities (a) and ionic strengths (b). Parameters: $\phi_0 = 5k_BT/e$, $f = 50$ Hz, $H = 25$ μm (the inset of (b) is at $z/H = 0.04$ ($z = 1$ μm)), $\delta = 2$ (a) and 4 (b), $D_+ = 1 \times 10^{-9}$ m^2/s (b), $c_\infty = 1$ mM (a).

double layer ($z = \kappa^{-1}$), the positive and negative ions move back and forth approximately symmetrically, with a barely perceptible impact of the ionic mobility mismatch. Outside of the double layer, though, the behavior is more complex (Fig. A.7(b)). The distributions of positive and negative ions become increasingly synchronized further away from the electrode. Even at $z = 10\kappa^{-1}$, which is still close to the electrode surface, the time variations of the two ions is approximately synchronized. The presence of a faster moving ion ($\delta = 4$) gives rise to a large asymmetry in the oscillations, compared to the case for equal mobilities ($\delta = 1$) which is closer to a perfect sinusoid.

The small (barely perceptible) mismatches in positive and negative ion concentrations shown in Fig. A.7 give rise to a net free charge density ($\tilde{\rho}^{(f)} = (n_+ - n_-)/n_\infty$) and corresponding electric field. Except for $\delta = 1$, the difference between the concentrations of cation and anion persists several microns away from the electrode (Fig. A.8(a)). The applied voltage alters the magnitude of the free charge but does not alter the shape of the distribution (Fig. A.8(b)), consistent with Fig. 2.3(a). In contrast, the applied frequency simultaneously changes the magnitude of $\tilde{\rho}^{(f)}$ and its peak position (Fig. A.8(c), compare to Fig. 2.3(b)). Finally, increasing the ionic strength diminishes the magnitude of the free charge density while the shape is conserved (Fig. A.8(d), and

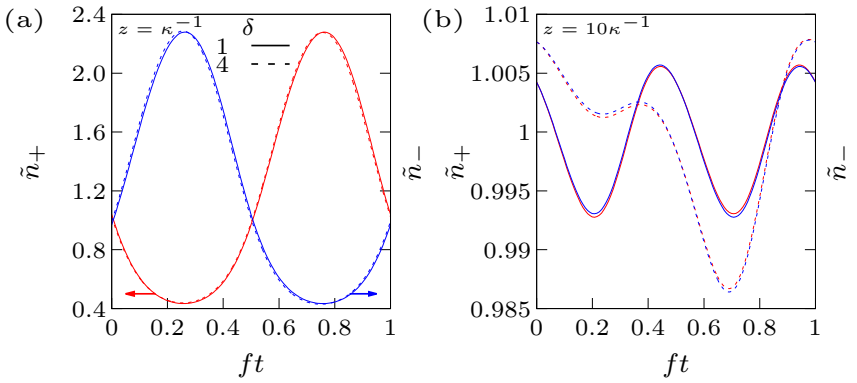

Figure A.7: Time variations of dimensionless cation and anion concentrations ($\tilde{n}_i = n_i/n_\infty$) at $z = \kappa^{-1}$ (a) and $10\kappa^{-1}$ (b). Parameters: $\phi_0 = 5k_BT/e$, $f = 50$ Hz, $H = 25$ μm, $D_+ = 1 \times 10^{-9}$ m^2/s, $c_\infty = 1$ mM.

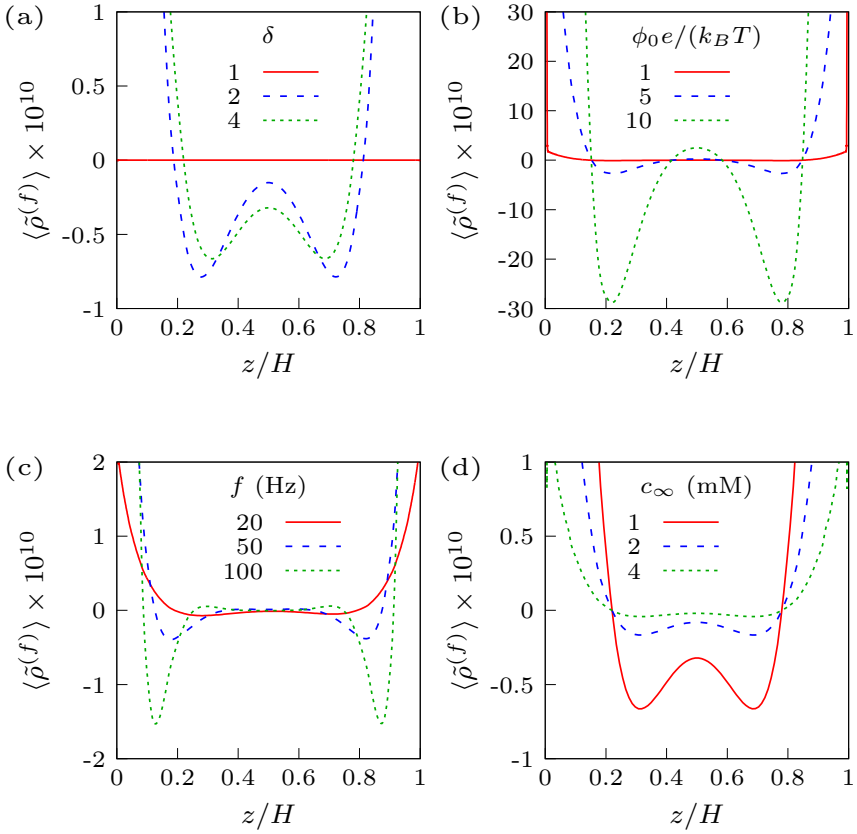

Figure A.8: Effects of ionic mobility mismatch (a), applied potential (b), applied frequency (c) and ionic strength (d) on the distribution of the dimensionless time average free charge density. Parameters: $\phi_0 = 5k_BT/e$ (a, c, d), $f = 50$ Hz (a, d) and 100 Hz (b), $H = 25$ μm (a, b, d) and 50 μm (c), $\delta = 4$ (b, c, d), $D_+ = 1 \times 10^{-9}$ m^2/s (a, b, d) and 1.3×10^{-9} m^2/s (c), $c_\infty = 1$ mM (a, b, c).

cf. Fig. A.6(b)).

The maximum instantaneous ion concentration we observe at the highest applied field strength is $(n_+ + n_-)/n_\infty \approx 4000$, which corresponds to a concentration of 4 mol/L. This value is one order of magnitude smaller than the maximum ion packing concentration described by Bazant et al.[32]

A.6 PARTICLE HEIGHT BIFURCATION

A.6.1 Hypothesis

Here we propose a hypothesis to explain the particle height bifurcation via fixed point analysis. Consider a charged colloidal particle near the electrode surface. Depending on the sign of the particle's charge and time average electric field, there would be an upward or downward force exerted on the particle. For example, a negatively charged particle in an electrolyte with $\delta > 1$ (e.g., polystyrene particle in NaOH electrolyte) would feel a force pushing it either toward or away from the electrode surface, depending on the particle location. The AREF-induced electrophoretic force can be used to find the equilibrium heights at which the charged colloidal particles can reside with zero net force. Taking into account the electrophoretic and gravitational forces, the net force becomes:

$$\langle F_z \rangle = 4\pi a^2 \varepsilon_\infty \varepsilon_0 \zeta \kappa \langle E_z \rangle - \left(\frac{4}{3}\pi a^3\right)\Delta\rho g. \tag{A.50}$$

An example of the force distribution is depicted in Fig. A.9. Intersections of the net force field and equilibrium line (i.e., net force of zero) indicate the fixed points of the problem. The stability of the fixed points alternates, so that the middle point is unstable with two neighboring stable points. Particles randomly distributed prior to application of the field will move electrophoretically in different directions depending on their initial position.

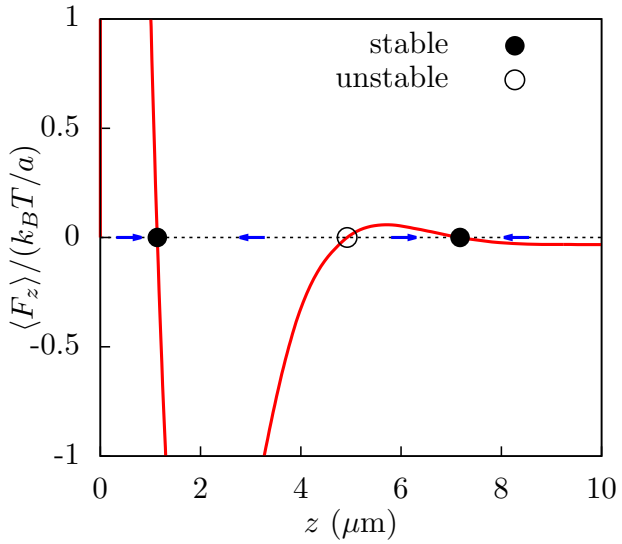

Figure A.9: Distribution of the time average force (electrophoretic and gravitational) acting on a colloidal particle. Parameters: $\phi_0 = 5k_BT/e$, $f = 500$ Hz, $H = 50$ μm, $\delta = 4$, $D_+ = 1.3 \times 10^{-9}$ m^2/s, $c_\infty = 1$ mM, $a = 0.5$ μm, $\zeta = -100$ mV, $\Delta\rho = 50$ kg/m^3.

A.6.2 Materials and methods

The experimental setup consisted of two parallel plate indium tin oxide electrodes (ITO, 5–15 Ω sheet resistance) separated by a 1 mm thick nonconductive poly(dimethylsiloxane) spacer. The

electrodes were washed and ultrasonicated for 10 minutes before experiments in RBS 35 detergent, acetone, and deionized (DI) water. 1 mM NaOH solutions were prepared (conductivity, $\sigma = 250$ μS/cm) using DI water (18.2 M$\Omega \cdot$ cm) and 2–μm diameter fluorescent sulfonated polystyrene (PS) particles were added at a volume fraction of 3×10^{-4} to the solution. The colloidal suspension was then washed three times by centrifugation and resuspension. The electrophoretic mobility measured via dynamic light scattering was -8.7 $\mu\text{m} \cdot \text{cm}/(\text{s} \cdot \text{V})$ (Malvern Zetasizer) with an ostensible zeta potential of -110 mV, approximated using the Helmholtz-Smoluchowski relation for small mobilities. Laser scanning confocal microscopy (Zeiss LSM 700) was used to measure the height of the colloids above the electrode as a function of applied voltage and frequency.

Initially, a small amount of the particle suspension was allowed to dry overnight causing particles to irreversibly adhere to the surface of the bottom electrode. Fresh particle suspension was then added to the fluid well to begin an experiment, and particles were allowed to settle by gravity for ~ 2 hours to the bottom electrode. The small fraction of remaining stuck particles were easily identified due to their lack of Brownian motion. Thus, the average center of the non-Brownian stuck particles could be used as a reference for the zero plane of the electrode. After the fresh particles were settled, a function generator was used to apply an oscillatory electric field. The fluorescent intensities of the Brownian and stuck reference particles were measured systematically as a function of vertical position (a standard z-stack), where the peak in the intensity curve from the z-stack corresponded to the average center height of the plane of particles. The absolute height of the Brownian particles could then be determined from the difference in height from the stuck reference plane. We note that the height measured in this manner represents the "average" height of the particles, averaged over many particles that fluctuate in position due to thermal motion. Finally, the electric field was removed, and the particles were allowed to disperse via Brownian motion for 10–15 min before repeating. All tests were performed in a randomized order to minimize possible systematic effects.

Appendix B

Generalized ICEK

This appendix serves as a supplemental material for Chapter 4.

B.1 VELOCITY PROFILES & STREAMLINES

Given the time average slip velocity in θ direction around the surface of a cylinder ($\langle u_\theta^s \rangle$), the time average fluid flow profile ($u_r(r,\theta)$ and $u_\theta(r,\theta)$) is derived. We consider two different cases of standard electroosmosis (EOS) and induced-charge electrokinetics (ICEK).

Standard Electroosmosis (EOS)

For a cylinder of radius a and intrinsic surface zeta potential of ζ_0 subject to a far-field $E(t) = E$, the slip velocity due to standard electroosmosis is given by

$$\langle u_\theta^s \rangle = -\frac{\varepsilon \zeta_0 E_\theta|_{r=a}}{\mu} = 2\frac{\varepsilon \zeta_0 E}{\mu} \sin(\theta) = 2U \sin(\theta). \tag{B.1}$$

We use stream function to solve this axisymmetric flow problem [113]. For a steady, creeping flow, the stream function equation is

$$\left[\frac{1}{r}\frac{\partial}{\partial r}\left(r\frac{\partial}{\partial r}\right) + \frac{1}{r^2}\frac{\partial^2}{\partial \theta^2}\right]^2 \Psi = 0, \quad u_r = \frac{1}{r}\frac{\partial \Psi}{\partial \theta}, \quad u_\theta = -\frac{\partial \Psi}{\partial r}, \tag{B.2}$$

subject to the following boundary conditions at $r = a$:

$$u_r(a,\theta) = 0, \quad u_\theta(a,\theta) = \langle u_\theta^s \rangle. \tag{B.3}$$

In addition, as $r \to \infty$ the velocities must remain finite.

We now guess a solution of the form

$$\Psi = f(r) \sin\theta. \tag{B.4}$$

On substitution into Eq. B.2 we get

$$r^4 f'''' + 2r^3 f''' - 3r^2 f'' + 3r f' - 3f = 0. \tag{B.5}$$

Inserting $f = cr^n$, we find the roots as $n = -1, 3$ and a double root for $n = 1$. The latter yields $r\ln(r)$ as another linearly independent solution. Therefore, the general solution to the stream function equation (Eq. B.2) becomes

$$\Psi = \left(\frac{c_1}{r} + c_2 r + c_3 r\ln(r) + c_4 r^3\right)\sin(\theta), \tag{B.6}$$

which subsequently yields the velocity distributions as

$$u_r = \left(\frac{c_1}{r^2} + c_2 + c_3\ln(r) + c_4 r^2\right)\cos(\theta), \quad u_\theta = \left(\frac{c_1}{r^2} - c_2 - c_3(\ln(r)+1) - 3c_4 r^2\right)\sin(\theta). \tag{B.7}$$

For velocities to remain finite far from the cylinder, c_3 and c_4 must be zero. Finally, applying the boundary conditions at $r = a$ from Eq. B.3, we find the velocity distributions and stream function as

$$u_r = \left(\frac{1}{\tilde{r}^2} - 1\right)U\cos(\theta), \tag{B.8a}$$

$$u_\theta = \left(\frac{1}{\tilde{r}^2} + 1\right)U\sin(\theta), \tag{B.8b}$$

$$\Psi = \left(\frac{1}{\tilde{r}} - \tilde{r}\right)aU\sin(\theta). \tag{B.8c}$$

where $\tilde{r} = r/a$.

Induced-Charge Electrokinetics (ICEK)

The slip velocity for ICEK is given by

$$\langle u_\theta^s\rangle = 2\frac{\varepsilon a E^2}{\mu}\sin 2\theta, \tag{B.9}$$

for a steady field $E(t) = E$, and

$$\langle u_\theta^s\rangle = \frac{\varepsilon a E^2}{\mu(\omega_0^2\tau_c^2 + 1)}\sin 2\theta, \tag{B.10}$$

for an oscillatory electric field $E(t) = E\cos(\omega_0 t + \gamma)$. For generality, we write

$$\langle u_\theta^s\rangle = 2U\sin 2\theta, \tag{B.11}$$

where the U expression depends on the electric field type.

This time we guess $\Psi = f(r)\sin(2\theta)$ and insert into Eq. B.2 to get

$$r^4 f'''' + 2r^3 f''' - 9r^2 f'' + 9r f' = 0. \tag{B.12}$$

Substituting $f = cr^n$, the roots are obtained as $n = -2, 0, 2, 4$; therefore the general solution is

$$\Psi = \left(\frac{c_1}{r^2} + c_2 + c_3 r^2 + c_4 r^4\right)\sin(2\theta). \tag{B.13}$$

The scalar velocity components are therefore

$$u_r = 2\left(\frac{c_1}{r^3} + \frac{c_2}{r} + c_3 r + c_4 r^3\right)\cos(2\theta), \quad u_\theta = \left(\frac{2c_1}{r^3} - 2c_3 r - 4c_4 r^3\right)\sin(2\theta). \tag{B.14}$$

Again, the condition of finite velocities as $r \to \infty$, eliminates c_3 and c_4 terms. Applying the boundary conditions at $r = a$ (Eq. B.3), the final forms of the velocity and stream function profiles are obtained as

$$u_r = 2\left(\frac{1-\tilde{r}^2}{\tilde{r}^3}\right)U\cos(2\theta), \tag{B.15a}$$

$$u_\theta = \frac{2}{\tilde{r}^3}U\sin(2\theta), \tag{B.15b}$$

$$\Psi = \left(\frac{1}{\tilde{r}^2} - 1\right)aU\sin(2\theta). \tag{B.15c}$$

Superposition

Now consider an electric field of the form

$$E(t) = E_0 + \sum_{j=1}^{\infty} E_j \cos(j\omega_0 t + \gamma_j). \tag{B.16}$$

By superposition one can find the distributions of scalar velocity components and stream function as given in Eq. 4.23.

B.2 GENERALIZED INDUCED DIPOLE STRENGTH

Here we provide the details of derivation of the induced dipole strength for an arbitrary electric field $E(t)$. Equating Eq. 4.4 and Eq. 4.6 yields

$$E(t)(1-g) = \tau_c\left[\frac{dE(t)}{dt}(1+g) + E(t)\frac{dg}{dt}\right], \tag{B.17}$$

where $\tau_c = \varepsilon\kappa a/\sigma$. This is rewritten as

$$\frac{d(E(\hat{t})g + E(\hat{t}))}{d\hat{t}} + E(\hat{t})g - E(\hat{t}) = 0, \tag{B.18}$$

with $\hat{t} \equiv t/\tau_c = t\sigma/(\varepsilon\kappa a)$. Substituting $v \equiv E(\hat{t})g + E(\hat{t})$ yields

$$\frac{dv}{d\hat{t}} + v = 2E(\hat{t}). \tag{B.19}$$

Multiplying by the integrating factor $e^{\hat{t}}$ and integration with respect to $\hat{t}$ yields

$$v = E(\hat{t})g + E(\hat{t}) = 2\frac{\int e^{\hat{t}}E(\hat{t})d\hat{t}}{e^{\hat{t}}} + ce^{-\hat{t}}. \tag{B.20}$$

The constant of integration c is zero for any periodic electric field $E(t)$. Solving for g yields the induced dipole strength in terms of an indefinite integral, i.e., Eq. 4.7.

Appendix C

Perturbation Solution

This appendix serves as a supplemental material for Chapter 5.

C.1 FIRST-ORDER SOLUTION ($\gamma = 0,\ \beta^2\Omega^2 = \frac{1}{4}$)

As discussed, characteristic equation of the first-order eigenvalue problem has repeated roots for $\gamma = 0$ and $\beta\Omega = \frac{1}{4}$. For this special case, the general solution to the first-order problem becomes:

$$\hat{n}_+^{(1)}(\tilde{x}) = A\sinh(\lambda\tilde{x}) - \frac{iS}{4\lambda}(A+B)\tilde{x}\cosh(\lambda\tilde{x}), \tag{C.1}$$

$$\hat{n}_-^{(1)}(\tilde{x}) = iSB\sinh(\lambda\tilde{x}) - \frac{1}{4\lambda}(A+B)\tilde{x}\cosh(\lambda\tilde{x}), \tag{C.2}$$

$$\hat{\phi}^{(1)}(\tilde{x}) = Cx + (iSB - A)\frac{\sinh(\lambda\tilde{x})}{2\lambda^2} + (A+B)(iS-1)\frac{\lambda\tilde{x}\cosh(\lambda\tilde{x}) - 2\sinh(\lambda\tilde{x})}{8\lambda^4}. \tag{C.3}$$

with

$$\lambda = \frac{1}{\sqrt{2}}\left(1 + 2i\Omega\right)^{1/2}, \tag{C.4a}$$

$$S = \mathrm{sgn}(\beta). \tag{C.4b}$$

The constants A, B, and C are determined as

$$A = \frac{4i\lambda^2}{\Gamma}\Big[\left(\left(4\lambda^2-1\right)S + i\right)\cosh(\lambda\kappa\ell) - (S-i)\lambda\kappa\ell\sinh(\lambda\kappa\ell)\Big], \tag{C.5}$$

$$B = \frac{4i\lambda^2}{\Gamma}\Big[\left(S + \left(4\lambda^2-1\right)i\right)\cosh(\lambda\kappa\ell) + (S-i)\lambda\kappa\ell\sinh(\lambda\kappa\ell)\Big], \tag{C.6}$$

$$C = -\frac{8iS\lambda\left(2\lambda^4 - 2\lambda^2 + 1\right)\cosh^2(\lambda\kappa\ell)}{\Gamma}. \tag{C.7}$$

The parameter Γ is

$$\Gamma = 2iS\lambda\kappa\ell\Big[4(\lambda^4 - \lambda^2 + 1) + 2\left(2\lambda^4 - 2\lambda^2 + 1\right)\cosh(2\lambda\kappa\ell) + \left(4\lambda^2 - 3\right)\frac{\sinh(2\lambda\kappa\ell)}{\lambda\kappa\ell}\Big]. \tag{C.8}$$

C.2 NUMERICAL SOLUTION TO Eq. 5.49

Here we explain a numerical algorithm for solving the Eq. 5.49. For most practical cases, the electrode spacing is several thousands of the Debye length. Under such conditions, using uniform grids for discretization is inefficient. Covering the entire domain with a uniform grid, fine enough to capture the sharp gradients within the Debye layer ($\sim \kappa^{-1}/100$), would require a total of several hundred thousands grids. Instead we use a stretched grid. Consider a one-dimensional domain of $\tilde{x} \in [-\kappa\ell, \kappa\ell]$ discretized nonuniformly as $\tilde{x}_i$ for $i = 1, \ldots, 2N+1$ (face centered grid, i.e., $x_1 = -\kappa\ell$, $x_{2N+1} = \kappa\ell$) and $h_i = \tilde{x}_{i+1} - \tilde{x}_i$. We set $h_1 = h_{2N} \sim 0.01$ (corresponding to having 100 grid points within the Debye layer), and gradually increase the grid size as $x_i \to 0$. Using Newton's tableau for 3 arbitrary points at locations $\tilde{x}_{i-1}, \tilde{x}_i, \tilde{x}_{i+1}$ and corresponding values of, respectively, $\langle\tilde{E}^{(2)}\rangle_{i-1}, \langle\tilde{E}^{(2)}\rangle_i, \langle\tilde{E}^{(2)}\rangle_{i+1}$, one can find the Laplacian stencil as

$$\frac{\partial^2\langle\tilde{E}^{(2)}\rangle_i}{\partial\tilde{x}^2} = \frac{2\langle\tilde{E}^{(2)}\rangle_{i-1}}{h_{i-1}(h_i + h_{i-1})} - \frac{2}{h_i h_{i-1}}\langle\tilde{E}^{(2)}\rangle_i + \frac{2\langle\tilde{E}^{(2)}\rangle_{i+1}}{h_i(h_i + h_{i-1})}. \tag{C.9}$$

Using the obtained Laplacian stencil, the discretized form of Eq. 5.49 becomes:

$$a_i\langle\tilde{E}^{(2)}\rangle_{i-1} + b_i\langle\tilde{E}^{(2)}\rangle_i + c_i\langle\tilde{E}^{(2)}\rangle_{i+1} = f_i, \tag{C.10}$$

where

$$a_i = \frac{2}{h_{i-1}(h_i + h_{i-1})}, \tag{C.11a}$$

$$b_i = -\left(\frac{2}{h_i h_{i-1}} + 1\right), \tag{C.11b}$$

$$c_i = \frac{2}{h_i(h_i + h_{i-1})}. \tag{C.11c}$$

In matrix form, the system of algebraic equations can be expressed as

$$\begin{pmatrix} b_2 & c_2 & & & \\ a_3 & b_3 & c_3 & & \\ & & \ddots & & \\ & & a_{2N-1} & b_{2N-1} & c_{2N-1} \\ & & & a_{2N} & b_{2N} \end{pmatrix} \begin{pmatrix} \langle\tilde{E}^{(2)}\rangle_2 \\ \langle\tilde{E}^{(2)}\rangle_3 \\ \vdots \\ \langle\tilde{E}^{(2)}\rangle_{2N-1} \\ \langle\tilde{E}^{(2)}\rangle_{2N} \end{pmatrix} = \begin{pmatrix} f_2 \\ f_3 \\ \vdots \\ f_{2N-1} \\ f_{2N} \end{pmatrix}, \tag{C.12}$$

which can be solved by standard iterative schemes or simply inverting the coefficient matrix.

C.3 PYTHON SOLVER OF Eq. 5.49

The following python code numerically solves the AREF equation (Eq. 5.49) using the algorithm described above. Run the program by `python3 AREF_CALC.py`.

Filename: AREF_CALC.py

```
"""
********************************************************************************** +
********************************** AREF_CALC ********************************** +
************************* S.M.H. Hashemi Amrei (Aref) ************************* +
********************************************************************************** +
This program evaluates AREF via a second-order perturbation solution to the PNP eqns.
AREF: asymmetric rectified electric field

References to cite:
1) A perturbation solution to the full PNP eqns yields an asymmetric rectified electric field
S. M. H. Hashemi Amrei, Gregory H. Miller, Kyle J. M. Bishop, & William D. Ristenpart
Soft Matter, DOI: 10.1039/D0SM00417K (2020)

2) Oscillating Electric Fields in Liquids Create a Long-Range Steady Field
S. M. H. Hashemi Amrei, S. C. Bukosky, S. P. Rader, W. D. Ristenpart, & G. H. Miller
Physical Review Letters 121, 185504 (2018)

The eqn numbers throughout this code refer to the corresponding equations in ref. 1.
-------------------------------------------------------------------------------
Correspondence should be addressed to:
i) Gregory H. Miller (grgmiller@ucdavis.edu)
ii) William D. Ristenpart (wdristenpart@ucdavis.edu)
Department of Chemical Engineering
University of California Davis, Davis, California, US
"""

from AREF_SOURCE import *

print('Program started... ')

# saving the input values for beta, gamma, Omega, and kl from the file Inputs.txt in a list
[dl_parameters, [ind, pm]] = user_input()
# grid and spacing generator
[x, h, im] = domain(dl_parameters[3][0], is_uniform, h_minimum, ref)
# preallocation of the legend list (plotting)
legendLabel = legend(ind, pm, dl_parameters)
# preallocation of the AREF peak magnitude vector (plotting)
y_max_vec = np.zeros(pm, dtype=float)
# calculating the AREF length scale (plotting)
len_d = l_aref(dl_parameters[3], dl_parameters[2], pm)
# evalauting the AREF for different set of dimensionless parameters (a total of pm sets) and plotting the results
for i in range(pm):
    # extracting the dimensionless parameters from the list
    [beta, gamma, Omega, kl] = [dl_parameters[0][i], dl_parameters[1][i], dl_parameters[2][i], dl_parameters[3][i]]
    # semi-analytical second-order approximation to AREF
    AREF_A = semi_analytical_aref(beta, gamma, Omega, kl, x, h, im)
    # finding the peak AREF magnitude to be used for the ylim (plotting)
    y_max_vec[i] = y_max_finder(x, kl, AREF_A, len_d, l_d_critical)
    # plotting the AREF distribution
    plt.plot(x, AREF_A, label=legendLabel[i])
    # writing the results (x, AREF) into a 2-column .txt file
    write_to_file(AREF_A, x, [beta, gamma, Omega, kl], param_string_latex)

# plot appearance (plotting)
print('Program finished.')
plot_app(dl_parameters[3][0], param_string_latex, ind, np.max(y_max_vec), pm)
```

Filename: AREF_SOURCE.py

```
from math import *
from cmath import sqrt, tanh, exp
import matplotlib.pyplot as plt
import numpy as np
from pylatexenc.latex2text import LatexNodes2Text
from fractions import Fraction
```

```
7
8
9  # ********************************************************** #
10 # ********************** USER INPUTS ********************** #
11 # ********************************************************** #
12
13 # saving the input values for beta, gamma, Omega, and kl from the file Inputs.txt in a list
14 # dl_parameters: dimensionless parameters list [beta, gamma, Omega, kl]
15 # ind: index of the varying parameter (0: beta, 1: gamma, 2: Omega)
16 # pm: total number of values of the varying parameter (beta, gamma, or Omega)
17 def user_input():
18     pm = 1
19     ind = 0
20
21     n_dlp = 4   # total number of dimensionless parameters (4: beta, gamma, Omega, kl)
22     dl_parameters = [[0.0]]*n_dlp   # initial allocation of the dimensionless parameters list
23
24     # reading the file into read_list
25     file_id = open("Inputs.txt", "r")
26     read_list = file_id.readlines()
27     skip_ln = read_list.index('Parameters:\n')
28
29     # storing the read_list information into the dl_parameters list
30     # errors will be displayed in case of invalid inputs
31     str_exist = ['param_beta', 'param_gamma', 'param_Omega', 'param_kl']
32     exist_check = [False, False, False, False]
33     num_var_param = 0
34     for n in range(n_dlp):
35         for elem in read_list[skip_ln:]:
36             if str_exist[n] in elem:
37                 exist_check[n] = True
38                 if '(' in elem:
39                     if n == 3:
40                         print('INVALID INPUT FOR ' + str_exist[n] +
41                               '. Single value is accepted! Follow the instructions in Inputs.txt.\nProgram Stopped.')
42                         exit()
43                     try:
44                         ind_l = elem.index('(')
45                         ind_h = elem.index(')')
46                         if len(elem[ind_l+1:ind_h-1].split(',')) != 3:
47                             print('INVALID INPUT FOR ' + str_exist[n] +
48                                   '! Follow the instructions in Inputs.txt.\nProgram Stopped.')
49                             exit()
50
51                         syn = 'np.linspace' + elem[ind_l:]
52                         dl_parameters[n] = eval(syn)
53                         num_var_param += 1
54                         ind = n
55                         pm = len(dl_parameters[n])
56                     except (TypeError, ValueError, SyntaxError):
57                         print('INVALID INPUT FOR ' + str_exist[n] +
58                               '! Follow the instructions in Inputs.txt.\nProgram Stopped.')
59                         exit()
60                 elif '[' in elem:
61                     if n == 3:
62                         print('INVALID INPUT FOR ' + str_exist[n] +
63                               '. Single value is accepted! Follow the instructions in Inputs.txt.\nProgram Stopped.')
64                         exit()
65                     try:
66                         ind_l = elem.index('[')
67                         syn = elem[ind_l:]
68                         dl_parameters[n] = eval(syn)
69                         num_var_param += 1
70                         ind = n
71                         pm = len(dl_parameters[n])
72                     except (TypeError, ValueError, SyntaxError):
73                         print('INVALID INPUT FOR ' + str_exist[n] +
74                               '! Follow the instructions in Inputs.txt.\nProgram Stopped.')
75                         exit()
76                 else:
77                     if ',' in elem:
78                         print('INVALID INPUT FOR ' + str_exist[n] +
79                               '! Follow the instructions in Inputs.txt.\nProgram Stopped.')
80                         exit()
81                     try:
82                         dl_parameters[n] = [eval(elem[elem.index('=')+1:])]
```

```
                    except (TypeError, ValueError, SyntaxError):
                        print('INVALID INPUT FOR ' + str_exist[n] +
                              '! Follow the instructions in Inputs.txt.\nProgram Stopped.')
                        exit()

    for i in range(n_dlp):
        if not exist_check[i]:
            print('INVALID INPUT! Parameter name(s) is wrong' +
                  '! Follow the instructions in Inputs.txt.\nProgram Stopped.')
            exit()

    if num_var_param > 1:
        print('INVALID INPUT! There are more than one varying parameter' +
              '! Follow the instructions in Inputs.txt.\nProgram Stopped.')
        exit()

    # updating the pm value
    for i in range(len(dl_parameters)):
        if i != ind:
            dl_parameters[i] *= pm

    err_text = r'INVALID INPUT! You need $\mid\beta\mid\le 1$ (beta),'\
               r'$\gamma\:\in\:[-1/5 -1/3 -1/2 0 1/2 1/3 1/5]$ (gamma),' \
               r'$\Omega>0$ (Omega), $\Phi_0>0$ (Phi0), $\kappa\ell>0$ (L).\\Program Stopped.'
    bool_beta = 1 >= max(dl_parameters[0][:]) and -1 <= min(dl_parameters[0][:])
    bool_gamma = True
    for i in range(pm):
        if dl_parameters[1][i] not in [-1/5, -1/3, -1/2, 0, 1/2, 1/3, 1/5]:
            bool_gamma = False
    bool_omega = 0 < min(dl_parameters[2][:])
    bool_kl = 0 < min(dl_parameters[3][:])

    if bool_beta is False or bool_gamma is False or bool_omega is False or bool_kl is False:
        print(LatexNodes2Text().latex_to_text(err_text))
        exit()

    file_id.close()
    return [dl_parameters, [ind, pm]]


# ************************************************************ #
# *************** DISCRETIZATION OF THE DOMAIN *************** #
# ************************************************************ #

# x: vector of the grid points (face-centered) from -kl to kl
# h: vector of the grid spacings (i.e., h[i] = x[i+1] - x[i])
# im: total number of grids
# param_kl: electrode spacing
# uniform/is_uniform: boolian, default value = False
# h_min/h_minimum: minimum grid spacing, default value = 0.01
# r/ref: powerlaw growth rate of the grid spacing, default value = 1.01
# discretization parameters
is_uniform = False
h_minimum = 0.01
ref = 1.01


# stretched grid constructor
def stretched_grid(param_kl, h_min, r):
    n = int(floor(log(1-(1-r)*(param_kl/h_min))/log(r))+1)
    h = np.array([0]*2*n, dtype=float)
    h[0] = h_min
    for i in range(1, n):
        h[i] = r*h[i-1]
    if np.sum(h[0:n]) > param_kl:
        h[n-1] = param_kl - np.sum(h[0:n-1])

    h[n:2*n] = np.flip(h[0:n])
    im = 2*n+1
    x = np.array([0.0]*im, dtype=float)
    x[0] = -param_kl
    for i in range(1, 2*n+1):
        x[i] = x[i-1] + h[i-1]
    return [x, h, im]


```

```
# grid and spacing generator
def domain(param_kl, uniform, h_min, r):
    if uniform is True:
        # unform grid spacing of size h_min
        deb_im = 2**(-floor(log(h_min, 2)))
        im = int(floor(2*param_kl*deb_im)+1)
        h = [2*param_kl/(im-1)]*(im-1)
        x = np.array([-param_kl+i*h[0] for i in range(im)], dtype=float)
    else:
        [x, h, im] = stretched_grid(param_kl, h_min, r)

    return [x, h, im]


# ************************************************************ #
# ************* NUMERICAL SOLUTION TO THE AREF EQN ************* #
# ************************** (eqn 49) ************************** #
# ************************************************************ #


# semi-analytical second-order approximation to AREF
# eqn numbers refer to the corresponding equations in ref. 1.
def semi_analytical_aref(param_beta, param_gamma, param_Omega, param_kl, x, h, im):
    # rhs of the AREF eqn
    rhs = np.array([0] * im, dtype=complex)
    sc_checker = 4*(param_beta*param_Omega)**2
    if param_gamma == 0 and sc_checker == 1:  # Special case (Appendix A)
        sgn = np.sign(param_beta)  # S (eqn A4b)
        lambda12 = sqrt((1+2j*param_Omega)/2)  # \lambda (eqn A4a)
        cap_gamma = 2*sgn*param_kl*(4*(lambda12**4-lambda12**2+1)*exp(-2*lambda12*param_kl) +
                                   (2*lambda12**4-2*lambda12**2+1)*(1+exp(-4*lambda12*param_kl)) +
                                   (4*lambda12**2-3)*(1-exp(-4*lambda12*param_kl))/(2*lambda12*param_kl))
        for i in range(im):
            # A\sinh(\lambda\tilde{x})
            a_sinh = lambda12/cap_gamma*(((4*lambda12**2-1)*sgn+1j)*(1+exp(-2*lambda12*param_kl)) -
                                         (sgn-1j)*lambda12*param_kl*(1-exp(-2*lambda12*param_kl)))*(
                                          exp(lambda12*(x[i]-param_kl))-exp(-lambda12*(x[i]+param_kl)))
            # B\sinh(\lambda\tilde{x})
            b_sinh = lambda12/cap_gamma*(((4*lambda12**2-1)*1j+sgn)*(1+exp(-2*lambda12*param_kl)) +
                                         (sgn-1j)*lambda12*param_kl*(1-exp(-2*lambda12*param_kl)))*(
                                          exp(lambda12*(x[i]-param_kl))-exp(-lambda12*(x[i]+param_kl)))
            # (A+B)\cosh(\lambda\tilde{x})
            apb_cosh = 4*lambda12**3*(sgn+1j)/cap_gamma*(1+exp(-2*lambda12*param_kl))*(
                       exp(lambda12*(x[i]-param_kl))+exp(-lambda12*(x[i]+param_kl)))
            # (A+B)\sinh(\lambda\tilde{x})
            apb_sinh = 4*lambda12**3*(sgn+1j)/cap_gamma*(1+exp(-2*lambda12*param_kl))*(
                       exp(lambda12*(x[i]-param_kl))-exp(-lambda12*(x[i]+param_kl)))
            # (A-iSB)\cosh(\lambda\tilde{x})
            amisb_cosh = lambda12/cap_gamma*((2*sgn*(4*lambda12**2-1)+1j*(1-sgn**2))*(1+exp(-2*lambda12*param_kl)) +
                                             (1j*(1-sgn**2)-2*sgn)*lambda12*param_kl*(1-exp(-2*lambda12*param_kl)))*(
                                              exp(lambda12*(x[i]-param_kl))+exp(-lambda12*(x[i]+param_kl)))
            # C
            c = -2*sgn/cap_gamma*(2*lambda12**4-2*lambda12**2+1)*(1+exp(-2*lambda12*param_kl))**2

            # \hat{n}_+^{(1)}: eqn A1
            n1_hat = a_sinh-1j*sgn/(4*lambda12)*x[i]*apb_cosh
            # \hat{n}_-^{(1)}: eqn A2
            n2_hat = 1j*sgn*b_sinh-1/(4*lambda12)*x[i]*apb_cosh
            # \hat{E}^{(1)}: -derivative of eqn A3 (the electric potential \hat{\phi}^{(1)})
            e_hat = -(c-amisb_cosh/(2*lambda12)-(1j*sgn-1)/(8*lambda12**3)*apb_cosh +
                      (1j*sgn-1)/(8*lambda12**2)*x[i]*apb_sinh)
            # complex conjugates: \bar{X}=\mathrm{conj}{\hat{X}}
            n1_bar = np.conj(n1_hat)
            n2_bar = np.conj(n2_hat)
            e_bar = np.conj(e_hat)
            # rhs of the AREF eqn: eqn 50
            rhs[i] = 1/8*((n1_hat+n2_hat)*e_bar+(n1_bar+n2_bar)*e_hat)
    else:
        cap_delta = 1-4*param_beta*param_Omega*(1j*param_gamma+param_beta*param_Omega)  # \Delta (eqn 32b)
        lambda1 = sqrt((1+2j*param_Omega+sqrt(cap_delta))/2)  # \lambda_+ (eqn 33)
        lambda2 = sqrt((1+2j*param_Omega-sqrt(cap_delta))/2)  # \lambda_- (eqn 33)
        s = 2j*param_beta*param_Omega+sqrt(cap_delta)  # s (eqn 32a)
        # Gamma: eqn 37
        cap_gamma = s**2-2*param_gamma*s+1-1/(2*param_kl)*(
                (param_gamma+1)*(s-1)**2*(lambda2*param_kl-tanh(lambda2*param_kl))/(lambda2**3) -
                (param_gamma-1)*(s+1)**2*(lambda1*param_kl-tanh(lambda1*param_kl))/(lambda1**3))
```

```
        for i in range(im):
            c1 = (exp(lambda1*(x[i]-param_kl))-exp(-lambda1*(x[i]+param_kl)))/(1+exp(-2*lambda1*param_kl))
            c2 = (exp(lambda2*(x[i]-param_kl))-exp(-lambda2*(x[i]+param_kl)))/(1+exp(-2*lambda2*param_kl))
            # \hat{n}_+^{(1)}: eqn 30
            n1_hat = 1/cap_gamma*((s-param_gamma)*(s-1)/(lambda2*param_kl)*c2
                                  + (1-param_gamma)*(s+1)/(lambda1*param_kl)*c1)
            # \hat{n}_-^{(1)}: eqn 31
            n2_hat = 1/cap_gamma*((1+param_gamma)*(s-1)/(lambda2*param_kl)*c2
                                  - (s-param_gamma)*(s+1)/(lambda1*param_kl)*c1)

            c1p = (exp(lambda1*(x[i]-param_kl))+exp(-lambda1*(x[i]+param_kl)))/(1+exp(-2*lambda1*param_kl))
            c2p = (exp(lambda2*(x[i]-param_kl))+exp(-lambda2*(x[i]+param_kl)))/(1+exp(-2*lambda2*param_kl))
            # \hat{E}^{(1)}: -derivative of eqn 34 (the electric potential \hat{\phi}^{(1)})
            e_hat = 1/param_kl+1/(2*param_kl*cap_gamma)*(
                    (1+param_gamma)*(s-1)**2/(lambda2**2)*(c2p-tanh(lambda2*param_kl)/(lambda2*param_kl)) +
                    (1-param_gamma)*(s+1)**2/(lambda1**2)*(c1p-tanh(lambda1*param_kl)/(lambda1*param_kl)))
            # complex conjugates: \bar{X}=\mathrm{conj}{\hat{X}}
            n1_bar = np.conj(n1_hat)
            n2_bar = np.conj(n2_hat)
            e_bar = np.conj(e_hat)

            # rhs of the AREF eqn: eqn 50
            rhs[i] = 1/8*(((1+param_gamma)**2*n1_hat + (1-param_gamma)**2*n2_hat)*e_bar + (
                    (1+param_gamma)**2*n1_bar + (1-param_gamma)**2*n2_bar)*e_hat)
    # constructing the linear system of algebraic equations (cf. Appendix B of ref. 1, eqn B4)
    # a: coefficient matrix
    # b: right hand side column vector
    a = np.zeros((im, im), dtype=float)
    b = np.transpose(rhs)

    for i in range(1, im-1):
        a[i, i-1] = 2/(h[i-1])/(h[i] + h[i-1])              # eqn B3a
        a[i, i] = -(1+2*(1/h[i]+1/h[i-1])/(h[i]+h[i-1]))    # eqn B3b
        a[i, i+1] = 2/(h[i])/(h[i]+h[i-1])                  # eqn B3c

    # computing AREF
    aref_a = np.array([0] * im, dtype=complex)
    aref_a[1:im-1] = np.linalg.solve(a[1:im-1, 1:im-1], b[1:im-1])

    return np.real(aref_a)


# ************************************************************ #
# ********************** WRITE INTO FILE ********************* #
# ************************************************************ #
param_string_latex = [r'$\beta$', r'$\gamma$', r'$\Omega$', r'$\kappa\ell$', r'$\Phi_0$']


# converting numbers into strings
def convert_to_string(val):
    if int(val) == val:
        string = str(int(val))
    else:
        order = log(abs(val), 10)
        if order > 0:
            string = str(round(val, 4))
        else:
            string = str(round(val, int(abs(floor(order))) + 3))

    return string


# writing the results (x, AREF) into a 2-column .txt file
def write_to_file(aref_a, x, dl_params, param_string):
    data = np.column_stack((x, aref_a))
    filename = 'results_beta=' + convert_to_string(dl_params[0]) + '_gamma=' + convert_to_string(dl_params[1]) \
               + '_Omega=' + convert_to_string(dl_params[2]) + '_kl=' + convert_to_string(dl_params[3]) + '.txt'
    file_id = open(filename, "w", encoding="utf-8")
    message = r'AREF_CALC results: $\kappa x$ (1st column) vs $\langle\tilde{E}\rangle/\Phi_0^2$ (2nd column)'
    file_id.write(LatexNodes2Text().latex_to_text(message))
    file_id.write('\n' + '='*50 + '\n')
    for i in range(len(dl_params)):
        param_message = param_string[i] + r' $=$ ' + convert_to_string(dl_params[i])
        file_id.write(LatexNodes2Text().latex_to_text(param_message))
        file_id.write('\n')

```

```
311     file_id.write('='*50 + '\n')
312     np.savetxt(file_id, data, fmt=['%+10.16f', '%10.16f'])
313     file_id.close()
314 
315     return 0
316 
317 
318 # ************************************************************ #
319 # ************************ PLOTTING ************************** #
320 # ************************************************************ #
321 
322 # plot options
323 app_params = {'figure.dpi': 100,
324               'font.size': 12,
325               'mathtext.fontset': 'stix',
326               'font.family': 'STIXGeneral',
327               'lines.linewidth': 2,
328               'xtick.direction': 'in',
329               'ytick.direction': 'in',
330               'xtick.top': True,
331               'ytick.right': True,
332               'figure.figsize': [7, 5]}
333 plt.rcParams.update(app_params)
334 plt.subplots_adjust(left=0.15, bottom=0.1, right=0.8, top=0.9)
335 l_d_critical = 0.32
336 
337 
338 # constructing the plot's legend
339 def legend(ind, pm, dl_parameters):
340     dl = dl_parameters[ind]
341     legend_label = [' ']*pm
342     for i in range(pm):
343         legend_label[i] = convert_to_string(dl[i])
344 
345     return legend_label
346 
347 
348 # plot appearance
349 def plot_app(param_kl, param_string, ind, y_max, pm):
350     if y_max == 0.0:
351         scale = 10**(-16)
352     else:
353         scale = 10**(round(log(y_max, 10)))
354 
355     plt.xlabel(r'$\kappa x$')
356     power = int(log(1/scale, 10))
357     if power == 1:
358         plt.ylabel(r'$\langle\tilde{E}\rangle/\Phi_0^2 \times 10$')
359     elif power == 0:
360         plt.ylabel(r'$\langle\tilde{E}\rangle/\Phi_0^2$')
361     else:
362         plt.ylabel(r'$\langle\tilde{E}\rangle/\Phi_0^2 \times 10^{' + str(power) + '}$')
363 
364     plt.xlim(-param_kl, param_kl)
365 
366     rat = [0, 1, 2, 3, 4, 5, 6, 7, 8, 9]
367     y_lim = rat[rat.index(int(floor(y_max/scale)))]+1
368     plt.ylim(-y_lim*scale, y_lim*scale)
369     yticks = [-y_lim*scale, -y_lim*scale/2, 0, y_lim*scale/2, y_lim*scale]
370     yticklabels = [' ']*5
371     for i in range(5):
372         yticklabels[i] = '$' + str(round(yticks[i]/scale, 1)) + '$'
373 
374     plt.yticks((-y_lim*scale, -y_lim*scale/2, 0, y_lim*scale/2, y_lim*scale),
375                (yticklabels[0], yticklabels[1], yticklabels[2], yticklabels[3], yticklabels[4]))
376     if pm > 1:
377         plt.legend(title=param_string[ind], fancybox=False, edgecolor='w', bbox_to_anchor=(1.01, 1), loc='upper left')
378 
379     plt.show()
380 
381 
382 # calculating the AREF length scale (eqn 53)
383 def l_aref(kl_vec, omega_vec, pm):
384     l_d_vec = [0.0]*pm
385     for i in range(pm):
386         l_d_vec[i] = (1/(omega_vec[i]*kl_vec[i]**2))**(1/2)
```

```
387
388     return np.min(l_d_vec)
389
390
391 # finding the peak AREF magnitude to be used for the ylim
392 def y_max_finder(x, param_kl, aref_a, l_d, l_d_c):
393     if l_d > l_d_c:
394         y_max = np.max(abs(aref_a))
395     else:
396         ind_micronscale = np.min(np.nonzero(x + param_kl > 2))
397         ind_midplane = int((len(x)-1)/2)
398         y_max_p = np.max(aref_a[ind_micronscale:ind_midplane])
399         y_max_m = np.min(aref_a[ind_micronscale:ind_midplane])
400         if y_max_p > abs(y_max_m):
401             y_max = y_max_p
402         else:
403             y_max = -y_max_m
404
405     return y_max
```

Filename: Inputs.txt

```
1  Enter the values for dimensionless parameters here.
2  Please follow the instructions below:
3
4  * For single value parameters write the value only.
5  e.g., beta = 1/2
6  * To have multiple values for a parameter use brackets [], with "," separating the values
7  e.g., beta = [-1, 0, 1/2, 4/5]
8  * To have a certain number of values for a parameter within a range use (min value, max value, number of values)
9  e.g., beta = (-1, 1, 11)
10
11 Remarks:
12 . You need |beta|<=1, gamma in {-1/5 -1/3 -1/2 0 1/2 1/3 1/5}, Omega>0, Phi0>0, L>0.
13 . DO NOT change the name of parameters.
14 . Only one of the 3 dimensionless parameters beta, gamma, & Omega can have multiple values
15 . Values can be expressed as integer, float, or fraction
16 . Use EXACTLY the provided instructions to avoid errors in reading.
17
18
19 Parameters:
20
21 param_beta = (-1,1,5)
22 param_gamma = 0
23 param_Omega = 0.1
24 param_kl = 10
```

Appendix D

Two-Mode Potentials & Symmetry Arguments

This appendix serves as a supplemental material for Chapter 7.

D.1 PERTURBATION SOLUTION (TWO-MODE)

D.1.1 Second-order perturbation solution (single-mode)

We briefly review the second-order solution to the PNP equations derived by Hashemi Amrei et al.[5] for a single-mode sinusoidal potential. The dimensionless governing equations are expressed as

$$-\frac{\partial^2 \tilde{\phi}}{\partial \tilde{x}^2} = \tfrac{1}{2}\tilde{n}_+ - \tfrac{1}{2}\tilde{n}_-, \tag{D.1}$$

$$\frac{\partial \tilde{n}_\pm}{\partial \tilde{t}} = -\frac{\tilde{j}_\pm}{\partial \tilde{x}}, \tag{D.2}$$

where the dimensionless ion flux is

$$\tilde{j}_\pm = -\frac{1}{1 \mp \beta}\left[\frac{\partial \tilde{n}_\pm}{\partial \tilde{x}} \pm \left(\tilde{n}_\pm \frac{\partial \tilde{\phi}}{\partial \tilde{x}}\right)\right]. \tag{D.3}$$

The dimensionless initial and boundary conditions are

$$\tilde{n}_\pm(\tilde{x}, 0) = 1, \tag{D.4}$$

$$\tilde{\phi}(\pm\kappa\ell, \tilde{t}) = \mp\Phi_0 \sin(\Omega\tilde{t}), \tag{D.5}$$

$$\tilde{j}_\pm(\pm\kappa\ell, \tilde{t}) = 0. \tag{D.6}$$

Here, the dimensionless variables and parameters are defined as

$$\tilde{n}_\pm = \frac{n_\pm}{n^\infty}, \quad \tilde{\phi} = \frac{\phi e}{k_B T}, \quad \tilde{x} = \kappa x, \quad \tilde{t} = t\kappa^2 D, \tag{D.7}$$

$$\Phi_0 = \frac{\phi_0 e}{k_B T}, \quad \Omega = \frac{\omega}{\kappa^2 D}, \quad \kappa\ell, \quad \beta = \frac{D_+ - D_-}{D_+ + D_-}, \tag{D.8}$$

where

$$D = \frac{2D_+ D_-}{D_+ + D_-}, \quad \kappa^{-1} = \sqrt{\frac{\varepsilon k_B T}{2e^2 n^\infty}}. \tag{D.9}$$

In the limit of small potentials ($\Phi_0 \ll 1$), the solution can be approximated by the power series

$$\tilde{n}_\pm(\tilde{x},\tilde{t}) = \tilde{n}_\pm^{(0)} + \Phi_0 \tilde{n}_\pm^{(1)} + \Phi_0^2 \tilde{n}_\pm^{(2)} + \Phi_0^3 \tilde{n}_\pm^{(3)} + \dots \tag{D.10}$$

$$\tilde{\phi}(\tilde{x},\tilde{t}) = \tilde{\phi}^{(0)} + \Phi_0 \tilde{\phi}^{(1)} + \Phi_0^2 \tilde{\phi}^{(2)} + \Phi_0^3 \tilde{\phi}^{(3)} + \dots \tag{D.11}$$

Zeroth and first order solutions

The zeroth-order solution is simply $\tilde{n}_\pm^{(0)} = 1, \tilde{\phi}^{(0)} = 0$, and the first-order solution is given by

$$\tilde{n}_\pm^{(1)}(\tilde{x},\tilde{t}) = \mathrm{Im}\left[\hat{n}_\pm^{(1)} e^{i\Omega\tilde{t}}\right], \tag{D.12}$$

$$\tilde{\phi}^{(1)}(\tilde{x},\tilde{t}) = \mathrm{Im}\left[\hat{\phi}^{(1)} e^{i\Omega\tilde{t}}\right], \tag{D.13}$$

where $\hat{n}_\pm^{(1)}$ and $\hat{\phi}^{(1)}$ are odd (with respect to x) complex functions given by Eq. 5.30–Eq. 5.37 in Hashemi Amrei et al.[5]

Second-order solution

The second-order governing equations for $\tilde{n}_\pm^{(2)}$ and $\tilde{\phi}^{(2)}$ are[5]

$$\frac{\partial \tilde{n}_\pm^{(2)}}{\partial \tilde{t}} + \frac{\partial \tilde{j}_\pm^{(2)}}{\partial \tilde{x}} = 0, \tag{D.14}$$

$$\frac{\partial^2 \tilde{\phi}^{(2)}}{\partial \tilde{x}^2} + \tfrac{1}{2}\tilde{n}_+^{(2)} - \tfrac{1}{2}\tilde{n}_-^{(2)} = 0. \tag{D.15}$$

Here the ion flux is given by

$$\tilde{j}_\pm^{(2)}(\tilde{x},\tilde{t}) = -\frac{1}{1 \mp \beta}\left[\frac{\partial \tilde{n}_\pm^{(2)}}{\partial \tilde{x}} \pm \frac{\partial \tilde{\phi}^{(2)}}{\partial \tilde{x}} + s_\pm^{(2)}\right], \tag{D.16}$$

with

$$s_\pm^{(2)} = \pm \tilde{n}_\pm^{(1)} \frac{\partial \tilde{\phi}^{(1)}}{\partial \tilde{x}} = \mp \tilde{n}_\pm^{(1)} \tilde{E}^{(1)}. \tag{D.17}$$

The boundary conditions are

$$\tilde{\phi}^{(2)}(\pm\kappa\ell,\tilde{t}) = 0, \quad \tilde{j}_\pm^{(2)}(\pm\kappa\ell,\tilde{t}) = 0. \tag{D.18}$$

Hashemi Amrei et al. focused only on the second-order time-average electric field which was shown to accurately predict AREF via a simple linear ordinary differential equation (ODE), the

AREF equation[5]

$$\frac{\partial^2\langle\tilde{E}^{(2)}\rangle}{\partial\tilde{x}^2} - \langle\tilde{E}^{(2)}\rangle = f^{(2)}, \tag{D.19}$$

with

$$f^{(2)} = \tfrac{1}{2}\langle s_-^{(2)}\rangle - \tfrac{1}{2}\langle s_+^{(2)}\rangle. \tag{D.20}$$

An important point is that Hashemi Amrei et al.[5] assumed $\langle\tilde{E}^{(2)}\rangle = 0$ at the boundaries $\tilde{x} = \pm\kappa\ell$, which was consistent with all of the numerical results for single-mode sinusoidal applied potentials. Here we justify this assumption. One can easily show that the RHS $f^{(2)}$ is an odd function. Recall that $\tilde{n}_\pm^{(1)}$ and $\tilde{\phi}^{(1)}$ are odd which makes $\tilde{E}^{(1)} = -\partial\tilde{\phi}^{(1)}/\partial\tilde{x}$ an even function. Hence, $f^{(2)}$ which includes $\mp\tilde{n}_\pm^{(1)}\tilde{E}^{(1)}$ is odd, and yields an odd second-order solution $\langle\tilde{E}^{(2)}\rangle$ (antisymmetric). Additionally, total charge neutrality requires $\langle\tilde{E}^{(2)}\rangle_{\kappa\ell} = \langle\tilde{E}^{(2)}\rangle_{-\kappa\ell} = K$. But for $\langle\tilde{E}^{(2)}\rangle$ to be odd K has to be 0 which justifies the assumption. An alternative would be to solve for the potential via the following rank-deficient problem:

$$-\frac{\partial^3\langle\tilde{\phi}^{(2)}\rangle}{\partial\tilde{x}^3} + \frac{\langle\partial\tilde{\phi}^{(2)}\rangle}{\partial\tilde{x}} = f^{(2)}, \tag{D.21}$$

subject to $\langle\tilde{\phi}^{(2)}\rangle = 0$ at $\tilde{x} = \pm\kappa\ell$. Solving the problem using singular–value–decomposition (SVD) along with the total charge neutrality condition,

$$\int_{-\kappa\ell}^{\kappa\ell}\frac{\partial^2\langle\tilde{\phi}^{(2)}\rangle}{\partial\tilde{x}^2}d\tilde{x} = 0, \tag{D.22}$$

yields the same results as that of setting $\langle\tilde{E}^{(2)}\rangle = 0$ at $\tilde{x} = \pm\kappa\ell$.

D.1.2 Second-order perturbation solution (two-mode)

In this section we follow the same procedure to derive the perturbation solution for the two-mode potential $\tilde{\phi}(\pm\kappa\ell,\tilde{t}) = \mp\Phi_0\left[\sin(\Omega\tilde{t}) + \sin(\alpha\Omega\tilde{t})\right]$.

Zeroth and first order solutions

For the two-mode system, the zeroth-order solution remains unchanged. The first-order solution is obtained by superposition of the first-order solutions due to Ω and $\alpha\Omega$ modes:

$$\tilde{n}_\pm^{(1)}(\tilde{x},\tilde{t}) = \mathrm{Im}\left[\hat{n}_\pm^{(1)}(\Omega)e^{i\Omega\tilde{t}} + \hat{n}_\pm^{(1)}(\alpha\Omega)e^{i\alpha\Omega\tilde{t}}\right], \tag{D.23}$$

$$\tilde{\phi}^{(1)}(\tilde{x},\tilde{t}) = \mathrm{Im}\left[\hat{\phi}^{(1)}(\Omega)e^{i\Omega\tilde{t}} + \hat{\phi}^{(1)}(\alpha\Omega)e^{i\alpha\Omega\tilde{t}}\right]. \tag{D.24}$$

Second-order solution

One can show that $f^{(2)}$ for the two-mode case is the superposition of the RHS due to Ω and $\alpha\Omega$. Hence, following Hashemi Amrei et al.,[5] we can solve the problem for the modes Ω and

$\alpha\Omega$ separately without any extra complications. More importantly, it shows that the second-order solution does not provide any information regarding the possible dissymmetric behavior of AREF. As mentioned, the RHS of the second-order AREF equation is odd and yields antisymmetric contributions (cf. Fig. D.1(a)).

Consequently, we suspect that the dissymmetric AREF is a third-order phenomena. To investigate this hypothesis we need to first fully solve the second-order system to find the temporal and spatial distributions of the ion concentrations and the potential/electric field. The first and second order solutions will provide the RHS of the third-order AREF equation.

We use Fourier series to solve the problem. Consider solutions of the form:

$$\tilde{n}_{\pm}^{(2)} = \sum_{k=-\infty}^{\infty} c_k^{\pm} e^{ik\Omega_c \tilde{t}}, \tag{D.25}$$

$$\tilde{\phi}^{(2)} = \sum_{k=-\infty}^{\infty} c_k^{\phi} e^{ik\Omega_c \tilde{t}}. \tag{D.26}$$

Here $\Omega_c = \Omega \gcd(1, \alpha)$ is the common angular frequency of the applied potential, i.e., $2\pi/\Omega_c$ is the period of the two-mode applied potential/harmonic solution. Inserting Eq. D.25 and Eq. D.26 into the second-order governing equations and boundary conditions yields the following differential equations for the coefficients of the Fourier series.

(i) $k = 0$

$$\frac{\partial^2 c_0^{\pm}}{\partial \tilde{x}^2} \pm \frac{\partial^2 c_0^{\phi}}{\partial \tilde{x}^2} = -\left\langle \frac{\partial s_{\pm}^{(2)}}{\partial \tilde{x}} \right\rangle, \tag{D.27a}$$

$$\frac{\partial^2 c_0^{\phi}}{\partial \tilde{x}^2} + \tfrac{1}{2} c_0^{+} - \tfrac{1}{2} c_0^{-} = 0, \tag{D.27b}$$

$$\frac{\partial c_0^{\pm}}{\partial \tilde{x}} \pm \frac{\partial c_0^{\phi}}{\partial \tilde{x}} = -\langle s_{\pm}^{(2)} \rangle \quad \text{at} \quad \tilde{x} = \pm\kappa\ell, \tag{D.27c}$$

$$c_0^{\phi}(\pm\kappa\ell) = 0. \tag{D.27d}$$

Eq. D.27a and Eq. D.27c can be combined to yield

$$\frac{\partial c_0^{\pm}}{\partial \tilde{x}} \pm \frac{\partial c_0^{\phi}}{\partial \tilde{x}} + \langle s_{\pm}^{(2)} \rangle = 0.$$

Now, taking the derivative of Eq. D.27b with respect to $\tilde{x}$, and subsequent substitution of $\partial c_0^{\pm}/\partial \tilde{x}$ from the above equation results in

$$\frac{\partial^3 c_0^{\phi}}{\partial \tilde{x}^3} - \frac{\partial c_0^{\phi}}{\partial \tilde{x}} = \tfrac{1}{2}\langle s_{+}^{(2)} \rangle - \tfrac{1}{2}\langle s_{-}^{(2)} \rangle. \tag{D.28}$$

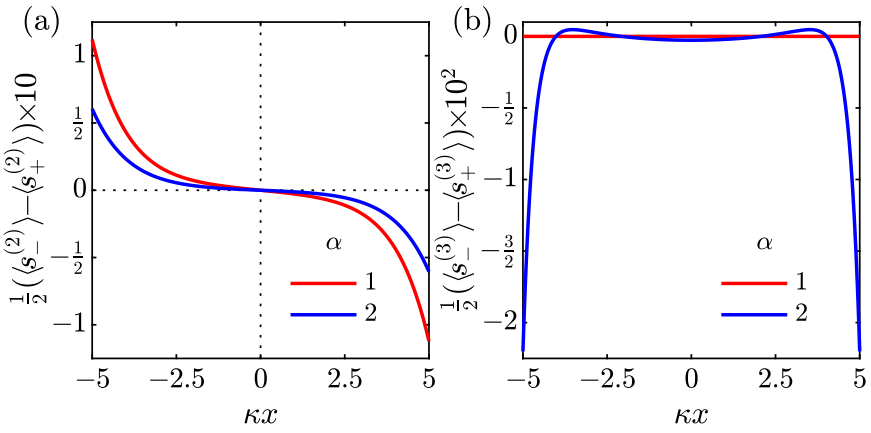

Figure D.1: RHSs of the second (a) and third (b) order AREF equations for $\alpha = 1$ and 2. Parameters: $\Omega = 0.1$, $\beta = -1/3$, $\kappa\ell = 5$.

Note that we could write this equation in terms of $c_0^E = -\partial c_0^\phi/\partial\tilde{x}$ to get:

$$\frac{\partial^2 c_0^E}{\partial\tilde{x}^2} - c_0^E = \tfrac{1}{2}\langle s_-^{(2)}\rangle - \tfrac{1}{2}\langle s_+^{(2)}\rangle,$$

which is equivalent to the linear ODE used by Hashemi Amrei et al.[5] to find AREF (Eq. D.19).

(ii) $k = -\infty, \ldots, \infty$

$$\frac{\partial^2 c_k^\pm}{\partial\tilde{x}^2} \pm \frac{\partial^2 c_k^\phi}{\partial\tilde{x}^2} - ik\Omega_c(1\mp\beta)c_k^\pm = -\left\langle \frac{\partial s_\pm^{(2)}}{\partial\tilde{x}} e^{-ik\Omega_c\tilde{t}} \right\rangle, \tag{D.29a}$$

$$\frac{\partial^2 c_k^\phi}{\partial\tilde{x}^2} + \tfrac{1}{2}c_k^+ - \tfrac{1}{2}c_k^- = 0, \tag{D.29b}$$

$$\frac{\partial c_0^\pm}{\partial\tilde{x}} \pm \frac{\partial c_0^\phi}{\partial\tilde{x}} = -\left\langle s_\pm^{(2)} e^{-ik\Omega_c\tilde{t}} \right\rangle \quad \text{at} \quad \tilde{x} = \pm\kappa\ell, \tag{D.29c}$$

$$c_k^\phi(\pm\kappa\ell) = 0. \tag{D.29d}$$

We solve the above equations numerically to find $c_k^\pm$ and c_k^ϕ ($k = -\infty, \ldots, \infty$). Of course we do not need to solve for $k \to \pm\infty$ and we truncate the series at a much smaller k value (i.e., $k = -K, \ldots, K$). Considering the source terms (Eq. D.17) as a multiplication of first-order solutions, the maximum possible frequency component can be obtained. For example, for a single-mode applied potential of angular frequency Ω, the first-order terms (i.e., $\tilde{n}_\pm^{(1)}, \tilde{E}^{(1)}$) oscillate with Ω and hence, the highest possible angular frequency of the source terms becomes $2\Omega = 2\Omega_c$ and $K = 2$. Similarly, for a two-mode system (Ω & $\alpha\Omega$), the highest angular frequency component, given $\alpha \geqslant 1$, is $2\alpha\Omega = 2\alpha\Omega_c/\gcd(1,\alpha) \to K = 2\alpha/\gcd(1,\alpha)$. Note that when $\alpha = 1$, $K = 2$ is recovered.

Third-order perturbation

The third-order system of equations is identical to that of the second order, except the source terms which are

$$s_{\pm}^{(3)} = \pm\left(\tilde{n}_{\pm}^{(1)}\frac{\partial\tilde{\phi}^{(2)}}{\partial\tilde{x}} + \tilde{n}_{\pm}^{(2)}\frac{\partial\tilde{\phi}^{(1)}}{\partial\tilde{x}}\right). \tag{D.30}$$

The third-order AREF equation is given by

$$\frac{\partial^2\langle\tilde{E}^{(3)}\rangle}{\partial\tilde{x}^2} - \langle\tilde{E}^{(3)}\rangle = f^{(3)}, \tag{D.31}$$

where

$$f^{(3)} = \tfrac{1}{2}\langle s_{-}^{(3)}\rangle - \tfrac{1}{2}\langle s_{+}^{(3)}\rangle. \tag{D.32}$$

An analyze of the RHS $f^{(3)}$ provides some insight regarding the dissymmetric AREF. We note that the second-order solutions $\tilde{\phi}^{(2)}$ and $\tilde{n}_{\pm}^{2}$ are even functions. Therefore, $f^{(3)}$ is an even function in space which, in turn, indicates that $\tilde{E}^{(3)}$ is even. Hence, when $f^{(3)} \neq 0$, the third-order electric field adds a dissymmetric contribution to the overall AREF. Fig. D.1(b) shows the calculated $f^{(3)}$ for $\alpha = 1$ and 2. We note that the $f^{(3)} \neq 0$ when $\alpha = 2$, corroborating the observed dissymmetric behavior. However, $f^{(3)} = 0$ for all other α values, including the ones that are expected (based on the numerical results) to result in dissymmetry. We argue that higher odd-order solutions $(5, 7, \dots)$ are responsible for the observed dissymmetry for other α values such as $\frac{3}{2}, \frac{4}{3}, 4, \dots$

Generalization

The k^{th} order solution ($k \geqslant 2$) contributes to the overall AREF via the ODE

$$\frac{\partial^2\langle\tilde{E}^{(k)}\rangle}{\partial\tilde{x}^2} - \langle\tilde{E}^{(k)}\rangle = f^{(k)}. \tag{D.33}$$

It can be shown that the source terms are odd functions with respect to the midplane for even k values, yielding an antisymmetric contribution to the solution. The source terms for odd orders are even functions in space, resulting an even contribution to the electric field. Therefore, if $s^{(k)}$ is nonzero for $k = 3, 5, \dots$, the perturbation solution suggests a dissymmetric shape for the AREF.

D.2 ANTIPERIODIC & NON-ANTIPERIODIC TWO-MODE POTENTIALS

We find the specific α values for which the $\psi(t) = \sin(\omega t)+\sin(\alpha\omega t)$ is antiperiodic/non-antiperiodic. We start by evaluating

$$\psi(t+\tau) = \sin(\omega t)\cos(\omega\tau)+\cos(\omega t)\sin(\omega\tau)+\sin(\alpha\omega t)\cos(\alpha\omega\tau)+\cos(\alpha\omega t)\sin(\alpha\omega\tau).$$

Since $\tau = \pi/(\omega \gcd(1,\alpha))$, we have $\omega\tau = n\pi$ and $\alpha\omega\tau = \alpha n\pi$ for an integer $n \geqslant 1$, and the expression simplifies to

$$\sin(\omega(t+\tau)) + \sin(\alpha\omega(t+\tau)) = \sin(\omega t)\cos(n\pi) + \sin(\alpha\omega t)\cos(\alpha n\pi).$$

Now if, in its simplified rational form, $\alpha = (2k+1)/(2j+1)$, then one can conclude that $n = 2j+1$ (αn is integer) and we get:

$$\psi(t+\tau) = \sin(\omega t)\cos((2j+1)\pi) + \sin(\alpha\omega t)\cos((2k+1)\pi) = -\sin(\omega t) - \sin(\alpha\omega t) = -\psi(t),$$

and therefore, $\psi(t)$ is antiperiodic. In a nutshell, *if α can be simplified as a rational number in the form $\{$odd integer$\}/\{$odd integer$\}$, the two-mode potential is antiperiodic; otherwise, the potential is non-antiperiodic.*

An alternative approach would be to find a time lag $2s\tau$ for which

$$\sin(\omega(t+2s\tau)) + \sin(\alpha\omega(t+2s\tau)) = -\sin(\omega t) - \sin(\alpha\omega t).$$

Note that $2s\tau\omega = (2j+1)\pi \rightarrow s = (2j+1)\pi/(2\omega\tau)$ introduces a phase lag of π to the first term. Then the phase lag of the second term becomes $2s\tau\alpha\omega = (2j+1)\alpha\pi$ which is an odd multiple of π for $\alpha = (2k+1)/(2j+1)$.

Bibliography

[1] S. M. H. Hashemi Amrei, S. C. Bukosky, S. P. Rader, W. D. Ristenpart, and G. H. Miller, *Oscillating electric fields in liquids create a long-range steady field*, Phys. Rev. Lett. 121 (2018) 185504.

[2] S. M. H. Hashemi Amrei, G. H. Miller, and W. D. Ristenpart, *Asymmetric rectified electric fields between parallel electrodes: numerical and scaling analyses*, Phys. Rev. E 99 (2019) 062603.

[3] S. C. Bukosky, S. M. H. Hashemi Amrei, S. P. Rader, J. Mora, G. H. Miller, and W. D. Ristenpart, *Extreme levitation of colloidal particles in response to oscillatory electric fields*, Langmuir 35 (2019) 6971–6980.

[4] S. M. H. Hashemi Amrei, G. H. Miller, and W. D. Ristenpart, *Asymmetric rectified electric fields generate flows that can dominate induced-charge electrokinetics*, Phys. Rev. Fluids 5 (2020) 013702.

[5] S. M. H. Hashemi Amrei, G. H. Miller, K. J. M. Bishop, and W. D. Ristenpart, *A Perturbation solution to the full Poisson–Nernst–Planck equations yields an asymmetric rectified electric field*, Soft Matter 16 (2020) 7052–7062.

[6] S. M. H. Hashemi Amrei, M. Tahernia, T. C. Hui, W. D. Ristenpart, and G. H. Miller, *Non-antiperiodic force excitations in isotropic media yield net motion of macroscopic objects*, (2021). In preparation.

[7] S. M. H. Hashemi Amrei, T. C. Hui, M. Tahernia, W. D. Ristenpart, and G. H. Miller, *Multimodal asymmetric rectified electric fields and long-range symmetry breaking in electric field orientation*, (2021). In preparation.

[8] M. Trau, D. A. Saville, and I. Aksay, *Field-induced layering of colloidal crystals*, Science 272 (1996) 706–709.

[9] M. Trau, D. A. Saville, and I. A. Aksay, *Assembly of colloidal crystals at electrode interfaces*, Langmuir 13 (1997) 6375–6381.

[10] D. C. Prieve, P. J. Sides, and C. L. Wirth, *2-D assembly of colloidal particles on a planar electrode*, Curr. Opin. Colloid Interface Sci. 15 (2010) 160–174.

[11] F. Ma, S. Wang, L. Smith, and N. Wu, *Two-dimensional assembly of symmetric colloidal dimers under electric fields*, Adv. Funct. Mater. 22 (2012) 4334–4343.

[12] C. S. Dutcher, T. J. Woehl, N. H. Talken, and W. D. Ristenpart, *Hexatic-to-disorder transition in colloidal crystals near electrodes: rapid annealing of polycrystalline domains*, Phys. Rev. Lett. 111 (2013) 128302.

[13] J. Voldman, *Electrical forces for microscale cell manipulation*, Annu. Rev. Biomed. Eng. 8 (2006) 425–454.

[14] T. Z. Jubery, S. K. Srivastava, and P. Dutta, *Dielectrophoretic separation of bioparticles in microdevices: a review*, Electrophoresis 35 (2014) 691–713.

[15] N. I. Gamayunov, V. A. Murtsovkin, and A. S. Dukhin, *Pair interaction of particles*

in electric-field. 1. Features of hydrodynamic interaction of polarized particles, Colloid J. 48 (1986) 197–203.

[16] A. S. Dukhin and V. A. Murtsovkin, *Pair interaction of particles in electric-field. 2. Influence of polarization of double-layer of dielectric particles on their hydrodynamic interaction in a stationary electric-field*, Colloid J. 48 (1986) 203–209.

[17] A. S. Dukhin, *Pair interaction of disperse particles in electric-field. 3. Hydrodynamic interaction of ideally polarizable metal particles and dead biological cells*, Colloid J. 48 (1986) 376–381.

[18] M. Z. Bazant and T. M. Squires, *Induced-charge electrokinetic phenomena: theory and microfluidic applications*, Phys. Rev. Lett. 92 (2004) 066101.

[19] T. M. Squires and M. Z. Bazant, *Induced-charge electro-osmosis*, J. Fluid Mech. 509 (2004) 217–252.

[20] A. Ramos, H. Morgan, N. G. Green, and A. Castellanos, *AC electrokinetics: a review of forces in microelectrode structures*, J. Phys. D: Appl. Phys. 31 (1998) 2338–2353.

[21] A. Ramos, H. Morgan, N. G. Green, and A. Castellanos, *AC electric-field-induced fluid flow in microelectrodes*, J. Colloid Interface Sci. 217 (1999) 420–422.

[22] A. Ajdari, *Pumping liquids using asymmetric electrode arrays*, Phys. Rev. E 61 (2000) R45(R).

[23] V. Studer, A. Pepin, Y. Chen, and A. Ajdari, *An integrated ac electrokinetic pump in a microfluidic loop for fast and tunable flow control*, Analyst 129 (2004) 944–949.

[24] W. B. Russel, D. A. Saville, and W. R. Schowalter, *Colloidal Dispersions* Cambridge University Press 1 ed. 1991.

[25] A. D. Hollingsworth and D. A. Saville, *A broad frequency range dielectric spectrometer for colloidal suspensions: cell design, calibration, and validation*, J. Colloid Interface Sci. 257 (2003) 65–76.

[26] E. H. B. Delacey and L. R. White, *Dielectric response and conductivity of dilute suspensions of colloidal particles*, J. Chem. Soc., Faraday Trans. 2 77 (1981) 2007–2039.

[27] E. J. Hinch, J. D. Sherwood, W. C. Chew, and P. N. Sen, *Dielectric response of a dilute suspension of spheres with thin double layers in an asymmetric electrolyte*, J. Chem. SOC., Faraday Trans. 2 80 (1984) 535–551.

[28] C. S. Mangelsdorf and L. R. White, *Dielectric response of a dilute suspension of spherical colloidal particles to an oscillating electric field*, J. Chem. Soc., Faraday Trans. 93 (1997) 3145–3154.

[29] L. H. Olesen, M. Z. Bazant, and H. Bruus, *Strongly nonlinear dynamics of electrolytes in large ac voltages*, Phys. Rev. E 82 (2010) 011501.

[30] R. F. Stout and A. S. Khair, *Moderately nonlinear diffuse-charge dynamics under an ac voltage*, Phys. Rev. E 92 (2015) 032305.

[31] O. Schnitzer and E. Yariv, *Nonlinear oscillations in an electrolyte solution under ac voltage.*, Phys. Rev. E 89 (2014) 032302.

[32] M. Z. Bazant, M. S. Kilic, B. D. Storey, and A. Ajdari, *Towards an understanding of induced-charge electrokinetics at large applied voltages in concentrated solutions*, Adv. Colloid Interface Sci. 152 (2009) 48–88.

[33] T. M. Squires, *Induced-charge electrokinetics: fundamental challenges and opportunities*, Lab Chip 9 (2009) 2477–2483.

[34] P. J. Beltramo, R. Roa, F. Carrique, and E. M. Furst, *Dielectric spectroscopy of concentrated colloidal suspensions*, J. Colloid Interface Sci. 408 (2013) 54–58.

[35] C. Grosse and A. V. Delgado, *Dielectric dispersion in aqueous colloidal systems*, Curr.

Opin. Colloid Interface Sci. 15 (2010) 145–159.

[36] A. S. Bandarenka, *Exploring the interfaces between metal electrodes and aqueous electrolytes with electrochemical impedance spectroscopy*, Analyst 138 (2013) 5540–5554.

[37] H. Wang, A. Thiele, and L. Pilon, *Simulations of cyclic voltammetry for electric double layers in asymmetric electrolytes: a generalized modified Poisson–Nernst–Planck model*, J. Phys. Chem. C 117 (2013) 18286–18297.

[38] R. Hidalgo-Alvarez, A. Martin, A. Fernandez, D. Bastos, F. Martinez, and F. J. de las Nieves, *Electrokinetic properties, colloidal stability and aggregation kinetics of polymer colloids*, Adv. Colloid Interface Sci. 67 (1996) 1–118.

[39] R. Pusset, S. Gourdin-Bertin, E. Dubois, J. Chevalet, G. Meriguet, O. Bernard, V. Dahirel, M. Jardat, and D. Jacob, *Nonideal effects in electroacoustics of solutions of charged particles: combined experimental and theoretical analysis from simple electrolytes to small nanoparticles*, Phys. Chem. Chem. Phys. 17 (2015) 11779–11789.

[40] R. Pethig, *Review Article—Dielectrophoresis: status of the theory, technology, and applications*, Biomicrofluidics 4 (2010) 022811.

[41] H. Zhao, *Double-layer polarization of a nonconducting particle in an alternating current field with applications to dielectrophoresis*, Electrophoresis 32 (2011) 2232–2244.

[42] S. Yeh, M. Seul, and B. I. Shraiman, *Assembly of ordered colloidal aggregates by electric-field-induced fluid flow*, Nature 386 (1997) 57–59.

[43] R. W. O'Brien and L. R. White, *Electrophoretic mobility of a spherical colloidal particle*, J. Chem. Soc., Faraday Trans. 2 74 (1978) 1607–1626.

[44] T. J. Woehl, B. J. Chen, K. L. Heatley, N. H. Talken, S. C. Bukosky, C. S. Dutcher, and W. D. Ristenpart, *Bifurcation in the steady-state height of colloidal particles near an electrode in oscillatory electric fields: evidence for a tertiary minimum*, Phys. Rev. X 5 (2015) 011023.

[45] S. C. Bukosky and W. D. Ristenpart, *Simultaneous aggregation and height bifurcation of colloidal particles near electrodes in oscillatory electric fields*, Langmuir 31 (2015) 9742–9747.

[46] J. Kim, J. L. Anderson, S. Garoff, and P. J. Sides, *Effects of zeta potential and electrolyte on particle interactions on an electrode under ac polarization*, Langmuir 18 (2002) 5387–5391.

[47] J. D. Hoggard, P. J. Sides, and D. C. Prieve, *Electrolyte-dependent pairwise particle motion near electrodes at frequencies below 1 kHz*, Langmuir 23 (2007) 6983–6990.

[48] J. D. Hoggard, P. J. Sides, and D. C. Prieve, *Electrolyte-dependent multiparticle motion near electrodes in oscillating electric fields*, Langmuir 24 (2008) 2977–2982.

[49] C. L. Wirth, P. J. Sides, and D. C. Prieve, *Electrolyte dependence of particle motion near an electrode during ac polarization*, Phys. Review. E 87 (2013) 032302.

[50] T. J. Woehl, K. L. Heatley, C. S. Dutcher, N. H. Talken, and W. D. Ristenpart, *Electrolyte-dependent aggregation of colloidal particles near electrodes in oscillatory electric fields*, Langmuir 30 (2014) 4887–4894.

[51] W. D. Ristenpart, I. A. Aksay, and D. A. Saville, *Electrohydrodynamic flow around a colloidal particle near an electrode with an oscillating potential*, J. Fluid Mech. 575 (2007) 83–109.

[52] S. S. Dukhin, *Electrokinetic phenomena of the 2nd kind and their applications*, Adv. Colloid Interface Sci. 35 (1991) 173–196.

[53] V. A. Murtsovkin, *Nonlinear flows near polarized disperse particles*, Colloid J. 58 (1996) 341–349.

[54] S. Gangwal, O. J. Cayre, M. Z. Bazant, and O. D. Velev, *Induced-charge elec-*

trophoresis of metallodielectric particles, Phys. Rev. Lett. 100 (2008) 058302.

[55] S. M. Davidson, M. B. Andersen, and A. Mani, *Chaotic induced-charge electro-osmosis*, Phys. Rev. Lett. 112 (2014) 128302.

[56] X. Yang and N. Wu, *Change the collective behaviors of colloidal motors by tuning electrohydrodynamic flow at the subparticle level*, Langmuir 34 (2018) 952–960.

[57] H. Zhou, L. R. White, and R. D. Tilton, *Lateral separation of colloids or cells by dielectrophoresis augmented by ac electroosmosis*, J. Colloid Interface Sci. 285 (2005) 179–191.

[58] Z. Zheng, B. Jing, M. Sorci, G. Belfort, and Y. Zhu, *Accelerated insulin aggregation under alternating current electric fields: relevance to amyloid kinetics*, Biomicrofluidics 9 (2015) 044123.

[59] K. Mukherjee, G. Schwaab, and M. Havenith, *Cation-specific interactions of protein surface charges in dilute aqueous salt solutions: a combined study using dielectric relaxation spectroscopy and Raman spectroscopy*, Phys. Chem. Chem. Phys. 20 (2018) 29306–29313.

[60] D. Koster, G. Du, A. Battistel, and F. L. Mantia, *Dynamic impedance spectroscopy using dynamic multi-frequency analysis: a theoretical and experimental investigation*, Electrochim. Acta 246 (2017) 553–563.

[61] A. V. Delgado, F. Gonzalez-Caballero, R. J. Hunter, L. K. Koopal, and J. Lyklema, *Measurement and interpretation of electrokinetic phenomena*, J. Colloid Interface Sci. 309 (2007) 194–224.

[62] P. R. C. Gascoyne and J. Vykoukal, *Particle separation by dielectrophoresis*, Electrophoresis 23 (2002) 1973–1983.

[63] A. Koklu, A. C. Sabuncu, and A. Beskok, *Enhancement of dielectrophoresis using fractal gold nanostructured electrodes*, Electrophoresis 38 (2017) 1458–1465.

[64] H. Frusawa, *Frequency-modulated wave dielectrophoresis of vesicles and cells: periodic U-turns at the crossover frequency*, Nanoscale Res. Lett. 13 (2018) 169.

[65] J. Catalano, H. V. M. Hamelers, A. Bentien, and P. M. Biesheuvel, *Revisiting Morrison and Osterle 1965: the efficiency of membrane-based electrokinetic energy conversion*, J. Phys. Condens. Matter 28 (2016) 324001.

[66] J. Catalano and P. M. Biesheuvel, *AC-driven electro-osmotic flow in charged nanopores*, Europhys. Lett. 123 (2018) 58006.

[67] M. Z. Bazant, K. Thornton, and A. Ajdari, *Diffuse-charge dynamics in electrochemical systems*, Phys. Rev. E 70 (2004) 021506.

[68] C. Hughes, L. Yeh, and S. Qian, *Field effect modulation of surface charge property and electroosmotic flow in a nanochannel: Stern layer effect*, J. Phys. Chem. C 117 (2013) 9322–9331.

[69] W. L. Briggs, V. E. Henson, and S. F. McCormick, *A Multigrid Tutorial* SIAM 2 ed. 2000.

[70] G. H. Miller, *Numerical Analysis for Engineers and Scientists* Cambridge University Press 2014.

[71] D. F. Martin and K. L. Cartwright, *Solving Poisson's equation using adaptive mesh refinement*, Technical Report, UCB/ERL M96/66, UC Berkeley, 1996.

[72] M. Z. Bazant, M. S. Kilic, B. D. Storey, and A. Ajdari, *Nonlinear electrokinetics at large voltages*, New J. Phys. 11 (2009) 075016.

[73] S. H. Strogatz, *Nonlinear Dynamics and Chaos* Addison-Wesley Publishing Company 1994.

[74] M. Z. Bazant and T. M. Squires, *Induced-charge electrokinetic phenomena*, Curr. Opin. Colloid Interface Sci. 15 (2010) 203–213.

[75] A. Ramos, P. Garcia-Sanchez, and H. Morgan, *AC electrokinetics of conducting microparticles: a review*, Curr. Opin. Colloid Interface Sci. 24 (2016) 79–90.

[76] N. I. Gamayunov, G. I. Mantrov, and V. A. Murtsovkin, *Study of flows induced in the vicinity of conducting particles by an external electric-field*, Colloid J. 54 (1992) 20–23.

[77] C. Peng, I. Lazo, S. V. Shiyanovskii, and O. D. Lavrentovich, *Induced-charge electro-osmosis around metal and Janus spheres in water: patterns of flow and breaking symmetries*, Phys. Rev. E 90 (2014) 051002.

[78] J. A. Levitan, S. Devasenathipathy, V. Studer, Y. Ben, T. Thorsen, T. M. Squires, and M. Z. Bazant, *Experimental observation of induced-charge electro-osmosis around a metal wire in a microchannel*, Colloids Surf. A 267 (2005) 122–132.

[79] C. Canpolat, S. Qian, and A. Beskok, *Micro-PIV measurements of induced-charge electro-osmosis around a metal rod*, Microfluid Nanofluid 14 (2013) 153–162.

[80] H. Feng, Y. Huang, T. N. Wong, and F. Duan, *Electrolyte effect in induced charge electroosmosis*, Soft Matter 13 (2017) 4864–4870.

[81] J. P. Urbanski, T. Thorsen, J. A. Levitan, and M. Z. Bazant, *Fast ac electro-osmotic micropumps with nonplanar electrodes*, Appl. Phys. Lett. 89 (2006) 143508.

[82] M. Z. Bazant, J. P. Urbanski, J. A. Levitan, K. Subramanian, M. S. Kilic, A. Jones, and T. Thorsen, *Electrolyte dependence of ac electro-osmosis*, Micro total analysis systems 2007, vol. 1. Chemical and Biological Microsystems Society (2007).

[83] B. D. Storey, L. R. Edwards, M. S. Kilic, and M. Z. Bazant, *Steric effects on ac electro-osmosis in dilute electrolytes*, Phys. Rev. E 77 (2008) 036317.

[84] P. Garcia-Sanchez, A. Ramos, A. Gonzalez, N. G. Green, and H. Morgan, *Flow reversal in traveling-wave electrokinetics: an analysis of forces due to ionic concentration gradients*, Langmuir 25 (2009) 4988–4997.

[85] M. S. Kilic, M. Z. Bazant, and A. Ajdari, *Steric effects in the dynamics of electrolytes at large applied voltages. I. Double-layer charging*, Phys. Rev. E 75 (2007) 021502.

[86] M. S. Kilic, M. Z. Bazant, and A. Ajdari, *Steric effects in the dynamics of electrolytes at large applied voltages. II. Modified Poisson–Nernst–Planck equations*, Phys. Rev. E 75 (2007) 021503.

[87] B. Balu and A. S. Khair, *Role of Stefan—Maxwell fluxes in the dynamics of concentrated electrolytes*, Soft Matter 14 (2018) 8267–8275.

[88] P. Garcia-Sanchez, A. Ramos, N. G. Green, and H. Morgan, *Experiments on ac electrokinetic pumping of liquids using arrays of microelectrodes*, IEEE Trans. Dielectr. Electr. Insul. 13 (2006) 670–677.

[89] T. M. Squires and M. Z. Bazant, *Breaking symmetries in induced-charge electro-osmosis and electrophoresis*, J. Fluid Mech. 560 (2006) 65–101.

[90] A. Boymelgreen, G. Yossifon, S. Park, and T. Miloh, *Spinning Janus doublets driven in uniform ac electric fields*, Phys. Rev. E 89 (2014) 011003.

[91] S. T. P. Psaltis and T. W. Farrell, *Comparing charge transport predictions for a ternary electrolyte using the Maxwell–Stefan and Nernst–Planck equations*, J. Electrochem. Soc. 158 (2011) A33–A42.

[92] A. Mani and K. M. Wang, *Electroconvection near electrochemical interfaces: experiments, modeling, and computation*, Ann. Rev. Fluid Mech. 52 (2020) 509–529.

[93] A. M. Drews, L. Cademartiri, M. L. Chemama, M. P. Brenner, G. M. Whitesides, and K. J. M. Bishop, *AC electric fields drive steady flows in flames*, Phys. Rev. E 86 (2012) 036314.

[94] A. M. Drews, L. Cademartiri, G. M. Whitesides, and K. J. M. Bishop, *Electric*

winds driven by time oscillating corona discharges, J. Appl. Phys. 114 (2013) 143302.

[95] C. S. Mangelsdorf and L. R. White, *Electrophoretic mobility of a spherical colloidal particle in an oscillating electric field*, J. Chem. Soc., Faraday Trans. 88 (1992) 3567–3581.

[96] A. W. Adamson, *A Textbook of Physical Chemistry* Academic Press, Inc. 2 ed. 1979.

[97] P. Reimann, *Brownian motors: noisy transport far from equilibrium*, Phys. Rep. 361 (2002) 57–265.

[98] A. K. Vidybida and A. A. Serikov, *Electrophoresis by alternating fields in a non-Newtonian fluid*, Phys. Lett. 108A (1985) 170–172.

[99] S. Flach, O. Yevtushenko, and Y. Zolotaryuk, *Directed current due to broken time-space symmetry*, Phys. Rev. Lett. 84 (2000) 2358–2361.

[100] O. Yevtushenko, S. Flach, Y. Zolotaryuk, and A. A. Ovchinnikov, *Rectification of current in ac-driven nonlinear systems and symmetry properties of the Boltzmann equation*, Europhys. Lett. 54 (2001) 141–147.

[101] S. Denisov, S. Flach, A. A. Ovchinnikov, O. Yevtushenko, and Y. Zolotaryuk, *Broken space-time symmetries and mechanisms of rectification of ac fields by nonlinear (non)adiabatic response*, Phys. Rev. E 66 (2002) 041104.

[102] M. Schiavoni, L. Sanchez-Palencia, F. Renzoni, and G. Grynberg, *Phase control of directed diffusion in a symmetric optical lattice*, Phys. Rev. Lett. 90 (2003) 094101.

[103] P. H. Jones, M. Goonasekera, and F. Renzoni, *Rectifying fluctuations in an optical lattice*, Phys. Rev. Lett. 93 (2004) 073904.

[104] R. Gommers, S. Bergamini, and F. Renzoni, *Dissipation-induced symmetry breaking in a driven optical lattice*, Phys. Rev. Lett. 95 (2005) 073003.

[105] R. Gommers, S. Bergamini, and F. Renzoni, *Quasiperiodically driven ratchets for cold atoms*, Phys. Rev. Lett. 96 (2006) 240604.

[106] S. Denisov, L. Morales-Molina, and S. Flach, *Quantum resonances and rectification in ac-driven ratchets*, Europhys. Lett. 79 (2007) 10007.

[107] S. Denisov, L. Morales-Molina, S. Flach, and P. Hänggi, *Periodically driven quantum ratchets: symmetries and resonances*, Phys. Rev. A 75 (2007) 063424.

[108] M. Adams et al., *Chombo Software Package for AMR Applications – Design Document*, Technical Report, LBNL-6616E, Lawrence Berkeley National Laboratory, 2019.

[109] P. Colella et al., *EBChombo Software Package for Cartesian Grid – Embedded Boundary Applications*, Technical Report, LBNL-6615E, Lawrence Berkeley National Laboratory, 2020.

[110] Y. Solomentsev, M. Bohmer, and J. L. Anderson, *Particle clustering and pattern formation during electrophoretic deposition: a hydrodynamic model*, Langmuir 13 (1997) 6058–6068.

[111] P. Moon and D. E. Spencer, *Field Theory Handbook* Springer 2 ed. 1988.

[112] M. Stimson and G. B. Jeffery, *The motion of two spheres in a viscous fluid*, Proc. R. Soc. A 111 (1926) 110–116.

[113] R. B. Bird, W. E. Stewart, and E. N. Lightfoot, *Transport Phenomena* John Wiley & Sons, Inc. 2 ed. 2002.